Mesoscale simulations and inversions of atmospheric CO_2 using airborne and ground-based data

Dissertation

zur Erlangung des akademischen Grades doctor rerum naturalium
(Dr. rer. nat.)

durchgeführt am Max-Planck-Institut für Biogeochemie Jena

vorgelegt dem Rat der Chemisch-Geowissenschaftlichen Fakultät
der
Friedrich-Schiller-Universität Jena

von M.Sc. (Physics), M.Tech. (Ocean Tech.) Dhanyalekshmi K. Pillai
geboren am 15.03.1981 in Varkala, India

Gutachter:

1. Dr. habil. Christoph Gerbig, Max-Planck-Institut für Biogeochemie, Jena

2. Prof. Dr. Christiane Schmullius, Friedrich-Schiller-Universität, Jena

Datum der öffentlichen Verteidung: 20th April 2011

TABLE OF CONTENTS

Chapter I

Chapter II

Chapter III

Chapter VI

Chapter VII

ABSTRACT

An improved quantitative understanding of the geographical distribution of CO_2 sources and sinks is indispensable in the context of ongoing climate change. Knowing the regional distribution of biosphere-atmosphere exchange is important for assessing potential feedbacks between climate and the carbon cycle. This is also crucial for implementing adequate emission reduction and sequestration strategies towards mitigating adverse effects of climate change. Measurements of atmospheric CO_2 concentrations contain information about CO_2 exchanges between the surface and the atmosphere.This information can be quantitatively deduced from atmospheric measurements via inverse transport modeling on different spatial and temporal scales, using a priori information on the spatial and temporal distribution of surface-atmosphere fluxes in a Bayesian framework. So far, mostly global inverse modeling tools together with global networks of observations, which have recently been augmented with tall tower observatories, have been used to estimate the source-sink distribution of CO_2. However, these tall-tower-based measurements are often influenced by strong variability of the surface fluxes in the near-field (within a 20-100 km radius of the observatories) and by mesoscale transport phenomena. These significant variations occur at scales that are not resolved by current global transport models, which have spatial scales of at most 1°×1°. These unresolved variations can introduce significant bias in flux estimates. Furthermore, fluxes in the near-field of the observatories are highly variable, calling for a-priori fluxes to be specified at high spatial resolution. This necessitates the development of high-resolution modelling frameworks.

This thesis presents a mesoscale inversion technique which takes into account the spatial variability of CO_2 at regional scales. A high-resolution modeling framework consisting of the models: the Weather Research Forecast (WRF; a weather prediction model), the Vegetation Photosynthesis and Respiration Model (VPRM; a diagnostic biosphere model), and the Stochastic Time-Inverted Lagrangian Transport model (STILT; a particle dispersion model) is set up to derive biosphere-atmosphere exchange at regional scales using airborne and ground-based measurements of CO_2. Using high-resolution simulations, the representation errors (spatial scale mismatch between CO_2 measurements and inverse models, i.e. the variability not resolved by

global models) associated with the utilization of satellite measurements in current generation global models are estimated over Europe. The estimated representation errors are found to be above the targeted accuracy of the satellite retrievals. A linear model is formulated that could explain about 50 % of the spatial patterns in the systematic (bias or correlated error) component of representation error during day- and nighttime. These findings suggest a possible parameterization of representation error that allows for the provision of structural information on the representation error to inverse models or data assimilation systems. Chapter 3 focuses on these.

Further, the ability of high-resolution modeling tools to simulate meteorological and CO_2 fields at a mountain observatory – the Ochsenkopf tall tower in Germany – is assessed. This is essential in order to utilize measurements made in complex orography (e.g. mountain and coastal sites) in an atmospheric inverse framework to better estimate regional fluxes of these trace gases. The tower measurements made at different heights for different seasons together with data collected during an aircraft campaign in the vicinity of the tower are used for this purpose. The results suggest that the high-resolution models can capture diurnal, seasonal and synoptic variability of observed mixing ratios much better than coarse global models. The effects of mesoscale transports such as mountain-valley circulations and mountain-wave activities on atmospheric CO_2 distributions are reproduced remarkably well in the high-resolution models. The study emphasizes the potential of using high-resolution models in the context of inverse modeling frameworks to utilize measurements provided from mountain or complex terrain sites. Chapter 4 addresses these.

A quantitative comparison between atmospheric CO_2 concentrations generated by the Eulerian based WRF and the Lagrangian based STILT models, while using identical surface-atmosphere fluxes and meteorological fields, is carried out in order to check the consistency of transport and turbulent mixing as represented by WRF and STILT. The inter-model differences are found to be small in most of the cases. A case study using airborne measurements during which both models showed larger deviations is analyzed in detail as an extreme case. It is shown that a refinement of the parameterization of turbulent velocity variance and Lagrangian time-scale in STILT is likely needed when using meteorological fields with high spatial resolution. In general, the inter-model differences in simulated CO_2 time series are estimated to be about a factor of two smaller than the model-data mismatch, which justifies using

STILT as an adjoint model of WRF but which at the same time indicates a requirement for further improvements when working at such high spatial resolutions. Chapter 5 focuses on these.

A mesoscale inverse technique to derive the biosphere-atmosphere exchange fluxes, utilizing atmospheric CO_2 concentration measurements from the Ochsenkopf tall tower, is presented. The modeling framework also uses the information provided by eddy covariance flux towers and remote sensing data streams which are used to constrain prior knowledge of the biosphere-atmosphere fluxes in inverse analysis. The posterior fluxes (after the inversion) are estimated and the reduction in uncertainties of these retrieved fluxes is assessed. Moreover these fluxes are compared with direct observations from independent eddy flux measurements. Chapter 6 presents these results.

Overall, the thesis shows that a mesoscale model-data fusion system consisting of a weather prediction model, a Lagrangian adjoint transport model, and a diagnostic biosphere flux model is capable of simultaneously utilizing information from tower-based mixing ratio observations, eddy covariance flux measurements, and remote sensing of the biosphere to estimate surface-atmosphere fluxes at an unprecedented spatial resolution of 2 km. The high-resolution allows for a much better representation of the near-field around atmospheric observing sites, significantly reducing model representation errors, specifically for complex terrain sites such as mountains, compared to previous inverse transport models. Future work will be needed to implement such a system for a full network of atmospheric observing stations.

x

ZUSAMMENFASSUNG

Ein verbessertes quantitatives Verständnis der geographischen Verteilung der Quellen und Senken von Kohlenstoffdioxid (CO_2) ist im Zuge des Klimawandels unerlässlich. Kenntnisse über die regionale Verteilung des Austausches von CO_2 zwischen Biosphäre und Atmosphäre sind wichtig, um mögliche Rückkopplungen zwischen Klima und Kohlenstoffkreislauf einschätzen zu können. Dies ist auch entscheidend für die Entwicklung von Strategien, die dem Klimawandel entgegenwirken, wie die Verminderung von CO_2-Emissionen oder die Sequestrierung von Kohlenstoff. Messungen der atmosphärischen CO_2-Konzentration geben Auskunft über den CO_2-Austausch zwischen Erdoberfläche und Atmosphäre. Diese Information kann quantitativ aus Messungen in der Atmosphäre in Kombination mit inverser Transportmodellierung auf verschiedenen räumlichen und zeitlichen Skalen abgeleitet werden. Dazu werden a-priori-Informationen über die zeitliche und räumliche Verteilung von Austauschflüssen zwischen Erdoberfläche und Atmosphäre in einem Bayesschen Ansatz verwendet. Bisher werden größtenteils Inversionssysteme auf globaler Skala verwendet, um die Verteilung der Quellen und Senken von CO_2 abzuschätzen. Das Beobachtungsnetz dieser Systeme umspannt den gesamten Globus und wurde kürzlich um Beobachtungsstationen auf hohen Türmen – sogenannten Tall Towers – erweitert. Jedoch werden die Messungen auf diesen hohen Türmen oft durch die starke Variabilität der CO_2-Flüsse an der Erdoberfläche im Bereich des Nahfeldes (Umkreis von 20-100 km von der Beobachtungsstation) und durch mesoskalige Transportphänomene in der Atmosphäre beeinflusst. Dies löst signifikante Änderungen der CO_2-Flüsse auf einer Skala aus, die von gängigen globalen Modellen (mit einer maximalen räumliche Auflösung von bis zu einem Grad), nicht mehr erfasst werden können. Dies kann zu systematischen Fehlern in der Abschätzung der Flüsse führen. Des Weiteren sind die Flüsse im Nahfeld der Beobachtungsstationen hochgradid variabel, was die Notwendigkeit einer Spezifizierung von hochaufgelösten a-priori-Austauschflüssen bedingt. Dies erfordert die Entwicklung eines hochaufgelösten Modellsystems.

Die hier vorliegende Dissertation stellt eine Inversionsmethode vor, welche die räumliche Variabilität von CO_2 auf der Mesoskala miteinbezieht. Ein hochaufgelöstes Modellsystem wird erstellt, um den Austausch von CO_2 zwischen Biosphäre und

Atmosphäre mithilfe von Flugzeug- und Bodenstationsmessungen zu ermitteln. Es besteht aus drei verschiedenen Modellen: Dem Wettervorhersagemodell WRF (Weather Research and Forecast model), dem diagnostischen Biosphärenmodell VPRM (Vegetation Photosynthesis and Respiration model) und dem Partikel-Dispersionsmodell STILT (Stochastic Time Inverted Lagrangian Transport Model). In Kapitel 3 dieser Arbeit wird anhand von hochaufgelösten Simulationen der Repräsentationsfehler – die Diskrepanz zwischen CO_2-Beobachtungen und Resultaten inverser Modelle auf räumlicher Ebene, d.h. die von globalen Modellen nicht erfasste Variabilität - für die jetzige Generation globaler Modelle ermittelt. Dies geschieht unter Verwendung von Satellitenmessungen. Die berechneten Repräsentationsfehler liegen oberhalb der angestrebten Genauigkeit von Satelliten-Retrievals. Daher wurde ein lineares Modell entwickelt, das etwa 50% des räumlichen Verteilungsmusters in der systematischen Komponente des Repräsentationsfehlers erklären kann. Diese Ergebnisse legen eine mögliche Parametrisierung des Repräsentationsfehlers nahe, die Strukturinformationen über diesen Fehler für die Anwendung in inversen Modellen oder Datenassimilationssystemen nutzbar macht.

In Kapitel 4 wird die Fähigkeit hochaufgelöster Modelle zur Simulation von dreidimensionalen meteorologischen und CO_2-Feldern an einer auf einem Berg gelegenen deutschen Beobachtungsstation – dem Ochsenkopf im Fichtelgebirge - untersucht. Diese Fähigkeit ist unerlässlich, um Messungen von Beobachtungsstationen, die sich in komplexer Orographie (z.B. auf Bergen oder an Küsten) befinden, in ein atmosphärisches Inversionssystem zur besseren Abschätzung der regionalen Flüsse von diesen Spurengasen einzubinden. Zu diesem Zweck wurden Messungen des Ochsenkopf-Turms in verschiedenen Höhen und zu verschiedenen Jahreszeiten, sowie Daten von einer Flugkampagne in der Nähe des Messturm verwendet. Die Resultate zeigen, dass hochaufgelöste Modelle den Tagesgang sowie die saisonale und synoptische Variabilität der beobachteten Mischungsverhältnisse wesentlich besser wiedergeben als globale Modelle. Die Effekte von mesoskaligen Transportphänomenen wie Berg-Tal-Zirkulation oder internen Schwerewellen auf die CO_2-Verteilung in der Atmosphäre werden in den hochaufgelösten Modellen bemerkenswert gut wiedergegeben. Diese Studie unterstreicht das Potential, hochaufgelöste Modelle in Inversionsmodellsystemen zu

verwenden, um Beobachtungen von Bergstationen oder generell Messstationen in komplexem Terrain zu verwenden.

In Kapitel 5 wurde ein quantitativer Vergleich zwischen CO_2-Simulationen des auf der Eulerschen Zerlegung basierenden WRF-Modells und des Lagrange´schen Transportmodells STILT durchgeführt. Hierbei wurden jeweils identische Meteorologie und Austauschflüsse zwischen Erdoberfläche und Atmosphäre verwendet, um die Konsistenz von Transport und turbulenter Mischung in beiden Modellen zu prüfen. Die Unterschiede zwischen beiden Modellen stellten sich in den meisten Fällen als klein heraus. Eine Fallstudie analysiert unter Benutzung von Flugzeugmessungen im Detail einen Extremfall, für den beide Modelle größere Abweichungen voneinander zeigen. Es zeigt sich, dass sehr wahrscheinlich eine genauere Einstellung der Parametrisierung für die turbulente Geschwindigkeitsvarianz und die Lagrange´schen Zeitskala im STILT-Modell für die Verwendung hochaufgelöster meteorologischer Felder notwendig sind. Im Vergleich zu realen Beobachtungen liegen die Unterschiede zwischen den von beiden Modellen simulierten CO_2-Zeitreihen generell einen Faktor zwei niedriger. Dies rechtfertigt es, das STILT-Modell als ein adjungiertes Modell zu WRF zu benutzen, weist aber gleichzeitig darauf hin, dass weitere Verbesserungen erforderlich sind, um auf solch einer hohen Auflösung zu arbeiten.

Ein mesoskaliges Inversionssystem zur Ermittlung der Austauschflüsse zwischen Erdoberfläche und Atmosphäre, das die atmosphärischen CO_2 Konzentrationsmessungen der Beobachtungsstation auf dem Ochsenkopf benutzt, wird in Kapitel 6 vorgestellt. Das Modellsystem verwendet zusätzlich Informationen von Eddy-Kovarianz Flussmessungen auf Türmen und Datenströme von Fernerkundungssystemen in der inversen Analyse. Der a-posteriori-Fluss (d.h. der Fluss nach der Inversion) wird ermittelt und die Abnahme der Unsicherheiten der erhaltenen CO_2-Flüsse berechnet. Darüberhinaus werden diese Flüsse mit direkten Beobachtungen von unabhängigen Eddy-Kovarianz Flussmessungen verglichen.

In ihrer Gesamtheit zeigt die Dissertation, dass ein mesoskaliges Modell-Daten-Fusionssystem, bestehend aus einem Wettervorhersagemodell, einem adjungierten Lagrange´schem Transportmodell und einem diagnostischen Biosphärenmodell, imstande ist, gleichzeitig Informationen über Mischungsverhältnisse von Turm-Messstationen, Eddy-Kovarianz Flussmessungen und Fernerkundungsdaten der

Biosphäre zu verwenden, um die Austauschflüsse zwischen Erdoberfläche und Atmosphäre auf einer bisher noch nicht da gewesenen räumlichen Auflösung von 2km zu berechnen. Die hohe Auflösung ermöglicht speziell für Orte mit komplexer Orographie, wie z.B. Berge, eine wesentlich bessere Darstellung des Nahfeldes im Umkreis der atmosphärischen Messstationen und eine signifikante Abnahme des Repräsentationsfehlers der Modelle im Vergleich zu bisherigen inversen Transportmodellen. Weitere Arbeiten werden allerdings notwendig sein, um eine solches System in ein komplettes Beobachtungsnetzwerk von atmosphärischen Messstationen einzubinden.

LIST OF FIGURES

xvi

LIST OF TABLES

Introduction

The Earth and its climate, upon which life depends, have recently become society's greatest concerns. Any anthropogenic interventions occurring on a scale capable of changing several complex physical, chemical and biological processes that involves linear as well as non-linear interactions among the atmosphere, hydrosphere and biosphere can affect the Earth's climate in a profound way. Humans have brought about large perturbations to the natural cycling of the major elements (e.g. carbon, nitrogen, sulfur, phosphorous and trace metals) in the planet's biogeochemical cycles in a variety of ways. Understanding the impact of these changes on the biogeochemical processes and their feedbacks on the climate system is critical for projecting changes in climate and is hence in high demand among various scientific, economic and political communities, both now and in the coming decades.

As an example, it is widely known in the scientific community that an increase in greenhouse gases[1] in the atmosphere can modify these processes and lead to a new stationary state (energy balance between incoming shortwave radiation and outgoing longwave radiation) with increased global surface temperature. Among the greenhouse gases of anthropogenic origin, the increase in atmospheric carbon dioxide (CO_2) is of major concern due to its large contribution (32 Wm^{-2}) to the total longwave radiative forcing[2] of 125 Wm^{-2} (Kiehl and Trenberth, 1997). Additionally, there is clear evidence from the continuous records provided by observatories (e.g. Thoning et al. (1989)) and ice-cores (e.g. Leuenberger et al. (1992)) that the amount

---

[1] Gases which absorb (and re-emit in all directions) the thermal longwave radiation emitted from the earth surface and increase the opacity of the atmosphere. As a consequence, the Earth's surface temperature is increased according to the Stefan-Boltzmann law (radiation is proportional to the fourth power of the Earth's surface temperature). This effect was discovered in 1824 by Joseph Fourier and quantified in 1896 by Svante Arrhenius. The major greenhouse gases are water vapor (H_2O), carbon dioxide (CO_2), methane (CH_4), tropospheric ozone (O_3) and nitrous oxide (N_2O).

[2] The radiative imbalance in the climate system caused by anthropogenic and natural influences. The Intergovernmental Panel on Climate Change (IPCC) defined radiative forcing is as follows: "a measure of how the energy balance of the Earth-atmosphere system is influenced when factors that affect climate are altered…Radiative forcing is usually quantified as the rate of energy change per unit area of the globe as measured at the top of the atmosphere, and is expressed in units of Watts per square meter (Wm^{-2}). When radiative forcing from a factor or group of factors is evaluated as positive, the energy of the Earth-atmosphere system will ultimately increase, leading to a warming of the system. In contrast, for a negative radiative forcing, the energy will ultimately decrease, leading to a cooling of the system." (Forster et al., 2007)

of CO_2 in the atmosphere has been increasing exponentially since the beginning of the industrial era (~260 years ago). Naturally the significant and long-lasting influence of CO_2 on the Earth's radiation budget and on the global climate system provides a strong motivation for scientific research on the global carbon cycle.

The purpose of this chapter is to review the present state of carbon research, which provides the impetus for this thesis. The first part of this chapter reviews the current understanding of the global carbon cycle, focusing on human perturbations to the climate system. The second part evaluates in brief the significance of managing the carbon cycle and the requirement to do so, as well as the key scientific questions in the context of international environmental treaties related to climate change. This is followed by recent progress in deriving the atmospheric CO_2 budget (third part). The fourth and fifth parts address recent developments in the observational and modeling methodologies to aid the efforts towards climate change mitigation and adaptation as well as carbon sequestration. Finally, in the sixth part, the scope and objectives of this thesis are presented together with the thesis outline.

1.1 Global carbon cycle

The major carbon reservoirs are the atmosphere, the hydrosphere (ocean including fresh water bodies), terrestrial biosphere, and the lithosphere (sediments and sedimentary rocks). Carbon is exchanged actively among the aforementioned first three reservoirs within the time frame of years to centuries (fast spheres). However the carbon flux rates are slower through the sediments and sedimentary rocks (via processes such as weathering, glacial erosion and volcanic activities) with millennial time scales (slow spheres), despite its larger storage capacity of about 9×10^7 Petagrams of carbon per year (Pg C yr^{-1}) (Sundquist, 1993). An overview of the carbon cycle is shown in **Fig. 1.1.** Since the carbon exchanges through the slow spheres are generally less significant in carbon budgets on time scales of a century or so, further discussions are limited to the fast reservoirs.

1.1.1 The atmosphere

As evident from Fig. 1.1, atmospheric carbon plays an important role in linking various biological, physical and anthropogenic processes. The carbon is mainly present in the atmosphere as CO_2 together with minor amounts of CH_4, CO and other

trace gases, mostly hydrocarbons. The long-term observational evidence of the atmospheric CO_2 mixing ratios suggests that the amount continues to rise with an average annual growth rate of 3.4 ± 0.1 Pg C yr^{-1}, reaching the present global average mixing ratio of 387.2 ppm (http://www.esrl.noaa.gov/gmd/ccgg/trends/). **Figure 1.2** shows, as an example, the longest record of direct measurements of atmospheric CO_2, available since 1958 at Mauna Loa Observatory, Hawaii (Keeling et al., 1976). Unequivocally, the increase in CO_2 from ~280 ppm in the pre-industrial times (Etheridge et al., 1996) to the present value has been caused by fossil fuel emissions, deforestation and other land-use changes. The higher amount of atmospheric CO_2 is reported to be the major cause of global warming (Le Treut et al., 2007).
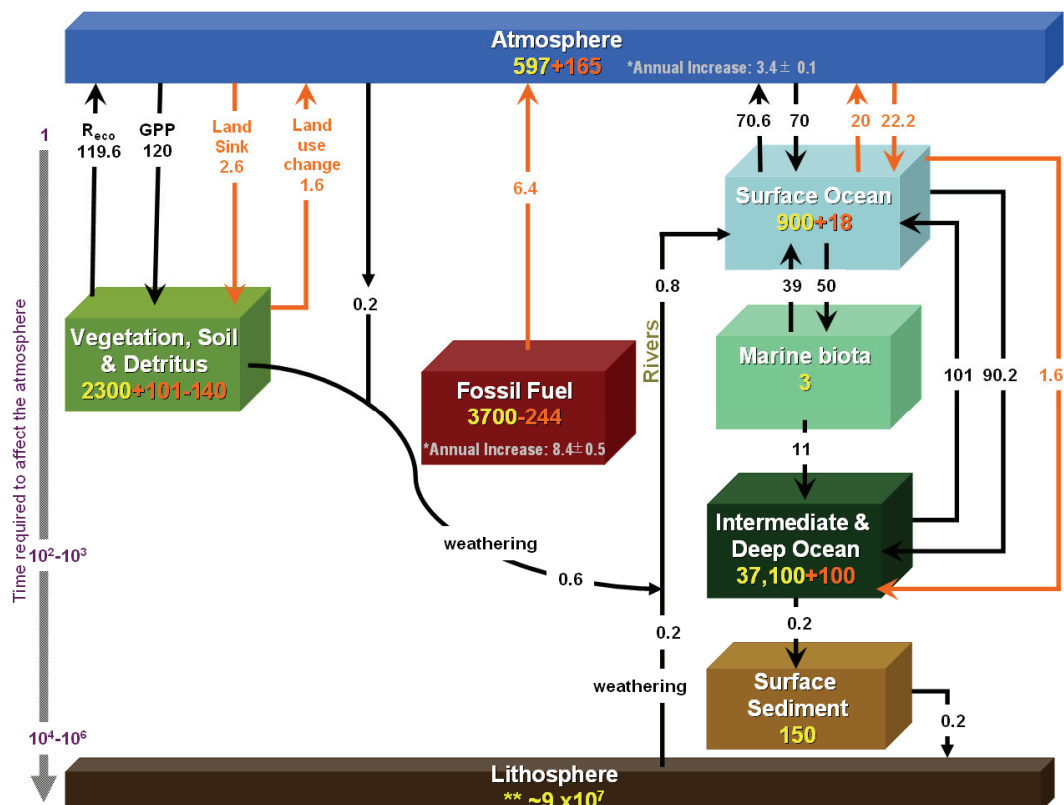
Figure 1.1 *A schematic overview of the global carbon cycle, showing the main annual mean fluxes of carbon in units of Pg C yr^{-1} (Petagrams of carbon per year; 1 Pg C = 10^{15} grams C). The annual estimates of natural fluxes are given in* <u>*black*</u> *and anthropogenic fluxes are in* <u>*orange*</u>*. The major reservoirs are depicted as cubes with the carbon storage size in Pg C. Inside the cube: the pre-industrial (prior to the year 1750) estimates of carbon content in the reservoirs are in* <u>*yellow*</u> *and the anthropogenic perturbations are in* <u>*orange*</u>*. The vertical bar in* <u>*grey*</u> *(at the left-hand side) denotes the time-scale on which various components of the global carbon cycle interact with the atmosphere. For more details on the estimates of fluxes and reservoirs shown here, the reader is referred to the IPCC report (http://www.ipcc.ch/pdf/assessment-report/ar4/wg1/ar4-wg1-chapter7.pdf). *: Recent updates from Friedlingstein (2010). **: taken from Sundquist (1993).*

The global fossil fuel emissions of CO_2, computed from statistics of energy consumption at the country level, are shown in **Fig. 1.3.** The emissions due to fossil fuel and cement emissions show an increasing growth rate until the year 2008 and then a decrease by 1.3% in the next year, owing to the financial crisis that began in the year 2008. The current fossil fuel and cement emissions are estimated to be 8.4 ± 0.5 Pg C, however they are projected to increase by 3% in the year 2010, according to economic growth predictions (Friedlingstein, 2010). On the other hand, a decreasing trend in emissions due to deforestation and land-use change is found, with current estimates of about 1.1 ± 0.7 Pg C (Canadell et al., 2007; Friedlingstein, 2010; Le Quéré et al., 2009).
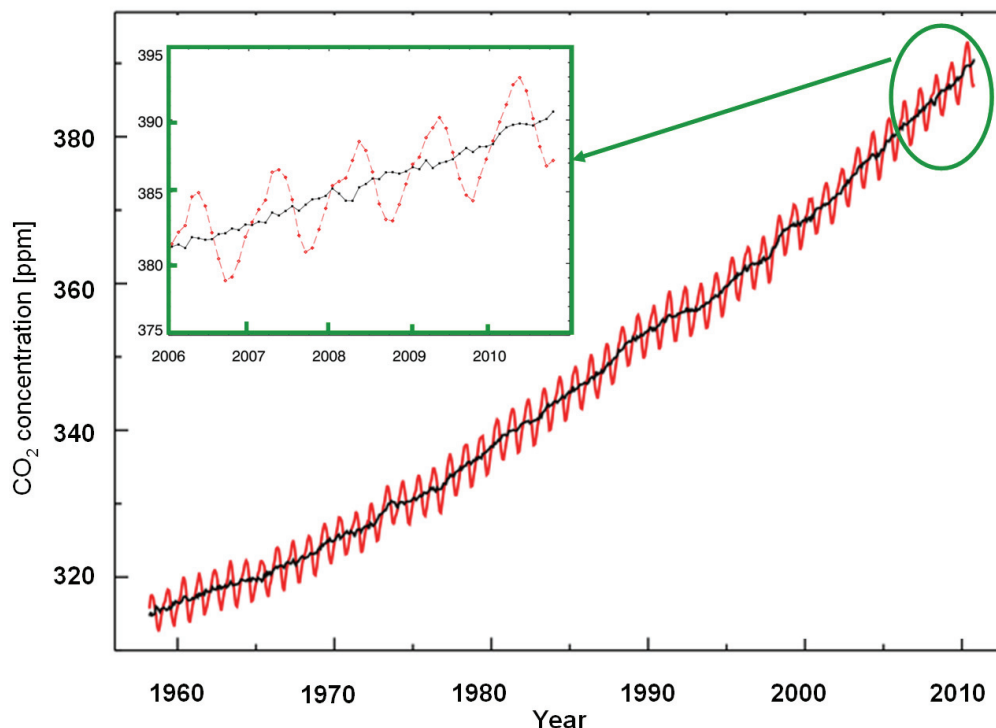
Figure 1.2 *The complete time series of monthly averaged atmospheric CO_2 mixing ratios (the* <u>*red*</u> *curve), expressed as parts per million [ppm] on Mauna Loa, Hawaii, the longest record of direct measurements of CO_2 in the atmosphere. The* <u>*black*</u> *curve represents the seasonally corrected data (as determined as a moving average of adjacent seasonal cycles). The inset zooms in on the period over the last four years. The annual CO_2 growth-rate at this site for the year 2009 is 1.92 ± 0.11 ppm yr^{-1}. Data are courtesy of* <u>*http://www.esrl.noaa.gov/*</u>*.*

As can be seen from Fig(s).1.2 and 1.3, the annual growth rate of atmospheric CO_2 is significantly smaller than the increment in the anthropogenic emissions, which is due to the fact that the terrestrial biosphere and the ocean (see following sections) act as

natural sinks to remove a large part of these CO_2 emissions from the atmosphere. The term airborne fraction[3] (AF) is used to assess the efficiency of these natural reservoirs and it is found to be 0.45 on average (Canadell et al., 2007; Marland et al., 2007), i.e. 45% of the anthropogenic CO_2 emissions remained in the atmosphere and the rest were absorbed by terrestrial and oceanic sinks. The AF exhibits large inter-annual variability due to varying responses of sources and sinks, particularly over land. The increasing trend of the AF and its statistical significance are still debated (Knorr, 2009) due to many unknowns such as coupling mechanisms between emission rates and source strengths as well as deforestation fluxes (van der Werf et al., 2009).
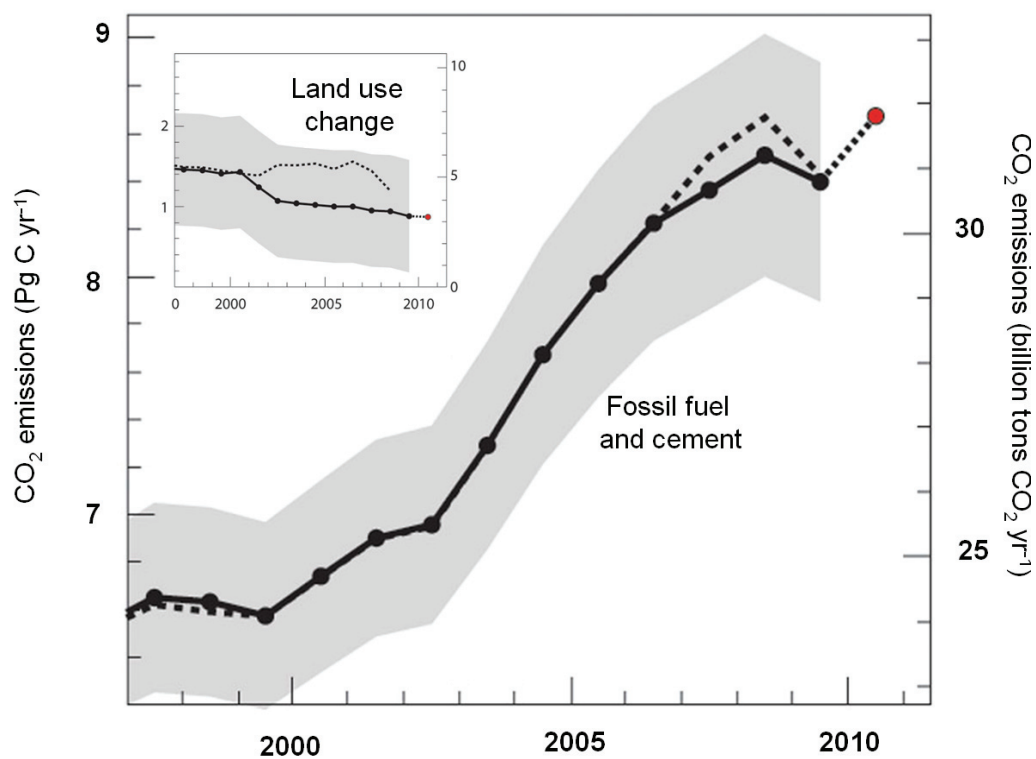
Figure 1.3 *Global CO_2 emissions from fossil fuel (based on United Nations Energy Statistics) and cement production (from the US Geological Survey). The inset shows CO_2 emissions from deforestation and land-use changes (based on statistics from the Food and Agriculture Organization of the United Nations). The* black solid *curve with circles shows results from Le Quéré et al. (2009) and the* black dashed *curve is the updated emission information from Friedlingstein (2010). The plot is reproduced from Friedlingstein (2010). The* red dot *denotes projections for the year 2010.*

[3] According to IPCC report, the airborne fraction is defined as the atmospheric CO_2 increase as a fraction of total anthropogenic CO_2 emissions, including the net land use fluxes.

1.1.2 Ocean-atmosphere exchange

The total amount of carbon in the ocean is approximately 38,100 Pg C, i.e. nearly 50 times more than that in the atmosphere. About 98.5% of this oceanic carbon exists as dissolved inorganic carbon (DIC) in the ocean, mostly in the form of bicarbonate and carbonate ions. The two independent estimates of ocean fluxes, based on (inverse) modeling (Fletcher et al., 2006) and on estimates of air-sea differences of partial pressure of CO_2 (pCO_2) (Takahashi et al., 2008), show good agreement (Gruber et al., 2009) with differences at the regional level less than 0.1 Pg C yr^{-1}. On the global average, for the period between 1995 and 2000, the above-mentioned inverse study predicted an uptake flux of anthropogenic carbon of 2.2 ± 0.3 Pg C yr^{-1}, while the pCO_2 climatology estimated 1.9 ± 0.7 Pg C yr^{-1}. The Southern Ocean (south of 44° S), being the strongest regional oceanic sink for anthropogenic CO_2, received much attention recently. The inverse simulations show that the Southern Ocean reacted in a highly sensitive manner to climate variability over the past 50 years, and will likely continue to do so for a given future climate change (Gruber et al., 2009). The limited observational evidences and the lack of consideration of long-term changes in the ocean carbon cycle make it difficult to determine with sufficient confidence whether or not the Southern Ocean sink is varying in a significant manner (Gruber, 2009). In the North Atlantic (the largest ocean sink for atmospheric CO_2 in the Northern Hemisphere), the sink of atmospheric CO_2 exhibits substantial interannual variability and the oceanic uptake in the region between 20° N and 65° N declined by 0.24 Pg C yr^{-1} from 1994-1995 to 2002-2005 (Schuster and Watson, 2007). However, it is too early to draw firm conclusions as to whether this decline is linked to a rearrangement of the global oceanic carbon cycle in response to climate variations or to natural variations in the North Atlantic Oscillation. More comprehensive studies are needed with appropriate observational systems to quantify accurate estimates of ocean carbon sinks and to assess future changes in the ocean carbon cycle.

1.1.3 Terrestrial biosphere

The amount of carbon stored in land vegetation is comparable to the amount contained in the atmosphere, while the soil contains nearly two to three times this amount. There is rapid exchange of carbon between the atmosphere, terrestrial biota and soils through processes such as photosynthesis and decomposition. The

complexity of the biological systems involving carbon storage, the large heterogeneity of terrestrial vegetation and soils and the effect of land-use changes make it difficult to quantify their role in the global carbon cycle. For this reason the net exchange of carbon between the terrestrial ecosystems and the atmosphere is highly uncertain, giving rise to the largest uncertainty in the global carbon budget[4] (e.g. Dolman et al. (2008), Schimel et al. (2001)).

Two methods including different processes namely, top-down (Peters, 2010; Peylin et al., 2005b; Rödenbeck et al., 2003a; Enting, 1993; Gurney et al., 2002; Lauvaux et al., 2008) and bottom-up (Desai et al., 2005; Hurtt et al., 2001; Luyssaert et al., 2007; Luyssaert et al., 2008) methods are currently used to estimate terrestrial sources and sinks. The top-down method (inverse approach) utilizes the observed atmospheric CO_2 concentrations to back-calculate the distribution of sources and sinks at regional or continental scales, using atmospheric transport models, while the bottom-up method estimates biospheric uptake directly from forest inventories or by process-based ecosystem models from local scales (leaf-level process information) to the region and to the globe. As there is no direct method to infer the carbon budget, the accuracy of the aforementioned approaches largely depends on the validity of the underlying assumptions. Both approaches often give contradictory results as shown in **Fig. 1.4**; hence a detailed analysis of the carbon balance is necessary to quantitatively separate sources and sinks to close the gap between these approaches.

Recently, attempts have been made to estimate the carbon balance of Europe and China by combining top-down and bottom-up approaches through various data and modeling streams such as inventories, field measurements, remote sensing, process-based ecosystem models, and atmospheric inversions (Piao et al., 2009; Schulze et al., 2009). These studies reported a terrestrial net carbon sink of 0.27 ± 0.16 Pg C yr^{-1} for continental Europe (Schulze et al., 2009) between the years 2000 and 2005 and 0.23 ± 0.04 Pg C yr^{-1} during the 1980s and 1990s (Piao et al., 2009).

---

[4] The balance between sources and sinks of CO_2 in the atmosphere, expressed in terms of anthropogenic emissions and fluxes between the main reservoirs and the build-up of CO_2 in the atmosphere.
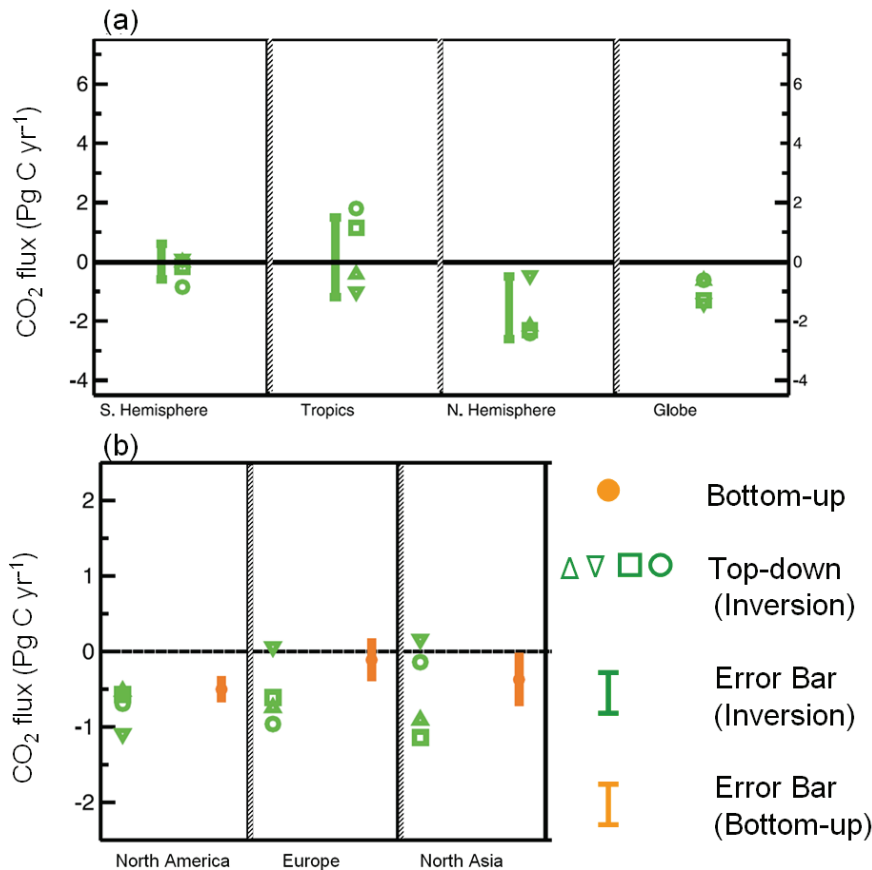
Figure 1.4 *(a) Global and (b) regional terrestrial CO_2 fluxes in Pg C yr^{-1}. The fluxes provided by inversion models are in <u>green</u>: square-Gurney et al.(2002), circle- Gurney et al. (2003), Triangle- Peylin et al. (2005a) and inverted triangle- Rödenbeck et al.(2003b). The bottom-up estimates of regional fluxes (in <u>orange</u>) are based on Fang (2001), Janssens et al.(2003), Kurz and Apps (1999), Pacala et al. (2001), Shvidenko and Nilsson (2003). Fluxes to the atmosphere are given as positive numbers and land uptake has a negative sign. Data courtesy of Denman et al. (2007).*

1.2 International Climate Treaty: Significance and Requirements

An international treaty, the United Nations Framework Convention on Climate Change (http://unfccc.int/2860.php), with the participation of 194 parties, entered into force on 21st March 1994, and laid out emission reduction and sequestration strategies toward climate change mitigation. The ultimate objective of the Convention is the "stabilization of greenhouse gas concentrations in the atmosphere at a level that will prevent dangerous human interference with the climate system." A more powerful addition to the treaty, the Kyoto Protocol (http://unfccc.int/kyoto_protocol/items/ 2830.php) was approved on 16th February 2005, as a first step for providing the essential architecture for any future international agreement on climate change. As a response to the Kyoto protocol, more than 100 countries have adopted a global warming limit of 2 °C or below. However, determining probabilistic climate change

in response to the future emission scenarios is challenging owing to the current uncertainties in the carbon cycle, radiative forcing and climate feedbacks[5]. Reliable estimates of sources and sinks at high-resolution temporal and spatial scales are indispensable in predicting future increases in atmospheric CO_2 to a high degree of certainty. Furthermore, the feedback mechanisms between the carbon cycle and the global climate system must be incorporated in general circulation models (GCM) for projecting changes in climate (Denman et al., 2007). These feedbacks are particularly important for implementing emission reduction and sequestration strategies (Meinshausen et al., 2009). The strong scientific interest in regional aspects of the global carbon cycle provides the impetus to better constrain the regional carbon balance. Moreover, under the Kyoto protocol, ratifying nations are required to provide state-level estimates of anthropogenic emissions of greenhouse gases from all sources together with the estimates of uptake by natural sinks (http://unfccc.int/essential_background/kyoto_protocol/items/1678.php).

In brief, the key questions in the scientific community are:

- Where and by which processes is anthropogenic CO_2 sequestered?
- What are the main feedback processes between the carbon cycle and the climate system?
- What is the carbon budget of a specific region (continent/country)?

1.3 Atmospheric Carbon budget

Over the last decades, significant progress has been attained in our knowledge of the magnitude of carbon fluxes on global (e.g.Denman et al.(2007), Le Quéré et al.(2009)), continental (e.g. Schulze et al.(2009), and regional (e.g. Dolman et al.(2009), Gerbig et al.(2009), Lauvaux et al.(2009)) scales by using bottom-up or top-down approaches or a combination of both. At small scales, eddy-covariance measurements can provide detailed insight to the exchange of CO_2 between the surface and the atmosphere (e.g. Law et al.(2002a), Reichstein et al.(2007b). These local scale flux estimates are scaled-up using process-based or diagnostic models

---

[5] The Intergovernmental Panel on Climate Change (IPCC) defined climate feedback is as follows: "An interaction mechanism between processes in the climate system is called a climate feedback, when the result of an initial process triggers changes in a second process that in turn influences the initial one. A positive feedback intensifies the original process, and a negative feedback reduces it."

utilizing satellite retrievals of geographical properties (vegetation cover, topography, etc.), climate records (temperature, precipitation, etc.) and statistical models (land-use change, energy consumption, etc.) to provide flux estimates on large scales (e.g. http://geo.arc.nasa.gov/sge/casa; (Reichstein et al., 2007a)). The accuracy of this approach relies on the representativeness of the local flux measurement site; hence one can expect significant uncertainties when extrapolating non-representative eddy flux tower measurements. Additionally, the evaluation of these spatial flux products is challenging as there are no direct measurements at these large scales.

Globally, inverse techniques are used to infer the magnitude and location of major fluxes from their signatures on atmospheric CO_2 concentrations via atmospheric transport models which describes the atmospheric transport from the source region to the observation sites (e.g. Enting (1993), Gurney et al.(2003), Rödenbeck et al.(2003b)). Those techniques are now increasingly mature with refinement of the modeling strategies (see Sect. 1.5) and the availability of new observations (see Sect. 1.4), and have successfully demonstrated their capability to assess the overall carbon budget from global to continental scales, albeit with substantial uncertainty (e.g. Stephens et al.(2007)). The derived fluxes are representative over a large region of several hundreds of kilometers and are on scales at which climate anomalies interact with biosphere; however these horizontal scales are too coarse to represent the responses of various vegetation types and the impact of human interventions (land use change and land management) on land-atmosphere fluxes. In order to investigate in detail the impact of the sub-grid scale processes listed above, inverse modeling studies are attempted on regional scales (Gerbig et al., 2003b; Matross et al., 2006; Lauvaux et al., 2008). However, inadequate measurement networks for atmospheric CO_2 concentrations and uncertainties in the simulated atmospheric transport can cause large uncertainties on the flux estimates derived from this approach.

Further discussion is restricted to topics related to regional inverse modeling studies in order to remain within the scope of this thesis. In the following sections, an overview on current measurement networks for monitoring atmospheric CO_2 (Sect. 1.4) and progress in modeling techniques are reviewed.

1.4   Measurement network

Measurements of atmospheric greenhouse gases and related tracers at high spatial and temporal resolutions are a prerequisite for inverse modeling approaches. This can be achieved by a global network of ground-based stations which routinely monitor atmospheric constituents with increasing accuracy together with in-situ and flask measurements made from different platforms such as airplanes, ships and buoys. These networks are currently complimented with observations from satellite-based remote sensing (e.g. Heimann (2009), Chevallier et al.(2009)) while ground-based (Fourier Transform Spectrometers) remote sensing is being used to validate satellite retrievals (e.g. Wunch et al.(2010)).

Long-term measurements, often from ground-based stations, contain valuable information about sources and sinks. Globally, about 100 stations provide continuous measurements of atmospheric CO_2 concentrations with an accuracy sufficient for modeling applications (www.wmo.int/gaw/; (Marquis and Tans, 2008); see **Fig. 1.5**). Until a decade ago, most of the monitoring sites were remotely located (i.e. near coasts or on mountain) in order to avoid the strongest influences from highly variable land-based sources and sinks (fossil fuel and biospheric fluxes). The observations from these remote stations, exhibiting small temporal and spatial variability, can hence be used to estimate global flux patterns and meridional concentration gradients. Conversely, these measurements cannot be used to construct regional flux patterns due to their lack of diurnal fluctuations in response to terrestrial fluxes (Gloor et al., 2000). An improved estimate of regional sources and sinks requires measurements over the continents and in the atmospheric boundary layer. At the same time, the influence from the very near-field fluxes (approximately within 10 km radius) has to be minimized in order to increase the representativeness of the measurements (Gloor et al., 2001; Gloor et al., 2000). This can be achieved by using tall towers equipped with in situ measurement devices at different heights (Bakwin et al., 1997; Bakwin et al., 1998). Over the last decades, several tall towers have been set up in the US (Bakwin et al., 1997; Bakwin et al., 1998; Hurst et al., 1997), Europe (see http://www.chiotto.org/; Vermeulen et al. (2010)), Siberia (Kozlova and Manning, 2009), and Japan (Inoue and Matsueda, 2001). Three of these tall towers: one in Siberia and two in Europe – Ochsenkopf in Germany (used for this study) (Thompson et

al., 2009), and Bialystok in Poland (Popa, 2007) – are operated by the Max Planck Institute of Biogeochemistry in Jena, Germany.

Additionally, the long-term isotopic measurements such as radiocarbon (^{14}C) can be used to differentiate anthropogenic signals from total atmospheric CO_2 concentrations (Levin and Karstens, 2007; Levin and Rödenbeck, 2008). This is possible because of the absence of ^{14}C in the fossil fuel CO_2 component due to their long storage time of several hundred million years. Other species such as carbon monoxide (CO) and oxygen (O_2) can also be used as tracers for anthropogenic fluxes of CO_2.
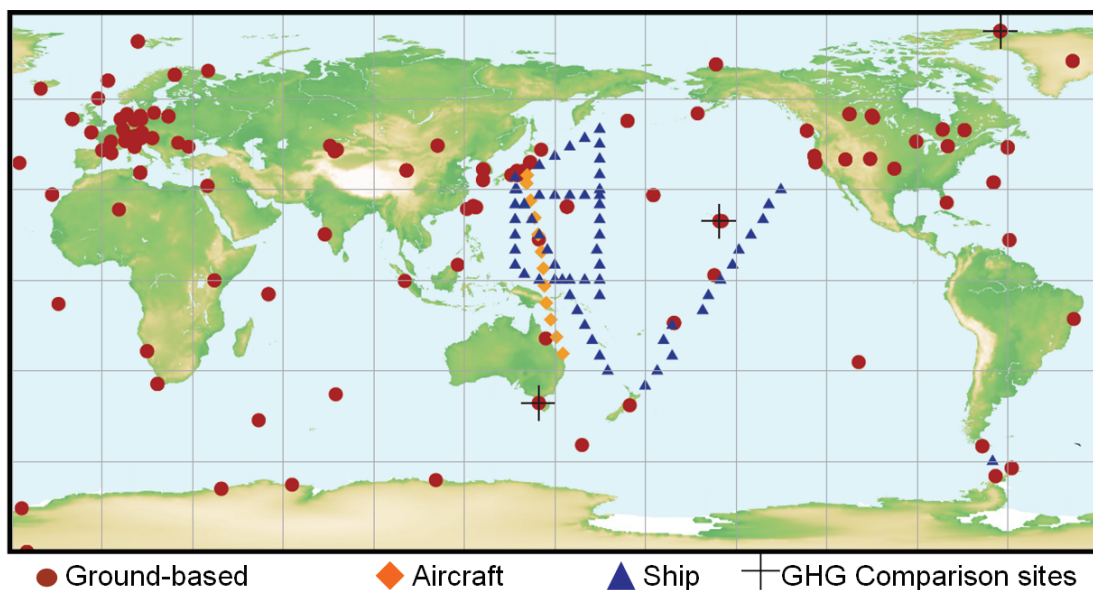
Figure 1.5 *The global observational network of atmospheric CO_2 concentrations provided by World Meteorological Organization (WMO).Figure courtesy of http://www.wmo.int/pages/prog/arep/gaw/ghg/documents/ghg-bulletin2008_en.pdf*

Airborne measurements with high precision and accuracy provide an important complement to the existing network. Aircraft campaigns, sampling air horizontally (from hundreds to thousands of kilometers) and vertically (from ground level up to about 12 km) are well suited to measure distributions of atmospheric tracers such as CO_2 at different temporal and spatial scales. These measurements help tremendously to understand the regional patterns of trace gases, the influence of surface fluxes in the near-field, as well as to validate atmospheric transport models (Dolman et al., 2006; Gerbig et al., 2003b; Lin et al., 2006; Sarrat et al., 2007). Over last decades there has been a move to conduct several aircraft campaigns or regular profiling in

the vicinity of ground stations (e.g. [CO_2 Budget and Rectification Airborne study (COBRA), (Gerbig et al., 2003a)]; [The CarboEurope Regional Experiment Strategy (CERES), (Dolman et al., 2006)]; [Terrestrial Carbon Observation System Siberia, (Levin et al., 2002)]; [Regional Assessment and Modelling of the Carbon Balance of Europe, (Gioli et al., 2004)]; [The Landes de Gascogne campaign, (Schmitgen et al., 2004)]; [The Ochsenkopf campaign using the METAIR-DIMO aircraft (http://www.metair.ch/), used for this study] . Furthermore, it is also possible to sample the air with measurement devices on board commercial airliners and to provide routine measurements at an altitude of 9 to 12 km which supplement the airborne campaigns (Machida et al., 2008; Chen, 2010).

Space-borne measurements providing column-integrated CO_2 concentrations with better spatial and temporal sampling as well as with adequate precision (~1 ppm) are expected to be a valuable addition to our current knowledge of regional sources and sinks, especially in tropical regions where long-term measurements are scarce (Miller et al., 2007; Rayner and O'Brien, 2001). An imaging spectrometer, SCIAMACHY (Scanning Imaging Absorption Spectrometer for Atmospheric Chartography) aboard ENVISAT (ENVIronmental SATellite; a polar-orbiting satellite by European Space Agency (ESA) launched on 2002) is the first satellite instrument measuring CO_2 concentration (Bovensmann et al., 1999). However, SCIAMACHY, with its large footprint size (about 50 km) was not particularly designed for CO_2 retrievals with the precision and accuracy required for inverse modeling studies. The Japan Aerospace Exploration Agency's (JAXA) Greenhouse gases Observing SATellite ('IBUKI'/GOSAT), specifically designed to provide highly accurate and precise measurements of CO_2 and CH_4 (Chevallier et al., 2009; Hamazaki et al., 2004) was successfully launched and has been mapping these gases since then, with a footprint size of 10.5 km. In addition, a US satellite mission, the Orbiting Carbon Observatory (OCO), by the National Aeronautics and Space Administration (NASA) is designed to provide highly accurate and precise measurements of CO_2, with a footprint size of 1.3 km (Crisp et al., 2004). Unfortunately the OCO spacecraft was lost in a launch vehicle failure in February 2009; however the next mission, OCO-2, to be launched by February 2013, is expected to replace the lost OCO (http://www.nasa.gov/mission_pages/oco/main). Furthermore, a new satellite mission proposal − Carbon monitoring SATellite (CarbonSat) (Bovensmann et al., 2010) −

has been selected in November 2010 by ESA for further development and is planned to be launched in 2018 for global measurements of CO_2 and CH_4 with a footprint size of 2 km and a measurement swath of 500 km, for maximum spatial coverage (http://www.esa.int/esaCP/SEMD9AGMTGG_index_0.html).

It has to be mentioned that the current in-situ observation network is not sufficient to adequately reduce uncertainties in surface flux estimates (e.g. Gurney et al.(2003)). Satellite-based measurements of column-integrated CO_2 concentrations are expected to improve the situation by providing global measurements of these greenhouse gases. However, the short-term measurements within the life span of those spacecraft would make it impossible to track the long-term evolution of sources and sinks of these trace gases (Heimann, 2009). The long-term and well-calibrated in-situ measurements are hence an irreplaceable part of any future network. .

1.5 Modeling strategies at the regional scale

As mentioned in Sect. 1.3, there is a strong need to apply atmospheric inverse modeling tools at regional scale and to utilize continental (non-background) measurements of CO_2 such as those made from tall tower observatories in order to investigate in detail the impact of small-scale processes on the distribution of carbon sources and sinks. Retrieving fluxes at these scales, however, poses considerable challenge since those measurements are often influenced by strong variability of surface fluxes (fossil fuel emissions and biosphere-atmosphere exchange) and by mesoscale (2 to 20 km) transport phenomena, complicating the interpretation of these measurements (Ahmadov et al., 2007; Gerbig et al., 2009; Pérez-Landa et al., 2007; van der Molen and Dolman, 2007). These variations, which are on scales that cannot be resolved by the current global models, which operate at spatial scales on the order of 100 km or more, can introduce significant biases in flux estimates derived from inverse modeling (Peters, 2010).

The aforementioned fine-scale structures can be effectively represented by mesoscale transport models with much higher horizontal resolutions of about 2 to 20 km (Ahmadov et al., 2007; Pérez-Landa et al., 2007; Sarrat et al., 2007; van der Molen and Dolman, 2007; Sarrat et al., 2009). A comprehensive model inter-comparison study over Europe, using various global and regional transport models with different horizontal and vertical resolutions, suggested that the fine-scale features are better

resolved at increased horizontal resolution down to 50 km compared to coarse models (Geels et al., 2007). Furthermore, Geels et al.(2007) discussed the several limitations on using measurements from short towers or mountain stations due to the models' (both global and regional scale models) inability to represent complex terrain and to capture mesoscale flow patterns in mountain sites. As a consequence, current inversion studies tend to exclude the data from these complex sites, impose less statistical weighting (larger uncertainty), or implement temporal data filtering to the measurements (e.g. selection of night-times only data at mountain sites). However, these fine structures in atmospheric CO_2 concentration patterns provide substantial information on the near-field fluxes (within a 20 km radius) due to their dominant influence on observed mixing ratios (see **Fig. 1.6**) and incorporating these in the inversion can therefore improve the regional flux estimates (e.g. Gerbig et al.(2009)). Also the temporal data filtering results in fewer constraints on the diurnal cycle of biospheric signals that are controlled by processes such as ecosystem respiration and photosynthesis. Moreover, using high temporal resolution measurements can provide large reductions in uncertainty in regional inversions (Law et al., 2002b).
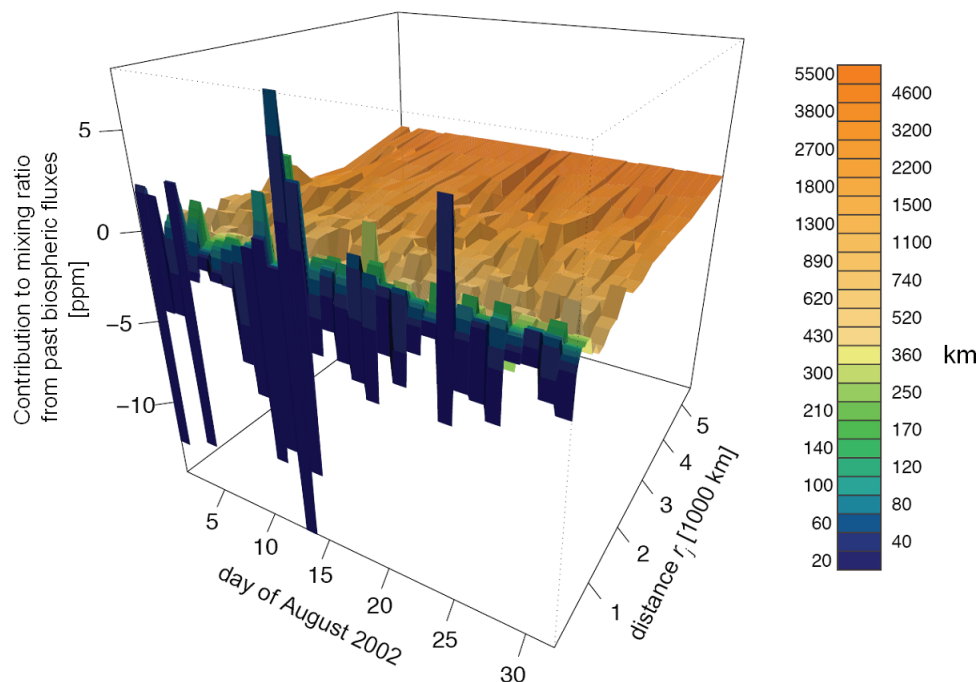
Figure 1.6 *Contributions to atmospheric CO_2 concentrations by biospheric fluxes (respiration and photosynthesis) at 15:00 local time for different distances from the measurement location. These contributions are calculated for different distance sectors and are shown in different color gradients. The color bar indicates the upper limit of each of the different distance sectors. The biospheric signal is positive in case of respired CO_2 release through respiration and negative in case of CO_2 uptake through photosynthesis. The dominant influences are caused by the fluxes from the first 20 km distance sector and then decrease rapidly. The figure courtesy of Gerbig et al.(2009).*

One must also utilize improved a priori knowledge of fluxes which represents this short-scale variability in regional scale inversions, together with associated uncertainty estimates and error correlations (Gerbig et al., 2006). A model-data fusion system, as proposed by Gerbig et al.(2009), which combines high-resolution atmospheric transport and biospheric models together with atmospheric and biospheric measurements, is expected to address the shortcomings of current inversion systems. The associated uncertainties in the different modeling components

Table 1.1: *Uncertainties involved in different components of model-data-fusion using mixing ratio measurements to derive regional fluxes of CO_2 (Gerbig et al., 2009).*

Source of uncertainty	*Type of uncertainty*	*Uncertainty estimates (ppm)*	*Reference*
Transport model	Advection PBL mixing Convection Mesoscale-processes	~5 ~3.5 No estimate ~2-3	Lin and Gerbig (2005) Gerbig et al.(2008) -- Tolk et al.(2008), van der Molen and Dolman (2007)
Transport and Flux models	Grid resolution	~1 ppm at 200 km	Gerbig et al.(2003a, 2003b)
Flux model	Prior uncertainty Aggregation	~2-8 variable	Peylin (2008, *Personal Communication*), Gerbig et al. (2009) Gerbig et al. (2006)
Measurement	Precision, accuracy	0.1	World Meteorological Organization

of such a model-data fusion system are quantified by Gerbig et al. (2008), Gerbig et al. (2006), Gerbig et al. (2003b), Lin and Gerbig (2005), Tolk et al. (2008) and van der Molen and Dolman (2007), and are listed in Table 1.1. The sum of transport-related uncertainties, nearly approaching 10 ppm as evident from Table 1.1, indicates the importance of improving atmospheric transport models, specifically for processes such as advection and convection in such model-data fusion systems. New modeling techniques that allow for high-resolution regional nesting around measurement sites in global models, as demonstrated by Rödenbeck et al.(2009), can thus provide regional CO_2 budgets at reduced uncertainty limits.

1.6 Thesis Objectives

In light of the importance of improving transport modeling in the current inversion systems and of reducing the uncertainties in the top-down estimates of fluxes, this thesis deals with a number of shortcomings in the current inversion framework, with special attention to atmospheric transport modeling, and discusses possible ways to mitigate these shortcomings in order to derive regional CO_2 to a significantly high degree of certainty. The study uses a model-data fusion system utilizing information from concentration and flux measurements to address the following scientific questions.

1. How much of the spatial variability of atmospheric CO_2 concentrations cannot be resolved by the current generation of global transport models?

2. Can we parameterize this variability in coarser models without using high-resolution simulations?

3. What is the effect of complex mesoscale flows on the observed atmospheric CO_2 fields? Can we represent this effect in the model?

4. How well are the measurements from complex sites such as mountain observatories reproduced by the high-resolution modeling framework as compared to current global models?

5. Can we use these measurements in future inversion studies?

6. How consistent are different components of the model-data fusion system?

7. Do we have an inversion technique which has the potential to provide regional flux estimates at reduced uncertainty limits?

The thesis is outlined as follows:

Chapter 2 provides an overview of the modeling tools in the model-data fusion system used for this study

Chapter 3 deals with the quantitative assessment of spatial variability of CO_2 over Europe based on high-resolution simulations. The study is carried out in the context of utilizing satellite retrievals for atmospheric column CO_2 concentrations in the current generation of inverse global models with a horizontal resolution of about 1 degree or more. The spatial scale mismatch between remotely-sensed CO_2 and global models can induce so-called representation errors, which can cause systematic biases in flux estimates. Chapter 3 is focused on estimating these representation errors and assessing how these errors can be parameterized in coarser models.

Chapter 4 addresses the ability of high-resolution modeling tools to represent the spatial and temporal variability of CO_2 over a complex terrain compared to coarser models. The study uses the measurements from the Ochsenkopf tall tower observatory, located on the second highest peak of the Fichtelgebirge mountain range (1022 m a.s.l.; 50° 1'48" N, 11°48'30" E) in Germany as well as profiles from a co-located airborne campaign. The complexity of mesoscale flows and their impact on observed mixing ratios are also assessed.

Chapter 5 provides an inter-comparison study with simulations of atmospheric CO_2 concentrations using two types of atmospheric models based on two different governing equations of motion – the Lagrangian and the Eulerian. A quantitative comparison between the two different approaches, while using the same initial/lateral boundary conditions, the same surface fluxes and the same domain, is required for having these components in the inverse modeling set-up used in this study. The consistency of those simulations is assessed with special attention to the details of horizontal and vertical transport and mixing of CO_2 concentrations in the atmosphere.

Chapter 6 presents an inversion technique which has the potential to provide regional flux estimates that are consistent with both mixing ratio and eddy flux measurements. The fluxes are estimated via an inverse technique utilizing concentration measurements from the Ochsenkopf tall tower. The reduction in uncertainties of retrieved fluxes is assessed and these fluxes are also compared with direct observations from eddy flux sites.

Chapter 7 provides the main conclusions and the outlook of this thesis.

1.7 References

Ahmadov, R., Gerbig, C., Kretschmer, R., Koerner, S., Neininger, B., Dolman, A. J., and Sarrat, C.: Mesoscale covariance of transport and CO_2 fluxes: Evidence from observations and simulations using the WRF-VPRM coupled atmosphere-biosphere model, J. Geophys. Res.-Atmos., 112, D22107, doi:22110.21029/22007JD008552, 2007.

Bakwin, P. S., Hurst, D. F., Tans, P. P., and Elkins, J. W.: Anthropogenic sources of halocarbons, sulfur hexafluoride, carbon monoxide, and methane in the southeastern United States, J. Geophys. Res.-Atmos., 102, 15915-15925, 1997.

Bakwin, P. S., Tans, P. P., Hurst, D. F., and Zhao, C. L.: Measurements of carbon dioxide on very tall towers: results of the NOAA/CMDL program, Tellus Ser. B-Chem. Phys. Meteorol., 50, 401-415, 1998.

Bovensmann, H., Burrows, J. P., Buchwitz, M., Frerick, J., Noël, S., Rozanov, V. V., Chance, K. V., and Goede, A. P. H.: SCIAMACHY: Mission objectives and measurement modes, Journal of the Atmospheric Sciences, 56, 127-150, 1999.

Bovensmann, H., Buchwitz, M., Burrows, J. P., Reuter, M., Krings, T., Gerilowski, K., Schneising, O., Heymann, J., Tretner, A., and Erzinger, J.: A remote sensing technique for global monitoring of power plant CO_2 emissions from space and related applications, Atmos. Meas. Tech., 3, 781-811, 2010.

Canadell, J. G., Le Quéré, C., Raupach, M. R., Field, C. B., Buitenhuis, E. T., Ciais, P., Conway, T. J., Gillett, N. P., Houghton, R. A., and Marland, G.: Contributions to accelerating atmospheric CO_2 growth from economic activity, carbon intensity, and efficiency of natural sinks, Proceedings of the National Academy of Sciences of the United States of America, 104, 18866-18870, 2007.

Chen, H.: Development of a high-accuracy continuous CO_2/CH_4/H_2O analyzer for deployment on board a commercial airliner, Dr. rer. nat., Chemisch-Geowissenschaftlichen Fakultät, Friedrich-Schiller-Universität Jena, Jena, 175 pp. pp., 2010.

Chevallier, F., Maksyutov, S., Bousquet, P., Bre´on, F. M., Saito, R., Yoshida, Y., and Yokota, T.: On the accuracy of the CO_2 surface fluxes to be estimated from the GOSAT observations, Geophysical Research Letters, 36, L19807, doi:10.1029/2009GL040108, 2009.

Crisp, D., Atlas, R. M., Breon, F.-M., Brown, L. R., Burrows, J. P., Ciais, P., Connor, B. J., Doney, S. C., Fung, I. Y., Jacob, D. J., Miller, C. E., O'Brien, D., Pawson, S., Randerson, J. T., Rayner, P., Salawitch, R. J., Sander, S. P., Sen, B., Stephens, G. L., Tans, P. P., Toon, G. C., Wennberg, P. O., Wofsy, S. C., Yung, Y. L., Kuang, Z., Chudasama, B., Sprague, G., Weiss, B., Pollock, R., Kenyon, D., and Schroll, S.: The Orbiting Carbon Observatory (OCO) mission, Advances in Space Research, 34, 700-709, 2004.

Denman, K. L., Brasseur, G., Chidthaisong, A., Ciais, P., Cox, P. M., Dickinson, R. E., Hauglustaine, D., Heinze, C., Holland, E., Jacob, D., Lohmann, U., Ramachandran, S., da Silva Dias, P. L., Wofsy, S. C., and Zhang, X.: Couplings Between Changes in the Climate System and Biogeochemistry. In: Climate Change 2007: The Physical Science Basis. Contribution of Working Group I to the Fourth Assessment Report of the Intergovernmental Panel on Climate Change [Solomon, S., D. Qin, M. Manning, Z. Chen, M. Marquis, K.B. Averyt, M.Tignor and H.L. Miller (eds.)]. Cambridge University Press, Cambridge, United Kingdom and New York, NY, USA., 2007.

Desai, A. R., Bolstad, P. V., Cook, B. D., Davis, K. J., and Carey, E. V.: Comparing net ecosystem exchange of carbon dioxide between an old-growth and mature forest in the upper Midwest, USA, Agric. For. Meteorol., 128, 33-55, 2005.

Dolman, A. J., Noilhan, J., Durand, P., Sarrat, C., Brut, A., Piguet, B., Butet, A., Jarosz, N., Brunet, Y., Loustau, D., Lamaud, E., Tolk, L., Ronda, R., Miglietta, F., Gioli, B., Magliulo, V., Esposito, M., Gerbig, C., Körner, S., Glademard, R., Ramonet, M., Ciais, P., Neininger, B., Hutjes, R. W. A., Elbers, J. A., Macatangay, R., Schrems, O., Pérez-Landa, G., Sanz, M. J., Scholz, Y., Facon, G., Ceschia, E., and Beziat, P.: The CarboEurope regional experiment strategy, Bulletin of the American Meteorological Society, 87, 1367-1379, 2006.

Dolman, A. J., Gerbig, C., Noilhan, J., Sarrat, C., and Miglietta, F.: Detecting regional variability in sources and sinks of carbon dioxide: a synthesis, Biogeosciences, 6, 1015-1026, 2009.

Enting, I. G.: Inverse problems in atmospheric constituent studies: III. Estimating errors in surface sources, Inverse Problems, 9, 649-665, 1993.

Etheridge, D. M., Steele, L. P., Langenfelds, R. L., Francey, R. J., Barnola, J.-M., and Morgan, V. I.: Natural and anthropogenic changes in atmospheric CO_2 over the last 1000 years from air in Antarctic ice and firn, J. Geophys. Res.-Atmos., 101, 4115-4128, 1996.

Fang, J., et al., : Changes in forest biomass carbon storage in China between 1949 and 1998, Science, 292, 2320–2322, 2001.

20

Fletcher, S. E. M., Gruber, N. P., Jacobson, A. R., Doney, S. C., Dutkiewicz, S., Gerber, M., Follows, M., Lindsay, K., Menemenlis, D., Mouchet, A., and Sarmiento, J. L.: Inverse estimates of anthropogenic CO_2 uptake, transport, and storage by the ocean, Global Biogeochemical Cycles, 20, GB2002, doi:2010.1029/2005GB002530, 2006.

Forster, P., Ramaswamy, V., Artaxo, P., Berntsen, T., Betts, R., Fahey, D. W., Haywood, J., Lean, J., Lowe, D. C., Myhre, G., Nganga, J., Prinn, R., Raga, G., Schulz, M., and Van Dorland, R.: Changes in Atmospheric Constituents and in Radiative Forcing, In: Climate Change 2007: The Physical Science Basis. Contribution of Working Group I to the Fourth Assessment Report of the Intergovernmental Panel on Climate Change., edited by: Solomon, S., D. Qin, M. Manning, Z. Chen, M. Marquis, K.B. Averyt, M.Tignor and H.L. Miller, Cambridge University Press, Cambridge, United Kingdom and New York, NY, USA., 2007.

Friedlingstein, P., Houghton, R.A.,Marland,G., Hackler,J.,Boden,T.A., Conway,T.J.,Canadell, J.G.,Raupach, M.R.,Ciais,P., Le Quéré,C: Update on CO_2 emissions, Nature Geoscience, doi:10.1038/ngeo1022, 2010.

Geels, C., Gloor, M., Ciais, P., Bousquet, P., Peylin, P., Vermeulen, A. T., Dargaville, R., Aalto, T., Brandt, J., Christensen, J. H., Frohn, L. M., Haszpra, L., Karstens, U., Rödenbeck, C., Ramonet, M., Carboni, G., and Santaguida, R.: Comparing atmospheric transport models for future regional inversions over Europe. Part 1: Mapping the atmospheric CO_2 signals, Atmos. Chem. Phys., 7, 3461-3479, 2007.

Gerbig, C., Lin, J. C., Wofsy, S. C., Daube, B. C., Andrews, A. E., Stephens, B. B., Bakwin, P. S., and Grainger, C. A.: Toward constraining regional-scale fluxes of CO_2 with atmospheric observations over a continent: 1. Observed spatial variability from airborne platforms, J. Geophys. Res.-Atmos., 108, 4756, doi:4710.1029/2002JD003018, 2003a.

Gerbig, C., Lin, J. C., Wofsy, S. C., Daube, B. C., Andrews, A. E., Stephens, B. B., Bakwin, P. S., and Grainger, C. A.: Toward constraining regional-scale fluxes of CO_2 with atmospheric observations over a continent: 2. Analysis of COBRA data using a receptor-oriented framework, J. Geophys. Res.-Atmos., 108, 4757, doi:4710.1029/2003JD003770, 2003b.

Gerbig, C., Lin, J. C., Munger, J. W., and Wofsy, S. C.: What can tracer observations in the continental boundary layer tell us about surface-atmosphere fluxes?, Atmos. Chem. Phys., 6, 539-554, 2006.

Gerbig, C., Körner, S., and Lin, J. C.: Vertical mixing in atmospheric tracer transport models: error characterization and propagation, Atmos. Chem. Phys., 8, 591-602, 2008.

Gerbig, C., Dolman, A. J., and Heimann, M.: On observational and modelling strategies targeted at regional carbon exchange over continents, Biogeosciences, 6, 1949-1959, 2009.

Gioli, B., Miglietta, F., De Martino, B., Hutjes, R. W. A., Dolman, H. A. J., Lindroth, A., Schumacher, M., Sanz, M. J., Manca, G., Peressotti, A., and Dumas, E. J.: Comparison between tower and aircraft-based eddy covariance fluxes in five European regions, Agric. For. Meteorol., 127, 1-16, 2004.

Gloor, M., Fan, S.-M., Pacala, S., and Sarmiento, J.: Optimal sampling of the atmosphere for purpose of inverse modeling: A model study, Global Biogeochemical Cycles, 14, 407-428, 2000.

Gloor, M., Bakwin, P., Hurst, D., Lock, L., Draxler, R., and Tans, P.: What is the concentration footprint of a tall tower?, J. Geophys. Res.-Atmos., 106, 17831-17840, 2001.

Gruber, N.: Fickle trends in the ocean, Nature, 458, 2009.

Gruber, N., Gloor, M., Fletcher, S., Doney, S. C., Dutkiewicz, S., Follows, M. J., Gerber, M., Jacobson, A. R., Joos, F., Lindsay, K., Menemenlis, D., Mouchet, A., Mü̈ller, S. A., Sarmiento, J. L., and Takahashi, T.: Oceanic sources, sinks, and transport of atmospheric CO_2, Global Biogeochemical cycles, 23, doi:10.1029/2008GB003349, 2009.

Gurney, K. R., Law, R. M., Denning, A. S., Rayner, P. J., Baker, D., Bousquet, P., Bruhwiler, L., Chen, Y.-H., Ciais, P., Fan, S., Fung, I. Y., Gloor, M., Heimann, M., Higuchi, K., John, J., Maki, T., Maksyutov, S., Masarie, K., Peylin, P., Prather, M., Pak, B. C., Randerson, J., Sarmiento, J., Taguchi, S., Takahashi, T., and Yuen, C.-W.: Towards robust regional estimates of CO_2 sources and sinks using atmospheric transport models, Nature, 415, 626-630, 2002.

Gurney, K. R., Law, R. M., Denning, A. S., Rayner, P. J., Baker, D., Bousquet, P., Bruhwiler, L., Chen, Y.-H., Ciais, P., Fan, S. M., Fung, I. Y., Gloor, M., Heimann, M., Higuchi, K., John, J., Kowalczyk, E., Maki, T., Maksyutov, S., Peylin, P., Prather, M., Pak, B. C., Sarmiento, J., Taguchi, S., Takahashi, T., and Yuen, C.-W.: TransCom 3 CO_2 inversion intercomparison: 1. Annual mean control results and sensitivity to transport and prior flux information, Tellus Ser. B-Chem. Phys. Meteorol., 55, 555-579, 2003.

Hamazaki, T., Kaneko, Y., and Kuze, A.: Carbon dioxide monitoring from the GOSAT satellite, Proceedings XXth ISPRS conference, Istanbul, Turkey, 12–23 July, 2004.

Heimann, M.: Searching out the sinks, Nature Geoscience, 2, 3-4, 2009.

Hurst, D. F., Bakwin, P. S., Myers, R. C., and Elkins, J. W.: Behavior of trace gas mixing ratios on a very tall tower in North Carolina, J. Geophys. Res.-Atmos., 102, 8825-8835, 1997.

Hurtt, G. C., Pacala, S. W., Moorcroft, P. R., Caspersen, J., Shevliakova, E., Houghton, R. A., and Moore, B.: Projecting the future of the U.S. carbon sink, Proceedings of the National Academy of Sciences of the United States of America, 99, 1389-1394, doi:10.1073/pnas.012249999, 2001.

Inoue, H. Y., and Matsueda, H.: Measurements of atmospheric CO_2 from a meteorological tower in Tsukuba, Japan, Tellus Series B - Chemical and Physical Meteorology, 53B, 205-219, 2001.

Janssens, I. A., Freibauer, A., Ciais, P., Smith, P., Nabuurs, G.-J., Folberth, G., Schlamadinger, B., Hutjes, R. W. A., Ceulemans, R., Schulze, E.-D., Valentini, R., and Dolman, A. J.: Europe's terrestrial biosphere absorbs 7 to 12% of European anthropogenic CO_2 emissions, Science, 300, 1538-1542, 2003.

Keeling, C. D., Bacastow, R. B., Bainbridge, A. E., Ekdahl, C. A., Guenther, P. R., and Waterman, L. S.: Atmospheric carbon dioxide variations at Mauna Loa Observatory, Hawaii, Tellus, vol. 28, 538-551, 1976.

Kiehl, J. T., and Trenberth, K. E.: Earth's annual global mean energy budget, Bulletin of the American Meteorological Society, 78, 197-208, 1997.

Knorr, W.: Is the airborne fraction of anthropogenic CO2 emissions increasing?, Geophysical Research Letters, 36, L21710, doi:10.1029/2009GL040613, 2009.

Kozlova, E. A., and Manning, A. C.: Methodology and calibration for continuous measurements of biogeochemical trace gas and O_2 concentrations from a 300-m tall tower in central Siberia, Atmospheric Measurement Techniques, 2, 205-220, 2009.

Kurz, W. A., and Apps, M.: A 70-years retrospective analysis of carbon fl uxes in the Canadian forest sector, Ecol. Appl, 9, 526–547, 1999.

Lauvaux, T., Uliasz, M., Sarrat, C., Chevallier, F., Bousquet, P., Lac, C., Davis, K. J., Ciais, P., Denning, A. S., and Rayner, P. J.: Mesoscale inversion: first results from The CERES campaign with synthetic data, Atmos. Chem. Phys., 8, 3459-3471, 2008.

Lauvaux, T., Gioli, B., Sarrat, C., Rayner, P. J., Ciais, P., Chevallier, F., Noilhan, J., Miglietta, F., Brunet, Y., Ceschia, E., Dolman, H., Elbers, J. A., Gerbig, C., Hutjes, R., Jarosz, N., Legain, D., and Uliasz, M.: Bridging the gap between atmospheric concentrations and local ecosystem measurements, Geophysical Research Letters, 36, L19809, doi:19810.11029/12009GL039574, 2009.

Law, B. E., Falge, E., Gu, L., Baldocchi, D. D., Bakwin, P., Berbigier, P., Davis, K., Dolman, A. J., Falk, M., Fuentes, J. D., Goldstein, A., Granier, A., Grelle, A., Hollinger, D., Janssens, I. A., Jarvis, P., Jensen, N. O., Katul, G., Mahli, Y., Matteucci, G., Meyers, T., Monson, R., Munger, W., Oechel, W., Olson, R., Pilegaard, K., Paw U, K. T., Thorgeirsson, H., Valentini, R., Verma, S., Vesala, T., Wilson, K., and Wofsy, S.: Environmental controls over carbon dioxide and water vapor exchange of terrestrial vegetation, Agric. For. Meteorol., 113, 97-120, 2002a.

Law, R. M., Rayner, P. J., Steele, L. P., and Enting, I. G.: Using high temporal frequency data for CO_2 inversions, Global Biogeochemical Cycles, 16, 1053, doi:1010.1029/2001GB001593, 2002b.

Le Quéré, C., Raupach, M. R., Canadell, J. G., and Marland, G. e. a.: Trends in the sources and sinks of carbon dioxide, Nature Geoscience, 2, 831-836, 2009.

Le Treut, H., R. Somerville, U. Cubasch, Y. Ding, C. Mauritzen, A. Mokssit, Peterson, T., and Prather, M.: Historical Overview of Climate Change, In: Climate Change 2007: The Physical Science Basis. Contribution of Working Group I to the Fourth Assessment Report of the Intergovernmental Panel on Climate Change [Solomon, S., D. Qin, M. Manning, Z. Chen, M. Marquis, K.B. Averyt, M. Tignor and H.L. Miller (eds.)]. Cambridge University Press, Cambridge, United Kingdom and New York, NY, USA., 2007.

Leuenberger, M., Siegenthaler, U., and Langway, C. C.: Carbon isotope composition of atmospheric CO_2 during the last ice age from an Antarctic ice core, Nature, 357, 488-490, 1992.

Levin, I., Ciais, P., Langenfelds, R., Schmidt, M., Ramonet, M., Sidorov, K., Tchebakova, N., Gloor, M., Heimann, M., Schulze, E.-D., Vygodskaya, N. N., Shibistova, O., and Lloyd, J.: Three years of trace gas observations over the EuroSiberian domain derived from aircraft sampling - a concerted action, Tellus Ser. B-Chem. Phys. Meteorol., 54, 696-712, 2002.

Levin, I., and Karstens, U.: Inferring high-resolution fossil fuel CO_2 records at continental sites from combined $^{14}CO_2$ and CO observations, Tellus Series B - Chemical and Physical Meteorology, 59, 245-250, 2007.

Levin, I., and Rödenbeck, C.: Can the envisaged reductions of fossil fuel CO_2 emissions be detected by atmospheric observations?, Naturwissenschaften, 95, 203-208, 2008.

Lin, J. C., and Gerbig, C.: Accounting for the effect of transport errors on tracer inversions, Geophysical Research Letters, 32, L01802, doi:01810.01029/02004GL021127, 2005.

Lin, J. C., Gerbig, C., Wofsy, S. C., Daube, B. C., Matross, D. M., Chow, V. Y., Gottlieb, E., Andrews, A. E., Pathmathevan, M., and Munger, J. W.: What have we learned from intensive atmospheric sampling field programmes of CO_2?, Tellus Ser. B-Chem. Phys. Meteorol., 58, 331-343, 2006.

Luyssaert, S., Inglima, I., Jung, M., Richardson, A. D., Reichstein, M., Papale, D., Piao, S. L., Schulze, E.-D., Wingate, L., Matteucci, G., Aragao, L., Aubinet, M., Beer, C., Bernhofer, C., Black, K. G., Bonal, D., Bonnefond, J.-M., Chambers, J., Ciais, P., Cook, B., Davis, K. J., Dolman, A. J., Gielen, B., Goulden, M., Grace, J., Granier, A., Grelle, A., Griffis, T., Grünwald, T., Guidolotti, G., Hanson, P. J., Harding, R., Hollinger, D. Y., Hutyra, L. R., Kolari, P., Kruijt, B., Kutsch, W., Lagergren, F., Laurila, T., Law, B. E., Le Maire, G., Lindroth, A., Loustau, D., Malhi, Y., Mateus, J., Migliavacca, M., Misson, L., Montagnani, L., Moncrieff, J., Moors, E., Munger, J. W., Nikinmaa, E., Ollinger, S. V., Pita, G., Rebmann, C., Roupsard, O., Saigusa, N., Sanz, M. J., Seufert, G., Sierra, C., Smith, M.-L., Tang, J., Valentini, R., Vesala, T., and Janssens, I. A.: CO_2 balance of boreal, temperate, and tropical forests derived from a global database, Global Change Biology, 13, 2509-2537, 2007.

Luyssaert, S., Schulze, E.-D., Börner, A., Knohl, A., Hessenmöller, D., Law, B. E., Ciais, P., and Grace, J.: Old-growth forests as global carbon sinks, Nature, 455, 213-215, 2008.

Machida, T., Matsueda, H., Sawa, Y., Nakagawa, Y., Hirotani, K., Kondo, N., Goto, K., Nakazawa, T., Ishikawa, K., and Ogawa, T.: Worldwide measurements of atmospheric CO_2 and other trace gas species using commercial airlines, Journal of Atmospheric and Oceanic Technology, doi:10.1175/2008JTECHA1082.1171, 2008.

Marland, G., Boden, T. A., and Andres, R. J.: Global, regional, and national fossil fuel CO_2 emissions from Fossil-Fuel Burning, Cement Production, and Gas Flaring, Oak Ridge, Tenn., U.S.A., Carbon Dioxide Information Analysis Center, Oak Ridge National laboratory, U.S. Department of Energy., 2007.

Marquis, M., and Tans, P.: Carbon crucible, Science, 320, 460-461, 2008.
Matross, D. M., Andrews, A., Pathmathevan, M., Gerbig, C., Lin, J. C., Wofsy, S. C., Daube, B. C., Gottlieb, E. W., Chow, V. Y., Lee, J. T., Zhao, C. L., Bakwin, P. S., Munger, J. W., and Hollinger, D. Y.: Estimating regional carbon exchange in New England and Quebec by combining atmospheric, ground-based and satellite data, Tellus Ser. B-Chem. Phys. Meteorol., 58, 344-358, 2006.

Meinshausen, M., Meinshausen, N., Hare, W., Raper, S. C. B., Frieler, K., Knutti, R., Frame, D. J., and Allen, M. R.: Greenhouse-gas emission targets for limiting global warming to 2°C, Nature, 458, 1158-1162, doi:10.1038/nature08017, 2009.

Miller, C. E., Crisp, D., DeCola, P. L., Olsen, S. C., Randerson, J. T., Michalak, A. M., Alkhaled, A., Rayner, P., Jacob, D. J., Suntharalingam, P., Jones, D. B. A., Denning, A. S., Nicholls, M. E., Doney, S. C., Pawson, S., Boesch, H., Connor, B. J., Fung, I. Y., O'Brien, D., Salawitch, R. J., Sander, S. P., Sen, B., Tans, P., Toon, G. C., Wennberg, P. O., Wofsy, S. C., Yung, Y. L., and Law, R. M.: Precision requirements for space-based XCO2 data, J. Geophys.Res, 112, 2007.

Pacala, S. W., Hurtt, G. C., Baker, D., Peylin, P., Houghton, R. A., Birdsey, R. A., Heath, L., Sundquist, E. T., Stallard, R. F., Ciais, P., Moorcroft, P., Caspersen, J. P., Shevliakova, E., Moore, B., Kohlmaier, G., Holland, E., Gloor, M., Harmon, M. E., Fan, S.-M., Sarmiento, J. L., Goodale, C. L., Schimel, D., and Field, C. B.: Consistent land- and atmosphere-based U.S. carbon sink estimates, Science, 292, 2316-2320, 2001.

Pérez-Landa, G., Ciais, P., Gangoiti, G., Palau, J. L., Carrara, A., Gioli, B., Miglietta, F., Schumacher, M., Millán, M. M., and Sanz, M. J.: Mesoscale circulations over complex terrain in the Valencia coastal region, Spain - Part 2: Modeling CO_2 transport using idealized surface fluxes, Atmos. Chem. Phys., 7, 1851-1868, 2007.

Peters, W.: Seven years of recent European net terrestrial carbon dioxide exchange constrained by atmospheric observations, Global Change Biology, 16, 1317-1337, 2010.

Peylin, P., Bousquet, P., Le Quéré, C., Sitch, S., Friedlingstein, P., McKinley, G., Gruber, N., Rayner, P., and Ciais, P.: Multiple constraints on regional CO_2 flux variations over land and oceans, Global Biogeochemical Cycles, 19, GB1011, doi:1010.1029/2003GB002214, 2005a.

Peylin, P., Rayner, P. J., Bousquet, P., Carouge, C., Hourdin, F., Heinrich, P., and Ciais, P.: Daily CO_2 flux estimates over Europe from continuous atmospheric measurements: 1, inverse methodology, Atmos. Chem. Phys., 5, 3173-3186, 2005b.

Piao, S., Fang, J., Ciais, P., Peylin, P., Huang, Y., Sitch, S., and Wang, T.: The carbon balance of terrestrial ecosystems in China, Nature, 458, doi:10.1038/nature07944, 2009.

Popa, M. E.: Continuous tall tower multispecies measurements in Europe for quantifying and understanding land-atmosphere carbon exchange, Dr. rer. nat., Chemisch-Geowissenschaftlichen Fakultät, Friedrich-Schiller-Universität Jena, Jena, 237 pp. pp., 2007.

Rayner, P. J., and O'Brien, D. M.: The utility of remotely sensed CO_2 concentration data in surface source inversions, Geophysical Research Letters, 28, 175-178, 2001.

Reichstein, M., Ciais, P., Papale, D., Valentini, R., Running, S., Viovy, N., Cramer, W., Granier, A., Ogée, J., Allard, V., Aubinet, M., Bernhofer, C., Buchmann, N., Carrara, A., Grünwald, T., Heimann, M., Heinesch, B., Knohl, A., Kutsch, W., Loustau, D., Manca, G., Matteucci, G., Miglietta, F., Ourcival, J. M., Pilegaard, K., Pumpanen, J., Rambal, S., Schaphoff, S., Seufert, G., Soussana, J.-F., Sanz, M.-J., Vesala, T., and Zhao, M.: Reduction of ecosystem productivity and respiration during the European summer 2003 climate anomaly: a joint flux tower, remote sensing and modelling analysis, Global Change Biology, 13, 634-651, 2007a.

Reichstein, M., Papale, D., Valentini, R., Aubinet, M., Bernhofer, C., Knohl, A., Laurila, T., Lindroth, A., Moors, E., Pilegaard, K., and Seufert, G.: Determinants of terrestrial ecosystem carbon balance inferred from European eddy covariance flux sites, Geophysical Research Letters, 34, L01402, doi:01410.01029/02006GL027880, 2007b.

Rödenbeck, C., Houweling, S., Gloor, M., and Heimann, M.: CO_2 flux history 1982-2001 inferred from atmospheric data using a global inversion of atmospheric transport, Atmos. Chem. Phys., 3, 1919-1964, 2003a.

Rödenbeck, C., Houweling, S., Gloor, M., and Heimann, M.: Time-dependent atmospheric CO_2 inversions based on interannually varying tracer transport, Tellus Ser. B-Chem. Phys. Meteorol., 55, 488-497, 2003b.

Rödenbeck, C., Gerbig, C., Trusilova, K., and Heimann, M.: A two-step scheme for high-resolution regional atmospheric trace gas inversions based on independent models, Atmos. Chem. Phys., 9, 5331-5342, 2009.

Sarrat, C., Noilhan, J., Lacarrère, P., Donier, S., Lac, C., Calvet, J. C., Dolman, A. J., Gerbig, C., Neininger, B., Ciais, P., Paris, J. D., Boumard, F., Ramonet, M., and Butet, A.: Atmospheric CO_2 modeling at the regional scale: Application to the CarboEurope regional experiment, J. Geophys. Res.-Atmos., 112, D12105, doi:12110.11029/12006JD008107, 2007.

Sarrat, C., Noilhan, J., Lacarrère, P., Masson, V., Ceschia, E., Ciais, P., Dolman, A., Elbers, J., Gerbig, C., and Jarosz, N.: CO_2 budgeting at the regional scale using a

Lagrangian experimental strategy and meso-scale modeling, Biogeosciences, 6, 113-127, 2009.

Schimel, D. S., House, J. I., Hibbard, K. A., Bousquet, P., Ciais, P., Peylin, P., Braswell, B. H., Apps, M. A., Baker, D., Bondeau, A., Canadell, J., Churkina, G., Cramer, W., Denning, A. S., Field, C. B., Friedlingstein, P., Goodale, C., Heimann, M., Houghton, R. A., Melillo, J. M., Moore, I. B., Murdiyarso, D., Noble, I., Pacala, S. W., Prentice, I. C., Raupach, M. R., Rayner, P. J., Scholes, R. J., Steffen, W. L., and Wirth, C.: Recent patterns and mechanisms of carbon exchange by terrestrial ecosystems. , Nature, 414, 169-172, 2001.

Schmitgen, S., Geiss, H., Ciais, P., Neininger, B., Brunet, Y., Reichstein, M., Kley, D., and Volz-Thomas, A.: Carbon dioxide uptake of a forested region in southwest France derived from airborne CO_2 and CO measurements in a quasi-Lagrangian experiment, J. Geophys. Res.-Atmos., 109, D14302, doi:14310.11029/12003JD004335, 2004.

Schulze, E. D., Luyssaert, S., Ciais, P., Freibauer, A., and Janssens, I. A., et al.: Importance of methane and nitrous oxide for Europe's terrestrial greenhouse-gas balance, Nature Geoscience, 2, doi:10.1038/ngeo686, 2009.

Schuster, U., and Watson, A. J.: A variable and decreasing sink for atmospheric CO_2 in the North Atlantic, Journal of Geophysical Research, 112, doi:10.1029/2006JC003941, 2007.

Shvidenko, A., and Nilsson, S.: A synthesis of the impact of Russian forests on the global carbon budget for 1961-1998, Tellus Series B - Chemical and Physical Meteorology, 55, 391-415, 2003.

Stephens, B. B., Gurney, K. R., Tans, P. P., Sweeney, C., Peters, W., Bruhwiler, L., Ciais, P., Ramonet, M., Bousquet, P., Nakazawa, T., Aoki, S., Machida, T., Inoue, G., Vinnichenko, N., Lloyd, J., Jordan, A., Heimann, M., Shibistova, O., Langenfelds, R. L., Steele, L. P., Francey, R. J., and Denning, A. S.: Weak northern and strong tropical land carbon uptake from vertical profiles of atmospheric CO_2, Science, 316, 1732-1735, 2007.

Sundquist, E. T.: The global carbon dioxide budget, Science, 259, 934-941, 1993.

Takahashi, T., Sutherland, S. C., Wanninkhof, R., Sweeney, C., Feely, R. A., Chipman, D. W., and Hales, B., et.al.: Climatological mean and decadal change in surface ocean pCO2, and net sea–air CO_2 flux over the global oceans Deep Sea Research Part II: Topical Studies in Oceanography, 56, 554-577, 2008.

Thompson, R. L., Manning, A. C., Gloor, E., Schultz, U., Seifert, T., Hänsel, F., Jordan, A., and Heimann, M.: In-situ measurements of oxygen, carbon monoxide and greenhouse gases from Ochsenkopf tall tower in Germany, Atmospheric Measurement Techniques, 2, 573-591, 2009.

Thoning, K. W., Tans, P. P., and Komhyr, W. D.: Atmospheric Carbon Dioxide at Mauna Loa Observatory 2. Analysis of the NOAA GMCC Data, 1974-1985, Journal of Geophysical Research- Atmospheres, 94, 8549-8565, 1989.

Tolk, L. F., Meesters, A. G. C. A., Dolman, A. J., and Peters, W.: Modelling representation errors of atmospheric CO_2 concentrations at a regional scale, Atmospheric Chemistry and Physics Discussions, 8, 3287-3312, 2008.

van der Molen, M. K., and Dolman, A. J.: Regional carbon fluxes and the effect of topography on the variability of atmospheric CO_2, J. Geophys. Res.-Atmos., 112, D01104, doi:01110.01029/02006JD007649, 2007.

van der Werf, G. R., Morton, D. C., DeFries, R. S., Olivier, J. G. J., Kasibhatla, P. S., Jackson, R. B., Collatz, G. J., and Randerson, J. T.: CO_2 emissions from forest loss, Nature Geoscience, 2, doi:10.1038/ngeo671, 2009.

Vermeulen, A. T., Hensen, A., Popa, M. E., van den Bulk, W. C. M., and Jongejan, P. A. C.: Greenhouse gas observations from Cabauw Tall Tower (1992–2010), Atmos. Meas. Tech. Discuss, 3, 4169-4230, doi:10.5194/amtd-3-4169-2010, 2010.

Wunch, D., Toon, G. C., Blavier, J.-F. L., Washenfelder, R., Notholt, J., Connor, B. J., Griffith, D. W. T., Sherlock, V., and Wennberg, P. O.: The Total Carbon Column Observing Network (TCCON), Philos. T. Roy. Soc. A, 2010.

2 Model Overview

As mentioned in the introduction (Chapter 1), a model-data fusion system is used to investigate the research questions addressed in this thesis. A schematic representation of the model-data fusion system is depicted in **Fig. 2.1**. The major modeling components of the fusion system consist of two transport models and a biosphere model. The purpose of this chapter is to give an overview of these components and to indicate the chapters in which these are used or described.
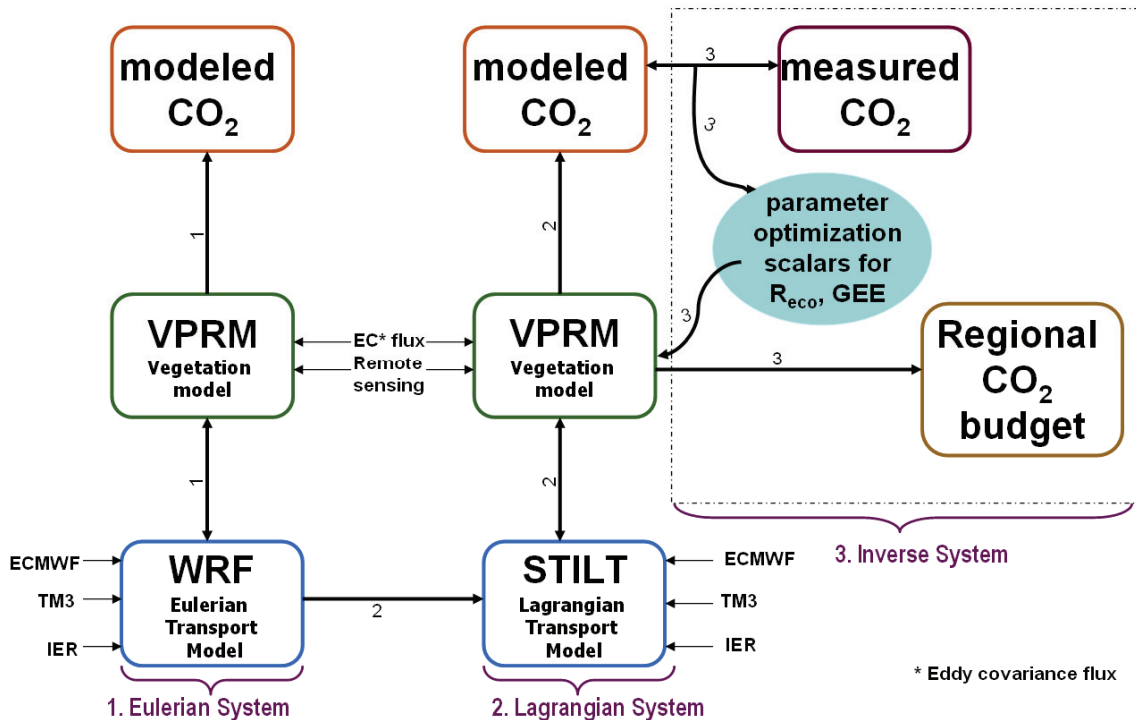
Figure 2.1 *Overview of the model-data fusion system used in this thesis. The numbers next to the arrows indicate the different steps in chronological order. The Eulerian system (step 1) is used for the results present in Chapter 3. The simulations generated by both the Eulerian (step 1) and the Lagrangian systems (step 2) are presented in Chapters 4 and 5. Chapter 6 describes the inverse system (step 3) and presents these results.*

2.1 Transport models

The fusion system consists of an Eulerian-based transport model, namely the Weather Research and Forecasting (WRF) model, and a Lagrangian-based particle dispersion model, namely the Stochastic Time-Inverted Lagrangian Transport (STILT) model, to take into account the distribution of CO_2 transported by advection, convection and turbulence.

2.1.1 WRF model

The WRF model is a mesoscale numerical weather prediction system which is extensively used for both operational forecasting and atmospheric research studies such as parameterized-physics research, regional climate simulations, air quality modeling, and atmosphere-ocean coupling (Skamarock et al., 2008). The source code is freely available at: http://www.wrf-model.org/. The principal components of the WRF system are depicted in **Fig. 2.2**. The WRF consists of dynamics solvers, physics packages that interface with the solvers, programs for initialization of meteorological and other fields and WRF-Chem. These components are described in detail in Skamarock et al. (2008). A brief description of the WRF model and its components are provided in this section.
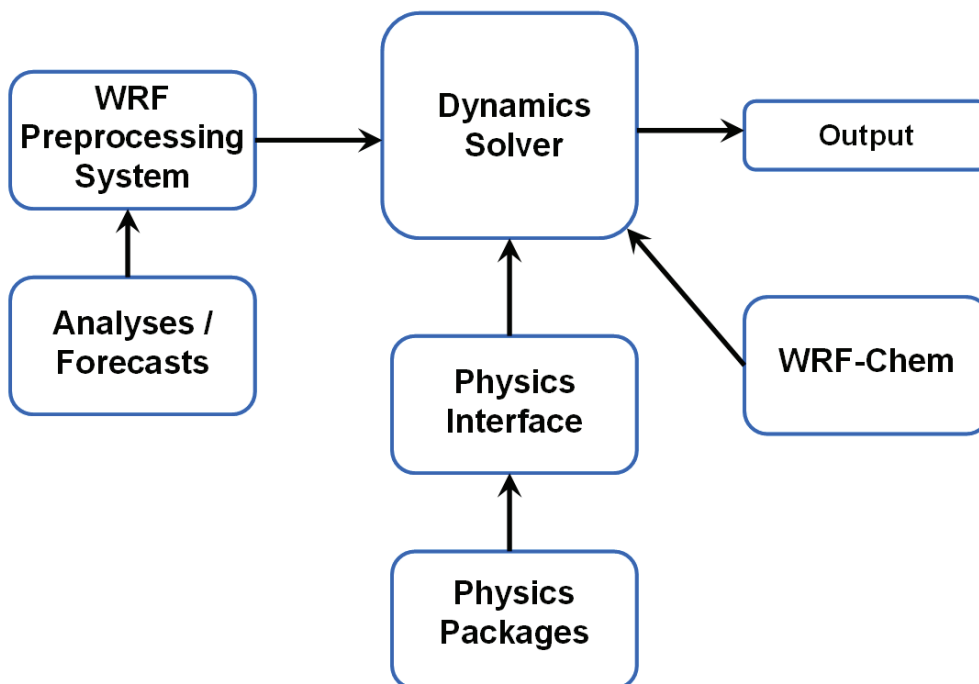
Figure 2.2 *Overview of the principal components of the WRF model system used in this thesis.*

The WRF preprocessing system (WPS) defines a physical grid (i.e. simulation domain) including a map projection type. The model currently supports four map projections – the Lambert conformal, polar stereographic, Mercator, and latitude-longitude grid – of which the Lambert conformal projection is used for this thesis. WPS interpolates static (i.e. terrain, land use etc.) as well as meteorological fields to

the projected domain. These fields are prescribed from either external analysis or forecast data (e.g. the U.S. Geological Survey (USGS), the European Centre for Medium-Range Weather Forecasts (ECMWF) model simulations etc.). The output of the WPS contains 3-dimensional meteorological fields (e.g. temperature, relative humidity, wind components, etc.), 2-dimensional static terrestrial fields (e.g. terrain elevation, vegetation/land use type, map scale factors, etc.) and 2-dimensional time-dependent fields (e.g. surface pressure, soil temperature, soil moisture, etc.) on the selected model's horizontal grid at the selected time slices. These fields are then passed to the dynamics solver for real-time simulations.

The dynamics solver is the key component of the WRF model, which is composed of several programs for real-time simulation and numerical integration. The model solves the non-hydrostatic Euler equations on an Arakawa C-staggered horizontal grid and these governing equations are cast in flux form in order to conserve mass, momentum, entropy and scalars. Prognostic variables for this solver are the column mass of dry air, velocities, potential temperature, and geopotential. Non-conserved variables (e.g. temperature, pressure, density) are diagnosed from the conserved prognostic variables. Using the Arakawa C-grid staggering for spatial discretization means that the horizontal velocity components (u, v) are located normal to the respective faces of the model grid cell, while the mass/thermodynamic/scalar variables (e.g. potential temperature (θ)) are defined at the center of the cell. The model equations are formulated using a terrain-following hydrostatic pressure vertical coordinate, η (Laprise, 1992). Note that the symbol η used here is the same as the definition of the σ coordinate (more specifically "sigma-pressure") used in many atmospheric models, but different from that of the traditional η coordinate (e.g. Warner (2010)). The η coordinate as used in the WRF community is defined as follows:

$$\eta = (p_h - p_{ht})/\mu \qquad \text{where } \mu = p_{hs} - p_{ht} \qquad (1)$$

and p_h is the hydrostatic component of the pressure. p_{hs} and p_{ht} represent values of pressure along the surface and the top boundaries respectively. By definition η monotonically decreases from 1 at the surface to 0 at the upper boundary of the model domain. Using this coordinate, the Euler equations can be expressed as follows:

$$U_t + (\nabla.\mathbf{V}u) + \mathrm{P}_x(p,\phi) = F_U \tag{2}$$
$$V_t + (\nabla.\mathbf{V}v) + \mathrm{P}_y(p,\phi) = F_V \tag{3}$$
$$W_t + (\nabla.\mathbf{V}w) + \mathrm{P}_\eta(p,\mu) = F_W \tag{4}$$
$$\Theta_t + (\nabla.\mathbf{V}\theta) = F_\Theta \tag{5}$$
$$\mu_t + (\nabla.\mathbf{V}) = 0 \tag{6}$$
$$\phi_t + \mu^{-1}[(\nabla.\mathbf{V}\phi) - gW] = 0 \tag{7}$$
$$(Q_m)_t + (\nabla.\mathbf{V}Q_m) = F_{Qm} \tag{8}$$

where p is the pressure, ϕ is the geopotential and g is the acceleration due to gravity. U, V, W and Θ are the flux form variables that include a map-scale factor, m.

i.e. $\mathbf{V} = \mu\mathbf{v} = (U, V, W)$; $U = (\mu u)/m$; $V = (\mu v)/m$; $W = (\mu w)/m$ and $\Theta = \mu\theta/m$

Q_m represents the mass of scalar variables (i.e. mass of water vapor, cloud water, rain, etc.). P_x, P_y, and P_η are the pressure gradient terms, and F_U, F_V, F_W, F_Θ, and F_{Qm} are the forcing terms arising from model physics, turbulent mixing, spherical projections, and the Earth's rotation respectively. The subscripts $- x$, y, η, and t – in the above equations denote partial differentiation.

The diagnostic relation for the full pressure is expressed as:

$$p = p_0(R_d\theta_m / p_0\alpha_d)^c \tag{9}$$

where p_0 is the reference pressure (typically 10^5 Pascals), R_d is the gas constant, α_d is the inverse density of the dry air and c =1.4 (ratio of the heat capacities for dry air).

Eq. (2) to (9) are solved in the dynamics solver. The interested reader is referred to Skamarock and Klemp (2008) for more details. A time-split integration scheme is used for the temporal discretization. The slow or low-frequency (meteorologically significant) modes are integrated using a third order Runge-Kutta time integration scheme, while the high frequency acoustic modes are integrated over smaller time

steps. The time-split integration for these flux form equations is described in Klemp et al.(2007).

A set of physics packages is used in WRF and these packages are divided into several categories, each containing several choices. The physics categories are as follows: (1) microphysics, (2) cumulus parameterization, (3) planetary boundary layer (PBL), (4) land-surface model and (5) radiation. More information on physics schemes used in WRF is available at http://www.mmm.ucar.edu/wrf/users/docs/wrf-phy.html. An interface between the physics packages and the dynamics solver has been designed to provide a user-friendly environment to either use a scheme selected from the existing categories or to add new other physics packages.

A fully coupled "online" WRF-Chemistry (WRF-Chem) package (Grell et al., 2005) with a passive transport option (i.e. without chemical mechanisms and deposition) is used together with the WRF core model (WRF 3.0 version used here) to simulate the tracer distribution. The term "online" means that the tracer transport is carried out simultaneously with the meteorological variables at each time step while using the same transport scheme, the same grid (both horizontal and vertical components) and the physics schemes. The surface fluxes are added to the lowest vertical level of the WRF grid at each simulation time step. The "tagged" tracer option in the model allows for the separation of tracers from different sources (e.g. anthropogenic, biospheric, oceanic etc).

2.1.2   STILT model

The STILT is a stochastic Lagrangian Particle Dispersion Model (LPDM) which has been used extensively in regional simulations and inversion studies for different greenhouse gases (Gerbig et al., 2003; Göckede et al., 2010; Gourdji, 2010; Lin et al., 2004; Miller et al., 2008). STILT is based on the source code from the Hybrid Single-Particle Lagrangian Integrated Trajectory (HYSPLIT) system (Draxler and Hess, 1998), but with a different turbulent scheme (Lin et al., 2003). A detailed description of the STILT model is given in Lin et al. (2003) and the source code is available at http://www.bgc-jena.mpg.de/bgc-systems/projects/stilt/.

The turbulent flow in STILT is modeled as a Markov chain. The velocity vector **u** can be decomposed as follows:

$$\mathbf{u} = \bar{\mathbf{u}} + \mathbf{u}' \tag{10}$$

where $\bar{\mathbf{u}}$ is the mean component and $\mathbf{u}'$ is the turbulent component of the velocity vector. Based on the Markov assumption, $\mathbf{u}'$ is expressed as:

$$\mathbf{u}'(t + \Delta t) = R(\Delta t)\mathbf{u}' + \mathbf{u}''(t) \tag{11}$$

where $\mathbf{u}''$ is a random vector drawn from a normal distribution with a width equal to the variance of the random velocity, Δt is the time step and R is an autocorrelation coefficient which determines the standard random walk for the turbulent velocity components for each time step (see Lin et al. (2003) and Chapter 5 for more details).

The main purpose of using STILT is to derive the sensitivity of the atmospheric mixing ratio measurements to the upstream surface-atmosphere fluxes (footprints). The model simulates ensembles of virtual particles representing air parcels of equal mass, transported backward in time from an observation point by mean winds and sub-grid turbulent winds. The wind fields (vertical profiles of both horizontal and vertical wind components) generated by either WRF or ECMWF are used in STILT to drive the particles starting from a receptor location. The resulting back trajectories are used to calculate the footprints. The footprints derived from the STILT model are used as an adjoint of the transport model, which is needed for the inverse system (see Chapters 5 and 6 for more details). These footprints are then mapped to the high-resolution surface fluxes as well as initial fields of CO_2 concentrations (see Sect. 2.2 and 2.4) in order to obtain the simulated CO_2 concentrations at the receptor location.

As in WRF and ECMWF, STILT also uses the terrain-following vertical coordinate system (more specifically "sigma-height") with coefficients that are calculated using the terrain height, pressure, and temperature fields provided either by WRF or ECMWF. The vertical coordinate used in STILT, σ, is defined as:

$$\sigma = \frac{z_{top} - z_{msl}}{z_{top} - z_{gl}} \tag{12}$$

where z_{top} is the model top height, z_{msl} is the height of the model level and z_{gl} is the height of the model terrain. The height of the planetary boundary layer (PBL) is calculated internally in STILT using profiles of atmospheric variables (temperature

and wind) and their gradients provided by other models (e.g. WRF, ECMWF). STILT also provides an option to use PBL height simulated from external sources.

For coupling STILT with WRF, the WRF source code is modified to generate the additional meteorological variables required to drive STILT (Nehrkorn et al., 2010). The variables simulated by WRF at η levels are linearly interpolated in height from η levels to σ levels. The reader is referred to Nehrkorn et al. (2010) for more details on the coupling between WRF and STILT.

2.2   Biosphere model

A diagnostic model, the Vegetation Photosynthesis and Respiration Model (VPRM), which combines remote sensing, meteorological and tower flux data (Mahadevan et al., 2008) is used to generate biospheric fluxes. Together with measured or simulated meteorological variables, the VPRM utilizes satellite estimates of the Enhanced Vegetation Index (EVI) and the Land Surface Water Index ($LSWI$) to calculate the Net Ecosystem Exchange (NEE) at high temporal and spatial resolutions. These satellite estimates are based on the measurements from the Moderate Resolution Imaging Spectroradiometer (MODIS) aboard the Terra and Aqua satellites operated by the National Aeronautics and Space Administration (http://modis.gsfc.nasa.gov/). A detailed description of the VPRM model is given in Mahadevan et al. (2008).

VPRM has a simple mathematical structure with a minimal number of model parameters. The basic structure of the VPRM model is depicted in **Fig. 2.3**. The vegetation cover in the model domain is represented by the SYNMAP data (Jung et al., 2006) with a spatial resolution of 1 km. The VPRM uses 5 vegetation classes over Europe, consisting of deciduous forest, evergreen forest, mixed forest, grassland, and cropland. The model calculates NEE as a sum of Gross Ecosystem Exchange (GEE) and Respiration (R_{eco}). The full VPRM model equation is expressed as:

$$NEE = \underbrace{-\gamma \times T_{scale} \times P_{scale} \times W_{scale} \times (1/[1+(PAR/PAR_0)]) \times EVI \times PAR}_{GEE} + \underbrace{(\alpha \times T) + \beta}_{R_{eco}} \quad (13)$$
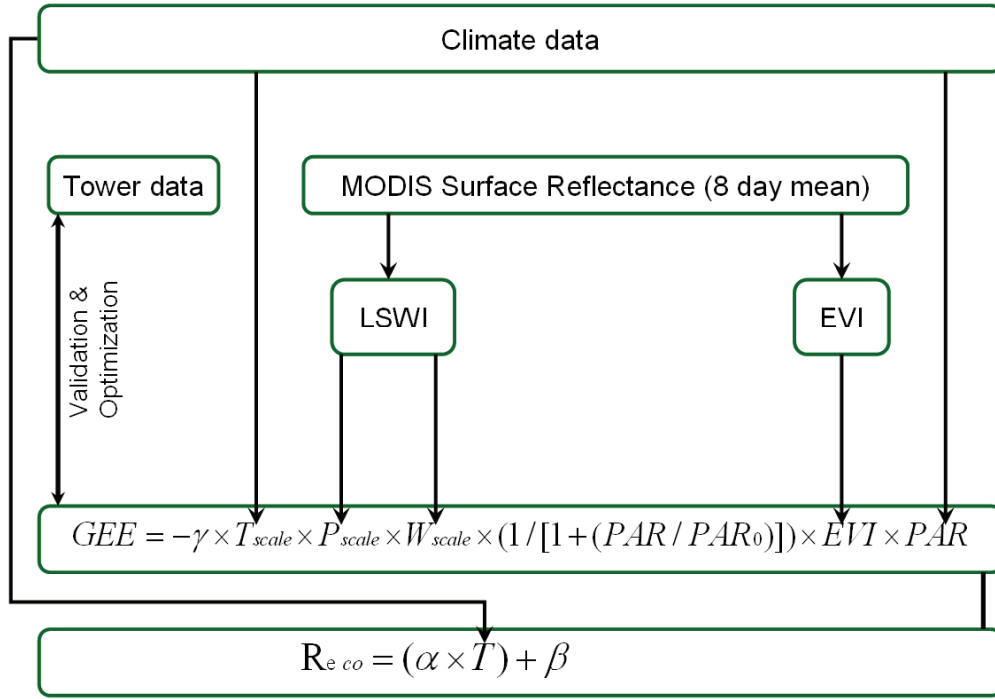
Figure 2.3 Schematic diagram of the Vegetation Photosynthesis Respiration Model (VPRM) estimating Gross Ecosystem Exchange (GEE) and Respiration (R_{eco}). The figure is adapted from Mahadevan et al. (2008).

where T_{scale}, P_{scale}, and W_{scale} are scalars for temperature, leaf phenology, and canopy water content respectively.

T_{scale} is the temperature dependence of the photosynthesis and is expressed as:

$$T_{scale} = \frac{(T - T_{min}) \times (T - T_{max})}{[(T - T_{min}) \times (T - T_{max})] - (T - T_{opt})^2} \qquad (14)$$

where T_{min}, T_{max} and T_{opt} are minimum, maximum and optimal temperatures for photosynthesis respectively and their values are fixed for each vegetation type. T is the surface air temperature. The value for T is taken either from model simulations (e.g. WRF simulations) or from site meteorology. T_{scale} is set to zero when T is less than T_{min}.

P_{scale} is used to account for the effect of leaf age on photosynthesis. Based on vegetation types, P_{scale} is set to either 1 (e.g. evergreen forest) or computed as a function of $LSWI$ (e.g. deciduous forest) with the following relation:

$$P_{scale} = \frac{(1 + LSWI)}{2} \qquad (15)$$

W_{scale} is used to account for the effects of water stress and is calculated as follows:

$$W_{scale} = \frac{(1 + LSWI)}{(1 + LSWI_{max})} \tag{16}$$

where $LSWI_{max}$ is the maximum value of $LSWI$ during the plant growing season for each site.

PAR is the photosynthetically-active radiation. PAR (or rather the short-wave radiation) can be measured at flux sites or prescribed from model simulations. PAR_0 is the half-saturation value. γ, PAR_0, α, and β are the adjustable model parameters in VPRM and are determined by comparison to the data from eddy covariance measurements. This way, the calculation of GEE in VPRM follows a light use efficiency (LUE) approach, where the photosynthetic flux is initially on linear relationship with radiation, and then saturates at radiation levels larger than PAR_0.

2.2.1   Satellite data

The eight-day mean surface reflectance data (MOD09A1) provided by MODIS are used in VPRM to calculate EVI and $LSWI$. The MOD09A1 product gives data for 9 MODIS pixels with a resolution of 1.5 km × 1.5 km. A preprocessing tool (http://www.bgc-jena.mpg.de/~rkretsch/vprmpreproc/; hereafter referred to as the VPRM preprocessor) was developed to process these satellite data for the aforementioned coupled models. The VPRM preprocessor includes software tools provided by the MODIS Land Quality Assessment Group (Roy et al., 2002) together with projection tool – MODIS Reprojection Tool (MRT) (https://lpdaac.usgs.gov/lpdaac/tools/modis_reprojection_tool) – to extract EVI and $LSWI$ from the Hierarchical Data Format (HDF), to apply lowess (locally weighted least squares) filtering to reduce data noise, and to transform EVI and $LSWI$ from the sinusoidal projection to the mapping projections used in WRF or STILT (Lambert Conformal for WRF and Cartesian for STILT).

2.3   Coupled transport-biosphere models: Eulerian and Lagrangian systems

The transport models described in Sect. 2.1 are coupled to the VPRM to simulate biospheric CO_2 concentrations (Ahmadov et al., 2007; Matross et al., 2006). The resultant modeling systems are termed WRF-VPRM and WRF/STILT-VPRM, where

the former represents the Eulerian part and the latter is its Lagrangian counterpart in the model-data fusion system (see Fig. 2.1). Modifications which have been made in the original source code for incorporating surface fluxes of CO_2 as well as initial/lateral boundary conditions of CO_2 concentrations are described in Ahmadov et al. (2007). The coupling of VPRM with WRF was performed in such a way that VPRM calculates CO_2 fluxes (i.e. *NEE*) using meteorological fields (surface temperature and short-wave radiation) simulated by WRF and then these fluxes are passed to WRF at each time step to be transported as a tracer (Ahmadov et al., 2007; Ahmadov et al., 2009). The STILT is coupled offline with VPRM to generate the CO_2 concentration at the receptor. The footprints generated by STILT are multiplied by CO_2 fluxes simulated by VPRM. More details on these coupled models are provided in Chapter 5. The surface fluxes and the initial/boundary conditions used are described in Sect. 2.4.

2.4   Initial/lateral boundary conditions and surface fluxes

The initial/lateral boundary conditions of the meteorological variables, the sea surface temperature (SST) and the soil initialization fields of each run are prescribed from the ECMWF model simulations (http://www.ecmwf.int) with a spatial resolution of about 20 km and 6-hourly temporal intervals. Global CO_2 concentration fields based on a simulation by an atmospheric tracer transport model, the TM3 (Heimann and Körner, 2003) is used to represent the initial/lateral boundary conditions of CO_2. These analyzed fields, with a spatial resolution of $4° \times 5°$, 19 vertical levels and a temporal resolution of 3 hours, are available at: http://www.bgc-jena.mpg.de/~christian.roedenbeck/download-CO2-3D/ Fossil fuel emission data from an inventory provided by the Institut für Energiewirtschaft und Rationelle Energieanwendung (IER), University of Stuttgart (http://carboeurope.ier.uni-stuttgart.de/) at a spatial resolution of 10 km are used to account for anthropogenic fluxes. The ocean fluxes are included for the simulations presented in Chapter 3, and these fluxes are prescribed from the monthly air-sea fluxes from Takahashi et al. (2002). The biospheric fluxes are simulated at a high spatial resolution (e.g. 2 km, 6 km and 10 km) and are used to account for CO_2 uptake and release from different biomes (see section 2.2).

2.5   Inversion system

The inverse system is used to derive biosphere-atmosphere exchange on regional scales from CO_2 concentration measurements, such as those made from tall towers. The system uses the Bayesian inversion technique which utilizes a priori knowledge of fluxes generated from VPRM. The scaling factors of *GEE* and R_{eco} will be further optimized as given by Gerbig et al. (2003), to match the atmospheric constraint imposed by the concentration measurements via the inversion technique. The inversion also takes into account the potential uncertainties including uncertainties in a priori fluxes, measurement and transport. The inversion theory and technique are described in detail in Chapter 6.

2.6   References

Ahmadov, R., Gerbig, C., Kretschmer, R., Koerner, S., Neininger, B., Dolman, A. J., and Sarrat, C.: Mesoscale covariance of transport and CO_2 fluxes: Evidence from observations and simulations using the WRF-VPRM coupled atmosphere-biosphere model, Journal of Geophysical Research-Atmospheres, 112, D22107, doi:22110.21029/22007JD008552, 2007.

Ahmadov, R., Gerbig, C., Kretschmer, R., Körner, S., Rödenbeck, C., Bousquet, P., and Ramonet, M.: Comparing high resolution WRF-VPRM simulations and two global CO_2 transport models with coastal tower measurements of CO_2, Biogeosciences, 6, 807-817, 2009.

Draxler, R. R., and Hess, G. D.: An overview of the HYSPLIT_4 modeling system for trajectories, dispersion, and deposition, Aust. Meteorol. Mag., 47, 295-308, 1998.

Gerbig, C., Lin, J. C., Wofsy, S. C., Daube, B. C., Andrews, A. E., Stephens, B. B., Bakwin, P. S., and Grainger, C. A.: Toward constraining regional-scale fluxes of CO_2 with atmospheric observations over a continent: 2. Analysis of COBRA data using a receptor-oriented framework, Journal of Geophysical Research-Atmospheres, 108, 4757, doi:4710.1029/2003JD003770, 2003.

Göckede, M., Michalak, A. M., Vickers, D., Turner, D. P., and Law, B. E.: Atmospheric inverse modeling to constrain regional-scale CO_2 budgets at high spatial and temporal resolution, J. Geophys. Res., 115, D15113, doi:10.1029/2009JD012257, 2010.

Gourdji, S. M., Hirsch, A. I., Mueller, K. L., Andrews, A. E., and Michalak, A. M.: Regional-scale geostatistical inverse modeling of North American CO_2 fluxes: a synthetic data study, Atmos. Chem. Phys., 10, 6151-6167, doi:10.5194/acp-10-6151-2010, 2010.

Grell, G. A., Peckham, S. E., Schmitz, R., McKeen, S. A., Frost, G., Skamarock, W. C., and Eder, B.: Fully coupled online chemistry within the WRF model, Atmos. Environ., 39, 6957-6975, 2005.

Heimann, M., and Körner, S.: The global atmospheric tracer model TM3. Technical Reports, Max-Planck-Institut für Biogeochemie, 5, pp.131, 2003.

Jung, M., Henkel, K., Herold, M., and Churkina, G.: Exploiting synergies of global land cover products for carbon cycle modeling, Remote Sens. Environ., 101, 534-553, 2006.

Klemp, J. B., Skamarock, W. C., and Dudhia, J.: Conservative Split-Explicit Time Integration Methods for the Compressible Nonhydrostatic Equations, Mon. Wea. Rev., 135, 2897-2913, doi: 10.1175/MWR3440.1, 2007.

Laprise, R.: The Euler Equations of motion with hydrostatic pressure as as independent variable, Mon. Wea. Rev., 120, 197–207, 1992.

Lin, J. C., Gerbig, C., Wofsy, S. C., Andrews, A. E., Daube, B. C., Davis, K. J., and Grainger, C. A.: A near-field tool for simulating the upstream influence of atmospheric observations: The Stochastic Time-Inverted Lagrangian Transport (STILT) model, Journal of Geophysical Research-Atmospheres, 108, 4493, doi:4410.1029/2002JD003161, 2003.

Lin, J. C., Gerbig, C., Wofsy, S. C., Andrews, A. E., Daube, B. C., Grainger, C. A., Stephens, B. B., Bakwin, P. S., and Hollinger, D. Y.: Measuring fluxes of trace gases at regional scales by Lagrangian observations: Application to the CO_2 Budget and Rectification Airborne (COBRA) study, Journal of Geophysical Research-Atmospheres, 109, D15304, doi:15310.11029/12004JD004754, 2004.

Mahadevan, P., Wofsy, S. C., Matross, D. M., Xiao, X., Dunn, A. L., Lin, J. C., Gerbig, C., Munger, J. W., Chow, V. Y., and Gottlieb, E. W.: A satellite-based biosphere parameterization for net ecosystem CO_2 exchange: Vegetation Photosynthesis and Respiration Model (VPRM), Global Biogeochemical Cycles, 22, GB2005, doi:2010.1029/2006GB002735, 2008.

Matross, D. M., Andrews, A., Pathmathevan, M., Gerbig, C., Lin, J. C., Wofsy, S. C., Daube, B. C., Gottlieb, E. W., Chow, V. Y., Lee, J. T., Zhao, C. L., Bakwin, P. S., Munger, J. W., and Hollinger, D. Y.: Estimating regional carbon exchange in New England and Quebec by combining atmospheric, ground-based and satellite data, Tellus Ser. B-Chem. Phys. Meteorol., 58, 344-358, 2006.

Miller, S. M., Matross, D. M., Andrews, A. E., Millet, D. B., Longo, M., Gottlieb, E. W., Hirsch, A. I., Gerbig, C., Lin, J. C., Daube, B. C., Hudman, R. C., Dias, P. L. S., Chow, V. Y., and Wofsy, S. C.: Sources of carbon monoxide and formaldehyde in North America determined from high-resolution atmospheric data, Atmos. Chem. Phys, 8, 7673-7696, 2008.

Nehrkorn, T., Eluszkiewicz, J., Wofsy, S. C., Lin, J. C., Gerbig, C., Longo, M., and Freitas, S.: Coupled weather research and forecasting–stochastic time-inverted lagrangian transport (WRF–STILT) model, Meteorol Atmos Phys, 107, 51-64, 2010.

Roy, D. P., Borak, J. S., Devadiga, S., Wolfe, R. E., Zheng, M., and Descloitres, J.: The MODIS Land Product Quality Assessment Approach, Remote Sens. Environ., 83, 62-76, 2002.

Skamarock , W. C., and Klemp, J. B.: A time-split nonhydrostatic atmospheric model for weather research and forecasting applications, Journal of Computational Physics, 227, 3465-3485, 2008.

Skamarock, W. C., Klemp, J. B., Dudhia, J., Gill, D. O., Barker, D. M., Duda, M. G., Huang, X.-Y., Wang, W., and Powers, J. G.: A description of the Advanced Research WRF Version 3, Tech. Note, NCAR/TN-475+STR, National Center for Atmos. Research, Boulder, Colorado, USA, 2008.

Takahashi, T., Sutherland, S. C., Sweeney, C., Poisson, A., Metzl, N., Tilbrook, B., Bates, N., Wanninkhof, R., Feely, R. A., Sabine, C., Olafsson, J., and Nojiri, Y.: Global sea-air CO_2 flux based on climatological surface ocean pCO_2, and seasonal biological and temperature effects, Deep-Sea Res. Part II-Top. Stud. Oceanogr., 49, 1601-1622, 2002.

Warner, T. T.: Numerical Weather and Climate Prediction, Cambridge University Press, 548 pp., 2010.

3   High-resolution modeling of CO_2 over Europe: Implications for representation errors of satellite retrievals

Abstract

Satellite retrievals for column CO_2 with better spatial and temporal sampling are expected to improve the current surface flux estimates of CO_2 via inverse techniques. However, the spatial scale mismatch between remotely sensed CO_2 and current generation inverse models can induce representation error, which can cause systematic biases in flux estimates. This study is focused on estimating the representation error associated with utilization of satellite measurements in global models with a horizontal resolution of about 1 degree or less. Simulated CO_2 fields are used for the analysis and those are generated from the high-resolution modeling framework WRF-VPRM, which links CO_2 fluxes from a diagnostic biosphere model to a weather forecasting model at 10 km × 10 km horizontal resolution. Sub-grid variability of column averaged CO_2, i.e. the variability not resolved by global models, reached up to 1.2 ppm with a median value of 0.4 ppm. Statistical analysis of the simulation results indicate that orography plays an important role. Using sub-grid variability of orography and CO_2 fluxes as well as resolved mixing ratio of CO_2, a linear model can be formulated that could explain about 50 % of the spatial patterns in the systematic (bias or correlated error) component of representation error in column and near-surface CO_2 during day- and night-times. These findings give hints for a parameterization of representation error which would allow for the representation error to be taken into account in inverse models or data assimilation systems.

3.1   Introduction

Atmospheric CO_2 has been rising since pre-industrial times due to anthropogenic emissions from fossil fuel combustion and deforestation, which are considered to be major causes of global warming (IPCC, 2007). Climate predictions using coupled carbon cycle climate models differ greatly in their feedbacks between the biosphere and climate, resulting in vastly differing mixing ratios of CO_2 at the end of this century (Friedlingstein et al., 2006). This calls for an improved understanding of biospheric CO_2 fluxes at regional scales. A global network of observations is being

used together with modeling tools to derive surface-atmosphere exchanges (via inverse techniques) which can help in quantifying biosphere-climate feedback and assist in monitoring CO_2 trends in the context of climate change mitigation.

However, past studies show that the current observation network is not sufficient to adequately account for uncertainties in surface flux estimates (Gurney et al., 2003). Satellite measurements of column-integrated CO_2 concentrations with better spatial and temporal sampling as well as with adequate precision (~1 ppm) are expected to improve this situation (Rayner and O'Brien, 2001; Miller et al., 2007). Passive satellite missions, such as the Orbiting Carbon Observatory (OCO) (Crisp et al., 2004), and the Greenhouse gases Observatory Satellite (GOSAT) (NIES, 2006) are designed to measure column integrated dry air mole fraction under clear sky conditions using reflected sunlight. GOSAT is now in orbit, but unfortunately the launch of OCO failed. In addition, active sensor missions are under investigation, such as ESA's Earth Explorer candidate mission A-SCOPE, the Advanced Space Carbon and Climate Observation of Planet Earth (ESA, 2008) and NASA's mission ASCENDS, the Active Sensing of CO_2 Emissions over Nights, Days and Seasons , which have the advantage of also being able to measure during the night and thus provide a stronger constraint on respiration fluxes.

The above mentioned satellite measurements are able to provide global coverage of column-averaged CO_2 dry air mole fraction which can improve current estimates of global carbon budgets (via inverse techniques). The footprint sizes of satellite missions using passive sensors (measuring reflected sun light) such as OCO and GOSAT are approximately 1.3 km and 10.5 km respectively (Crisp et al., 2004; NIES, 2006). Active missions such as A-SCOPE using LIDAR technology, have smaller footprint sizes of around 0.1 km which allows for better sampling under partially cloudy conditions by making use of the cloud gaps (ESA, 2008). However, active missions need some averaging for these 0.1 km footprints to improve the signal-to noise. These footprints are at least an order of magnitude smaller than the highest resolution global inverse models (Peters et al., 2007).

All remote sensing methods to measure atmospheric CO_2 require clear sky conditions, thus a small footprint is desirable since it allows sampling during scattered cloud conditions. On the other hand, the retrievals may not be representative

for average CO_2 concentration in such coarse model grids, and may thus introduce a larger representation error (a spatial mismatch of satellite retrievals within larger grid cells). The representation error is expected to depend on the strength and horizontal extent of CO_2 flux variability and on meteorology, both of which influence the variability in atmospheric CO_2. Previous studies show that the representation error increases with decreasing horizontal resolution (Gerbig et al., 2003) and is higher when mesoscale circulation is important (Tolk et al., 2008; Ahmadov et al., 2007). Based on measurements from airborne platforms during the CO_2 Budget and Rectification study (COBRA-2000), Gerbig et al. (2003) concluded that transport models require a horizontal resolution smaller than 30 km to capture important spatial variability of CO_2 in the continental boundary layer, which could be attributed to the spatial variability of surface fluxes. The representation error corresponding to typical global grid cells can be up to 1 to 2 ppm, which is an order of magnitude larger than the sampling errors (Gerbig et al., 2003). The sampling error referred in Gerbig et al., 2003 includes both limitations in instrument precision and accuracy and uncertainty caused by unresolved atmospheric variability of CO_2 within the mixed layer due to turbulent eddies. Further, topography plays a role in representation error. It is reported that representation error induced by small scale orographic features can be as large as 3 ppm at scales of 100 km (Tolk et al., 2008). van der Molen and Dolman (2007), in their case study around Zotino in Central Siberia, showed that topographic heterogeneity of 500 m within a spatial scale of 200 km can generate horizontal gradients in CO_2 concentrations of 30 ppm. Hence it is highly important to address representation error caused by these spatial mismatches, also for column-integrated measurements from remote sensing, prior to the quantitative assimilation of the information into global modelling systems.

There are a number of studies which have estimated the representation error within a model grid cell when using satellite column measurements. Based on high-resolution CO_2 simulations, taking the difference between the simulated grid cell mean and the sampled mean, Corbin et al. (2008) estimated the representation error over North and South America and concluded that satellite retrievals cannot be used in current inverse models to represent large regions with significant CO_2 variability unless transport models are to be run at high resolution. Alkhaled et al. (2008) estimated the representation error based on statistical methods, using spatial covariance information

of CO_2 based on model simulation of global CO_2 distribution at a spatial scale of $2^o \times 2.5^o$ over the sampled regions together with information about the retrieved soundings without the knowledge of the true mean value. Representation error is quantified using a hypothetical transport model with a spatial resolution of $1^o \times 1^o$ and a 3 km^2 retrieval footprint.

This study focuses on estimating possible representation error of column mixing ratios from remote sensing in global transport models, and on the causes of the spatial variability of CO_2 within a grid cell. Spatial variability of CO_2 is assessed quantitatively based on high-resolution simulations for a domain centered over Europe. Using a high-resolution transport model, coupled to surface-atmosphere fluxes of CO_2, allows accounting for mesoscale phenomena such as land-sea breeze effects (Ahmadov et al., 2007). Such effects can not be represented in a statistical method as deployed by Alkhaled et al. (2008). Possible representation error is estimated as the sub-grid variability of near surface CO_2 and column averages of CO_2 within typical global model grid cells. Hypothetical A-SCOPE track data are used with MODIS cloud pixel information to realistically represent satellite observations. In this context it is relevant to see the possibility of a sub-grid parameterization scheme based on resolved variables to capture the representation error. Such a parameterization scheme could pave the way to describing representation error in coarser models without using high-resolution simulations.

The outline of this chapter is as follows: Section 3.2 provides a brief overview of the modeling framework which is used to simulate the CO_2 fields. Section 3.3 presents the methodology adopted to estimate representation error associated with utilizing satellite column measurements in global inversion studies. In Sect. 3.4, statistical analyses of sub-grid variability of CO_2 fields within grid cells of 100 km × 100 km size are presented to estimate possible representation error for retrieved satellite column mixing ratios. The correlations of sub-grid variability with resolved variables are investigated to assess the possibility of parameterization schemes for representation error in coarser models.

3.2   Modeling framework

The modeling system, WRF-VPRM (Ahmadov et al., 2007), which combines the Weather Research and Forecasting model, WRF (http://www.mmm.ucar.edu/wrf/),

with a diagnostic biosphere model, the Vegetation Photosynthesis and Respiration Model, VPRM (Mahadevan et al., 2008) is used. The coupling of these models is done in such a way that VPRM utilizes near surface temperature (T_2) and short wave radiation (SNDOWN) from WRF in order to compute CO_2 fluxes and to provide these to WRF to be transported as a passive tracer.

The principal component of the modelling system consists of a mesoscale transport model, WRF, using the passive tracer transport option from WRF-Chem (Grell et al., 2005) to simulate the distribution of CO_2 transported by advection, convection and turbulence. Some modifications were made in order to implement simulations of CO_2 transport, which are described in detail in Ahmadov et al. (2007). An overview of the WRF physics/dynamics options used for the simulations is given in Table 3.1.

Table 3.1 *An overview of the WRF physics/dynamics options used.*

Vertical coordinates	Terrain-following hydrostatic pressure vertical coordinate
Basic equations	Non-hydrostatic, compressible
Grid type	Arakawa-C grid
Time integration	3rd order Runge-Kutta split-explicit
Spatial integration	3rd and 5th order differencing for vertical and horizontal advection respectively; both for momentum and scalars
Time step	60 sec
Domain configuration	1 domain with horizontal resolution of 10 km; size 2500×2300 km; 31 vertical levels;
Physics schemes	Radiation - Rapid Radiative Transfer Model (RRTM) Long wave and Dudhia; Microphysics - WSM 3-class simple ice scheme; Cumulus - Kain-Fritsch (new Eta) scheme (only for the coarse domain) PBL – YSU; Surface layer – Monin-Obukhov Land-surface – NOAH LSM

The satellite-constrained biosphere model, VPRM is used here to account for CO_2 uptake and emission for different biomes. It is a diagnostic model which uses MODIS (http://modis.gsfc.nasa.gov/) satellite indices, the Enhanced Vegetation Index (EVI), and the Land Surface Water Index ($LSWI$) at 500 m resolution to calculate hourly Net Ecosystem Exchange (NEE). NEE is calculated here as a sum of Gross Ecosystem Exchange (GEE) and Respiration (R_{eco}). GEE is calculated by using EVI and $LSWI$ from MODIS, and temperature at 2 m (T_2) and shortwave radiation fluxes (SNDOWN), provided by WRF. R_{eco} is calculated as a linear function of WRF-simulated temperature (Mahadevan et al., 2008). To represent land cover in VPRM, a global land cover product – SYNMAP (Jung et al., 2006) – is used with a spatial resolution of 1 km and 8 vegetation classes which are suitable for the European domain. The VPRM parameters which control the CO_2-uptake by photosynthesis and the CO_2-emission by respiration for each vegetation class have been optimized using eddy flux measurements for different biomes in Europe collected during the CarboEurope IP experiment (for details see Ahmadov et al.(2007). VPRM captures the spatiotemporal variability of biosphere-atmosphere exchange remarkably well, as shown by comparison with various flux measurements sites corresponding to different vegetation types for longer periods (Ahmadov et al., 2007; Mahadevan et al., 2008). GEE and R_{eco} computed in VPRM is passed on to WRF to simulate the distribution of total CO_2 concentration.

In addition to VPRM biospheric fluxes, anthropogenic and ocean fluxes are included in WRF. High-resolution fossil fuel emission data from Institut für Energiewirtschaft und Rationelle Energieanwendung (IER), University of Stuttgart (http://carboeurope.ier.uni-stuttgart.de/) are used for the year 2000, at a spatial resolution of 10 km. Temporal emission patterns were preserved by shifting the IER data for 2000 by a few days to match the weekdays in 2003. The total mass of the emissions was conserved when mapping onto the WRF grid. To account for ocean fluxes in WRF, the monthly air-sea fluxes from Takahashi et al. (2002) are used.

Initial and lateral tracer boundary conditions are prescribed from global CO_2 concentration fields based on a simulation by a global atmospheric Tracer transport model, TM3 (Heimann et al., 2003), with a spatial resolution of 4° × 5°, and a temporal resolution of 3 hours. TM3 is driven by re-analyzed meteorological data

from NCEP and surface fluxes optimized by atmospheric inversion (Rödenbeck et al., 2003). As initial and lateral meteorological boundary conditions for WRF, analyzed fields from ECMWF (http://www.ecmwf.int/) with a horizontal resolution of approximately 35 km and a 6-hour time step are used. The model setup largely follows the TransCom-continuous protocol (Law et al., 2008), allowing for a comparison of the mesoscale simulation with a number of measurement sites, but also with a large number of global models used for inversion studies. Note, however, that the anthropogenic and the biospheric fluxes are different from the ones used within the TransCom-continuous Experiment.

Mesoscale simulations are carried out for 2 to 30 July 2003 (29 days of data in total), with a horizontal resolution of 10 km (hereafter referred to as "fine-scale"), and 30 vertical levels extending from the surface up to about 100 hPa for a domain centered over Europe (**Fig. 3.1**). Each day of simulation starts at 18 UTC of the previous day, and continues for 30 hours, of which the first 6 hours are used for spin up. These fine-scale simulations attempt to reproduce the atmospheric tracer distribution on scales much closer to the actual footprint of remote sensing instruments (~0.1 to 10 km). Model validation has been carried out at a number of measurement sites, and also in comparison with output from TransCom models which are used for global inversion studies. Table 3.2 shows a summary of statistics of the WRF-VPRM simulation compared to measurements, along with results from two other models used in the TransCom-continuous Experiment, the global model TM3 and the regional model REMO (Chevillard et al., 2002). WRF-VPRM performs reasonably well in comparison to other models for most of the measurement sites, indicated by a high fraction of explained variance (squared correlation coefficient, R^2), but also, more importantly in the context of this study, a quite realistic representation of the variability with relative standard deviations (ratio of modeled to observed standard deviation) close to unity for most sites. However note that the variability is poorly represented when blending the high-resolution fluxes used in WRF (VPRM and IER emissions) with the coarse fluxes used in the TransCom continuous experiment (CASA biospheric fluxes and fossil98 emissions at $1° \times 1°$ resolution); in this case the performance is comparable to REMO also in terms of relative standard deviations (not shown in the table).

Table 3.2 *Statistics for the comparison of WRF-VPRM simulations to measurements, along with results from two transport models used in the TransCom Continuous experiment.*

Squared correlation coefficient, R^2

	Model [Horizontal Resolution]		
Station	*WRF-VPRM [10 km × 10 km]*	*REMO [$0.5^0 × 0.5^0$]*	*TM3_vfg [$1.875^0 × 1.875^0$]*
Heidelberg	0.29	0.48	0.37
Hegyhatsal 48m	0.44	0.35	0.28
Hegyhatsal 115	0.41	0.48	0.25
Schauinsland	0.16	0.07	0.06
Mace Head	0.24	0.48	0.29
Monte Cimone	0.38	0.13	0.17

Ratio of modeled to measured standard deviation

	Model [Horizontal Resolution]		
Station	*WRF-VPRM [10 km × 10 km]*	*REMO [$0.5^0 × 0.5^0$]*	*TM3_vfg [$1.875^0 × 1.875^0$]*
Heidelberg	0.95	2.72	1.03
Hegyhatsal 48m	1.21	2.75	1.64
Hegyhatsal 115	1.19	1.61	1.28
Schauinsland	0.99	0.92	0.82
Mace Head	0.6	1.02	0.79
Monte Cimone	1.82	0.65	0.79

3.3   Methodology

3.3.1   Calculating representation error for satellite-derived CO_2 columns

Since satellite measurements represent column averages, mass weighted average column CO_2 mixing ratios are calculated from the modeled CO_2 fields. Due to the differences in the averaging kernel for different space-borne sensors, no specific averaging kernel was used. Column averaging excluded the topmost model level in order to exclude boundary effects. The average column CO_2 mixing ratio is thus given by:

$$CO_{2,col} = \frac{\sum_{i=1}^{nz}(m_i \cdot CO_{2,i})}{\sum_{i=1}^{nz} m_i}$$

Here m_i is the dry grid cell air mass and $CO_{2,i}$ is the mixing ratio at model level i, and nz is the number of levels used.

In this context, the term "representation error" refers to possible discrepancies when utilizing satellite information in current global models, due to the spatial scale mismatches between satellite retrievals and larger model grids. Representation error ($\sigma_{c,col}$) is thus estimated for every time step (hourly) as sub-grid variability (standard deviation of fine-scale $CO_{2,col}$) within the spatial resolution of current global models. The spatial scale of 100 km is chosen to represent the lower limit of grid cell size found in global models used for inversions. The calculated column averages do not include the entire stratosphere, which amounts to a fraction of 10% of the total atmospheric column (pressure at model top is 100 mbar). Since horizontal variability of CO_2 in the stratosphere on scales below 100 km is small (at least not larger than in the troposphere), neglecting this part of the column might thus result at maximum in a 10% overestimation of the sub-grid variability.

The monthly averaged $\sigma_{c,col}$ (ie, $\bar{\sigma}_{c,col}$, specific for a given hour of the day) includes random and systematic components of representation error. It is important to assess which component of this representation error is purely random, i.e. noise introduced by weather, and which part is systematic in nature (the "bias", or "correlated error" term). Random, uncorrelated errors are expected to decrease when averaging over longer time periods, e.g. for deriving monthly fluxes. In order to exclude random errors, daily values of CO_2 mixing ratios (at a specific time, e.g 14:00 GMT) are averaged for the whole month and subsequently estimated sub-grid variability from this averaged concentration (ie, $\sigma (\overline{CO}_{2,col})$). This gives a representation error ($\sigma_{c,col(bias)}$) that is purely of systematic nature on a monthly time scale. The term "bias" introduced here is defined as the part of the error that is correlated over the timescale of a month. Note that the bias component of error is always denoted with subscript "(bias)".

In addition to $\sigma_{c,col}$, near-surface CO_2 mixing ratios ($CO_{2,sur}$) at an altitude of about 150 m above the surface (the second model level) are also analyzed in terms of sub-grid variability $\sigma_{c,sur}$. A similar analysis is again carried out for a spatial resolution of 200 km (not shown).

3.3.2   Using A-SCOPE track information including MODIS cloud information

The simulated A-SCOPE sampling track is utilized in order to realistically represent satellite retrievals with the model simulations. Temporal resolution of the track is 0.5 seconds, corresponding to a spatial distance between subsequent samples of 3.5 km (F.M Bréon, Laboratoire des Sciences du Climat et de l'Environnement, *Personal Communication*). The samples are initially aggregated to a horizontal resolution 10 km and these 10 km samples are used for further analysis. Note that this aggregation causes the representation error to be underestimated. Since satellite retrievals require clear sky conditions, the simulations are sampled for the pixels with clear sky. Cloud free conditions are picked up based on MODIS cloud pixel information (http://modis-atmos.gsfc.nasa.gov/MOD35_L2/index.html) at 1 km resolution for the period of simulation. 46438 samples of cloud free columns are extracted including 27605 samples (60 %) over land. These samples were aggregated to a spatial scale of 100 km along the A-SCOPE track. There is an average of 6.6 cloud free 10 km samples along the A-SCOPE track within each 100 km grid cell. The representation error for A-SCOPE derived CO_2 columns (σ_{ascope}) is calculated as the standard deviations of the difference of 100 km × 100 km flight track averages using only A-SCOPE 10 km samples along the flight track, and the 100 km × 100 km averages based on all 10 km grid cells (σ [A-SCOPE 100 km averages - true 100 km averages]).

3.4   Results and Discussion

In this section the results based on WRF-VPRM simulations of the distribution of atmospheric CO_2 in July 2003 are presented. An example of the WRF-VPRM output is given in **Fig. 3.1**, showing simulated (a) $CO_{2,sur}$ and (b) $CO_{2,col}$ on 12 July at 14:00 GMT. Strong spatial variability of the boundary layer CO_2 can be seen near the coasts (Fig. 3.1a) due to the 3D-rectification effect (the temporal covariance between sea-land breeze transport and biosphere-atmosphere fluxes, both of which are radiation controlled) (Ahmadov et al., 2007), which causes respired CO_2 to be advected over the ocean by synoptic winds or by the land-breeze circulation and to be concentrated

in a shallow layer due to the lack of vertical mixing over the ocean. There is also strong variability associated with frontal activity towards the north-eastern edge of the domain, with strong gradients in CO_2 associated with the location of a cold front. Such behavior has previously been reported (Parazoo et al., 2008), and has been attributed to the deformational flow along the fronts. A similar pattern is followed in the CO_2 column average (Fig. 3.1b) near coasts as well as towards the north-eastern edge of the domain, which suggests a strong contribution of boundary layer concentrations to column averages. Movies showing the complete simulation can be seen at: http://www.bgc.mpg.de/bgc-systems/news/near-surface_co2.html/   and http://www.bgc.mpg.de/bgc-systems/news/column_co2.html/
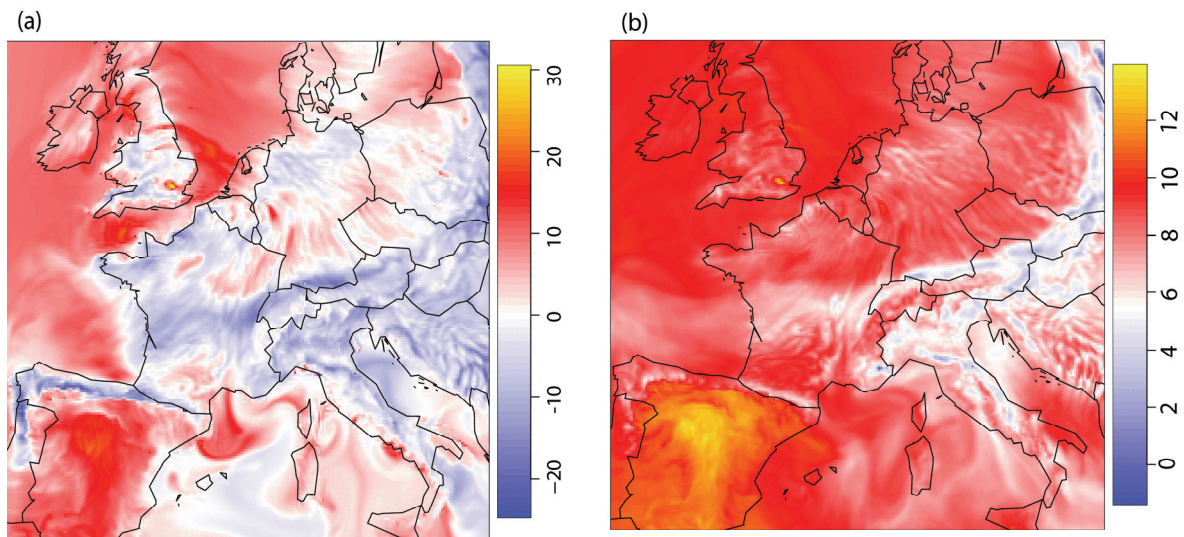
Figure 3.1   WRF-VPRM simulations of CO_2 mixing ratios (a) for an altitude of about 150 m above ground (2nd model level), $CO_{2,sur}$ and (b)mass weighted average CO_2 column, $CO_{2,col}$ during 12th July at 14:00 GMT with horizontal resolutions of 10 km for a domain centered over Europe. An offset of 365 ppm is to be added to get total CO_2 in ppm. Note the scale change between near surface and column CO_2.

3.4.1   Subgrid variability of near surface and column averages of CO_2 concentrations

Figure 3.2 shows the monthly averaged $\sigma_{c,sur}$ and $\sigma_{c,col}$ (at 14:00 GMT only) for July 2003. Coastal and mountain regions are distinct, with strong sub-grid variability both in near surface and in column averages of CO_2 concentrations. This is due to relatively strong gradients of surface fluxes in these regions.

The similarity in spatial patterns of $\sigma_{c,col}$ and $\sigma_{c,sur}$ (Fig(s). 3.2a and 3.2b) indicates that the CO_2 column values are correlated with surface values. **Figure 3.3** shows the

profile distribution of monthly averaged (at 14:00 GMT) σ_c within different bins of vertical model levels. Most of the higher values of σ_c are found to be within the lowest 2 km. σ_c strongly decreases with increasing altitude, showing less influence of
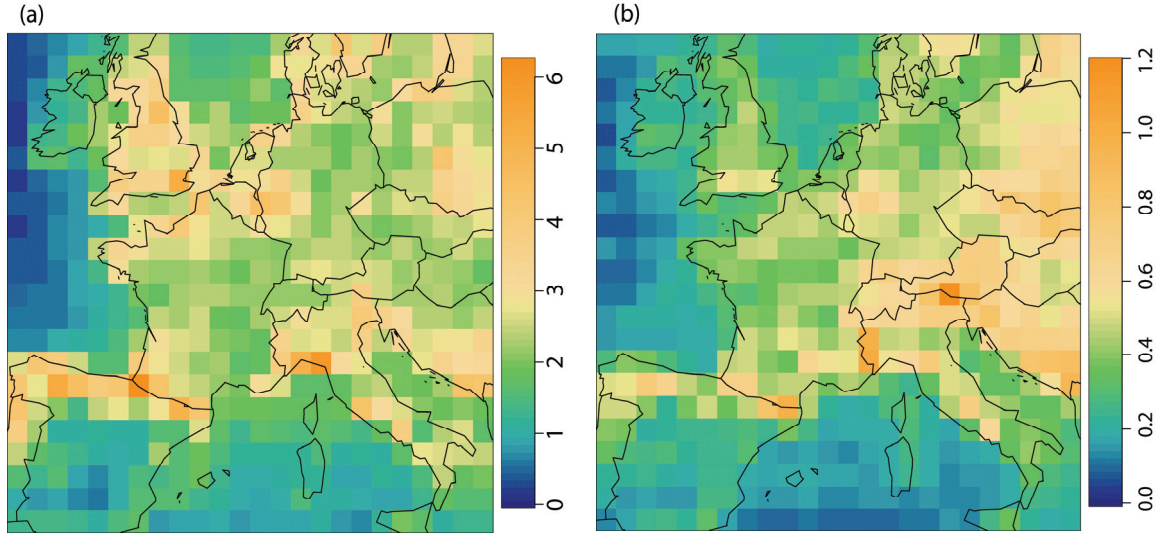
Figure 3.2 *The monthly averaged subgrid variability of CO_2 concentrations for: (a) near-surface, $\sigma_{c,sur}$ and (b) column average, $\sigma_{c,col,}$ for July 2003, using 14:00 GMT only. All values are in ppm.*
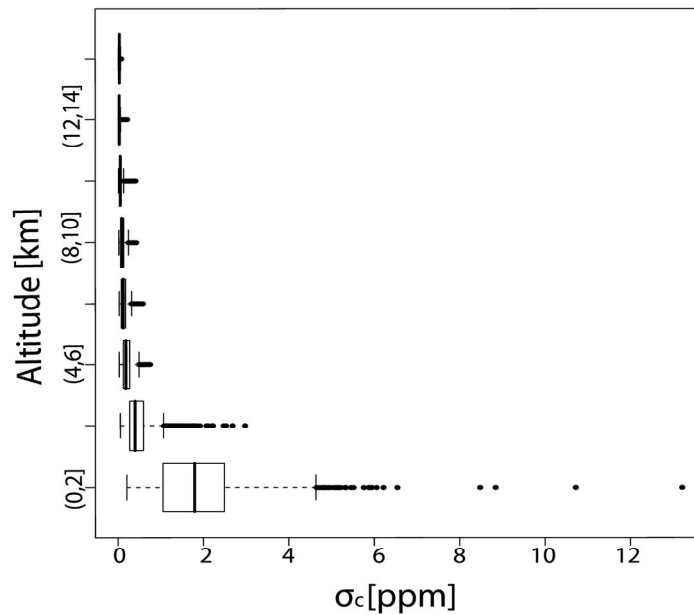
Figure 3.3 *Box and whisker plot for different altitudes (from ground) ranges of the sub-grid concentration variability (σ_c) for July 2003 (14:00GMT only). Boxes indicate the central 50%, the bar across the box is the median value, and whiskers indicate the range of the central 95% of data points. Individual data points are shown outside the central 95%.*

surface fluxes at higher altitudes. These results are consistent with van der Molen and Dolman (2007) which shows that the effect of surface heterogeneity is generally

54

observed in lower atmospheric layers. This indicates the dominance of boundary layer concentration variability in column averages. These dominances can be significant during synoptic scale events, where CO_2 column variability is strongly correlated (squared correlation coefficient, $R^2 = 0.37$) to boundary layer concentrations (see Fig. 3.1), but not strongly correlated (squared correlation coefficient, $R^2 = 0.12$) to concentrations in the free troposphere around 4 km (not shown).

The analysis shows that the monthly averaged $\sigma_{c,col}$ for the domain is, on average, 0.4 ppm, with maximum values around 1.2 ppm and the 90% percentile 0.6 ppm (see Fig. 3.2). Partitioning the data into ocean and land pixels shows that $\sigma_{c,col}$ is more than twice as large over land (0.5 ppm) as compared to over ocean areas (0.2 ppm) as is expected due to the stronger magnitude and variability of terrestrial fluxes. This is not negligible compared to the targeted accuracy of future satellite retrievals. The monthly bias error, $\sigma_{c,col(bias)}$, is smaller than the full error, but shows a similar pattern with maximum values around 0.9 ppm for mountain and coastal regions (**Fig. 3.4**).
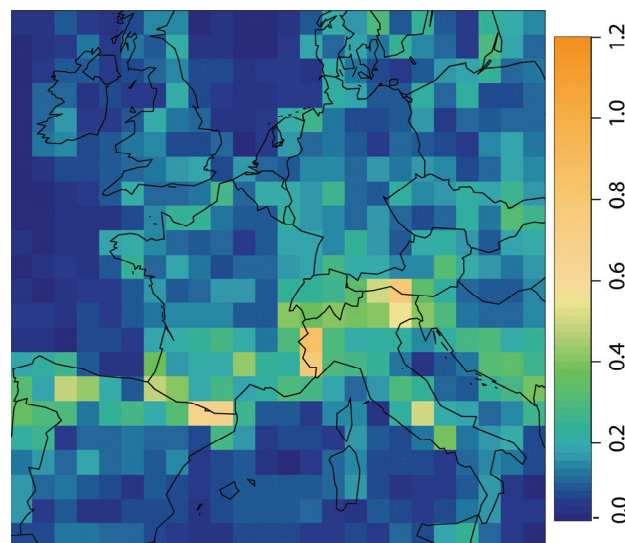
Figure 3.4 *The monthly averaged subgrid variability of temporally aggregated CO_2 column averages (bias) [ppm] for July 2003, using 14:00 GMT only.*

3.4.2   Representation error for satellite derived CO_2 columns

3.4.2.1 Hypothetical satellite track

Representation error is quantified here using a hypothetical satellite track going through each 100 km $\times$ 100 km cell. Following the sampling conditions used by Alkhaled et al. (2008) (hereafter referred to as A08), two spatial distributions of satellite retrievals are assumed: (1) a full North-South swath (10 pixels from south to north) in each grid cell (idealized sampling condition), and (2) a single retrieval at the corner of each grid cell (adverse sampling condition). The representation error of hypothetical satellite-derived CO_2 columns (σ_{hypo}) is estimated for these two spatial distributions of satellite retrievals within each 100 km $\times$ 100 km grid cell. **Figure 3.5** shows the distribution of σ_{hypo} for a full North-South swath at the center of each 100 $\times$ 100 km grid cell. The σ_{hypo} for the previously mentioned sampling conditions are estimated and compared with A08 in July for the European domain, and are given in Table 3.3.   The larger representation error is seen over land for both sampling conditions, and is about a factor of two larger when compared to ocean (see Table 3.3).   The statistical approach suggested by A08 gives much smoother behaviour compared to these results and also neglects land-ocean differences in the European
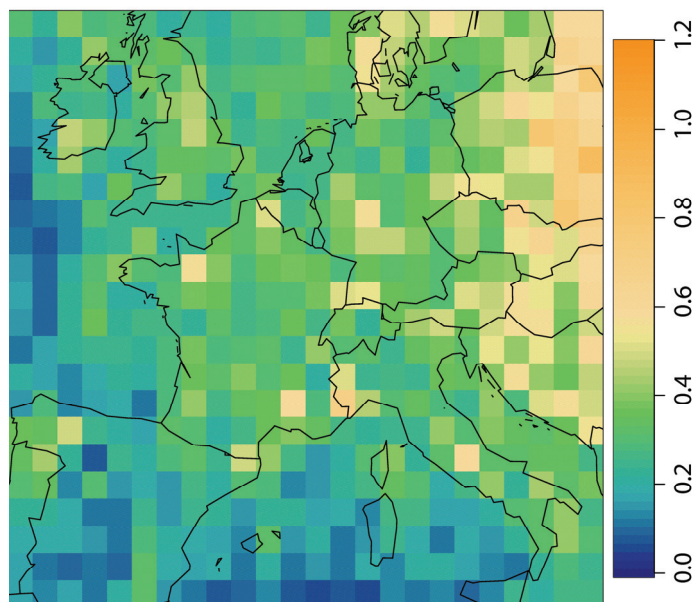
Figure 3.5 *The subgrid variability of column averages of CO_2 concentrations [ppm] based on hypothetical north-south swath at the centre of each 100 km grid cell for July 2003 (monthly averaged at 14:00 GMT).*

56

domain. Under idealized sampling conditions (10 pixel swath), the representation error estimates are nearly an order of magnitude larger than those by A08, and under adverse sampling conditions (single corner pixel) the estimates are a factor of two larger compared to those provided by A08 (Table 3.3). This finding is in line with experimental evidence: A08 found agreement between their estimates and observation-based estimates from Lin et al. (2004), however the latter were a conservative (low-end or lower limit) estimate of subgrid variability. In fact the power variogram model used by Lin et al. (2004) underestimated the observed variogram estimates by a factor of 3 to 5 at scales smaller than 200 km (see Figure 2 in Lin et al. (2004)). This corresponds to about a factor of two differences in single pixel representation error, which is remarkably similar to the factor found between the high-resolution model based estimate and the one provided by A08. This suggests that it is not generally possible to extract information about the representation error from coarse model simulations as suggested in A08. Such a method is likely to fail in cases of mesoscale complexity.

Table 3.3 *The possible representation error when using A-SCOPE and hypothetical satellite tracks for different sampling conditions. The values given in square brackets indicate (monthly bias component). All values are in ppm.*

Representation error	*All*	*Land*	*Ocean*	*(Alkhaled et al., 2008), EU domain**
Hypothetical Satellite (Single corner pixel)	0.59 [0.22]	0.72 [0.28]	0.35 [0.09]	0.30-0.40
Hypothetical Satellite (North-South Swath)	0.38 [0.16]	0.46 [0.20]	0.24 [0.05]	0.04-0.06
ASCOPE	0.34 [0.12]	0.39 [0.15]	0.30 [0.08]	

*extracted from (Alkhaled et al., 2008), Fig 2c and 2d for the domain used here.

3.4.2.2 A-SCOPE 100 km averages

σ_{ascope} is evaluated using the A-SCOPE satellite track information as described in Sect. 3.2. When combining all A-SCOPE samples within each 100 km grid cell, the resulting representation error σ_{ascope} is reduced compared to the single pixel error. Note that this is due to the fact that several pixels contribute to each A-SCOPE

sample, whose error can partially cancel out. As for the hypothetical satellite tracks, larger representation error for A-SCOPE is seen over land (0.4 ppm) as compared to over ocean areas (0.3 ppm) (Table 3.3).

3.4.3   Dependence of representation error on explanatory variables

Knowledge about the size and the spatial and temporal patterns of the representation error is expected to improve inverse modeling of satellite data, but this would involve using a high-resolution model to estimate the representation error. The goal is to construct a linear model based on a subset of those explanatory variables which explains a significant fraction of sub-grid variability, and which can be used in the context of global inverse modelling to capture the spatiotemporal patterns. Such a linear model is the simplest subgrid parameterization scheme for representation error in coarser models, only accounting for local effects and neglecting any effects from advection of subgrid variability.

Statistical relationships between the representation error and the following variables are explored (not shown): the standard deviation of the fluxes (σ_f), the mean of the fluxes ($\bar{f}$), the absolute mean of the fluxes ($|\bar{f}|$), the mean terrain height ($\bar{h}$), standard deviation of the terrain heights (σ_h) and the mean mixing ratio near the

Table 3.4 *The statistical estimation (squared correlation coefficient) of the bias component of the representation error ($\sigma_{c(bias)}$) explained by each variable and the proposed linear model.*

Explanatory Variables	Day-time		Night-time	
	Column $\sigma_{c,col}$	Surface $\sigma_{c,sur}$	Column $\sigma_{c,col}$	Surface $\sigma_{c,sur}$
σ_f [$\mu.moles/m^2s^{-1}$]	0.34	0.66	0.09	0.13
σ_h [m]	0.51	0.20	0.59	0.33
$\bar{c}$ [ppm]	0.18	0.09	0.02	0.16
Linear model with σ_f, σ_h & $\bar{c}$	0.63	0.67	0.63	0.46

surface ($\bar{c}$). $\bar{c}$ is included since it can be expected that variability is associated with the magnitude of the mixing ratios. The analysis showed that the representation error is best explained by the variables σ_h, σ_f and $\bar{c}$ during day-time as well as night-time. Hence a linear model is constructed using three variables: σ_h, σ_f and $\bar{c}$. Table 3.4 gives the statistical estimation of the variability explained by each of these variables. The similar linear model is also applied for $\sigma_{c,sur}$. The explained variability by each of these variables differs between day- and night-time, also between column and near-surface mixing ratios. The proposed linear models have the same variable structure, but different coefficients for the explanatory variables.

Figure 3.6 shows the dependence of $\sigma_{c,col(bias)}$ on each of these variables. Figure 3.6a shows a monotonic increase of $\sigma_{c,col(bias)}$ with increasing σ_f at the 100 km scale and explains 34% of $\sigma_{c,col(bias)}$ during day-time, however the relationship with σ_f is absent during night-time (Fig. 3.6d). It is found in general that $\sigma_{c(bias)}$ is well explained by σ_f (34% of the total column variability and 66% of the surface variability) during day-time; however correlations are weaker during night-time (Table 3.4). This can be explained as follows: the fluxes are larger and more spatially variable during daytime than during nighttime. In addition, strong vertical mixing during day-time couples the mixing ratios over a deeper part of the column to the patterns in surface fluxes, while during night there is less vertical mixing, with more advection and drainage flow in the stable nocturnal boundary layer, smearing out the signatures from patchy surface fluxes.

The effect of heterogeneity in topography on $\sigma_{c,col(bias)}$ can be seen in Fig(s). 3.6b and 3.6e. $\sigma_{c,col(bias)}$ increases in response to increase in σ_h and explains good fraction (51-59%) of sub-grid variability of mixing ratios. Nocturnal $\sigma_{c,sur(bias)}$ is more correlated with σ_h (33%), rather than day-time $\sigma_{c,sur(bias)}$ (20%) (see Table 3.4; not shown the Figure). This shows that topography has more influence on representation error of CO_2 concentrations in the lower boundary layer during night when transport is more dominant than surface flux variability $\bar{c}$ is negatively correlated with $\sigma_{c,col(bias)}$ during day-time (see Table 3.5) and explains 18% of variability, whereas the correlation is absent during night-time (Fig(s). 3.6c and 3.6f). In contrast to this, the correlation of $\bar{c}$ with $\sigma_{c,surl(bias)}$ is absent during day-time, but explains 16% of nocturnal variability (Table 3.4).
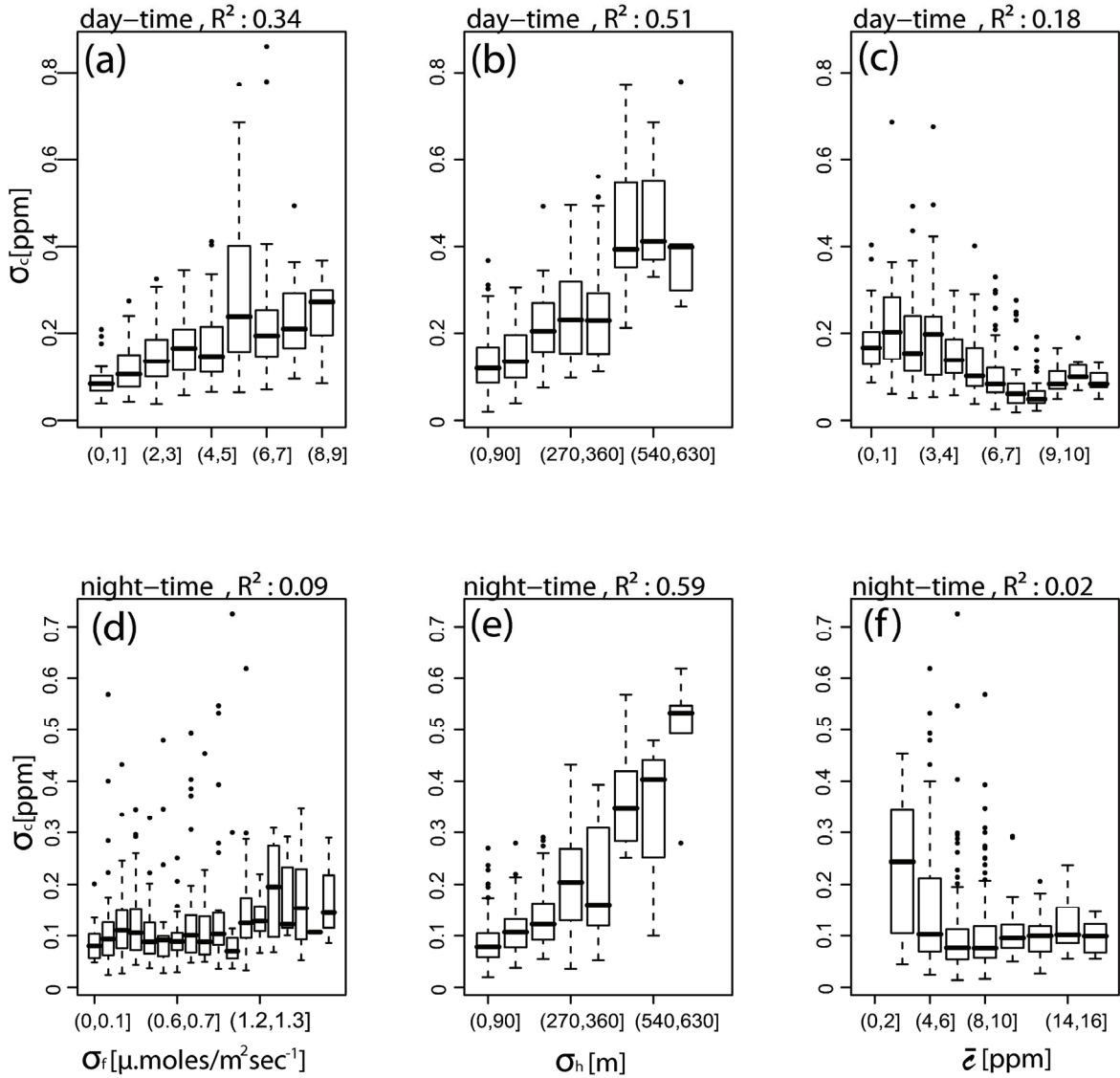
Figure 3.6 *Distribution of the bias component of column CO_2 sub-grid variability ($\sigma_{c,col(bias)}$) on (a, d) σ_f, (b, e) σ_h, (c, f) $\bar{c}$ for July 2003 [(a)-(c):14:00GMT only, (d)-(f): 02:00GMT only]. Boxes indicate the central 50%, the bar across the box the median, and whiskers the central 95%. Individual data points are shown outside the central 95%.*

The linear model using all three variables explains about 50 % of the spatial patterns in the (monthly) bias component of sub-grid variability during day- and night-times (Table 3.4). It is found that nocturnal $\sigma_{c,sur}$ is better explained (60% in comparison to 46%) by the linear model when including the variable $\bar{f}$, however no further improvements for $\sigma_{c,col}$ or day-time $\sigma_{c,sur}$ are found (not shown). **Figure 3.7** illustrates how well the representation error is captured with the proposed linear model. It seems therefore possible to introduce this parameterization of representation error in coarser models so that data assimilation systems using coarser transport models can use realistic estimates for representation error that have the appropriate spatial and temporal dependence. Table 3.5 gives the linear model coefficients for

each of these explanatory variables. Note that coefficients are horizontal scale dependent, and it is expected them to also vary between seasons due to differences in flux patterns and transport characteristics.

Table 3.5. *Coefficients of the linear model for the monthly bias component of the representation error ($\sigma_{c(bias)}$). The standard errors of the coefficients are given in italics.*

	Day-time				Night-time			
	Column $\sigma_{c,col}$ $\times 10^{-2}$		Surface $\sigma_{c,sur}$ $\times 10^{-2}$		Column $\sigma_{c,col}$ $\times 10^{-2}$		Surface $\sigma_{c,sur}$ $\times 10^{-2}$	
Resolution [km × km]	100	200	100	200	100	200	100	200
σ_f [μ.moles/ m^{2}s^{-1}]	1.2 *0.15*	1.7 *0.32*	26.5 *1.03*	34.1 *2.00*	-0.01 *0.60*	0.81 *1.35*	12.6 *10.17*	28.6 *18.91*
σ_h [m]	0.04 *0.00*	0.04 *0.00*	0.07 *0.02*	0.05 *0.03*	0.05 *0.00*	0.05 *0.00*	0.50 *0.03*	0.40 *0.05*
$\bar{c}$ [ppm]	-0.47 *0.07*	-0.40 *0.16*	0.38 *0.47*	0.10 *1.02*	-0.58 *0.09*	-0.91 *0.23*	16.2 *1.50*	17.4 *3.26*
Intercept [ppm]	8.5 *0.58*	11.6 *1.58*	19.3 *4.16*	26.7 *9.85*	10.9 *0.77*	17.1 *2.04*	-27 *13.05*	-18 *28.64*

The implementation of the proposed parameterization scheme in global models requires these three explanatory parameters: σ_h can be easily calculated from any high-resolution topographic elevation data, for example USGS GTOPO dataset (http://eros.usgs.gov/products/elevation/gtopo30.php). The information on fluxes (σ_f) can be accessed from biosphere models with high spatial resolution, e.g VPRM. $\bar{c}$ is represented in global model simulations or from the satellite retrievals. However, care has to be taken to remove long-term trends and seasonal cycles when simulating longer periods, otherwise representation error estimates would be falsely influenced by these. Such a simple parameterization would reduce the impact of representation error significantly, although an inverse modeling study would be required to investigate the reduction of the impact on flux retrievals.
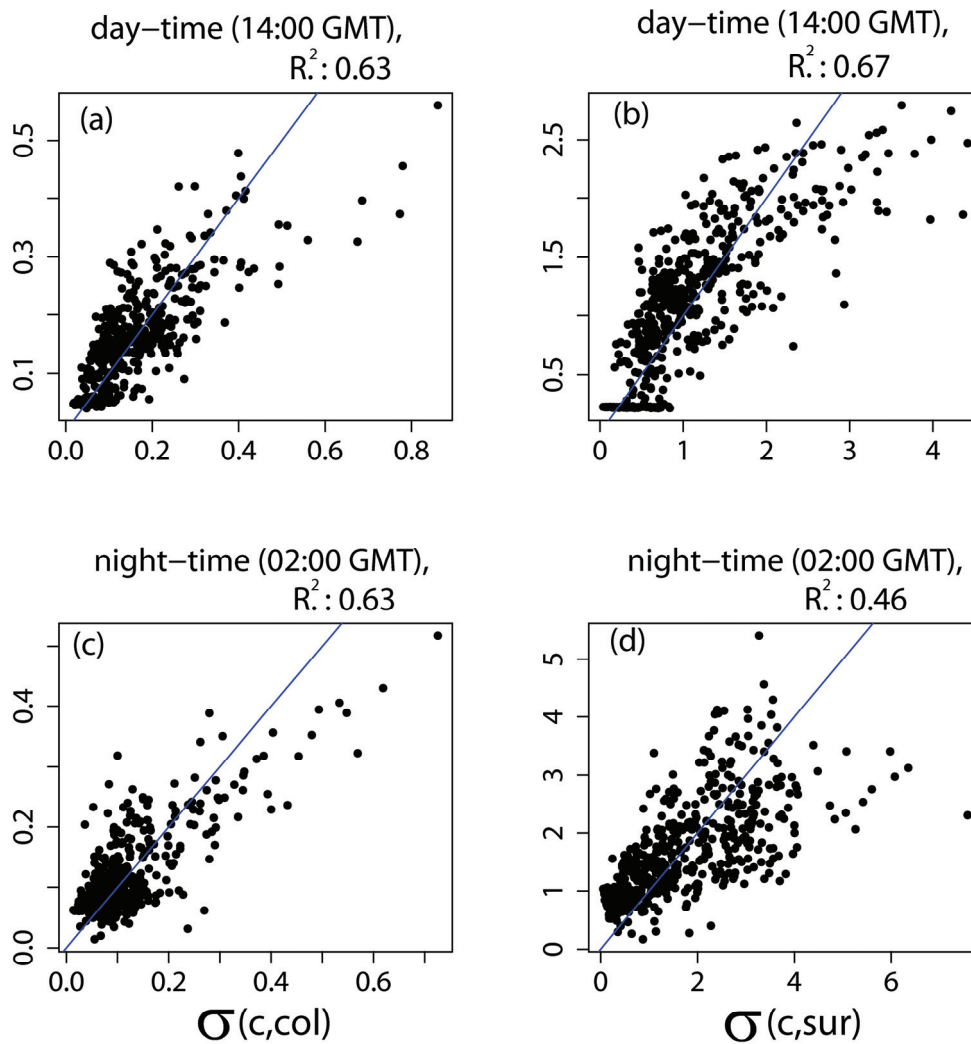
Figure 3.7 *The linear model (bias) estimates of representation error (X-axis) compared to the values from the WRF-VPRM simulations (Y-axis) for (a,c)column averages, $\sigma_{c,col(bias)}$ and (b,d)near-surface, $\sigma_{c,sur(bias)}$ for July 2003 [(a)-(b):14:00GMT only, (c)-(d): 02:00GMT only]. The 1:1 line is shown in blue.*

3.5   Summary and Outlook

Satellite retrievals of column CO_2 provide a global coverage of measurements; these often correspond to small footprints of the order of a few kilometers or less. The analysis of high-resolution WRF-VPRM fields of CO_2 show that when these column retrievals representing small spatial scales are used in inverse studies with current global transport models with grid sizes of 100 km, the scale mismatches can introduce representation error of up to 1.2 ppm, which is above the targeted precision of most satellite measurements. This leads to a systematic bias in flux estimates when using inverse modeling approaches.

Compared to estimates based on variogram analysis of coarse models (Alkhaled et al., 2008), representation error for a full swath of 10 km width of a hypothetical satellite (idealized sampling condition) was found to be nearly an order of magnitude larger. This clearly shows the necessity of using high-resolution simulations to assess variability on scales not resolved by global models. The analysis with A-SCOPE track data together with MODIS cloud pixel information shows a larger representation error (0.39 ppm) over land compared to other regions.

Furthermore, an attempt is made to model sub-grid scale variability (or representation error) as a linear function of local, grid-resolved variables. A linear model is constructed separately for day- and night-times as well as for column and near-surface, which has the same variable structure (σ_h, σ_f and $\bar{c}$), but different coefficients for the explanatory variables. The proposed linear model (using all three variables) could explain about 50 % of the spatial patterns in the bias component of sub-grid variability during day- and night-times. These findings suggest a parameterization which would enable a substantial fraction of the representation error to be taken into account more quantitatively.

Future steps are to implement this parameterization in an inverse modeling system and to assess, using pseudo-data experiments, to what degree biases in retrieved fluxes due to representation error can be avoided. A further refinement of the method will be to treat the subgrid variance as a tracer itself, allowing for advection of subgrid variance within the coarse transport models similar to the study by Galmarini et al. (2008), with the difference that the focus is not on micro-scale, but rather on mesoscale variability. This would allow for a better description of the representation error over the ocean near the coasts, which with the current linear (local) model cannot be described. When including such a realistic description of the representation error into a data assimilation system that uses remotely-sensed column CO_2, it is expected that the retrieved information, such as regional carbon budgets and uncertainties thereof, will improve significantly.

3.6   References

Ahmadov, R., Gerbig, C., Kretschmer, R., Koerner, S., Neininger, B., Dolman, A. J., and Sarrat,C.: Mesoscale covariance of transport and CO_2 fluxes: Evidence from observations and simulations using the WRF-VPRM coupled atmosphere-biosphere model, J. Geophys. Res.Atmos., 112, D22107, doi:22110.21029/22007JD008552, 2007.

Alkhaled, A. A., Michalak, A. M., and Kawa, S. R.: Using CO_2 spatial variability to quantify representation errors of satellite CO_2 retrievals, Geophys. Res. Lett., 35, L16813, doi:10.1029/2008GL034528, 2008.

Chevillard, A., Karstens, U., Ciais, P., Lafont, S., and Heimann, M.: Simulation of atmospheric CO_2 over Europe and western Siberia using the regional scale model REMO, Tellus B, 54B, 872–894, 2002.

Corbin, K. D., Denning, A. S., Lu, L., Wang, J.-W., and Baker, I. T.: Possible representation errors in inversions of satellite CO_2 retrievals, J. Geophys. Res.-Atmos., 113, D02301, doi:10.1029/2007JD008716, 2008.

Crisp, D., Atlas, R. M., Breon, F.-M., Brown, L. R., Burrows, J. P., Ciais, P., Connor, B. J.,Doney, S. C., Fung, I. Y., Jacob, D. J., Miller, C. E., O'Brien, D., Pawson, S., Randerson, J.T., Rayner, P., Salawitch, R. J., Sander, S. P., Sen, B., Stephens, G. L., Tans, P. P., Toon, G. C., Wennberg, P. O., Wofsy, S. C., Yung, Y. L., Kuang, Z., Chudasama, B., Sprague, G.,Weiss, B., Pollock, R., Kenyon, D., and Schroll, S.: The Orbiting Carbon Observatory (OCO) mission, Adv. Space Res., 34, 700–709, 2004.

ESA: European Space Agency Mission Assessment Reports-ASCOPE, online available at: http://esamultimedia.esa.int/docs/SP1313-1 ASCOPE.pdf, 2008   .

Friedlingstein, P., Cox, P., Betts, R., Bopp, L., von Bloh, W., Brovkin, V., Cadule, P., Doney, S., Eby, M., Fung, I., Bala, G., John, J., Jones, C., Joos, F., Kato, T., Kawamiya, M., Knorr, W.,Lindsay, K., Matthews, H. D., Raddatz, T., Rayner, P., Reick, C., Roeckner, E., Schnitzler, K.-G., Schnur, R., Strassmann, K., Weaver, A. J., Yoshikawa, C., and Zeng, N.: Climate carbon cycle feedback analysis: Results from the C4MIP model intercomparison, J. Climate, 19, 3337–3353, 2006.

Galmarini, S., Vinuesa, J.-F., and Martilli, A.: Modeling the impact of sub-grid scale emission variability on upper-air concentration, Atmos. Chem. Phys., 8, 141–158, 2008, http://www.atmos-chem-phys.net/8/141/2008/.

Gerbig, C., Lin, J. C., Wofsy, S. C., Daube, B. C., Andrews, A. E., Stephens, B. B., Bakwin, P. S., and Grainger, C. A.: Toward constraining regional-scale fluxes of CO_2 with atmospheric observations over a continent: 1. Observed spatial variability from airborne   platforms,   J.   Geophys.   Res.-Atmos.,   108,   4756, doi:4710.1029/2002JD003018, 2003.

Grell, G. A., Peckham, S. E., Schmitz, R., McKeen, S. A., Frost, G., Skamarock, W. C., and Eder, B.: Fully coupled online chemistry within the WRF model, Atmos. Environ., 39, 6957– 6975, 2005.

Gurney, K. R., Law, R. M., Denning, A. S., Rayner, P. J., Baker, D., Bousquet, P., Bruhwiler, L., Chen, Y.-H., Ciais, P., Fan, S. M., Fung, I. Y., Gloor, M., Heimann, M., Higuchi, K., John, J., Kowalczyk, E., Maki, T., Maksyutov, S., Peylin, 5 P., Prather, M., Pak, B. C., Sarmiento, J., Taguchi, S., Takahashi, T., and Yuen, C.-W.: TransCom 3 CO_2 inversion intercomparison: 1. Annual mean control results and sensitivity to transport and prior flux information, Tellus B, 55, 555–579, 2003.

Heimann, M., Koerner, S., Tegen, I., and Werner, M.: The global atmospheric tracer model TM3. Technical Reports, Max-Planck-Institut für Biogeochemie, 5, 131 p., 2003.

IPCC: Climate Change 2007: Synthesis Report. Contribution of Working Groups I, II and III to the Fourth Assessment Report of the Intergovernmental Panel on Climate Change, edited by: Core Writing Team, Pachauri, R. K., and Reisinger, A., IPCC, Cambridge University Press, Cambridge, 104 pp., 2007.

Jung, M., Henkel, K., Herold, M., and Churkina, G.: Exploiting synergies of global land cover products for carbon cycle modeling, Remote Sens. Environ., 101, 534–553, 2006.

Law, R. M., Peters, W., Rödenbeck, C., Aulagnier, C., Baker, I., Bergmann, D. J., Bousquet, P., Brandt, J., Bruhwiler, L., Cameron-Smith, P. J., Christensen, J. H., Delage, F., Denning, A. S., Fan, S., Geels, C., Houweling, S., Imasu, R., Karstens, U., Kawa, S. R., Kleist, J., Krol, M. C., Lin, S.-J., Lokupitiya, R., Maki, T., Maksyutov, S., Niwa, Y., Onishi, R., Parazoo, N., Patra, P. K., Pieterse, G., Rivier, L., Satoh, M., Serrar, S., Taguchi, S., Takigawa, M., Vautard, R., Vermeulen, A. T., and Zhu, Z.: TransCom model simulations of hourly atmospheric CO_2: Experimental overview and diurnal cycle results for 2002, Global Biogeochem. Cy., 22, GB3009, doi:3010.1029/2007GB003050, 2008.

Lin, J. C., Gerbig, C., Daube, B. C., Wofsy, S. C., Andrews, A. E., Vay, S. A., and Anderson, B. E.: An empirical analysis of the spatial variability of atmospheric CO_2: Implications for inverse analyses and space-borne sensors, Geophys. Res. Lett., 31, L23104, doi:23110.21029/22004GL020957, 2004.

Mahadevan, P., Wofsy, S. C., Matross, D. M., Xiao, X., Dunn, A. L., Lin, J. C., Gerbig, C., Munger, J. W., Chow, V. Y., and Gottlieb, E. W.: A satellite-based biosphere parameterization for net ecosystem CO_2 exchange: Vegetation Photosynthesis and Respiration Model (VPRM), Global Biogeochem. Cy., 22, GB2005, doi:2010.1029/2006GB002735, 2008.

Miller, C. E., Crisp, D., DeCola, P. L., Olsen, S. C., Randerson, J. T., Michalak, A. M., Alkhaled, A., Rayner, P., Jacob, D. J., Suntharalingam, P., Jones, D. B. A., Denning, A. S., Nicholls, M. E., Doney, S. C., Pawson, S., Boesch, H., Connor, B. J., Fung, I. Y., O'Brien, D., Salawitch, R. J., Sander, S. P., Sen, B., Tans, P., Toon, G. C., Wennberg, P. O., Wofsy, S. C., Yung, Y. L., and Law, R. M.: Precision requirements for space-based XCO2 data, J. Geophys. Res., 112, D10314, doi:10.1029/2006JD007659, 2007.

NIES: GOSAT: Greenhouse Gases Observing Satellite, Tsukuba, Japan, 2006. Parazoo, N. C., Denning, A. S., Kawa, S. R., Corbin, K. D., Lokupitiya, R. S., and

Baker, I. T.: Mechanisms for synoptic variations of atmospheric CO_2 in North America, South America and Europe, Atmos. Chem. Phys., 8, 7239–7254, 2008, http://www.atmos-chem-phys.net/8/7239/2008/.

Peters, W., Jacobson, A. R., Sweeney, C., Andrews, A. E., Conway, T. J., Masarie, K., Miller, J. B., Bruhwiler, L. M. P., P´ etron, G., Hirsch, A. I., Worthy, D. E. J., van der Werf, G. R., Randerson, J. T., Wennberg, P. O., Krol, M. C., and Tans, P. P.: An atmospheric perspective on North American carbon dioxide exchange: CarbonTracker, P. Natl. Acad. Sci. USA, 104, 18925–18930, 2007.

Rayner, P. J. and O'Brien, D. M.: The utility of remotely sensed CO_2 concentration data in surface source inversions, Geophys. Res. Lett., 28, 175–178, 2001.

Roedenbeck, C., Houweling, S., Gloor, M., and Heimann, M.: CO_2 flux history 1982–2001 inferred from atmospheric data using a global inversion of atmospheric transport, Atmos. Chem. Phys., 3, 1919–1964, 2003, http://www.atmos-chem-phys.net/3/1919/2003/.

Takahashi, T., Sutherland, S. C., Sweeney, C., Poisson, A., Metzl, N., Tilbrook, B., Bates, N., Wanninkhof, R., Feely, R. A., Sabine, C., Olafsson, J., and Nojiri, Y.: Global sea-air CO_2 flux based on climatological surface ocean pCO2, and seasonal biological and temperature effects, Deep-Sea Res. II, 49, 1601–1622, 2002.

Tolk, L. F., Meesters, A. G. C. A., Dolman, A. J., and Peters, W.: Modelling representation errors of atmospheric CO_2 mixing ratios at a regional scale, Atmos. Chem. Phys., 8, 6587–6596, 2008, http://www.atmos-chem-phys.net/8/6587/2008/.

van der Molen, M. K. and Dolman, A. J.: Regional carbon fluxes and the effect of topography on the variability of atmospheric CO_2, J. Geophys. Res.-Atmos., 112, D01104, doi:01110.01029/02006JD007649, 2007.

4 High-resolution simulations of atmospheric CO_2 over complex terrain- representing the Ochsenkopf mountain tall tower

Abstract

Accurate simulation of the spatial and temporal variability of tracer mixing ratios over complex terrain is challenging, but essential in order to utilize measurements made in complex orography (e.g. mountain and coastal sites) in an atmospheric inverse framework to better estimate regional fluxes of these trace gases. This study investigates the ability of high-resolution modeling tools to simulate meteorological and CO_2 fields around Ochsenkopf tall tower, situated in Fichtelgebirge mountain range, Germany (1022 m a.s.l.; 50°1'48" N, 11°48'30" E). Tower measurements made at different heights for different seasons are used together with the measurements from an aircraft campaign. Two tracer transport models – WRF (Eulerian based) and STILT (Lagrangian based), both with a 2 km horizontal resolution – are used together with the satellite-based biospheric model VPRM to simulate the distribution of atmospheric CO_2 concentration over Ochsenkopf. The results suggest that the high-resolution models can capture diurnal, seasonal and synoptic variability of observed mixing ratios much better than coarse global models. The effects of mesoscale transports such as mountain-valley circulation and mountain-waves on atmospheric CO_2 distributions are reproduced remarkably well in the high-resolution models. With this study, it is emphasized that the high-resolution modeling simulations are important in the context of inverse modeling frameworks to utilize measurements provided from mountain or complex terrain sites.

4.1 Introduction

It is well known that atmospheric CO_2 is rising due to fossil fuel combustion and deforestation. Being the most important anthropogenic greenhouse gas, accumulation of CO_2 in the atmosphere is reported to be the major cause of global warming (Le Treut et al., 2007). Out of the total emitted CO_2, about 55% is taken up by natural reservoirs (the land biosphere and ocean), while the rest, the so-called "airborne fraction", stays in the atmosphere. However, this fraction exhibits large interannual variability due to the varying source and sinks of CO_2, mainly over land. Quantifying these sources and sinks is highly demanded in predicting future increases in

atmospheric CO_2 to a high degree of certainty. This requires profound understanding of natural process involved in sequestrating carbon and their variability. Furthermore, it is essential to understand the feedback mechanisms between the carbon cycle and the global climate system to enable, in the near future, the implementation of emission reduction and sequestration strategies towards mitigating adverse effects of climate change.

Two approaches are currently used to infer the source-sink distribution of CO_2 globally, namely the bottom-up and top-down methods. In the bottom-up approach, the local scale process information, such as that obtained from eddy covariance towers, is scaled-up using diagnostic or process-oriented models in combination with remote sensing measurements to derive net CO_2 exchanges between the land surface and the atmosphere on regional or global scales. However, the accuracy of this approach relies on the representativeness of the local flux measurement site, hence one can expect significant uncertainties due to the extrapolation of non-representative eddy flux tower measurements. On the other hand, in the top-down approach, the variability in atmospheric CO_2 concentrations are observed to better understand the causes of variability in the source-sink distribution by inverting the atmospheric transport matrix (inverse modeling). The scarcity of concentration data and uncertainties in simulating atmospheric transport can introduce large uncertainties in this approach.

A number of studies used inverse modelling tools at global and regional scales (Enting, 1993; Tans et al., 1990; Jacobson et al., 2007; Rödenbeck et al., 2003; Gurney et al., 2002; Gourdji et al., 2008; Lauvaux et al., 2008) together with global networks of observations, which also recently include tall tower observatories, to calculate the source-sink distribution of CO_2. Tall tower observatories sample the lower atmosphere over continents up to altitudes of 200 m or more, and the resulting CO_2 concentration profiles provide information on regional fluxes. In order to better resolve the responses of various vegetation types and the impact of human interventions (land use change and land management) on land-atmosphere fluxes, inversions need to focus on smaller scales and to utilize continental (non-background) measurements of CO_2. This becomes problematic since the aforementioned in-situ measurements are often influenced by strongly spatially and temporally varying surface fluxes (fossil fuel emissions and biosphere-atmosphere exchange) in the near

field and by mesoscale transport phenomena, thus reducing their scale of representativeness to about 100 km (Gerbig et al., 2009).

Mountain sites, on the other hand, provide measurements with larger scale representativeness compared to measurements made from towers over flat terrain. Moreover, the longest greenhouse gas records are often from mountain sites (e.g. Schauinsland in Germany and Monte Cimone in Italy) (Levin et al., 1995; Reiter et al., 1986), making them a valuable ingredient for assessing longer term variations in carbon budgets. However, the mesoscale atmospheric transports at these sites such as mountain-valley circulation and terrain induced up-down slope circulations are found to have a strong influence on the atmospheric distribution of trace gas mixing ratios (Gangoiti et al., 2001; Pérez-Landa et al., 2007; van der Molen and Dolman, 2007). These significant variations of atmospheric concentrations appear at relatively small scales that are not resolved by current global transport models used in inversions, complicating the interpretation of these measurements. The unresolved variations can introduce significant biases in flux estimates and renders the flux estimation strongly site-selection dependent, sometimes causing the net annual sink strength of a whole continent to change by nearly a factor of two (Peters, 2010). A model inter-comparison study over Europe, using various transport models with different horizontal and vertical resolutions, suggested that the fine-scale features are better resolved at increased horizontal resolution (Geels et al., 2007). Moreover, the study of Geels et al. (2007) discusses the limitations of using atmospheric concentration data from mountain stations in inversions due to the model's (both global and regional scale models) inability to represent complex terrain and to capture mesoscale flow patterns in mountain sites. Therefore, inversion studies usually tend to exclude the data from mountain or complex terrain sites, impose less statistical weighting (larger uncertainty), or implement temporal data filtering to the measurements (e.g. selection of nighttimes only data at mountain sites).

The effect of transport errors on tracer concentrations are investigated in many studies (Lin and Gerbig, 2005; Gerbig et al., 2008; Denning et al., 2008) and the uncertainties for modeled mixing ratios during growing seasons due to the difference in advection and vertical mixing, can be as large as 5.9 ppm (Lin and Gerbig, 2005) and 3.5 ppm (Gerbig et al., 2008) respectively. Thus, it is pertinent to minimize these large and dominant uncertainties in inverse modeling systems. One approach would

be to increase the spatial resolution of the models in order to capture the "fine-structures" as well as to use improved boundary layer schemes to better represent the vertical mixing. Furthermore, fluxes in the near-field of the observatories are highly variable, calling for a-priori fluxes to be specified at high spatial resolution. Detailed validations of such high-resolution forward models using networks of atmospheric measurements are needed to assess how well the transport and variability of atmospheric tracers are represented. A number of studies using high-resolution models for resolving mesoscale transport in the atmosphere showed substantial improvements in simulating atmospheric CO_2 concentrations under various mesoscale flow conditions (Ahmadov et al., 2009; Sarrat et al., 2007; van der Molen and Dolman, 2007; Tolk et al., 2008).

High-resolution modeling tools are used together with airborne campaign measurements to address the representativeness of greenhouse gas measurements at one particular mountain site, the Ochsenkopf station. A 163 m tall tower at Ochsenkopf, continuously monitoring CO_2 and other trace gases, is located in the second highest peak of Fichtelgebirge mountain range (1022 m a.s.l.; 50° 1'48" N, 11°48'30" E) in Germany (**Fig. 4.1**). The site has complex terrain (Fig. 4.1b), where slopes influence atmospheric transport and consequently the observed mixing ratios (Thompson et al., 2009). Due to the difficulties in interpreting these measurements, the Ochsenkopf data were excluded in the global inversions of (Rödenbeck, 2005;Peters, 2010). A modeling framework consisting of a high-resolution Eulerian transport model, Weather Research Forecasting (WRF) (http://www.wrf-model.org/) coupled to a diagnostic vegetation model, Vegetation Photosynthesis and Respiration Model (VPRM) (Mahadevan et al., 2008) is used to assess whether measurements can be represented sufficiently well when increasing the models' spatial resolution. The coupled model, WRF-VPRM (Ahmadov et al., 2007) simulates CO_2 concentrations at high spatial resolution using high-resolution CO_2 fluxes from net ecosystem exchange (*NEE*) and from fossil fuel emissions. In addition, a Lagrangian particle dispersion model, Stochastic Time-Inverted Lagrangian Transport Model (STILT) (Lin et al., 2003), driven with high-resolution assimilated meteorological fields, is used to simulate the upstream influence on the observation point (i.e. the footprints), which are then multiplied by VPRM fluxes (*NEE*) as well as fluxes from fossil fuel emissions in order to simulate CO_2 concentrations at the observation location.
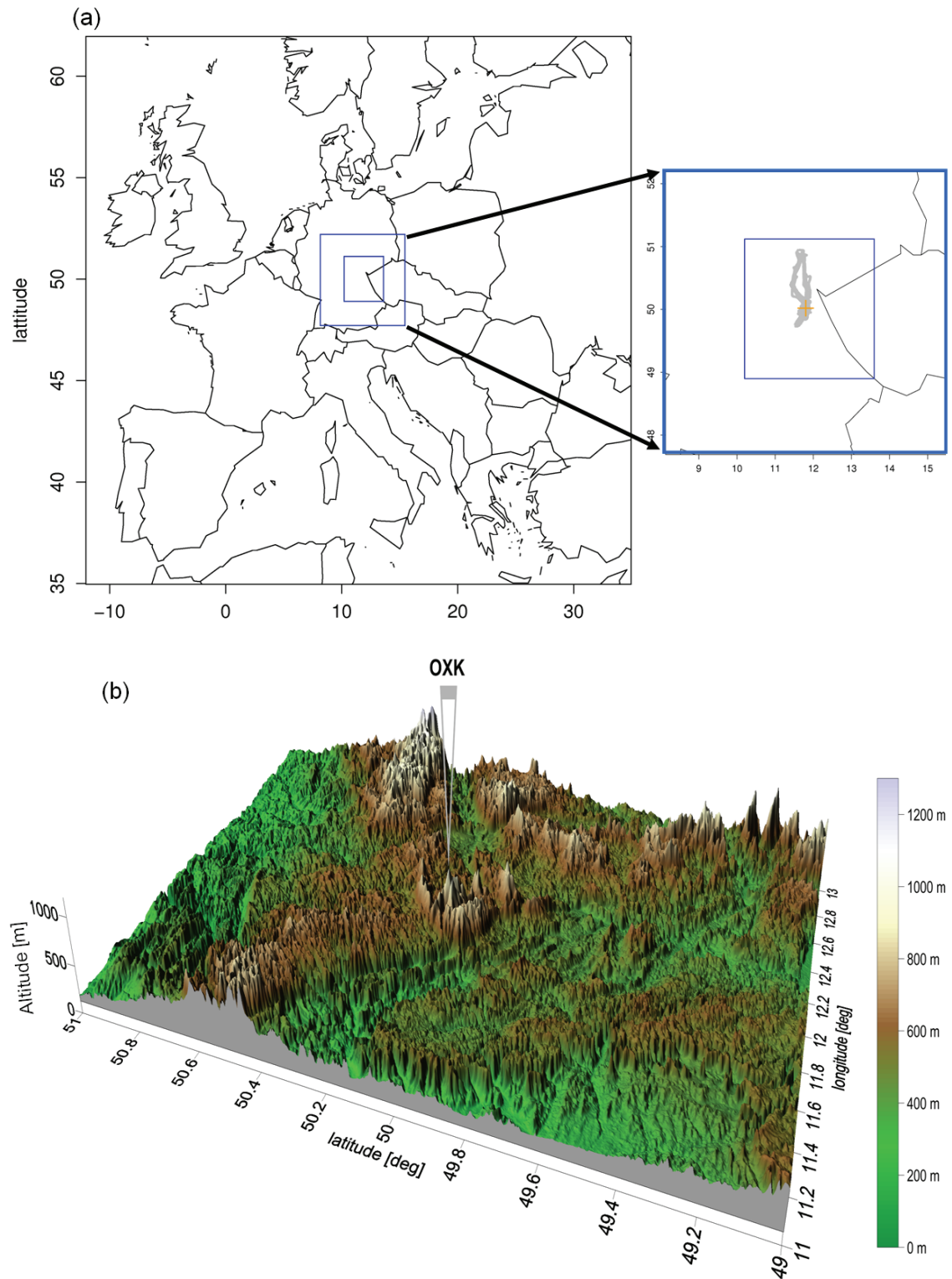
Figure 4.1 *(a) Map showing model domains used for WRF and STILT. STILT uses the larger domain covering Europe with two nests indicated by the <u>blue</u> rectangles. These two rectangles in blue represent the WRF domains, which are centered over OXK (50^0 01" N, 11^0 48" E, marked with "+"). A zoom of the WRF domain is showed in right-hand side of the main figure with an example of a DIMO flight track overlaid in grey lines. (b) Topography around OXK (the color gradient shows terrain height above sea-level).*

When the transport is adequately represented, the footprints calculated in the modeling system can be used to retrieve the source-sink distribution from CO_2 measurements over complex terrain at much higher spatial and temporal resolution than achievable with current global models.

The main goals of this study are: 1) to test the ability of high-resolution modeling tools to represent the spatial and temporal variability of CO_2 over complex terrain, compared to coarser models, 2) to infer the effect of mesoscale flows, such as mountain-valley circulation and mountain waves, on the observed atmospheric CO_2 fields and to assess how well these are reproduced in the high-resolution models, 3) to evaluate the models' reproducibility in capturing synoptic, seasonal and diurnal variability of observed CO_2 concentrations and 4) to assess the possibility of using these measurements in future inversion studies. The chapter is structured as follows: Section 4.2 describes briefly the data and the model set-up. In Sect. 4.3, the simulations from the high-resolution modeling framework are presented together with the observations as well as global model simulations. These results are discussed and conclusions are given in Sect(s) 4.4 and 4.5.

4.2   Data and Modeling system

4.2.1   Tower and Airborne measurements

The Ochsenkopf tall tower (from now on referred to as OXK) was instrumented as part of the European project – CHIOTTO (Continuous High-precision Tall Tower Observations of greenhouse gases) to establish a tall tower observation network for the continuous monitoring of the most important greenhouse gases over the European continent. The tower has been operated by the Max Planck Institute for Biogeochemistry, Jena, for continuous measurements of CO_2, CH_4, N_2O, CO, SF_6, O_2/N_2, and isotopes, in addition to meteorological parameters, and after re-equipping with instruments data are available since the beginning of 2006 (Thompson et al., 2009). For this study, high-precision (± 0.02 ppm) CO_2 measurements made at three heights (23 m, 90 m and 163 m) on OXK for different seasons are used. CO_2 is sampled at 2-minute intervals from all three heights in a 3-hour cycle with 1 hour for each height. The meteorological observations from the tower: temperature and relative humidity at 90 m and 163 m, pressure at 90 m, and wind speed and direction at 163 m, are also analyzed.

Measurements from wind profilers can be used to infer the state of air flow and dynamics within the tropospheric column. These can be used to evaluate the model in predicting vertical gradients of meteorological variables, which are associated with the transport of tracer constituents in the atmosphere. For this purpose, wind profiler measurements at Bayreuth, Germany (49.98^0 N, 11.68^0 E, 514 m a.s.l, http://www.metoffice.gov.uk/science/specialist/cwinde/profiler/bayreuth.html) are used. These comparisons shall give insight into the mesoscale flow patterns around OXK and help assess how well these are represented in the model.

Apart from tower-based data, the measurements from an airborne campaign with the METAIR-DIMO aircraft (http://www.metair.ch/) over Ochsenkopf are used. The high-precision aircraft measurements, sampling air horizontally and vertically, are designed to understand the regional patterns of CO_2, the influence of surface fluxes in the near-field, as well as atmospheric mesoscale transport and vertical mixing. In particular at Ochsenkopf, it is necessary to assess the influence of terrain-induced circulations on the mixing of atmospheric trace gases, which would create errors in inverse estimates of fluxes. The campaign was carried out during October 2008, covering an area around OXK (see Fig. 4.1) where the air was sampled for species such as CO_2, CO and meteorological parameters, such as wind velocity, pressure, relative humidity and potential temperature, were measured. The boundary layer, up to several kilometers upwind of Ochsenkopf, was probed with multiple profiles during these flights. The fast and accurate measurement of CO_2 was achieved with an open path IRGA LI-7500 (greenhouse-gas analyzer), fitted to a LICO2 (modified closed path IRGA LI-6262) and then to flask samples, with a resolution of 20 Hz, which was down-sampled to 10 Hz to give an accuracy of better than 0.5 ppm. For more details about measuring systems, see http://www.metair.ch/.

4.2.2 Modeling system

Two high-resolution transport models, WRF (Eulerian) and STILT (Lagrangian), coupled to a biosphere model, VPRM, are used to simulate distribution of atmospheric CO_2. Both of these coupled models, WRF-VPRM and STILT-VPRM were provided with same high-resolution surface fluxes as well as initial tracer concentrations at the boundaries.

VPRM computes biospheric fluxes (*NEE*) at high spatial resolution by using MODIS satellite indices (http://modis.gsfc.nasa.gov/), i.e. Enhanced Vegetation Index (*EVI*) and Land Surface Water Index (*LSWI*), and simulated WRF meteorological fields, i.e. temperature at 2m and short wave radiation fluxes. VPRM uses eight vegetation classes with different parameters for each class to calculate CO_2 fluxes. These parameters were optimized against eddy flux measurements for different biomes in Europe collected during the CarboEurope IP experiment (http://www.carboeurope.org/). Further details on VPRM can be found in (Mahadevan et al., 2008).

High-resolution fossil fuel emission data, at a spatial resolution of 10 km, are prescribed from an inventory at IER (Institut für Energiewirtschaft und Rationelle Energieanwendung), University of Stuttgart, Germany (http://carboeurope.ier.uni-stuttgart.de/) to account for anthropogenic fluxes. Initial and lateral CO_2 tracer boundary conditions are calculated by a global atmospheric Tracer transport model, TM3 (Heimann and Koerner, 2003), with a spatial resolution of $4° \times 5°$, 19 vertical levels and a temporal resolution of 3 hours. Specifically, the analyzed CO_2 fields (available at http://www.bgc-jena.mpg.de/~christian.roedenbeck/download-CO2-3D/) that are consistent with atmospheric observations at many observing stations around the globe, generated by the forward transport of previously optimized fluxes (i.e. by an inversion) are used.

In the coupled model, WRF-VPRM, the domain is set up for a small region (~ 500 km × 500 km, hereafter referred as 'WRF domain') centered over OXK, and is nested with a horizontal resolution of 6 km (parent) and 2 km (nested) as well as with 41 vertical levels (thickness of the lowest layer is about 18 m) (Fig. 4.1a). Each day of simulation starts at 18 UTC of the previous day, and continues with hourly output for 30 hours of which the first 6 hours are used for meteorological spin-up. CO_2 fields for each subsequent 30- hour run are initialized after the meteorological spin up with the previous day's final CO_2 fields. The coupled model STILT-VPRM (Matross et al., 2006) is set up with a domain covering most of Europe, and virtual particles were transported backward in time for a maximum of 15 days. Trajectories were driven with WRF meteorology until particles left the WRF domain, and with ECMWF (http://www.ecmwf.int/) meteorology (horizontal resolution of approximately 25 km)

for the rest of the domain. The sub-grid scale turbulence in STILT-VPRM is modeled as stochastic Markov chain.   In STILT-VPRM, receptors are either located at different measurement levels on the tower or at different altitudes covering the flight track of the aircraft. The vertical mixing height (zi) is slightly different in WRF and STILT, although the same meteorological (for the STILT nested domains) and surface flux fields were used (see Sect. 5.3.1.1). For more detailed information on these coupled models (WRF-VPRM and STILT-VPRM), the reader is referred to Ahmadov et al., 2007; Nehrkorn, 2010; Pillai et al., 2010a. Note that STILT-VPRM uses a different model domain (Europe) than WRF-VPRM, using additional meteorological information from ECMWF outside the WRF domain as mentioned above.

A continuous record of meteorological fields and CO_2 concentrations from a tower allows the evaluation of models for different seasons as well as for different measurement levels. Model simulations were carried out for May (spring), August (summer), October (autumn) in 2006, and March (winter) in 2008. In addition to this, simulations were carried out for October 2008 in order to evaluate the models against the DIMO aircraft measurements to assess the model's ability to reproduce CO_2 distributions over the Ochsenkopf mountain region.

4.3   Results

High-resolution simulations of meteorology (by WRF) and CO_2 (by WRF-VPRM and STILT-VPRM) at 2 km resolution around OXK are presented here. The models are evaluated using wind profiler, tower and airborne measurements of meteorological parameters and CO_2 concentrations. These model evaluations assess the ability of the high-resolution model framework to simulate atmospheric transport and to capture the spatial and temporal variability of atmospheric CO_2.

4.3.1   Model Evaluation: Meteorology

4.3.1.1 Wind Profiler

Vertical profiles of meteorological fields are validated for 2nd to 30th August 2006 with the measurements provided by the Bayreuth wind profiler, located about 10 km south-west of OXK. For demonstration, a comparison of measured and modeled wind and temperature profiles on 3rd August 2006 at 15 UTC is shown in **Fig(s). 4.2a** and

4.2b. The observed prevailing wind direction was northerly for the atmospheric column below 2 km which was also reproduced by the model simulation. For a thin vertical layer, between 2.3 and 3.2 km, the prevailing wind direction changed to south-east; however the model simulated a north-westerly wind. Above 3.2 km, both observations and simulations indicated a south-westerly wind. The magnitude of the wind was slightly overestimated in the model, particularly in the boundary layer (bias:~ +2 m/s).
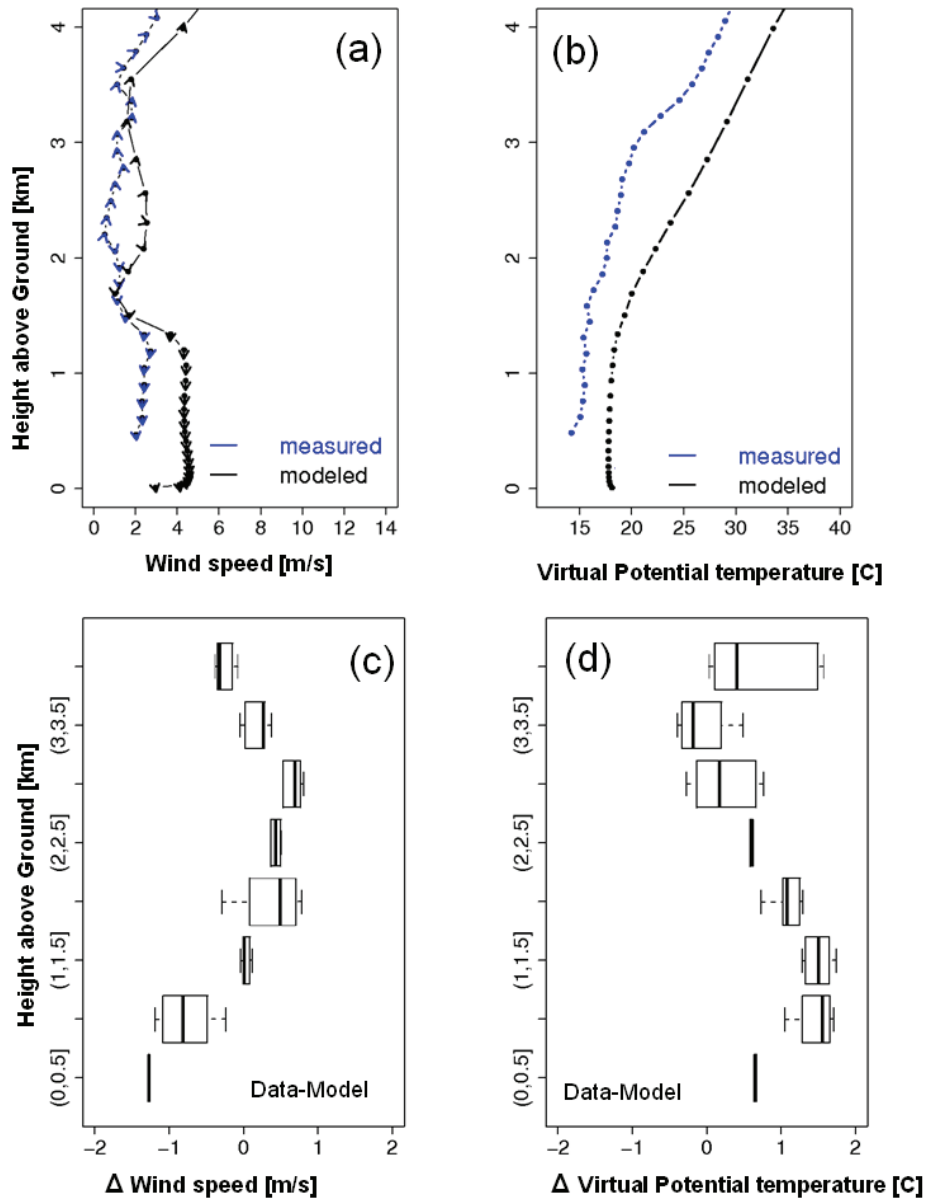
***Figure 4.2** (a-b) Profiles of observed vs. modeled wind fields and virtual potential temperature for 3ʳᵈ August 2006 at 15 UTC. The horizontal direction of wind is indicated with arrowheads (c-d) the data-model mismatch for the monthly averages of these fields at 15 UTC, plotted against different altitude bins. The box indicates 95% quartile, the whisker denotes minimum and maximum of deviations and the vertical bar inside the box denotes the median.*

An observation-model comparison of the vertical profile of virtual potential temperature (θ_v) showed that the model simulates θ_v reasonably well, but with a warm bias. A relatively sharp decrease in θ_v for the thin vertical layer between 2.3 and 3.2 km could not be captured in the model. A possible reason for the decrease in θ_v could be the intrusion of air from south-east direction on this layer (see Fig. 4.2a for wind direction) that existed for a short period of time.

To analyze the overall agreement, the monthly averages of profiles for wind-speed and θ_v, both measured and simulated, are produced at 15 UTC and the data-model mismatches are shown in Fig(s). 4.2c and 4.2d. The result shows that the model slightly overestimated wind-speed in the boundary layer and in contrast showed an underestimation for the free troposphere. In general, the model slightly underestimated θ_v profiles. Overall, the model could capture much of the variability in the vertical profiles of wind-speed and θ_v.

4.3.1.2 Tower

Evaluations of the modeled meteorology are carried out at different measurement levels on the tower for different seasons. An example of those validations is demonstrated here. **Figure 4.3** shows time series' of observed and WRF-simulated parameters (temperature, relative humidity and wind components) for August 2006. The plot shows the prevailing weather situation and also the model capability to predict these parameters, which can drive atmospheric CO₂ variability over OXK.

Simulated atmospheric temperatures at two different levels (90 m and 163 m) on the tower agree well with observations (squared correlation coefficient, R^2= 0.86) (Fig(s). 4.3a and 4.3b) and captured reasonably well the diurnal variability of temperature. Note that the model layers relative to the model terrain are used for all comparisons unless otherwise mentioned. A warm bias is observed at OXK during this period while there is a cold bias at Bayreuth (wind profiler). This good temperature agreement suggests that uncertainties in the (simulated) temperature dependent VPRM respiration fluxes caused by temperature biases are expected to be small on synoptic time scales.

The transport of moisture (comparable to CO_2 transport) in the model was validated by comparing the measured and simulated relative humidity at two levels. The model agrees well with the observations (R^2 =0.60-0.74) with a slight negative bias of 0.2 to 4.7 between levels (Fig(s). 4.3c and 4.3d).
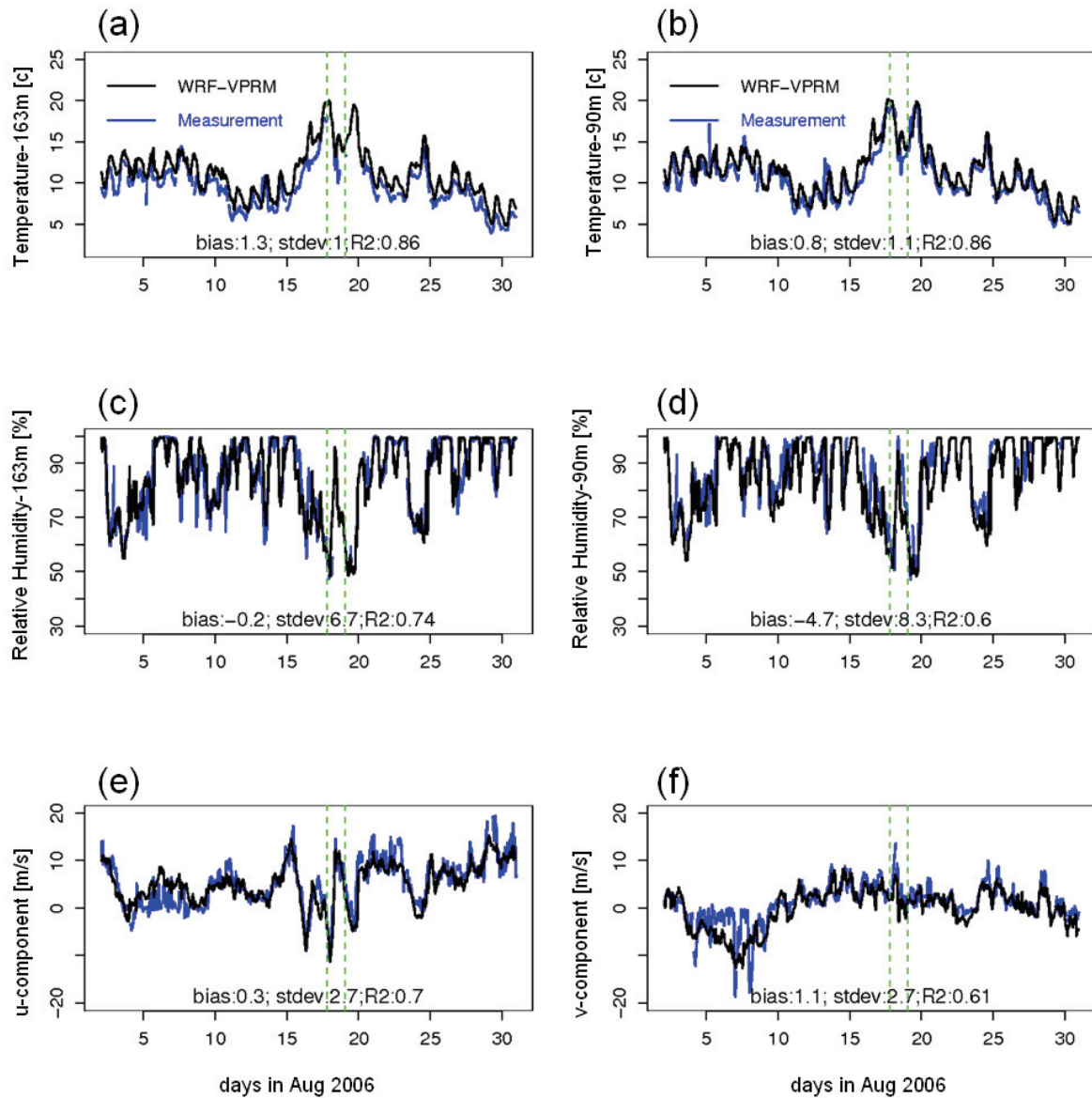
Figure 4.3 *Comparison of measured and modeled meteorological parameters for August 2006 at the OXK site: (a-b) temperature at 163 m and 90 m, (c-d) relative humidity at 163 m and 90 m and (e-f) horizontal components of wind at 163 m. The <u>green</u> dotted vertical lines denotes the passage of a cold front investigated in detail (see Sect. 4.4.1).*

The wind speed and direction was also predicted reasonably well. A comparison of horizontal components of observed and modeled wind components u (east-west) and v (north-south) at 163 m (Fig(s). 4.3e and 4.3f) demonstrates fairly good agreement between observations and simulations (R^2 =0.70 and 0.61 respectively).

78

Table 4.1 *Summary statistics of observed and simulated (WRF) meteorological fields (model bias (bias), standard deviation (sd) and squared correlation coefficient (R^2)) using hourly time series at available measurement levels for different seasons.*

Season	level	Temperature			Relative Humidity			u-component			v-component		
		bias	sd	R^2	bias	sd	R^2	bias	sd	R^2	bias	sd	R^2
Spring	163	1.2	1.4	0.81	2.8	9.8	0.84	0.9	3.1	0.92	1.2	2.3	0.66
(May 06)	90	0.7	1.3	0.80	0.4	10.9	0.71	-	-	-	-	-	-
Summer	163	1.3	1.0	0.86	-0.2	6.7	0.74	0.3	2.7	0.70	1.1	2.7	0.61
(Aug 06)	90	0.8	1.1	0.86	-4.7	8.3	0.60	-	-	-	-	-	-
Autumn	163	0.2	1.7	0.68	6.2	14.0	0.79	2.2	3.4	0.81	0.2	3.0	0.65
(Oct 06)	90	-0.1	1.6	0.67	3.8	14.7	0.62	-	-	-	-	-	-
Winter	163	1.4	0.9	0.93	-1.9	9.0	0.52	0.6	6.4	0.48	1.2	5.0	0.33
(Mar 08)	90	1.2	1.0	0.91	-6.4	12.2	0.48	-	-	-	-	-	-

Table 4.1 gives the overall model performance (model bias, standard deviation of model-data mismatch and squared correlation coefficient of the model-data agreement) from comparing the hourly time series of observed and simulated meteorological fields at the available measurement levels for different seasons. The summary statistics indicate that WRF could follow reasonably well the seasonal changes in the atmospheric transport and dynamics.

4.3.1.3 DIMO Campaign

Vertical distributions of meteorological fields were validated against the DIMO profiles around the Ochsenkopf mountain region for all campaign days. The box-whisker plot (**Fig(s). 4.4a** and **4.4b**) of the data-model mismatch (from all aircraft
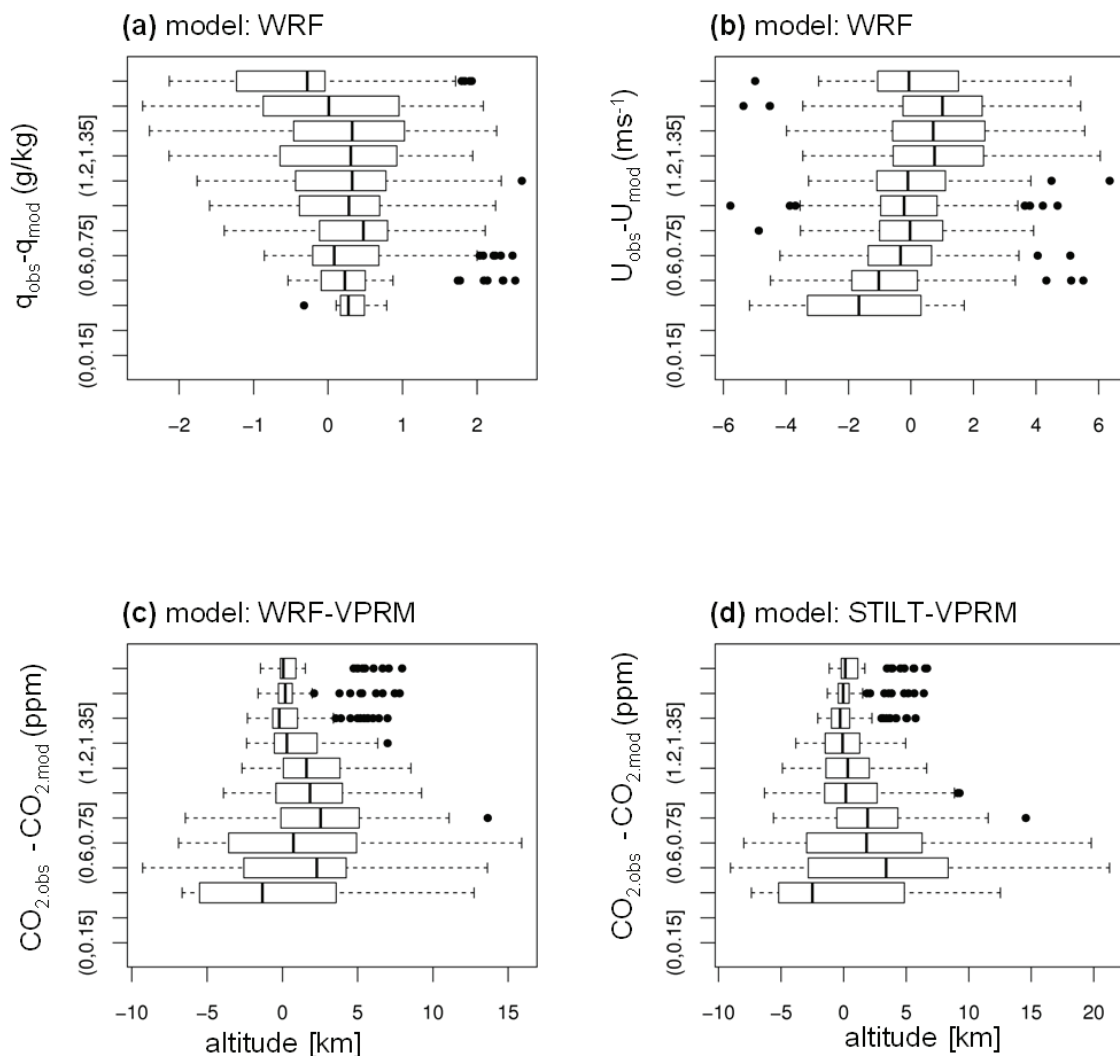
Figure 4.4 The box-whisker plot of model mismatch (observations-simulations) using all aircraft profiles for a) specific humidity, b) wind speed and c) CO₂ (WRF-VPRM) d) CO₂ (STILT-VPRM).The box indicates 95% quartile, the whisker denotes minimum and maximum of deviations and the vertical bar inside the box denotes the median. Black dots are outliers.

80

profiles) provides an overview of the model performance on simulating specific humidity and wind speed. In general, WRF meteorological simulations agree well with the DIMO observations as indicated by the lower median (+0.25g/kg for water-vapor mixing ratio and -0.06 m/s for wind speed while using all available observations and simulations) and 95% quartile (1.5 g/kg for specific humidity and 3.2 m/s for wind speed). Noteworthy is that the data-model mismatch for water vapor mixing ratio increases with increasing height.
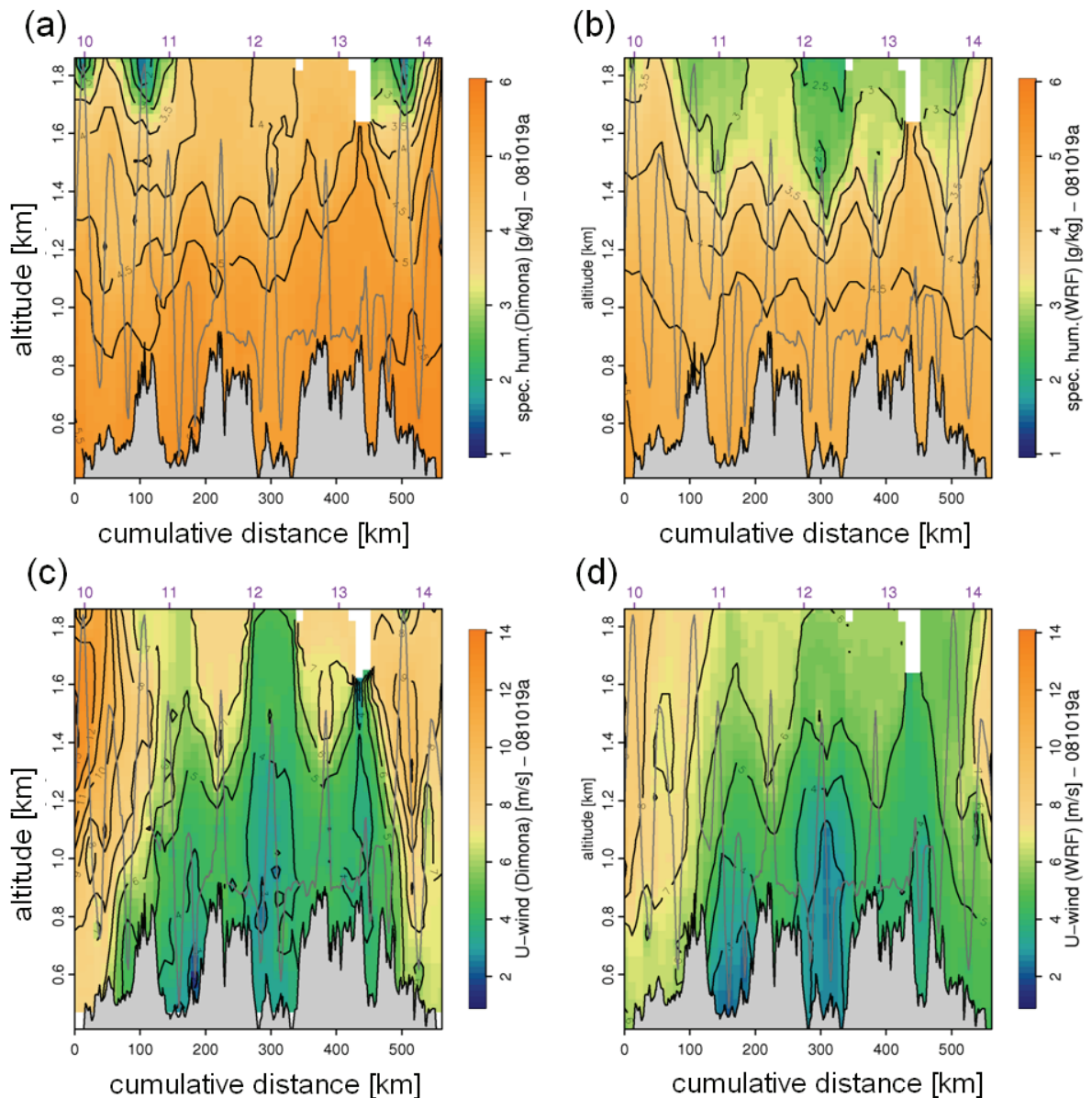
Figure 4.5 *Vertical cross section (using a distance weighted interpolation) of the observed and simulated meteorological fields as a function of distance flown by the aircraft for 19th October 2006: a-b) specific humidity in g/kg c-d) Wind speed in ms-1. (a) and (c) represent measurements and (b) and (d) represent WRF simulations. The grey lines indicate flight track and the shaded grey region represents terrain elevation. See Figure 4.7d for aircraft track showing altitude above ground. Time of the measurements/simulations is given in the top X-axis.*

As an example, the model-data comparison for 19th October 2008 from 10 to 14 UTC is demonstrated. During this period, the air was sampled intensively near the top of OXK and the surrounding mountain ridges and valleys (see Fig. 4.7d). **Figure 4.5** shows the vertical cross-section of the observed and modeled meteorological fields (wind speed and specific humidity) as a function of distance flown by the aircraft (Cumulative Distance, hereafter referred to simply as distance). WRF reproduced specific humidity fairly well at the surface layers; however, it showed a slight underestimation in the upper vertical levels (Fig(s). 4.5a and 4.5b). A relatively calm wind (2-5 m/s) was observed over Ochsenkopf mountain ranges during this period except in the early hours of the campaign. This was predicted remarkably well in WRF with negligible bias (Fig(s). 4.5c and 4.5d).

4.3.2   Model Evaluation: CO₂ concentrations

Similar to Sect. 4.3.1, observations of CO₂ fields at OXK and during the DIMO aircraft campaign are used for the evaluation of the models (WRF-VPRM and STILT-VPRM).

4.3.2.1 Tower

The observed atmospheric CO_2 concentrations at different measurement levels are compared with simulations generated by WRF-VPRM and STILT-VPRM for different seasons. For illustration, the time series comparison of CO_2 concentrations at 90 m level on the tower for the period from 2 to 30 of August 2006 (**Fig. 4.6**) is shown. The period is chosen due to its enhanced biospheric activity and the existence of strong diurnal patterns in transport and fluxes which can complicate the measurement interpretation. For comparison, the CO_2 analyzed fields from TM3 with 3-hourly time steps are also included. The observed atmospheric CO_2 shows large diurnal and synoptic variability and notably, these large variations in atmospheric CO_2 were not captured in the TM3 global model. Note that the generation of analyzed CO_2 fields (by atmospheric inversion) did not include OXK CO_2 data, so in this sense they can be used for independent validation. The comparison becomes more favorable when high-resolution transport and fluxes are used. Most of the observed variability in CO_2 concentrations on the tower is reproduced well in both high-resolution models when compared to TM3 (Fig. 4.6). This points to the fact that most of the variations in CO_2 are due to surface flux variations and mesoscale transport

processes on scales not resolved by TM3, which has a grid-cell size of several hundred kilometers. Also note that TM3 uses coarse resolution terrain elevation data.
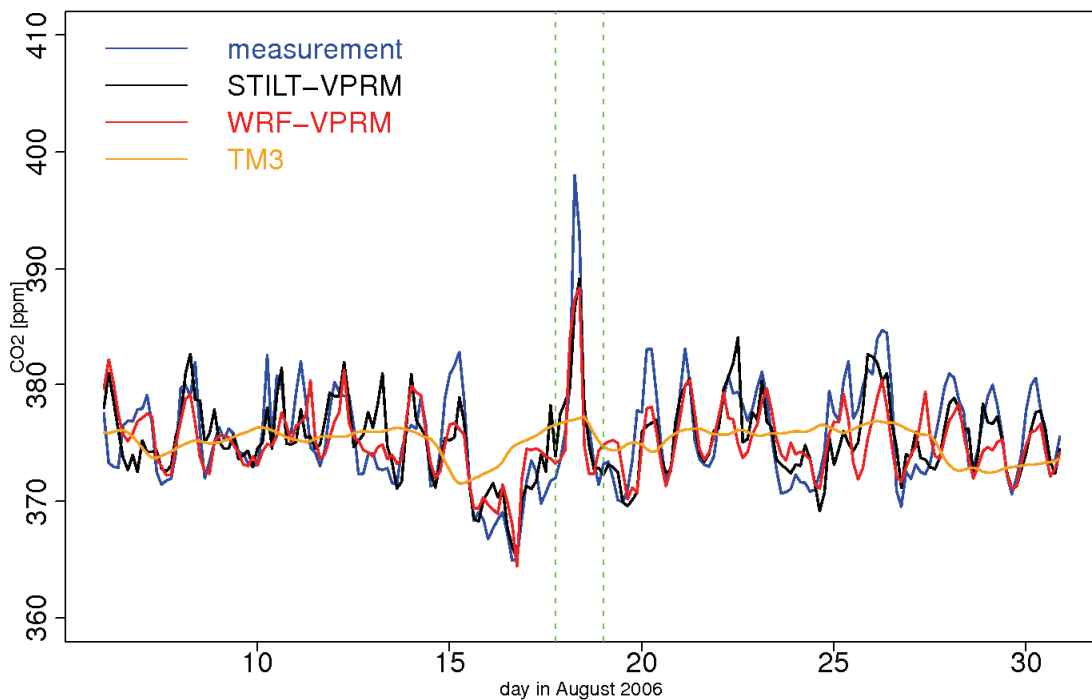
Figure 4.6 *Comparison of measured and modeled CO_2 concentrations for August 2006 at 90 m on the OXK. A period between dashed <u>green</u> vertical bars denotes a synoptic event during 0 to 15 UTC on 18th August 2006 (see also Sect. 4.4.1).*

In addition to August (summer) 2006, CO_2 concentrations are also validated for other seasons and the summary statistics (similar to Table 4.1) of the model-data comparison are given in Table 4.2. Observations from other levels (23 m and 163 m) on the tower are also used to assess the models' performance in reproducing the vertical structure of CO_2 in the atmospheric column. The summary statistics clearly indicate that high-resolution models are able to predict remarkably well the temporal patterns of CO_2, measured at three different vertical levels on the tower, for different seasons. Section 4.4.3 discusses further the seasonal variability of CO_2 concentrations.

4.3.2.2 DIMO Campaign

The profiles of atmospheric CO_2 concentrations obtained from the aircraft campaign were used to examine how well the models can reproduce the vertical distribution of tracer concentrations over the Ochsenkopf mountain region. Figure 4.4c shows the statistical analysis of data-model mismatches using CO_2 profiles for all days in the

Table 4.2 *Summary statistics of observed and simulated CO_2 fields (model bias (bias), standard deviation (sd) and squared correlation coefficient (R^2)) using 3-hourly time series at available measurement levels for different seasons. Simulated fields are provided by TM3, STILT-VPRM and WRF-VPRM.*

Season	Level	TM3			STILT-VPRM			WRF-VPRM		
		bias	sd	R^2	bias	sd	R^2	bias	sd	R^2
Spring	163	-1.9	3.1	0.11	-1.7	3.0	0.33	1.4	2.7	0.41
(May 06)	90	-1.7	3.2	0.16	-1.7	2.8	0.50	1.4	2.4	0.57
	23	-1.1	4.1	0.09	-1.6	2.8	0.58	1.6	2.8	0.58
Summer	163	0.5	4.0	0.01	0.6	2.8	0.50	0.8	2.9	0.46
(Aug 06)	90	0.4	4.8	0.02	0.3	3.2	0.58	0.6	3.3	0.55
	23	0.8	5.0	0.01	-0.1	3.4	0.52	0.5	3.1	0.62
Autumn	163	2.6	3.9	0.39	-0.5	3.1	0.59	0.6	3.3	0.51
(Oct 06)	90	3.4	4.7	0.29	-0.4	3.4	0.62	0.6	3.9	0.52
	23	4.6	5.5	0.21	-0.4	4.4	0.52	0.3	4.7	0.49
Winter	163	1.6	2.1	0.17	-0.5	2.2	0.20	0.5	2.3	0.23
(Mar 08)	90	1.5	2.1	0.19	-0.8	1.8	0.42	0.4	2.2	0.30
	23	2.1	2.6	0.14	-0.8	2.4	0.37	0.5	2.6	0.32

campaign. The median of all residuals is 0.5 (1.1) ppm for STILT-VPRM (WRF-VPRM). The data-model mismatch of CO_2 for both models increases with decreasing heights, the opposite of what was found for water vapor. The reason is twofold: 1) the large variability of CO_2 at the surface compared to higher levels (Pillai et al., 2010b) and 2) improper representation of boundary layer vertical mixing in the models.

The same period that was chosen for DIMO meteorological validations is used also here as an example to demonstrate the vertical distribution of CO_2. **Figure 4.7** shows
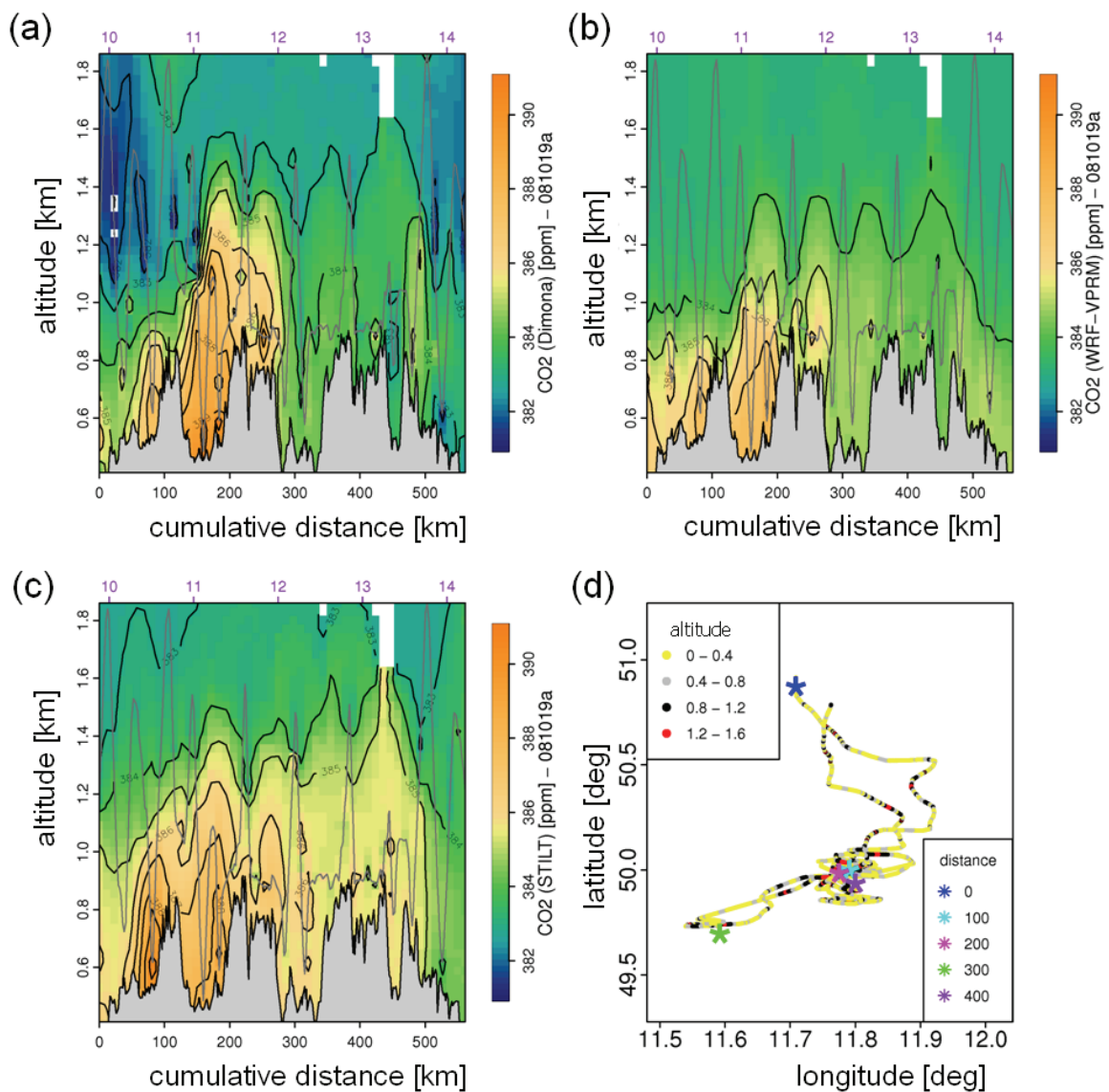
Figure 4.7 Vertical cross section (using a distance weighted interpolation) of the observed and simulated CO_2 fields (given in ppm) as a function of distance flown by the aircraft (cumulative distance) for 19th October 2006: a) measurements b) WRF-VPRM c) STILT-VPRM and d) Flight track with color gradient showing altitude range (legend at the top left-hand side of the panel) above ground. The symbol "" denotes cumulative distance in km (legend at the bottom right-hand side of the panel). In (a-c), the time of measurements/simulations is given in the top X-axis.*

the vertical cross section of the observed and simulated CO_2 concentration as a function of distance for 19th October 2006 from 10 to 14 UTC. Compared to summer months, higher values of CO_2 are generally expected due to lower biosphere uptake and shallower vertical mixing. Accumulation of CO_2 in the valley south of OXK was observed in the morning (10:30-11:30 UTC) between the aircraft's cumulative flown distance range 120 and 200 km (see Fig. 4.7a). CO_2 can accumulate in valleys under shallow vertical mixing in the nocturnal boundary layer as well as under nocturnal drainage conditions in complex terrain. The valley-mountain gradient in CO_2 concentrations in the valley decreased rapidly in the afternoon with the establishment of convective mixing and consequently enhanced vertical turbulence. STILT-VPRM and WRF-VPRM were able to capture relatively well the CO_2 accumulation in the valley in the morning (distance between 100 and 200 km); however WRF-VPRM slightly underestimated the vertical extent of valley accumulation during this period. At noon (distance between 280 and 320 km), STILT-VPRM overestimated the CO_2 concentrations and this overestimation can also be seen in the afternoon when the boundary layer is well mixed.

4.4   Discussion

4.4.1   Synoptic Variability

The observations show considerable synoptic variability in CO_2 concentrations which are driven by atmospheric transport and surface flux heterogeneity. These synoptic variations in tracer concentrations provide valuable information on spatiotemporal patterns of surface fluxes and thus can be used in atmospheric inversion to construct regional fluxes. A synoptic event (cold front), observed on 18th August 2006, during which the observed CO_2 showed an enhancement of more than 20 ppm, is analyzed in detail to examine how such variations are represented by the mesoscale models. In the beginning of the event, the air temperature dropped significantly with a relatively sharp decrease in relative humidity (Fig(s). 4.3a to 4.3d). The wind speed was relatively high, reaching a maximum of 15 m/s. The atmospheric CO_2 observation shows a large peak during this period, which was captured by both models as seen in Fig(s). 4.6, **4.8**a and 4.8b. However the models predict this elevated concentration with a considerable low bias of ~15 ppm. During the event, the air was coming from the south-west, and the time integrated footprints derived from STILT (sensitivity of mixing ratio at 7:00 UTC on 18th August to surface fluxes integrated over the past 48

hours), shows a strong influence from the highly industrialized area in the south-west part of Germany occurring 10 hours prior to the measurement (Fig. 4.8c). Tracer
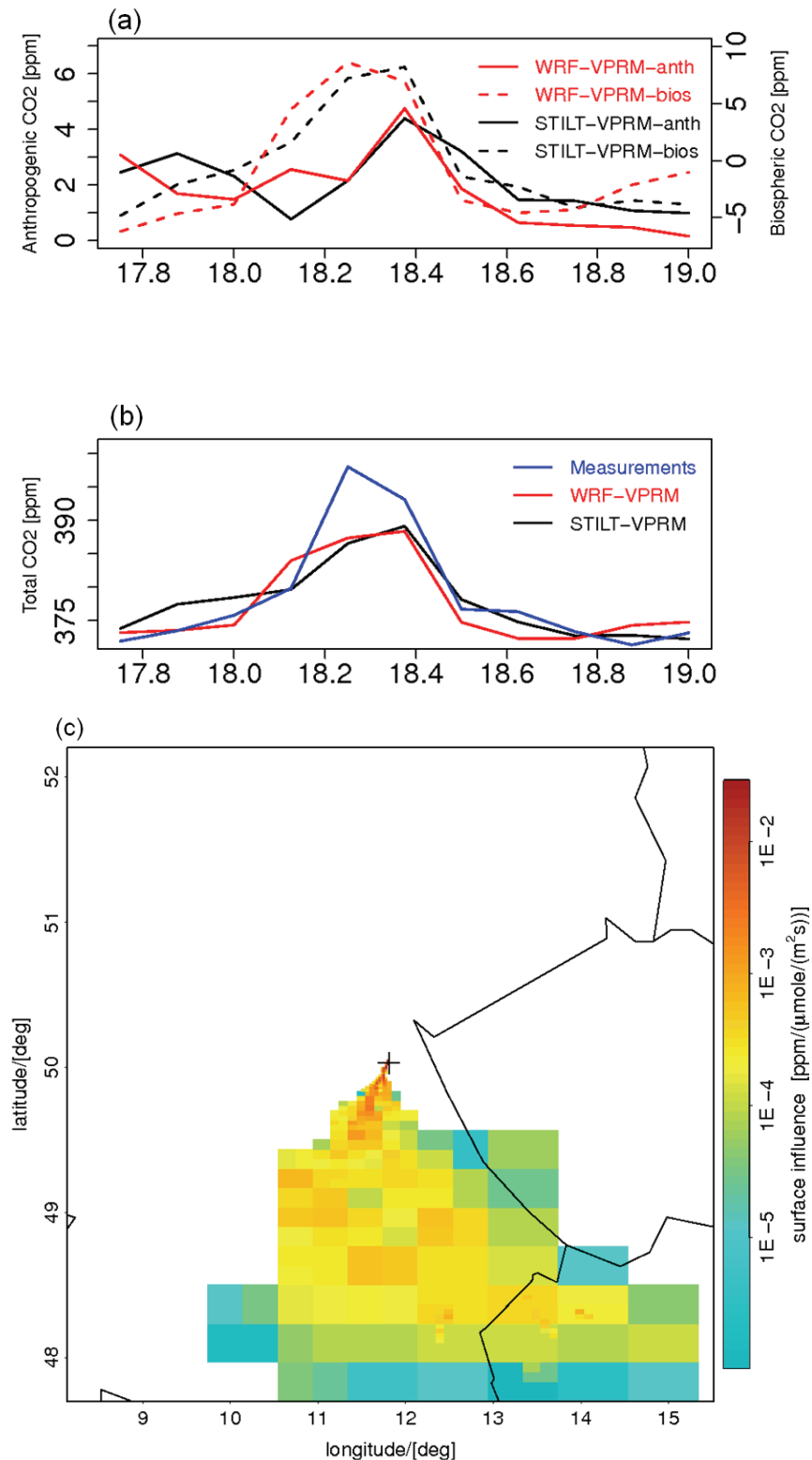
Figure 4.8 *Influence of surface fluxes on measured CO₂ concentration at OXK: a and b) Time series of simulated anthropogenic and biospheric CO₂ signals (contribution of anthropogenic and biospheric fluxes to the total CO₂) at 90 m on the tower during 17-18 August 2006. c) Time integrated footprints derived by STILT on 18th August 2006 at 7:00 UTC for particles running -48 hours (backward in time) from tower (indicated with + sign).*

simulations, where anthropogenic and biospheric contributions within the domain are separated, show a large contribution from respiration and emission fluxes for the event (Fig. 4.8a) and consequently an increase in CO_2 concentration in the atmosphere (Fig. 4.8b), which reached a peak in the early morning, owing to the shallow mixing in the nocturnal boundary layer. These higher concentrations started decreasing with the development of the convective mixed layer combined with the drawdown of CO_2 by photosynthesis. The above analysis suggests that OXK during this event was highly influenced by air carrying a large contribution from respiration, but also emissions originating from densely populated and industrialized area. The underestimation of the CO_2 peak in the models could be due to several reasons: 1) uncertainties in vertical mixing (this is the more likely scenario as it would strongly affect the vertical distribution of tracer concentrations, producing large model-data mismatches) 2) uncertainties in advection (WRF underestimated the wind speed in the beginning of the event and predicted south-easterly wind rather than the observed south-westerly wind direction. The strong south-westerly wind might be associated with advection of large plumes of CO_2 (respired and anthropogenic) to the measurement location) 3) the underestimation of anthropogenic emissions in the inventory for this area of influence (uncertainties of emission inventories at small spatial and short temporal scales can easily be as large as 50% (Olivier et al., 1999) 4) uncertainties in the VPRM respiration fluxes (note that VPRM simulates respiration fluxes as a linear function of the simulated surface temperature (at 2m). The uncertainty due to a temperature bias is likely to be small because the simulated temperature for this period is fairly in good agreement with observations. However, the respiration fluxes in reality are not only controlled by temperature but also by other factors such as soil moisture.) 5) underestimation of TM3 initial fields (it is more unlikely that a short term event, which originated outside of Europe domain, would have had an influence on this). This emphasizes the complexities of mechanisms involved in such short-term scale events. The vertical profiling of CO_2 (as like DIMO aircraft campaign) or wind profiler measurements can be helpful to assess the impact of vertical mixing on tracer concentrations).

In general, both high-resolution models could capture the general trend of CO_2 variability during this synoptic event, by simulating well the influence of surface fluxes in the near-field and the atmosphere dynamics.

4.4.2   Orographic Effect

The mountainous terrain can influence the regional circulation pattern around the tower site, resulting in local flow patterns which can have an impact on diurnal patterns in tracer concentration measurements. The local flow patterns are developed by the formation of 1) thermally forced mountain-valley circulations in response to radiative heating and cooling of the surface and 2) topographically induced stationary gravity waves (i.e., mountain waves) when stable flow encounters a mountain barrier. The downslope flows are more common at OXK during nighttime although mountain gravity waves are also likely in winter periods (based on WRF simulations as well as photographs taken during DIMO campaign).

4.4.2.1 Mountain-Valley Circulations

The mountain valley flows can change the atmospheric vertical mixing and can thus influence tracer measurements at OXK (Thompson et al., 2009). An example of such an event occurred at nighttime between 26 and 27th August 2006 is demonstrated in **Fig. 4.9**. During this period, the expected nocturnal CO_2 build up at OXK was found to be nearly absent owing to the thermally induced drainage flow. The data shown are the time series of meteorological and CO_2 observations at each level on the tower for a period from 26 to 28 August 2006. The period between the brown vertical dashed lines in Fig. 4.9 shows evidence of mountain-valley circulation. Also the period was under weak synoptic pressure gradient conditions (as indicated by the simulated potential temperature) with a prevailing westerly flow (as indicated by the simulated wind speed) (**Fig(s). 4.10**a and 4.10c). The observed temperature and wind speed during this period (Fig(s). 4.9a and 4.9b) also suggest that the conditions were favorable for the formation of a buoyancy-driven downslope flow. Following radiative cooling of the surface on 26th August, relatively dry air intruded from the free troposphere into the nocturnal boundary layer, which was observed as a sharp decrease in the relative humidity (Fig. 4.9b). Noticeable time lags in the transition from moist to dry air were seen at the different sampling levels, which also indicate the intrusion of air from above. The evidence of dry air subsidence from the residual layer can also be seen later at 06 UTC on 27th August. Consequently, a decrease in CO_2 concentration was observed at 00 UTC and at 06 UTC on 27th August due to the
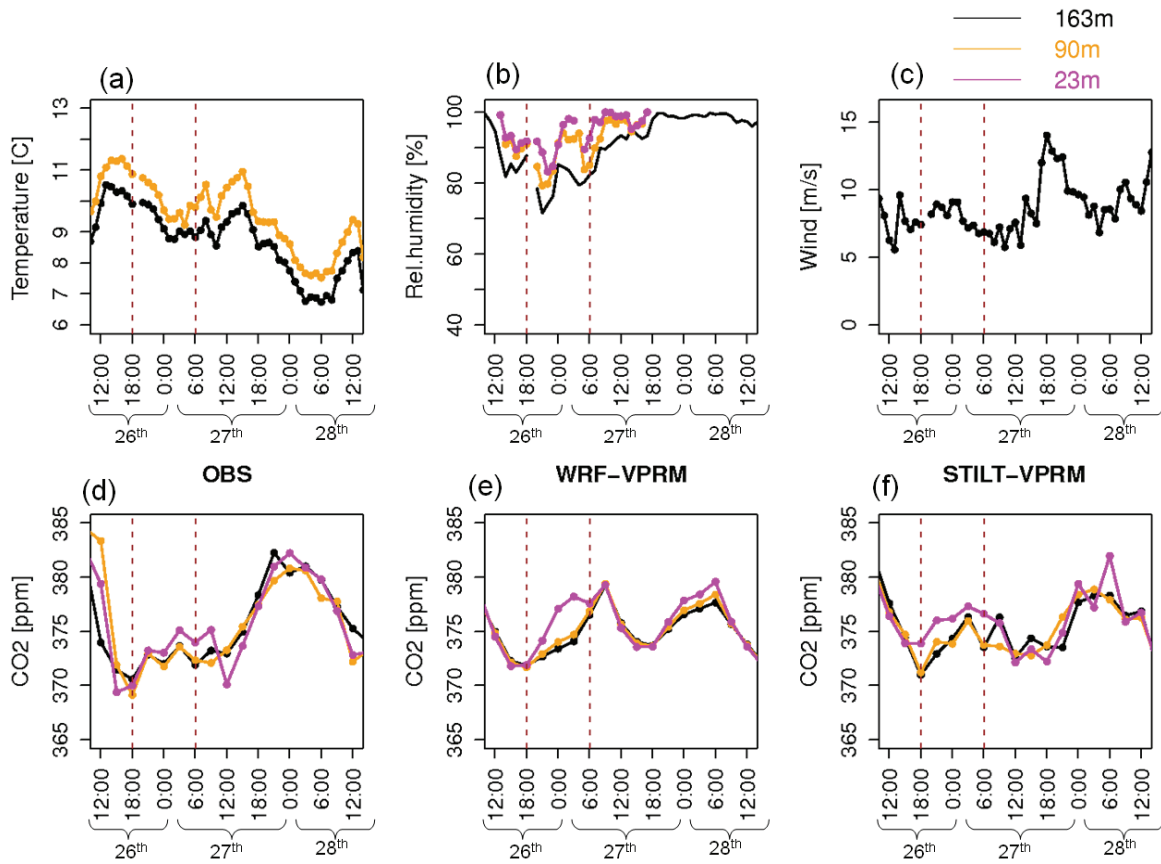
Figure 4.9 *Time series of meteorological parameters and CO_2 concentrations for different levels at OXK site during 26-28 August 2006: a-c) observed air-temperature, relative humidity and wind speed respectively d-f) CO_2 concentration, observed and modeled by WRF and STILT, respectively. The area between dashed <u>brown</u> vertical bars denotes the period under mountain-valley circulation. The X-axis shows hours in UTC; the horizontal extent of curly bracket at the bottom of X-axis shows the day on August 2006.*

replacement of air by the residual layer containing lower CO_2 concentration. STILT-VPRM captured well the lowering of CO_2 concentration at 06 UTC in response to the drainage flow and simulated well-mixed tracer concentrations in the nocturnal boundary layer. However WRF-VPRM showed an unrealistic accumulation of CO_2 concentration at the lower level which might be associated with the underestimation in the vertical extent of the entrainment air reaching the tower site. The presence of katabatic flow on the lee side of the mountain was predicted in WRF, indicated by the negative vertical velocity (downward movement of air) and increased wind speed along the mountain slope (Fig. 4.10d). The (simulated) impact of drainage flow on the tracer concentrations on the lee side of the mountain can be seen as a region of lower CO_2 contours in Fig. 4.10b.
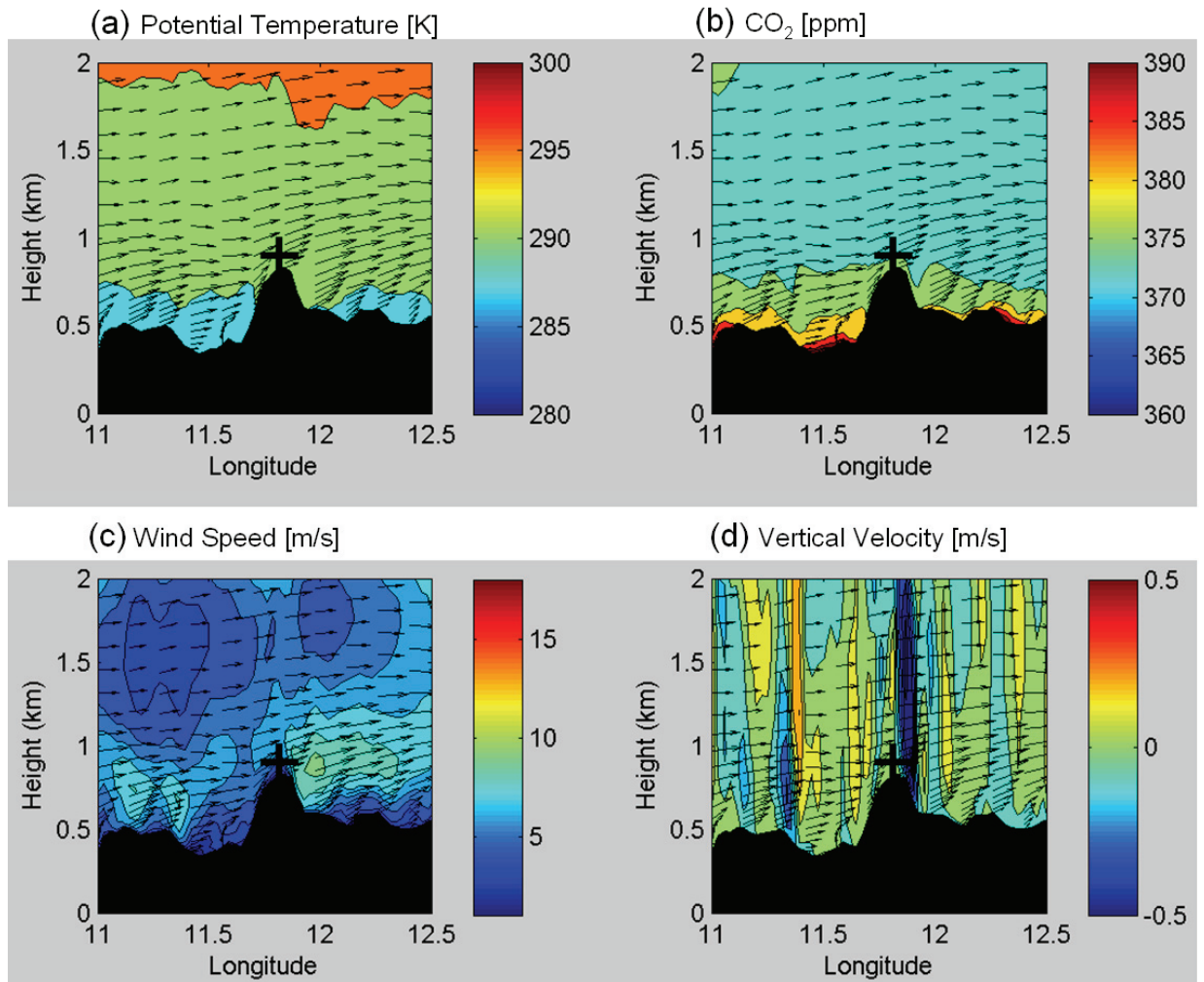
Figure 4.10 *Vertical cross section along OXK latitude (50^0 01" N) on 27th August 2006 at 01:00 UTC, showing WRF-VPRM simulated a) Potential temperature in Kelvin b) CO_2 concentration in ppm c) Wind speed in ms^{-1} and d) Vertical velocity in ms^{-1}. The overlaid arrows indicate prevailed wind direction; the symbol "+" indicates OXK location.*

4.4.2.2 Mountain Wave Activity

The buoyancy driven upslope and downslope flows, which are discussed above, are less common in winter due to low surface heating. As mentioned earlier, under stable stratified nocturnal boundary conditions, mountain gravity waves can be formed when air flow is perturbed with a barrier (e.g. mountain). Propagation of gravity waves transporting mass and energy in the stable boundary layer can affect tracer concentrations measured at the tower. The possible occurrence of gravity waves can be assessed by estimating the Froude number (Stull, 1988), Fr (the ratio of inertial to gravitational forces, $= \dfrac{U}{(N \times h)}$) which relates the prevailing horizontal wind speed

(U), mountain height (h) and buoyancy oscillation frequency (Brunt–Väisälä

91

frequency, N - calculated as a function of potential temperature). When Fr is near unity, the wavelength of the air flow is in resonance with the mountain size, creating trapped mountain lee waves which results in strong downslope winds and enhanced turbulence on the lee side of the mountain.

However, the mountain wave activity is much more complex in reality and is difficult to interpret its effects on measurements. An ideal case of such an activity was occurred at a nighttime between 16 and 17th October 2006 (between brown dashed lines in **Fig. 4.11**). A temperature inversion was observed during this period (Fig. 4.11a) indicating the stable atmospheric conditions. The sharp decrease in observed
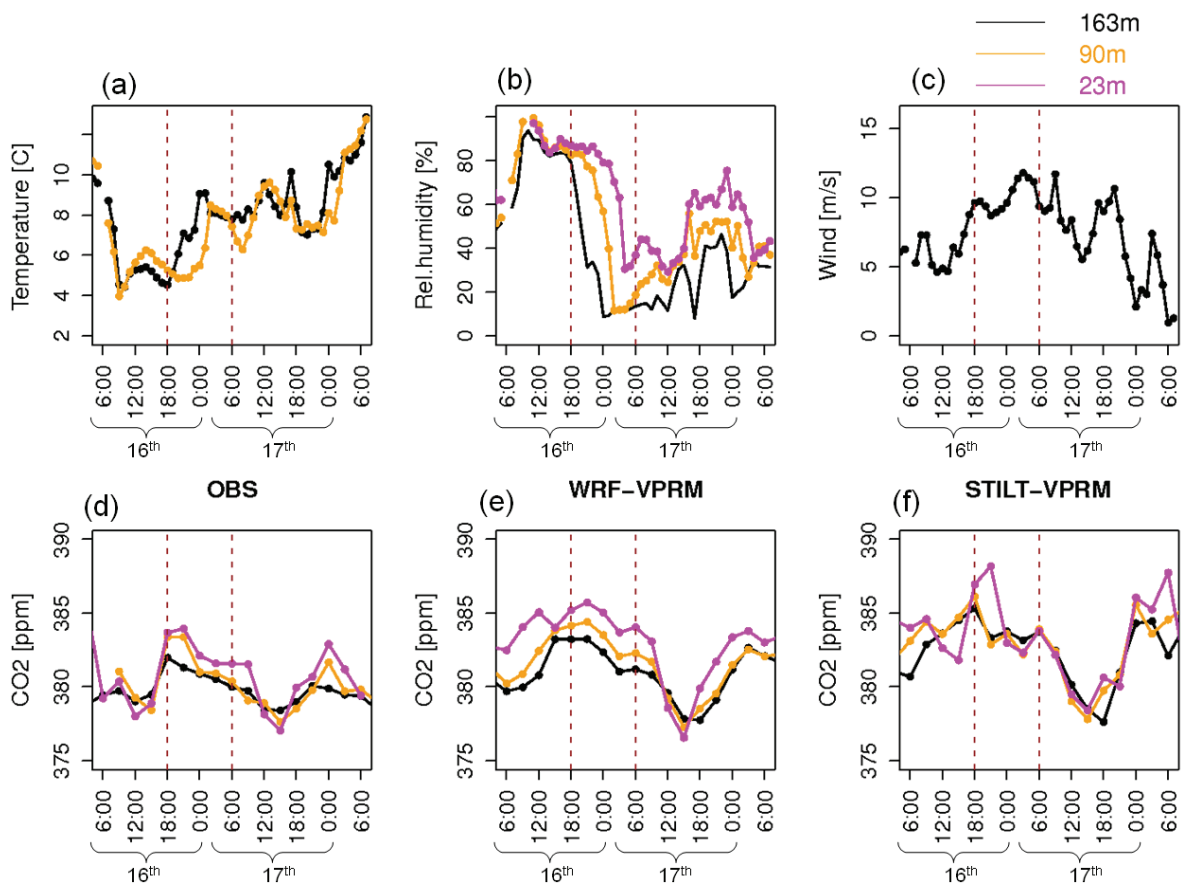
Figure 4.11 *Time series of meteorological parameters and CO₂ concentrations for different levels at Ochsenkopf tower site during 16-17 October 2006: a-c) observed air-temperature, relative humidity and wind speed respectively d-f) CO₂ concentration-observed, modeled by WRF and STILT respectively. The area between dashed <u>brown</u> vertical bars denotes the period under mountain wave activity. The X-axis shows hours in UTC; the horizontal extent of curly bracket at the bottom of X-axis shows the day on October 2006.*

relative humidity on the tower under relatively high wind speed indicates the presence of possible mountain wave activity with intrusion of dry air on the lee side of the mountain. These meteorological features were predicted reasonably well by the WRF model and the west-east cross section of simulated vertical velocity shows the downward movement of air at the lee side of the mountain (**Fig. 4.12d**). Note that the
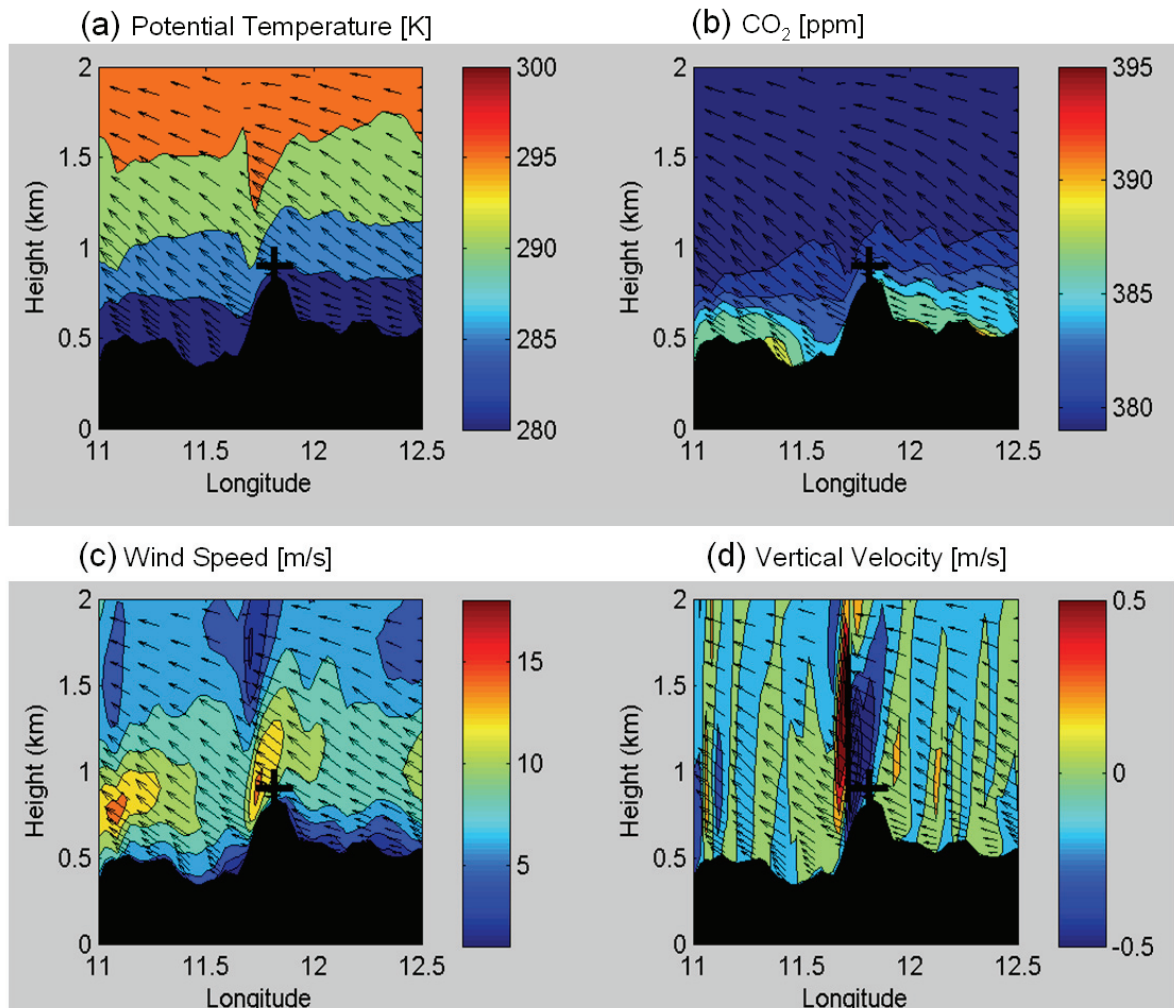
Figure 4.12 *Vertical cross section along OXK latitude (50^0 $01"$ N) on 17th October 2006 at 02:00 UTC, showing WRF-VPRM simulated a) Potential temperature in Kelvin b) CO_2 concentration in ppm c) Wind speed in ms^{-1} and d) Vertical velocity in ms^{-1}. The overlaid arrows indicate wind direction.*

WRF simulations might not always capture the waves correctly and the caution has to be taken to interpret the structures of the vertical velocity fields which can also be formed due to the numerical noise. The increased gradient in the simulated potential temperature, together with higher values of simulated vertical velocity (50 cm s^{-1}) and strong wind speed, suggests the occurrence of mountain wave phenomena at the OXK site (Fig. 4.12). The Froude number was found to be close to unity, indicating the

93

likelihood of gravity wave (mountain wave) activity. In addition to this, the simulated wavelengths $\lambda \, (= \dfrac{U}{N})$ for the region over the mountain were found to be close to the mountain height, showing the existence of vertically propagating mountain waves.

Following the collapse of the convective boundary layer on 16 October, CO_2 started to build up in the nocturnal shallow boundary layer and showed a distinctive gradient between layers for a few hours between 18-21 UTC. These nocturnal developments of CO_2 were captured fairly well in STILT-VPRM, however the vertical mixing between levels at 23 m and 90 m was underestimated. Corresponding to the prevailing mesoscale feature, the observed nocturnal gradient in tracer concentrations disappeared in response to the decent of air from the free troposphere. This was reproduced well in STILT-VPRM, while WRF-VPRM showed the decreasing tendency of CO_2 concentrations on this period but with an unrealistic gradient between the layers, which might be due to the underestimated mixing process. Note that vertical mixing is parameterized slightly differently in WRF-VPRM and STILT-VPRM. The influence of mountain waves on generating turbulent vertical mixing of nocturnal tracer concentrations at the lee side of the valley can be seen in the WRF-VPRM simulations (Fig. 4.12b). Owing to the strong downward movement of air and vertical mixing, a layer of lower CO_2 concentration was simulated for the western slope of the mountain, despite the nocturnal build-up period. The nocturnal build-up of CO_2 under shallow mixing and weak biological CO_2 uptake were simulated for the other valleys (Fig. 4.12b).

The above two case studies suggest that changes in the atmospheric transport and mixing in response to mesoscale phenomena, such as mountain-valley circulation and mountain waves, can strongly affect the diurnal patterns of CO_2 concentrations at OXK, and that these can be represented reasonably well in mesoscale models at the resolution of 2 km.

4.4.3 Seasonal Variability

Different seasonal aspects, such as changes in thermal circulation patterns (changes in solar radiation), changes in diurnal patterns of vertical mixing, effects of snow cover and diurnal variations in surface fluxes, can have an important influence on measured tracer concentrations. Seasonal changes in the diurnal patterns of CO_2 concentration

are observed at Ochsenkopf mountain station as it can be influenced by heterogeneous land sources and sinks as well as by synoptic atmospheric conditions. **Figure 4.13** shows averaged diurnal cycles of observed and modeled CO_2 at different measurement levels and for different seasons. Except for the level 163 m in winter and autumn, the CO_2 concentration maxima were observed during nighttime due to the accumulation of CO_2 concentration in the shallow nocturnal boundary layer. The measurement level at 163 m during winter and autumn is more representative of free tropospheric or residual layer air, as indicated by the weak diurnal changes in observed concentrations and by the decoupling relative to the lower levels. The slight daytime increase at the 163 m level, delayed by about six hours compared to the lower levels, is consistent with the daytime mixing of air previously trapped in the stable mixed layer, containing remnants of respired CO_2 from the previous night. The amplitude of the diurnal cycle is larger in spring and summer months (~8 ppm), consistent with the enhanced biospheric activity (photosynthesis and ecosystem respiration), whereas the amplitude is smaller in autumn and winter months owing to the reduced diurnal variability in the terrestrial fluxes. The low values of CO_2 are noticeable in August (active growing season) due to enhanced biospheric CO_2 uptake. The model-data agreement is fairly good for higher resolution models, except for the level 163 m in winter and autumn seasons where both models overestimate the vertical mixing. The coarse resolution TM3 analyzed CO_2 fields (taken from 940 hectopascal (hPa) TM3 pressure level which corresponds to the measurement levels above sea level, i.e. relative to the sea level; indicated as "TM3" in Fig. 4.13) show little diurnal change during all seasons and at all levels. On the other hand, TM3 analyzed CO_2 fields corresponding to the model levels close to the measurement levels from the surface, i.e. relative to the model terrain (taken from 1013 hPa and 1002 hPa TM3 pressure levels corresponding to the levels on the tower; indicated as "TM3-surface" in Fig. 4.13) show large diurnal variability due to the strong influence of surface fluxes near the ground, but with large positive biases in most of the cases. This discrepancy can lead to potential biases in flux estimates when using measurements from a site like OXK, as discussed above. Again, this suggests the importance of using high-resolution models to resolve the large variability of atmospheric CO_2 concentrations in response to variability in surface fluxes and mesoscale transport. In order to examine whether the poor performances of TM3 are caused by the coarse resolution flux fields (horizontal resolution: $4° \times 5°$), the
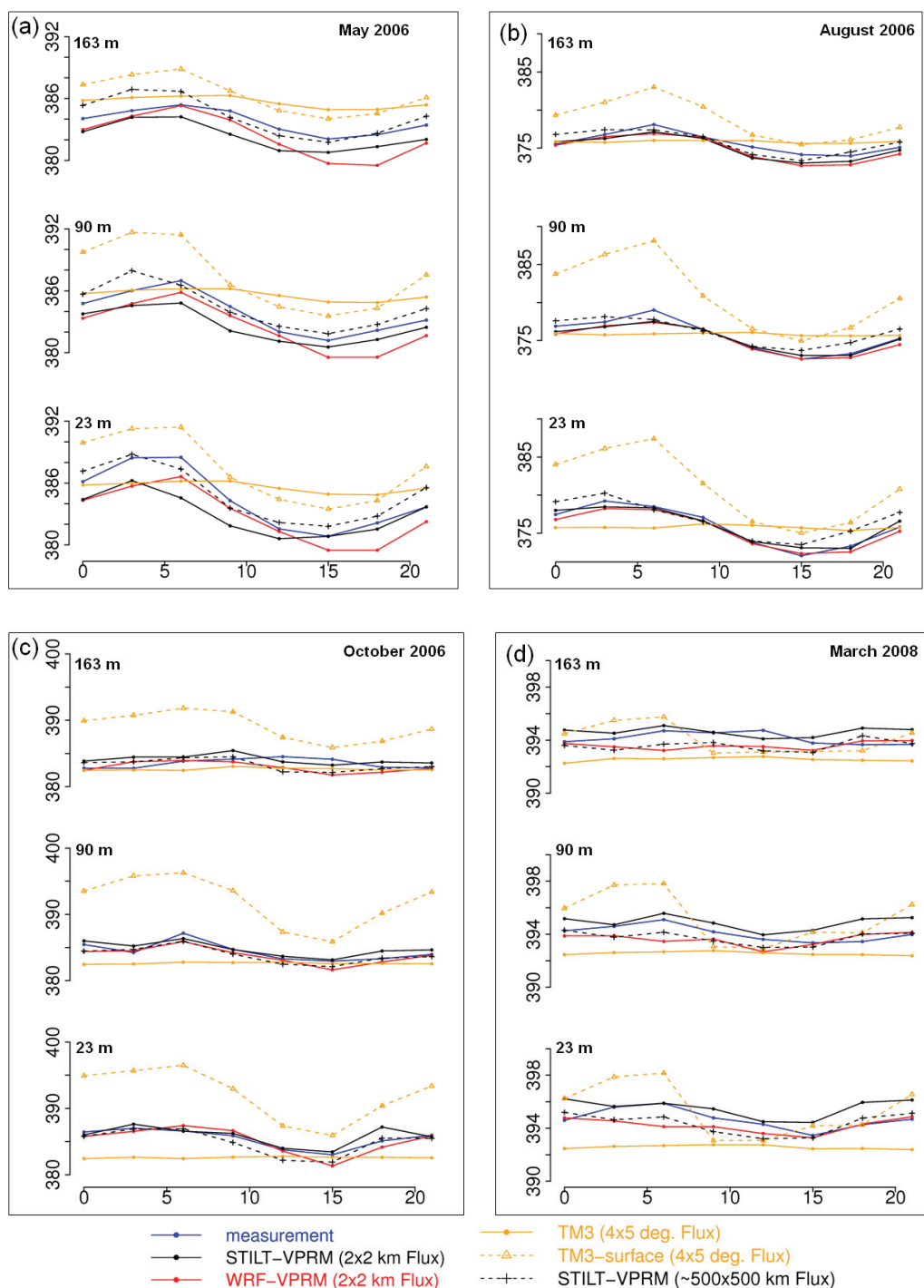
Figure 4.13 *Averaged diurnal cycle of observed and modeled CO$_2$ for OXK at different measurement levels and for different seasons: a) May 2006 (spring), b) August 2006 (summer), c) October 2006 (autumn) and d) March 2008 (winter). In each plots, top to bottom panels represents CO$_2$ at 163 m, 90 m and 23 m respectively. X-axis: hour; Y-axis: CO$_2$ concentration in ppm.*

STILT-VPRM is run with biospheric fluxes aggregated to ~500 km × 500 km resolution, comparable to the TM3 resolution. CO$_2$ simulated by this coarse resolution version of STILT-VPRM shows remarkable similarity to the high-

resolution simulations by STILT and WRF in the diurnal cycle for the different seasons.

4.4.4   Vertical distribution of CO$_2$ concentrations

The vertical profiling of atmospheric CO$_2$ during aircraft campaigns provides more information on vertical mixing in the atmosphere and provide the opportunity to evaluate current transport models. The discrepancies in predicting atmospheric mixing can lead to a strong bias in the simulated vertical distribution of CO$_2$ concentrations. An example of such an effect can be seen in Fig(s). 4.5 and 4.7. The underestimation of the vertical extent of CO$_2$ accumulation (as mentioned in Sect. 4.3.2.2) can be caused by the overestimation of vertical mixing in WRF. The effect of this overestimation can also be seen in the modeled specific humidity (Fig. 4.5b) as low values (underestimation) in the upper layers. Note that the wind speed was predicted well in WRF with negligible bias.

It should also be mentioned that the difference in observed and modeled wind speed found at the Ochsenkopf valley for another day of the campaign (23rd October 2008) generated an underestimation of CO$_2$ concentration in both WRF-VPRM and STILT-VPRM (figure not shown). WRF underestimated the flow of air, advected from upstream locations and consequently failed to capture the huge contribution of the advected respired signal to the measurement locations. STILT-VPRM also shows a similar underestimation of CO$_2$ concentration for the same reason.

These two case studies of model evaluation with the airborne measurements show the necessity of accurately predicting the mesoscale atmospheric transport, such as advection and convection, as well as vertical mixing. Both models are able to capture the spatial variability of measured CO$_2$ concentration in the complex terrain for most of the cases and the discrepancy between models and measurements are mainly attributed to the difference in representing atmospheric PBL dynamics.

4.5   Summary and Conclusions

High-resolution modeling simulations of meteorological fields and atmospheric CO$_2$ concentrations, provided by WRF-VPRM and STILT-VPRM, are presented together with measurements obtained from the Ochsenkopf tower (OXK) and from an aircraft

campaign, to address the representativeness of greenhouse gas measurements over a complex terrain associated with surrounding mountain ranges. The spatial and temporal patterns of CO_2 are reproduced remarkably well in high-resolution models for different seasons when compared to the coarse model (TM3). This emphasizes the importance of using high-resolution modeling tools in inverse frameworks, since a small deviation in CO_2 concentration can lead to potentially large biases in flux estimates. The actual reduction in uncertainties of flux estimates when using high-resolution models (compared to lower-resolution models) in the inverse framework needs to be further investigated.

The measurements of CO_2 at OXK show diurnal, synoptic and seasonal variability of CO_2 due to different aspects such as changes in the diurnal patterns of vertical mixing, diurnal variations in surface fluxes, effect of front passage, changes in thermal circulation patterns etc. These variations in tracer concentrations provide valuable information on spatiotemporal patterns of surface fluxes and thus can be used in atmospheric inversions to construct regional fluxes. Both high-resolution models were able to capture this variability by simulating well the influence of surface fluxes in the near-field and the atmosphere dynamics.

The mesoscale flows, such as mountain wave activity and mountain-valley circulations, can have a strong influence on the observed atmospheric CO_2 at OXK by changing the vertical mixing of the tracer concentrations. The meteorological simulations by WRF indicate that the buoyancy driven drainage flows are more common at OXK during nighttimes (especially in summer) and mountain gravity waves are likely to occur in winter periods. Resolving these circulation patterns in models is a prerequisite for utilizing observations from mountain stations such as OXK with a reduced representation error.

The discrepancies in predicting vertical mixing can lead to strong biases in simulated CO_2 concentrations and these kinds of uncertainties are typical for complex terrain regions. The vertical profiling of CO_2 (like the DIMO aircraft campaign) or wind profiler measurements can be helpful in assessing the impact of vertical mixing on tracer concentrations. The study shows that much of the variability in CO_2 concentrations can be reproduced well by appropriate representation of mesoscale

transport processes, such as advection, convection and vertical mixing as well as surface flux influences in the near-field.

This study demonstrates the potential of using high-resolution models in the context of inverse modeling frameworks to utilize measurements provided from mountain or complex terrain sites. The future work will focus on regional inversions using STILT-VPRM at high-resolution with a nested option. The feasibility of using these high-resolution nests in global models has already been demonstrated by Rödenbeck et al., 2009. This provides justified hope that measurements from mountain stations can be utilized in inverse modeling frameworks to derive regional CO_2 budgets at reduced uncertainty limits.

4.6   References

Ahmadov, R., Gerbig, C., Kretschmer, R., Koerner, S., Neininger, B., Dolman, A. J., and Sarrat, C.: Mesoscale covariance of transport and CO_2 fluxes: Evidence from observations and simulations using the WRF-VPRM coupled atmosphere-biosphere model, Journal of Geophysical Research-Atmospheres, 112, D22107, doi:22110.21029/22007JD008552, 2007.

Ahmadov, R., Gerbig, C., Kretschmer, R., Körner, S., Rödenbeck, C., Bousquet, P., and Ramonet, M.: Comparing high resolution WRF-VPRM simulations and two global CO_2 transport models with coastal tower measurements of CO_2, Biogeosciences, 6, 807-817, 2009.

Denning, A. S., Zhang, N., Yi, C. X., Branson, M., Davis, K., Kleist, J., and Bakwin, P.: Evaluation of modeled atmospheric boundary layer depth at the WLEF tower, Agricultural and Forest Meteorology, 148, 206-215, 2008.

Enting, I. G.: Inverse problems in atmospheric constituent studies: III. Estimating errors in surface sources, Inverse Problems, 9, 649-665, 1993.

Gangoiti, G., M. M. Millan., R. Salvador., and Mantilla., E.: Long-range transport and re-circulation of pollutants in the western Mediterranean during the project Regional Cycles of Air Pollution in the west-central Mediterranean area, Atmos. Environ., 35(36), 6267–6276, 2001.

Geels, C., Gloor, M., Ciais, P., Bousquet, P., Peylin, P., Vermeulen, A. T., Dargaville, R., Aalto, T., Brandt, J., Christensen, J. H., Frohn, L. M., Haszpra, L., Karstens, U., Rödenbeck, C., Ramonet, M., Carboni, G., and Santaguida, R.: Comparing atmospheric transport models for future regional inversions over Europe. Part 1: Mapping the atmospheric CO_2 signals, Atmos. Chem. Phys, 7, 3461-3479, 2007.

Gerbig, C., Körner, S., and Lin, J. C.: Vertical mixing in atmospheric tracer transport models: error characterization and propagation, Atmos. Chem. Phys, 8, 591-602, 2008.

Gerbig, C., Dolman, A. J., and Heimann, M.: On observational and modelling strategies targeted at regional carbon exchange over continents, Biogeosciences, 6, 1949-1959, 2009.

Gourdji, S. M., Mueller, K. L., Schaefer, K., and Michalak, A. M.: Global monthly averaged CO_2 fluxes recovered using a geostatistical inverse modeling approach: 2. Results including auxiliary environmental data, Journal of Geophysical Research - Atmospheres, 113, doi:10.1029/2007JD009733, 2008.

Gurney, K. R., Law, R. M., Denning, A. S., Rayner, P. J., Baker, D., Bousquet, P., Bruhwiler, L., Chen, Y.-H., Ciais, P., Fan, S., Fung, I. Y., Gloor, M., Heimann, M., Higuchi, K., John, J., Maki, T., Maksyutov, S., Masarie, K., Peylin, P., Prather, M., Pak, B. C., Randerson, J., Sarmiento, J., Taguchi, S., Takahashi, T., and Yuen, C.-W.: Towards robust regional estimates of CO_2 sources and sinks using atmospheric transport models, Nature, 415, 626-630, 2002.

Heimann, M., and Koerner, S.: The global atmospheric tracer model TM3, Technical Reports, Max-Planck-Institute for Biogeochemie, 5, 131 p., 2003.

Jacobson, A. R., Mikaloff Fletcher, S. E., Gruber, N., Sarmiento, J. L., and Gloor, M.: A joint atmosphere-ocean inversion for surface fluxes of carbon dioxide: 1. Methods and global-scale fluxes, Global Biogeochemical Cycles, 21, GB1019, doi:1010.1029/2005GB002556, 2007.

Lauvaux, T., Uliasz, M., Sarrat, C., Chevallier, F., Bousquet, P., Lac, C., Davis, K. J., Ciais, P., Denning, A. S., and Rayner, P. J.: Mesoscale inversion: first results from The CERES campaign with synthetic data, Atmos. Chem. Phys, 8, 3459-3471, 2008.
Le Treut, H., R. Somerville, U. Cubasch, Y. Ding, C. Mauritzen, A. Mokssit, Peterson, T., and Prather, M.: Historical Overview of Climate Change, In: Climate Change 2007: The Physical Science Basis. Contribution of Working Group I to the Fourth Assessment Report of the Intergovernmental Panel on Climate Change [Solomon, S., D. Qin, M. Manning, Z. Chen, M. Marquis, K.B. Averyt, M. Tignor and H.L. Miller (eds.)]. Cambridge University Press, Cambridge, United Kingdom and New York, NY, USA., 2007.

Levin, I., Graul, R., and Trivett, N.: Long-term observations of atmospheric CO_2 and carbon isotopes at continental sites in Germany, Tellus Series B, Chemical and physical meteorology, 47, 23-34, 1995.

Lin, J. C., Gerbig, C., Wofsy, S. C., Andrews, A. E., Daube, B. C., Davis, K. J., and Grainger, C. A.: A near-field tool for simulating the upstream influence of atmospheric observations: The Stochastic Time-Inverted Lagrangian Transport (STILT) model, Journal of Geophysical Research-Atmospheres, 108, 4493, doi:4410.1029/2002JD003161, 2003.

Lin, J. C., and Gerbig, C.: Accounting for the effect of transport errors on tracer inversions, Geophysical Research Letters, 32, L01802, doi:01810.01029/02004GL021127, 2005.

Mahadevan, P., Wofsy, S. C., Matross, D. M., Xiao, X., Dunn, A. L., Lin, J. C., Gerbig, C., Munger, J. W., Chow, V. Y., and Gottlieb, E. W.: A satellite-based biosphere parameterization for net ecosystem CO_2 exchange: Vegetation Photosynthesis and Respiration Model (VPRM), Global Biogeochemical Cycles, 22, GB2005, doi:2010.1029/2006GB002735, 2008.

Matross, D. M., Andrews, A., Pathmathevan, M., Gerbig, C., Lin, J. C., Wofsy, S. C., Daube, B. C., Gottlieb, E. W., Chow, V. Y., Lee, J. T., Zhao, C. L., Bakwin, P. S., Munger, J. W., and Hollinger, D. Y.: Estimating regional carbon exchange in New England and Quebec by combining atmospheric, ground-based and satellite data, Tellus Series B-Chemical and Physical Meteorology, 58, 344-358, 2006.

Nehrkorn, T., Eluszkiewicz, J.,Wofsy, S.C., Lin, J.C. ,Gerbig, C. , Longo,M., Freitas, S.: Coupled weather research and forecasting–stochastic time-inverted lagrangian transport (WRF–STILT) model, Meteorol Atmos Phys, 107, 51-64, 2010.

Olivier, J. G. J., Bouwman, A. F., Berdowski, J. J. M., Veldt, C., Bloos, J. P. J., Visschedijk, A. J. H., and van der Maas, C. W. M.: Sectoral emission inventories of greenhouse gases for 1990 on a per country basis as well as on 1°x1°, Environmental Science & Policy, 2, 241-263, 1999.

Pérez-Landa, G., Ciais, P., Gangoiti, G., Palau, J. L., Carrara, A., Gioli, B., Miglietta, F., Schumacher, M., Millán, M. M., and Sanz, M. J.: Mesoscale circulations over complex terrain in the Valencia coastal region, Spain - Part 2: Modeling CO_2 transport using idealized surface fluxes, Atmos. Chem. Phys, 7, 1851-1868, 2007.

Peters, W.: Seven years of recent European net terrestrial carbon dioxide exchange constrained by atmospheric observations, Global Change Biology, 16, 1317-1337, 2010.

Pillai, D., Gerbig, C., Kretschmer, R., Beck, V., Karstens, U., and Neininger, B.: Comparing Lagrangian and Eulerian models for CO_2 transport- a step towards Bayesian Inverse Modeling using WRF/STILT-VPRM, in preparation, 2010a.

Pillai, D., Gerbig, C., Marshall, J., Ahmadov, R., Kretschmer, R., Koch, T., and Karstens, U.: High resolution modeling of CO_2 over Europe: implications for representation errors of satellite retrievals, Atmos.Chem.Phys, 10, 83-94, 2010b.

Reiter, R., Sladkovic, R., and Kanter, H. J.: Concentration of trace gases in the lower troposphere, Part I: Carbon dioxide, Meteorology and Atmospheric Physics, 35, 187-200, 1986.

Rödenbeck, C., Houweling, S., Gloor, M., and Heimann, M.: CO_2 flux history 1982-2001 inferred from atmospheric data using a global inversion of atmospheric transport, Atmos. Chem. Phys, 3, 1919-1964, 2003.

Rödenbeck, C.: Estimating CO_2 sources and sinks from atmospheric mixing ratio measurements using a global inversion of atmospheric transport. Technical Report 6, Max-Planck Institut für Biogeochemie, Jena, Germany, 53 pp., 2005.

Rödenbeck, C., Gerbig, C., Trusilova, K., and Heimann, M.: A two-step scheme for high-resolution regional atmospheric trace gas inversions based on independent models, Atmos. Chem. Phys, 9, 5331-5342, 2009.

Sarrat, C., Noilhan, J., Lacarrère, P., Donier, S., Lac, C., Calvet, J. C., Dolman, A. J., Gerbig, C., Neininger, B., Ciais, P., Paris, J. D., Boumard, F., Ramonet, M., and Butet, A.: Atmospheric CO_2 modeling at the regional scale: Application to the CarboEurope regional experiment, Journal of Geophysical Research-Atmospheres, 112, D12105, doi:12110.11029/12006JD008107, 2007.

Stull, R. B.: An Introduction to Boundary Layer Meteorology, Kluwer Academic Publishers, Dordrecht, 666 pp. Webb, E.K., Pearman, 1988.

Tans, P. P., Fung, I. Y., and Takahashi, T.: Observational constraints on the global atmospheric CO_2 budget, Science, 247, 1431-1438, 1990.

Thompson, R. L., Manning, A. C., Gloor, E., Schultz, U., Seifert, T., Hänsel, F., Jordan, A., and Heimann, M.: In-situ measurements of oxygen, carbon monoxide and greenhouse gases from Ochsenkopf tall tower in Germany, Atmospheric Measurement Techniques, 2, 573-591, 2009.

Tolk, L. F., Meesters, A. G. C. A., Dolman, A. J., and Peters, W.: Modelling representation errors of atmospheric CO_2 mixing ratios at a regional scale, Atmos. Chem. Phys, 8, 6587-6596, 2008.

van der Molen, M. K., and Dolman, A. J.: Regional carbon fluxes and the effect of topography on the variability of atmospheric CO_2, Journal of Geophysical Research-Atmospheres, 112, D01104, doi:01110.01029/02006JD007649, 2007.

5 Comparing Lagrangian and Eulerian models for CO_2 transport – a step towards Bayesian inverse modeling using WRF/STILT-VPRM

Abstract

Simulations of atmospheric CO_2 concentrations provided by two modeling systems, run at high spatial resolution are presented. The modeling systems consist of the Eulerian-based Weather Research Forecasting (WRF) model and the Lagrangian-based Stochastic Time-Inverted Lagrangian Transport (STILT) model, both of which are coupled to a satellite-based biospheric model, the Vegetation Photosynthesis and Respiration Model (VPRM). A quantitative comparison between the two different approaches, while using identical surface-atmosphere fluxes and meteorological fields, is a prerequisite for applying STILT as an adjoint of WRF for inverse modeling. The consistency of the simulations is assessed with special attention paid to the details of horizontal as well as vertical transport and mixing of CO_2 concentrations in the atmosphere. A case study using airborne measurements during which both models showed large deviations is analyzed in detail as an extreme case. Using aircraft observations and pulse release simulations, it is identified that differences in the representation of details in the interaction between turbulent mixing and advection through wind shear as the main cause of discrepancies between WRF and STILT transport. Based on observations and inter-model comparisons of atmospheric CO_2 concentrations, it is shown that a refinement of the parameterization of turbulent velocity variance and Lagrangian time-scale in STILT is needed to achieve a better match between the Eulerian and the Lagrangian transport at such a high spatial resolution. Nevertheless, the inter-model differences in simulated CO_2 time series for a tall tower observatory at Ochsenkopf in Germany are about a factor of two smaller than the model-data mismatch and about a factor of three smaller than the mismatch between the current global model simulations and the data, which justifies using STILT as an adjoint model of WRF.

5.1 Introduction

Inverse modeling tools use the atmosphere as an "integrator" to obtain information on the source-sink distribution of CO_2 on different spatial and temporal scales. A common practice is to use a global atmospheric transport model together with a

network of atmospheric measurements to estimate the relationship between flux and tracer distributions via inverse techniques. The reliability of the inverse flux estimation depends largely on the quality of the transport represented in the models (Gerbig et al., 2008; Lin and Gerbig, 2005; Stephens et al., 2007; Geels et al., 2007).

Atmospheric transport models can be based on either Eulerian or Lagrangian formulations of the fluid transport process. In the Lagrangian formulation, the motion of fluid elements is described by solving the Lagrangian equations of mass and momentum along the trajectory of the particle/fluid element and calculating the change of the particle/fluid element location and the velocity components. In the Eulerian approach, the mass concentration of fluid elements is calculated as a function of space and time instead of calculating trajectories of fluid elements. The governing equations are similar to the Navier-Stokes equations, with additional terms in the momentum equations to account for the turbulent dispersion. Both Eulerian and Lagrangian modeling approaches are used in the inverse modeling community to estimate source-sink distributions (Gerbig et al., 2003a; Lauvaux, 2008; Rödenbeck et al., 2003)

The atmospheric distribution of trace gases is variable on small scales (both temporal and spatial), caused by strong surface flux variability in the near field and by mesoscale transport phenomena. However, the current global models, with spatial resolutions of no more than $1° \times 1°$, fail to resolve these variations on measured atmospheric CO_2, which potentially leads to biases in flux estimates (Ahmadov et al., 2009). In order to better represent measurements made in the mixed layer (the lowest 1 to 2 km of the atmosphere) by stations such as tall towers, the inverse system requires the atmospheric transport models to be set up at high spatial resolution (2 to 20 km). In addition, the fluxes in the near-field of the observatories can be highly variable (Gerbig et al., 2003b), calling for a-priori fluxes to be specified at high spatial resolution. Recent studies have demonstrated improvement in capturing the variability of observed CO_2 concentrations when increasing the spatial resolution of the transport models (Ahmadov et al., 2007; Pérez-Landa et al., 2007; Sarrat et al., 2007; van der Molen and Dolman, 2007).

Gerbig et al. (2003a) describes a receptor-oriented framework using a Lagrangian Particle Dispersion Model (LPDM) together with lateral boundary conditions and a

104

biospheric flux model to derive regional fluxes at high spatial and temporal resolution. The "footprints" (sensitivity of model output (e.g. concentration) to input variables (e.g. surface fluxes)) derived from an LPDM is similar to the adjoint of an Eulerian Transport model (Errico, 1997). Using these footprints has the advantage of resolving the fine structures originating from surface flux variations on scales smaller than the grid size of the meteorological fields used. In the case of the Eulerian approach, the models are affected by numerical diffusion, limiting the resolution to scales larger than the grid size in the underlying meteorology. The framework is thus analogous to a regional adjoint model in an Eulerian framework, providing an alternative to generating and implementing adjoint model code for an Eulerian transport model.

A framework similar to that introduced by Gerbig et al. (2003a) which consists of a receptor-oriented transport model driven offline by assimilated meteorological fields, an Eulerian online transport model and a diagnostic biospheric model is used to derive regional flux estimates. The receptor-oriented transport model is the Stochastic Time-Inverted Lagrangian Transport (STILT) model (Gerbig et al., 2003b), the Eulerian transport model is the Weather Research Forecasting (WRF) model (http://www.wrf-model.org/)   and the biosphere model is the Vegetation Photosynthesis and Respiration Model (VPRM) (Mahadevan et al., 2008). The term "online" indicates here that the meteorological fields are simulated during the model run, while "offline" refers to the use of already simulated meteorological fields. A schematic representation of the modeling framework is illustrated in **Fig. 5.1**.

The wind fields generated by WRF are used in STILT to calculate ensembles of back trajectories starting at a receptor location. Resulting footprints (sensitivities to upstream surface-atmosphere fluxes) are then mapped to high-resolution surface fluxes as well as initial/lateral boundary conditions from a global model. This part of the framework – offline Lagrangian modeling system – provides time series of CO_2 mixing ratios at the receptor location. The other part of the framework – the online Eulerian modeling system – generates 3D fields of CO_2 concentration, using the same surface fluxes and boundary conditions as the Lagrangian system. Hence the framework allows for a direct comparison of Eulerian (forward) and Lagrangian (adjoint) models to assess the consistency in simulating transport, which is a prerequisite for using STILT for the inverse estimation of fluxes.
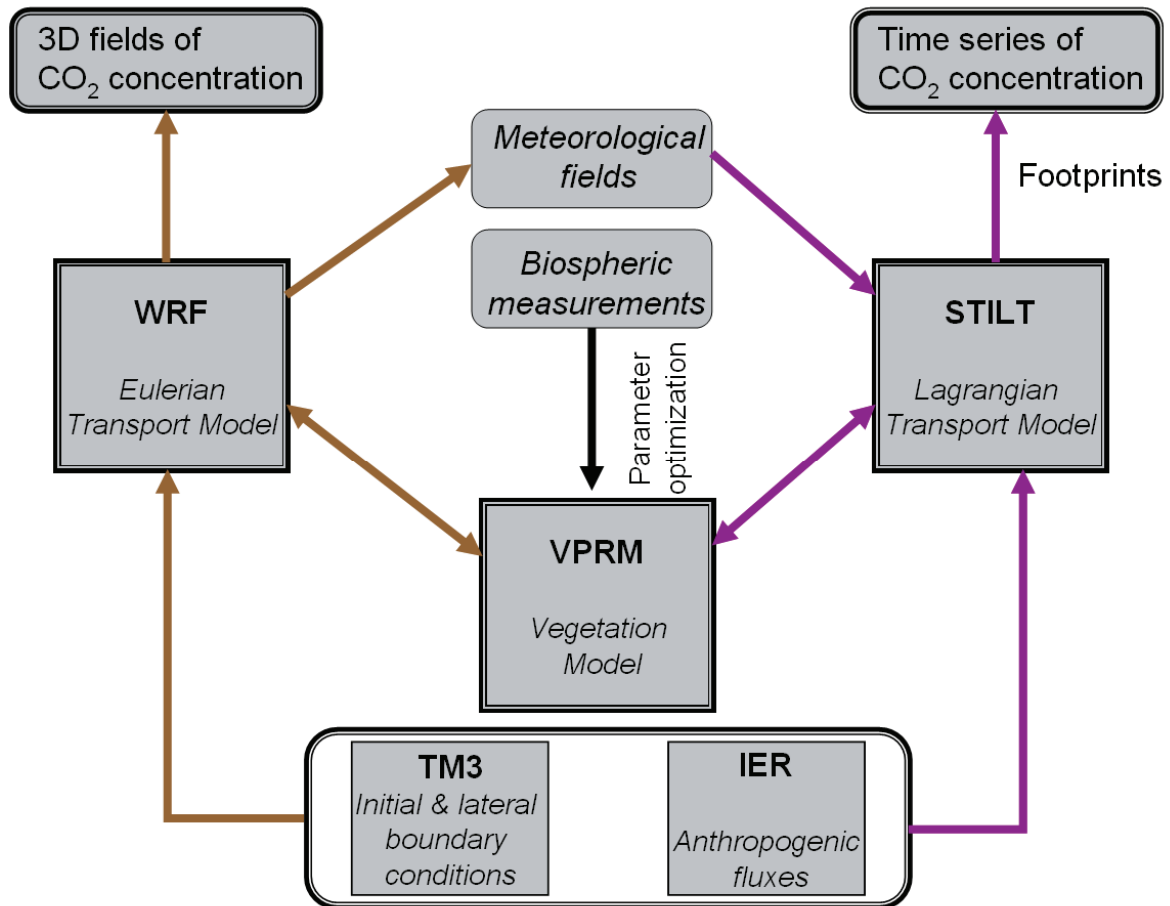
Figure 5.1 *Schematic diagram showing WRF-VPRM (Eulerian) and WRF/STILT-VPRM (Lagrangian) modeling framework.*

This chapter presents the simulated CO_2 time series generated by the Eulerian and Lagrangian transport models at high resolution for the domain over Ochsenkopf in Germany. The consistency of those two simulations is assessed with special attention paid to the details of horizontal and vertical transport and mixing. The chapter is organized as follows: Section 5.2 describes the major components of the modeling framework and the model domain. Results are presented and discussed in Sect. 5.3, exploring reasons for possible discrepancies between modeled mixing ratios from two modeling systems. Section 5.4 provides the conclusion of this study.

5.2   Modeling Framework

Major components of the Eulerian and the Lagrangian parts of the modeling framework – the coupled models WRF-VPRM (Eulerian) which provides spatial and temporal distributions of CO_2 and WRF/STILT-VPRM (Lagrangian) which simulates the temporal distribution of CO_2 at the observation point (receptor) – are described

here. Including the Eulerian and Lagrangian models in a single framework allows for the quantitative comparison between the two different approaches, while using the same domain, surface fluxes and initial/ lateral boundary conditions.

5.2.1   WRF-VPRM model

The mesoscale weather prediction model WRF is used with a passive tracer option from WRF-Chem (version 3.0) (Grell et al., 2005) together with the VPRM model to simulate the distribution of CO_2. The tagged tracer option is used to distinguish different components (i.e. biospheric, anthropogenic etc.) of total CO_2. A K-diffusion scheme with heat exchange coefficient – K_h – is used in WRF-Chem (hereafter referred to as WRF) to account for turbulent vertical mixing of tracers. Note that the vertical diffusion of meteorological parameters is performed by the boundary layer scheme in WRF. For more details, interested reader is referred to Grell et al. (2005). Modifications which are made in the WRF source code for coupling the biosphere model VPRM to WRF and to implement simulations of CO_2 transport are

Table 5.1 *Overview of model set-up used in WRF.*

Vertical coordinates	Terrain-following hydrostatic pressure vertical coordinate
Basic equations	Non-hydrostatic, compressible
Time integration	3rd order Runge-Kutta split-explicit
Spatial integration	3rd and 5th order differencing for vertical and horizontal advection respectively; both for momentum and scalars
Time step	36 sec
Physics schemes	Radiation - Rapid Radiative Transfer Model (RRTM) scheme (Long wave) and Dudhia scheme (Shortwave) ; Microphysics - WSM 3-class simple ice scheme; Cumulus - Kain-Fritsch (new Eta) scheme PBL – YSU; Surface layer – Monin-Obukhov Land-surface – NOAH LSM

described in detail by Ahmadov et al. (2007). An overview of the WRF physics/dynamics options used here is given in Table 5.1. Past applications of WRF-VPRM to regional CO_2 simulations have shown remarkable skill in capturing fine-scale spatial variability of CO_2 mixing ratios (Ahmadov et al., 2007; Ahmadov et al., 2009; Pillai et al., 2010b).

VPRM is a satellite-based diagnostic biosphere model (Mahadevan et al., 2008) which uses MODIS (http://modis.gsfc.nasa.gov/) satellite indices at high spatial resolution to calculate Net Ecosystem Exchange (NEE). NEE is calculated as a function of Enhanced Vegetation Index (EVI), Land Surface Water Index ($LSWI$) – both from MODIS – simulated surface temperature (temperature at 2 meter above ground: T_2) and shortwave radiation fluxes (SWDOWN) – both provided by WRF. SYNMAP data (Jung et al., 2006) with a spatial resolution of 1 km and 8 different vegetation classes is used to represent vegetation cover in the domain. The VPRM parameters are optimized against eddy flux measurements for different biomes in Europe collected during the CarboEurope IP (http://www.bgc-jena.mpg.de/bgc-processes/ceip/).

In the coupled WRF-VPRM model, VPRM computes biospheric fluxes utilizing the meteorological variables from WRF as described above and then passes these fluxes to WRF to be transported in the passive tracer mode. Fossil fuel emission data at a spatial resolution of 10 km are prescribed from an inventory provided by IER (Institut für Energiewirtschaft und Rationelle Energieanwendung), University of Stuttgart (http://carboeurope.ier.uni-stuttgart.de/) to account for anthropogenic fluxes. Both biospheric and anthropogenic surface flux inputs are projected to the Lambert Conical Cartesian co-ordinate system used by WRF-VPRM. Projection of gridded fossil fuel emissions to the WRF grid is done using mass conserving routines. Initial/lateral CO_2 tracer boundary conditions for CO_2 tracer are taken from analyzed CO_2 fields (Rödenbeck, 2005), generated by the global atmospheric tracer transport model, TM3 (Heimann and Koerner, 2003), based on optimized fluxes transported at a spatial resolution of $4° \times 5°$, and a temporal resolution of 3 hours (ana96_v3.0, http://www.bgc-jena.mpg.de/~christian.roedenbeck/download-CO2-3D/). Analyzed meteorological fields from the ECMWF model (http://www.ecmwf.int/), at a

temporal and horizontal resolution of 6 hours and approximately 25 km respectively, serve as initial and lateral meteorological boundary conditions for the WRF-VPRM. WRF-VPRM is nested with a horizontal resolution of 6 km (parent) and 2 km (nested) as well as 41 vertical levels (lowest layer at about 18 m). Each simulation day starts at 18 UTC of the previous day, and continues with hourly output for 30 hours. The first 6 hours are used as meteorological spin-up time. The initial conditions of the tracer concentrations are prescribed from the previous day of the simulation except for the first day of simulation where TM3 fields are used as mentioned above. The lateral boundary conditions are specified from TM3 fields.

5.2.2   WRF/STILT-VPRM model

STILT is a Lagrangian Particle Dispersion Model, which simulates ensembles of particles representing air parcels of equal mass, transported backward in time from an observation point (receptor) by mean winds and sub-grid turbulent winds. The turbulent flow is modeled as a Markov chain, where particles are transported at each time step using following equation:

$$\mathbf{u}'(t + \Delta t) = R(\Delta t)\mathbf{u}' + \mathbf{u}''(t) \tag{1}$$

where $\mathbf{u}'$ is the turbulent component of the mean velocity vector $\mathbf{u}$, $\mathbf{u}''$ is a random vector drawn from a normal distribution with a width equal to the variance of the vertical velocity (σ_w), Δt is the time step, and R is an autocorrelation coefficient which determines the standard random walk for the turbulent velocity components for each time step. R is expressed as:

$$R(\Delta t) = \exp(-\frac{\Delta t}{\mathrm{T}_L}) \tag{2}$$

where T_L is the Lagrangian time-scale in the horizontal (u) or vertical direction (w) that determines the degree to which particles keep the memory of previous motion. T_L is set to zero for a random walk and large T_L represents the advection by mean wind. Profiles for T_L and σ_w are derived from WRF meteorological fields (Gerbig et al., 2003b).

Here STILT footprints are driven by meteorological fields from the high-resolution mesoscale model, WRF (hereafter referred as "WRF/STILT" to indicate that the STILT is driven by WRF meteorology). The WRF-VPRM source code is modified to

output the meteorological variables required to drive STILT (Nehrkorn et al., 2010). The STILT model has been used extensively in regional simulations and inversion studies for different greenhouse gases (Lin et al., 2003; Gerbig et al., 2003b; Lin et al., 2004; Miller et al., 2008; Gourdji et al., 2010; Göckede et al., 2010).

WRF/STILT computes changes in the tracer concentration $C(\mathbf{x}_r, t_r)$ at the receptor location $\mathbf{x}_r$ measured at time t_r as the sum of changes in the tracer concentration at the receptor due to surface fluxes F in the domain V between initialization time t_0 and t_r (denoted as " $C_{surface}(\mathbf{x}_r, t_r)$ ") and the contribution from the initial tracer field $C(\mathbf{x}, t_0)$ (denoted as " $C_{ini}(\mathbf{x}_r, t_r)$ ") (Gerbig et al., 2003b). $C(\mathbf{x}_r, t_r)$ is expressed as:

$$
C(\mathbf{x}_r, t_r) = \underbrace{\int_{t_0}^{t_r} dt \int_V d^3\mathbf{x} I(\mathbf{x}_r, t_r \mid \mathbf{x}, t) S(\mathbf{x}, t)}_{C_{surface(xr,tr)}} + \underbrace{\int_V d^3\mathbf{x} I(\mathbf{x}_r, t_r \mid \mathbf{x}, t) C(\mathbf{x}, t_0)}_{C_{bg(xr,tr)}}
\tag{3}
$$

i.e. $C(\mathbf{x}_r, t_r) = C_{surface}(\mathbf{x}_r, t_r) + C_{bg}(\mathbf{x}_r, t_r)$ (3a)

Here $I(\mathbf{x}_r, t_r \mid \mathbf{x}, t)$ is the influence function which links spatially and temporally resolved surface source or sinks $S(\mathbf{x}, t)$ to the tracer concentration at the receptor and is expressed as:

$$
I(\mathbf{x}_r, t_r \mid \mathbf{x}, t) = \frac{\rho(\mathbf{x}_r, t_r \mid \mathbf{x}, t)}{N_{tot}}
\tag{3b}
$$

for a given number of particles (N_{tot}) released from the receptor and particle density $\rho(\mathbf{x}_r, t_r \mid \mathbf{x}, t)$ at location $\mathbf{x}$ and time t.

The tracer concentration at the receptor due to fluxes F, denoted as $C_{surface}(\mathbf{x}_r, t_r)$, is expressed as:

$$
C_{surface}(\mathbf{x}_r, t_r) = \sum_{i,j,k} \frac{m_{air}}{h. \overline{\rho}(x_j, y_k, t_i)} . \frac{1}{N_{tot}} \left(\sum_{p=1}^{N_{tot}} \Delta t_{p,i,j,k} \right) . F(x_j, y_k, t_i)
$$

$$
= \sum_{i,j,k} f(\mathbf{x}_r, t_r \mid x_j, y_k, t_i) . F(x_j, y_k, t_i)
\tag{4}
$$

where $f(\mathbf{x}_r, t_r \mid x_j, y_k, t_i)$ is given by

$$
f(\mathbf{x}_r, t_r \mid x_j, y_k, t_i) = \frac{m_{air}}{h \times \overline{\rho}(x_j, y_k, t_i)} \times \frac{1}{N_{tot}} \left(\sum_{p=1}^{N_{tot}} \Delta t_{p,i,j,k} \right)
\tag{5}
$$

Here h represents the column height into which the tracer is diluted (half of the planetary boundary layer (PBL) height in the current application), $\overline{\rho}$ - the column

averaged air density and m_{air} is the molar mass of air. The interested reader is refereed to Gerbig et al.(2003b) for more details. The term $f(\mathbf{x}_r, t_r \mid x_j, y_k, t_i)$ links surface fluxes to concentration changes at the receptor and is denoted as the "footprint". The footprint derived here is analogous to the adjoint of WRF transport (Lin et al., 2003; Gerbig et al., 2003a; Errico, 1997).

A total of 100 particles is released from a receptor point and WRF/STILT transports particles backward in time for a maximum of 3 days or until particles leave the domain. WRF/STILT is used with a nested option where the wind fields are provided at the spatial resolution of the WRF inner domain (2 km × 2 km) until the particles leave the inner domain and afterwards at the spatial resolution of the parent domain (6 km × 6 km). The footprints are calculated according to equation (5) and are gridded to a maximum resolution of 2 km × 2 km. The horizontal size of the grid cells for resolving the footprint is dynamically adjusted according to the increase in footprint area in order to save computation time as well as to avoid under-sampling of surface fluxes when the statistical probability of finding a particle in particular grid box becomes smaller (Gerbig et al., 2003b).

The surface fluxes including the VPRM biospheric fluxes, simulated at a spatial resolution of 2 km × 2 km, and the IER (anthropogenic) fluxes, interpolated to 2 km × 2 km are coupled to the transport according to equation (4) in order to estimate the associated surface flux contributions to the concentration field at the receptor ($C_{surface}(\mathbf{x}_r, t_r)$). The total CO_2 concentration at the receptor ($C(\mathbf{x}_r, t_r)$) is calculated by adding the global background tracer distribution – $C_{bg}(\mathbf{x}_r, t_r)$ – to $C_{surface}(\mathbf{x}_r, t_r)$ as given in equation (3a), where the lateral tracer boundary conditions are prescribed from the TM3 global model. Note that the same surface fluxes and initial/lateral boundary conditions as given in Sec 5.2.1 are used, but the surface fluxes are projected to the Cartesian co-ordinates system used by WRF/STILT.

5.2.3   Model Domain and Period of Simulations

WRF-VPRM simulations of CO_2 and meteorological fields are carried out for the period from 2 to 30 August, 2006, and for a single day in 2008 (20th October 2008) for a domain centered over Ochsenkopf in Germany (see **Fig. 5.2**). A period during summer (August 2006) is chosen as a case for the comparison of transport models

because an increase of biological activity as well as strong variability of diurnal patterns of surface fluxes and mesoscale transport can be expected. The period on 20th
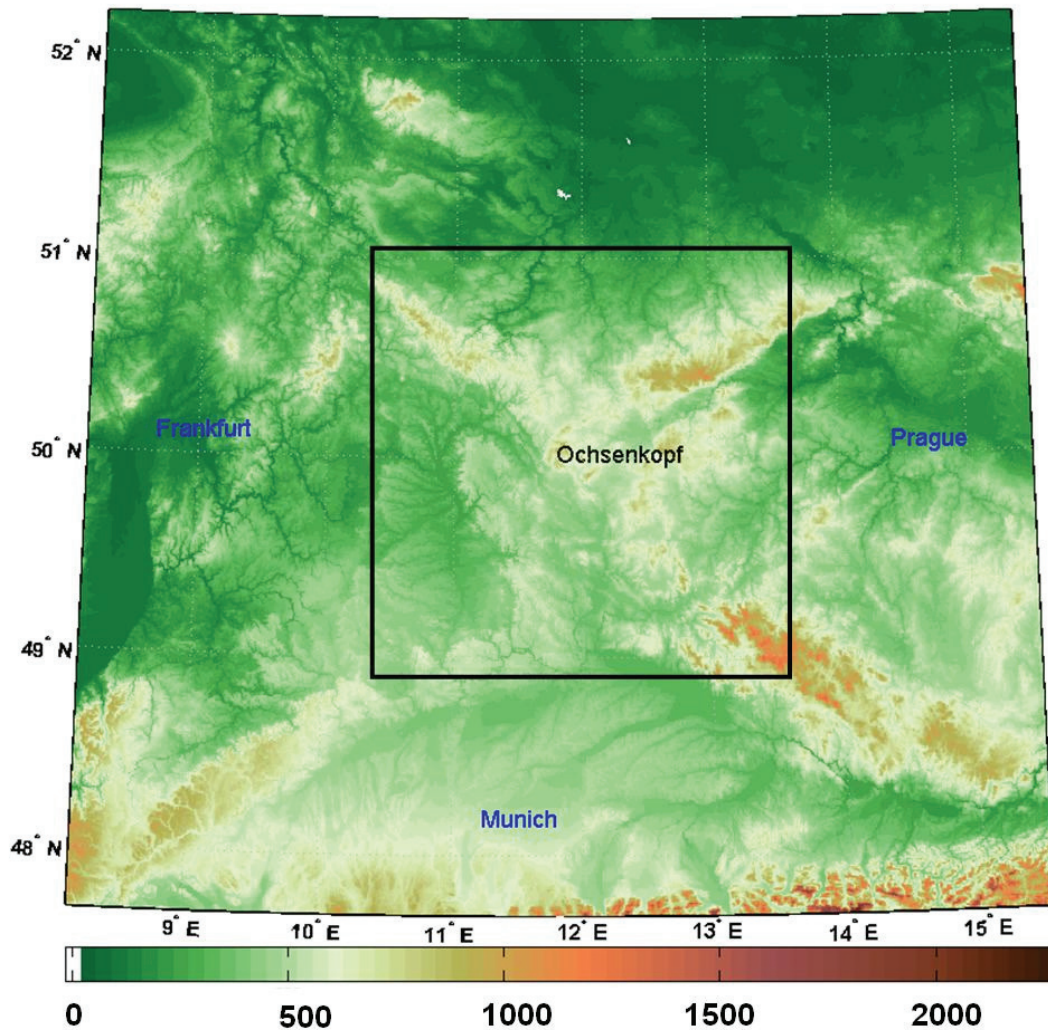
Figure 5.2 *Model Domains showing topography: The rectangle inside the domain indicates the boundaries of nested domain with 2 km × 2 km resolution. The domain outside the nested domain is with 6 km × 6 km resolution. The elevation data is from USGS elevation model-GTOPO30s-with spatial resolution of approximately 1 km.*

October 2008, was chosen due to the availability of vertical profiles of CO_2 concentrations measured during an aircraft campaign with the METAIR-DIMO aircraft (http://www.metair.ch/) over Ochsenkopf. These profiles provide a quality assessment on the performance of the transport models and also assist in finding the potential source of any model mismatch. Corresponding to this, WRF/STILT-VPRM simulations of CO_2 are carried out for different receptor locations around Ochsenkopf for the above mentioned periods. The receptor locations correspond to either different vertical levels of the Ochsenkopf tower or to the flight-track during the airborne measurement campaign at Ochsenkopf.

5.3   Results and Discussions

Figure 5.3 shows the time series of CO_2 concentrations at 90 m above ground at the Ochsenkopf tower site for August 2006 which have been simulated by the WRF/STILT-VPRM and WRF-VPRM modeling systems. Both models produce similar results as demonstrated in Fig. 5.3 with the squared correlation coefficient, R^2= 0.67. A summary of the statistics calculated from the model simulations for different model levels in the boundary layer is given in Table 5.2. As evident from the
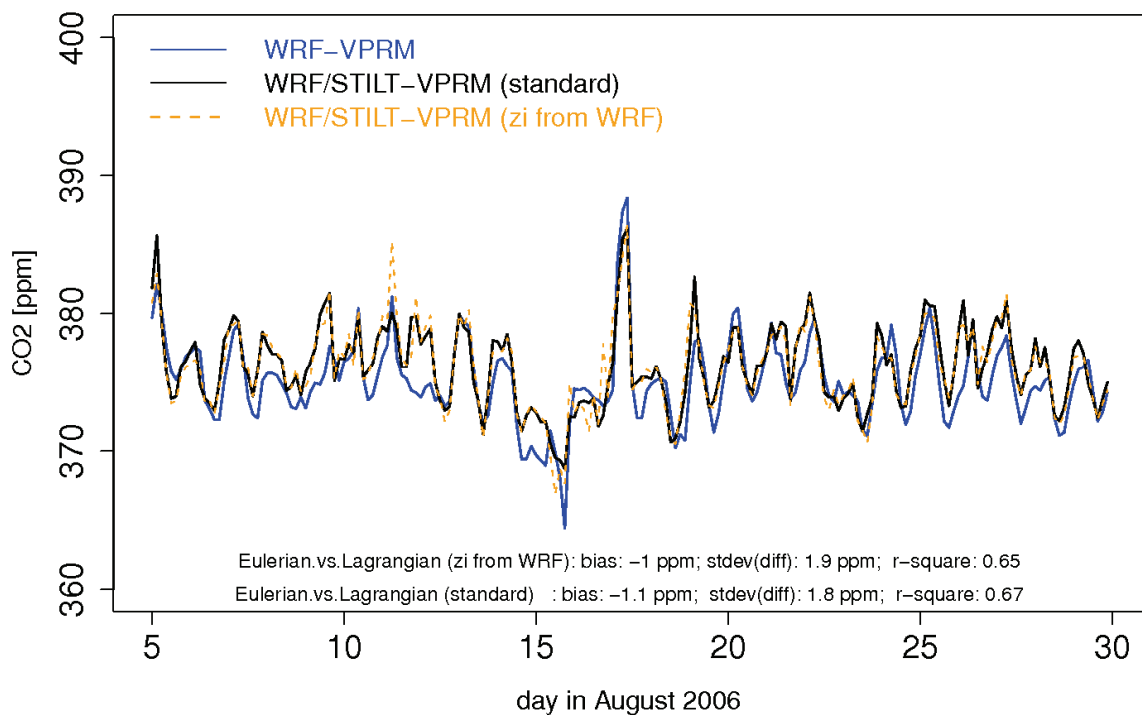
Figure 5.3   Comparison of simulated CO_2 concentrations (3-hourly averages) between WRF-VPRM and WRF/STILT-VPRM at 90 m over the Ochsenkopf tower site for August 2006. The orange dotted line denotes the WRF/STILT-VPRM prediction when prescribing mixing height from WRF.

summary statistics, the models also produced similar results for other model levels in the boundary layer. Inter-model differences, e.g. for the 90 m level with a standard deviation of about 1.8 ppm, are smaller than model-observation differences (see Table 5.2; see Pillai et al.(2010) for observed time-series of CO_2 concentrations). However, the discrepancies between the simulations, albeit smaller than the model-observation differences, prompt further investigation, especially since both models are driven with same meteorological and surface flux fields. Possible factors that can cause these discrepancies are (1) differences in specification of boundary layer

Table 5.2 *Summary statistics of inter-model and data-model comparisons for different model levels (in meters) at Ochsenkopf tall tower observatory for August 2006: Abbreviations: WRF-STILT: WRF-VPRM simulations minus WRF/STILT-VPRM simulations; WRF-STILT.zi_{wrf} : WRF-VPRM simulations minus WRF/STILT-VPRM simulations using mixing height prescribed from WRF; Obs-STILT: Observations minus WRF/STILT-VPRM; Obs-WRF: Observations minus WRF –VPRM. mean: mean of the differences between data and model (data minus model); sd: standard deviations of the differences between data and model (data minus model); R^2: squared correlation coefficient between data and model.*

level (m)		mean [ppm]	sd [ppm]	R^2
23	WRF-STILT	-1.2	2.2	0.63
	WRF-STILT.zi_{wrf}	-1.2	2.1	0.68
	Obs-STILT	-0.8	3.5	0.49
	Obs-WRF	0.5	3.1	0.62
90	WRF-STILT	-1.1	1.8	0.67
	WRF-STILT.zi_{wrf}	-1.0	1.9	0.65
	Obs-STILT	-0.6	3.4	0.51
	Obs-WRF	0.6	3.3	0.55
163	WRF-STILT	-1.0	1.8	0.65
	WRF-STILT.zi_{wrf}	-0.9	1.8	0.65
	Obs-STILT	-0.3	3.0	0.40
	Obs-WRF	0.8	2.9	0.46

parameterizations, (2) potential violation of mass conservation in the driving meteorology due to discrepancies in coordinate transformations during data processing procedures, (3) differences in input flux fields and (4) different realization of advection or convection in the models. Time reversibility of STILT (Gerbig et al., 2003b) and mass conservation in STILT when using WRF wind fields (Nehrkorn et al., 2010) have been confirmed for this setup, ruling out the lack of mass conservation

as a possible reason. The following sections examine which of the remaining factors contribute to the deviation between the models.

5.3.1   Consistency check: Explicit and Implicit model parameters

5.3.1.1 Mixing height Parameterization

A difference in mixing height (z_i) can lead to different vertical distributions of surface flux influences to the atmospheric column and can thus cause differences in mixing ratios as large as 3.5 ppm (Gerbig et al., 2008). Hence it is appropriate to examine the consistency of vertical mixing and associated turbulence parameterized in the models.

WRF derives z_i using a boundary layer parameterization namely the Yonsei University (YSU) scheme (Hong and Dudhia, 2003; Hong et al., 2006) which is based on a bulk Richardson number criterion. WRF/STILT also uses the bulk Richardson number method locally to calculate z_i, utilizing profiles of atmospheric variables (temperature and wind) and their gradients provided by WRF.

The bulk Richardson number Ri_b in both models is calculated as follows:

$$Ri_b = \frac{gz}{\theta_{v,s}} \frac{(\theta_{v,k} - \theta_{v,s})}{(u_k^2 + v_k^2)} \tag{6}$$

where g is the field strength of gravity, z is the height above ground and θ_v is the virtual potential temperature. u and v refer to lateral wind components. The subscripts s and k refer to the lowest and k^{th} model levels. The mixing height is defined as the first level at which Ri_b becomes greater than the critical Richardson number Ri_c (set to be 0.25).

The mixing height derived from WRF and WRF/STILT at the Ochsenkopf tower site for August 2006 is compared and is illustrated in **Fig. 5.4a**. The z_i derived by WRF-VPRM is found to be lower than that of WRF/STILT in certain periods of the nocturnal boundary conditions. Mixing heights from the two models are not in perfect agreement, with a squared correlation coefficient of $R^2 = 0.65$. This discrepancy is due to the mismatches in deriving z_i during cloudy conditions. A closer look at mixing height fields simulated by WRF indicates a strong spatial variability for periods with broken cloud cover (not shown), so that the slight differences in horizontal

interpolation of the meteorological fields result in large differences in diagnosed mixing heights. Indeed, removal of cloudy periods improved the inter-model agreement significantly ($R^2 = 0.91$). However an average z_i discrepancy of about 35 % (when using all data) cannot be neglected from causing corresponding deviations in
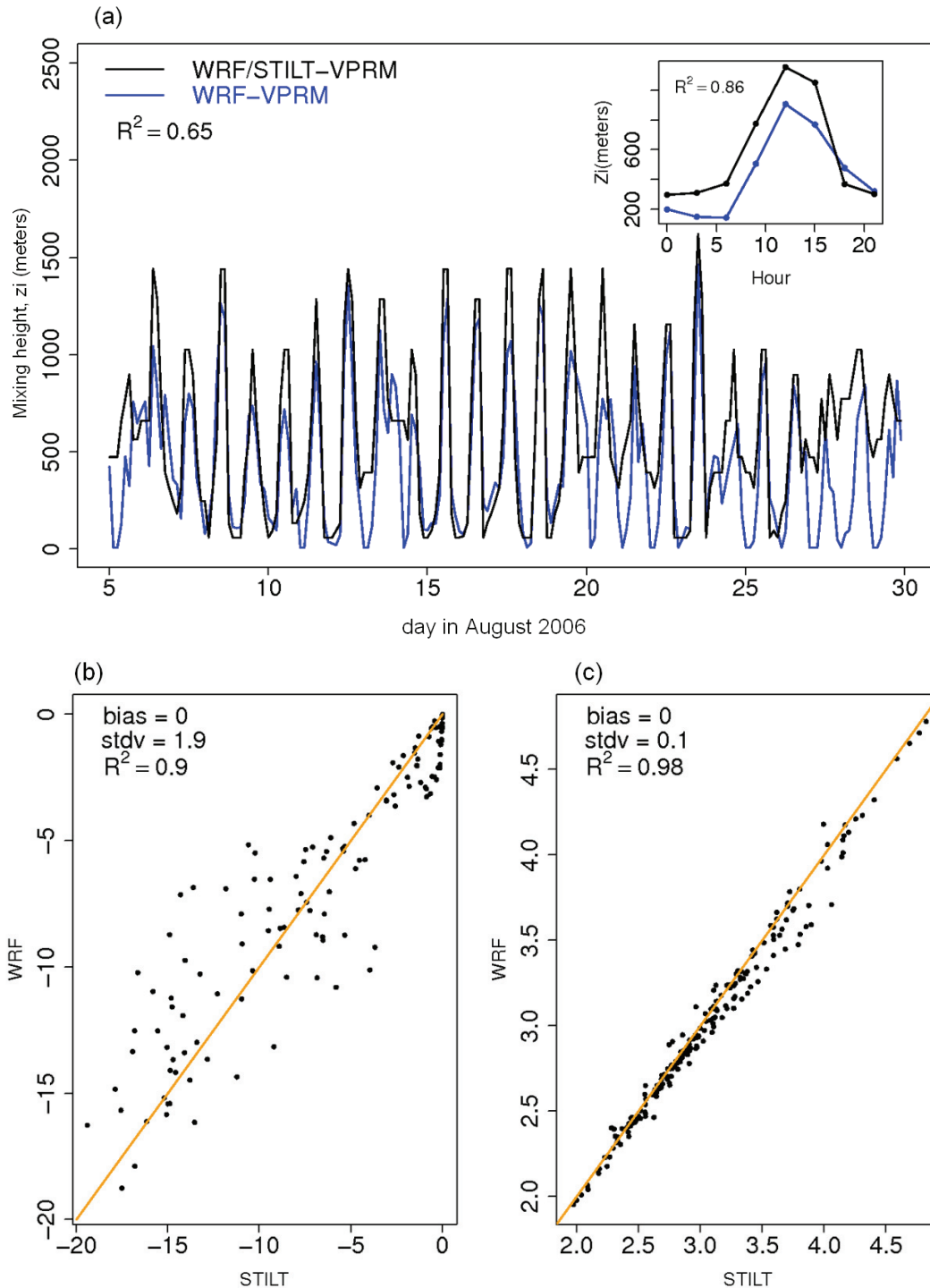
***Figure 5.4*** *Time-series of (a) mixing height (z_i) in meters with inset showing the diurnally averaged z_i simulated by WRF-VPRM and WRF/STILT-VPRM for August 2006. (b & c) Inter-model comparison of Gross Ecosystem Exchange (GEE) and Respiration fluxes (both are in the units of μmole/m^{2}s^{-1}) simulated for the same period. The orange line denotes one-to-one line.*

tracer mixing ratios. The sensitivity of simulated CO_2 concentrations to the inter-model difference in the parameterization of mixing heights is tested by using WRF derived z_i in WRF/STILT and the results are compared with the standard WRF/STILT set-up. Surprisingly, the comparison between standard and modified z_i set-up in WRF/STILT reveals only slight differences (see orange dotted and black lines in Fig. 5.3). The probable reason for the smallness of the difference between these modeled tracer concentrations is the existence of simulated patchy mixing height fields as generated by WRF at a spatial resolution of 2 km × 2 km (not shown). In the case of patchy spatial patterns of z_i , the tracer which was once in the boundary layer at one time step can be in the free troposphere (FT) at the next time step. Hence the mixing height, which usually acts as a barrier for vertical mixing, cannot act as such a barrier for very patchy mixing height fields, when advection over small distances can turn mixed layer air into FT air and vice versa. Differences in profiles of the variance of turbulent vertical velocities between standard and test runs (WRF-derived z_i) in WRF/STILT (not shown) are negligible, which also indicates that the local z_i differences cannot affect the turbulent mixing of tracers. In summary, this confirms that the differences in simulated CO_2 concentrations between WRF and WRF/STILT are not caused by differences in mixing heights. The summary statistics of this test run are also included in Table 5.2.

5.3.1.2 Biospheric Fluxes, VPRM

Discrepancies in the biospheric fluxes between the modeling systems can cause differences in simulated CO_2. The biospheric fluxes (GEE and Respiration) at the receptor location, derived from both modeling systems, are diagnosed for the proper treatment of given meteorological fields (temperature and radiation) and the VPRM input parameters. Fig(s). 5.4b and 5.4c shows the simulated biospheric fluxes at the tower site for the period of August 2006 and suggests that the fluxes are consistent between the modeling systems (GEE: $R^2 = 0.9$, Respiration: $R^2 = 0.98$). A 10 % (2%) deviation in simulated GEE (Respiration) between models is caused by the temporal interpolation of radiation and temperature fields in STILT. The possible differences in CO_2 concentrations caused by the flux discrepancy of about 10 % are estimated to be only 0.1 ppm (bias). This estimation was based on simulations of CO_2 concentrations generated by STILT with 10 % enhancement in GEE. Hence it is

indicated that the model differences cannot be attributed to biospheric flux discrepancies.

5.3.1.3 Advection Scheme: WRF and WRF/STILT

Another factor which can induce inter-model discrepancy is related to the differences in the details of vertical mixing and advection (shear) of both models, as their combination is responsible for horizontal spread in simulated plumes. The analysis of the vertical structure of tracer transport can give more insight. For this purpose the observations of CO_2 vertical profiles obtained during the Ochsenkopf aircraft campaign are utilized, which can provide qualitative assessment on the model simulations. Both models, in general, are able to capture the vertical distribution of CO_2 variability relatively well and showed similar performance (Pillai et al., 2010a). A period on 20th October 2008 is chosen here as an extreme case where WRF-VPRM and WRF/STILT-VPRM showed larger deviations. An elevated concentration of CO_2 was found in the valley south of Ochsenkopf (hereafter referred simply as the valley) during this period at around 10 UTC (i.e. before the full development of the convective mixed layer) (see **Fig. 5.5**). WRF-VPRM predicted a large contribution from fossil fuel fluxes (determined by using tagged tracer $CO_{2.foss}$) and simulated higher CO_2 total concentration in the valley, consistent with observations, while WRF/STILT-VPRM failed to capture this large accumulation of CO_2 in the valley. However, WRF/STILT-VPRM reproduced the CO_2 accumulation when the contribution from advected fossil fuel emissions ($CO_{2.foss}$) is replaced with that given by WRF-VPRM (not shown). This result reveals that the "missing" accumulation of CO_2 in WRF/STILT-VPRM during this particular period is due to the failure in capturing the advection of the fossil fuel contribution in WRF/STILT-VPRM.

It is perhaps a surprising result when considering other periods in which WRF-VPRM and WRF/STILT-VPRM showed similar results on simulating CO_2 concentrations. Hence it is appropriate to investigate further the causes of this large discrepancy in simulating advection of tracers. The following section explores this by conducting different model sensitivity tests in WRF/STILT-VPRM, assuming WRF-VPRM gives fairly good predictions in this specific period based on its more reasonable performance in the above case study.
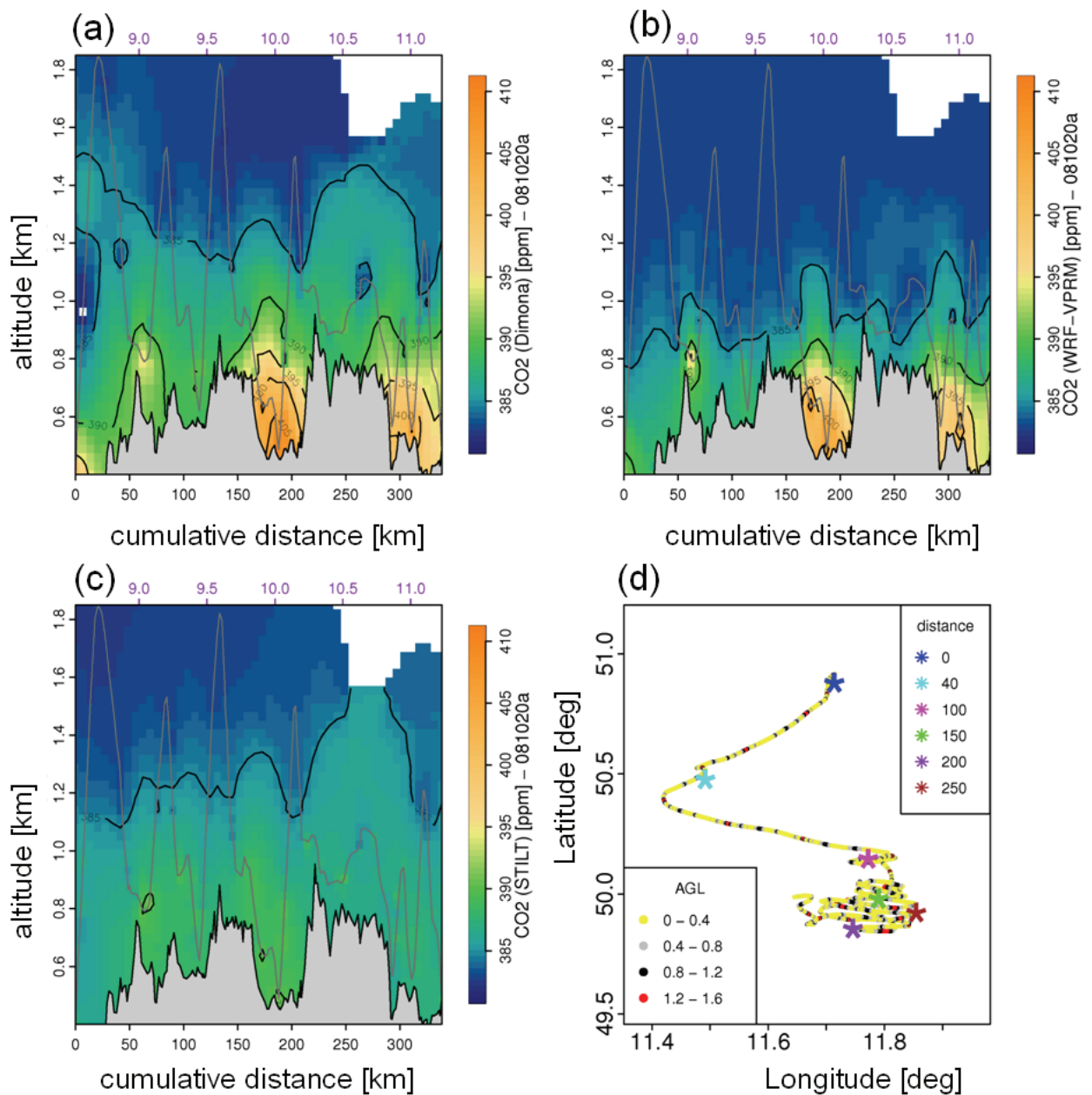
Figure 5.5 *The altitude-distance cross-section showing CO_2 distribution around Ochsenkopf during the DIMO aircraft campaign on 20th October 2008: (a) Observations (b) WRF-VPRM, (c) WRF/STILT-VPRM and (d) aircraft track colored with flight altitude range. In a-c: The time of the flight are given in purple at the top X-axis. In d: the cumulative distance flown by the aircraft are labeled with * symbol.*

5.3.2   Pulse Release Experiment in WRF/STILT and WRF

A more comprehensive comparison of advection of tracers in both models can be studied by following simulated trajectories of a plume emitted at a given location. This can give an immediate and vivid picture on any possible deviation of advection between models. Hence it is attempted to release an emission pulse from a given location where a strong potential influence of surface fluxes (as determined by STILT

footprints for the above mentioned extreme period) and a relatively strong fossil fuel emission source is found, in order to quantify the effect of this emission on downstream CO_2 concentrations as simulated by both models. In this way, one can assess the potential reason for the aforementioned missing contribution from advected fossil fluxes in WRF/STILT-VPRM. The details of this experiment are as follows:

The emission source is defined in such a way that it emits a "pulse" with a total concentration of S_{conc} at a particular time t. To simulate the pulse in STILT, N_{tot} particles were released from the emission point (48.5 ^{o} N, 11.0 ^{o} E, release point 8 m agl) at 4 UTC and transported forward in time. Note that the source location (the above spatial co-ordinate) was defined according to upstream influence locations at 4 UTC on 20 October 2008, predicted using STILT backward trajectories when particles were transported backward from a receptor point (valley) at 10 UTC. The resulting tracer concentration at a specified location downstream $R_{conc.STILT}$ is given by:

$$R_{conc.STILT} = \frac{N_R}{N_{tot}} \times S_{conc} \qquad\qquad (7)$$

where N_R is the particle density at the receptor after taking into account air density differences between source and receptor locations.

The receptor boxes were defined along the WRF/STILT particle trajectory locations at a given time with a horizontal dimension of 6 km × 6 km. The vertical dimension of the receptor boxes was roughly equal to the thickness of each WRF vertical layers and was placed at the respective WRF vertical level. In this way, one can reproduce STILT plume distributions with a grid cell size of 6 km × 6 km and with vertical levels corresponding to WRF.

In WRF the pulse emission was implemented as a tagged tracer flux field with a spatial resolution of 6 km × 6 km (corresponding to the spatial resolution of plume simulations generated by STILT) and with a single non-zero value entry at the prescribed source pixel for time t = 4 UTC. S_{conc} in Eq. 7 was given by the corresponding tagged tracer concentration at the first model level (~8 m above ground) of the source pixel in WRF.

A comparison of the WRF/STILT and the WRF simulated plumes at 10 UTC, when the enhanced CO_2 was measured near Ochsenkopf, is shown in **Fig. 5.6** (a and d) for
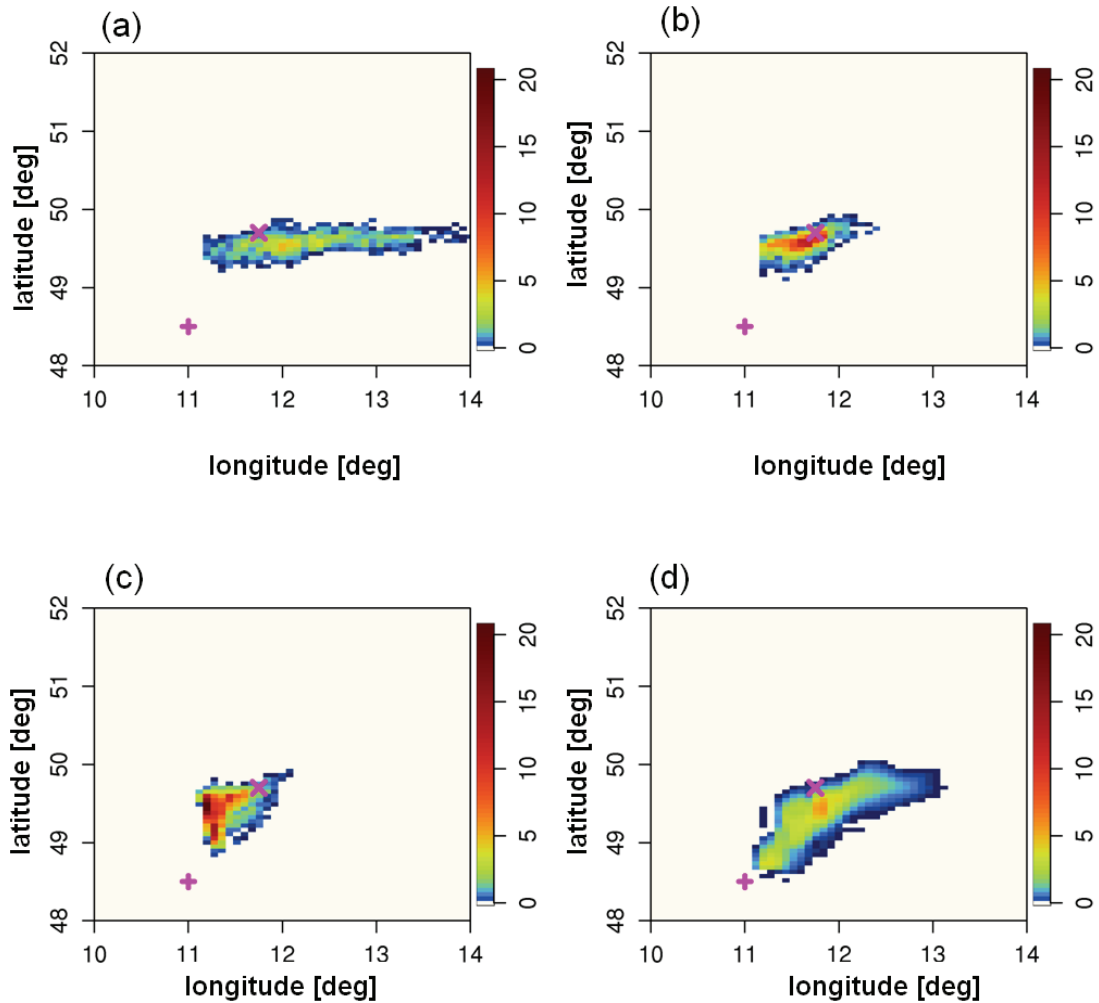
Figure 5.6 *Total contribution of a pseudo-emission source on downstream concentration of different receptors predicted by WRF/STILT (forward) under different model parameter set up and by WRF models. CO_2 concentrations in units of ppm for an atmospheric column from surface to 190 m (pressure weighted) simulated by a) WRF/STILT (control run) b) WRF/STILT with reduced free troposphere turbulence to 1 cms^{-1} c) WRF/STILT with reduced free troposphere turbulence to 1 cms^{-1} and reduced Lagrangian time scale-T_L= 0.1*$T_{L-original}$ and d) WRF are shown. The "+" symbol (in magenta) denotes the source point and the "×" symbol (in magenta) denotes the approximate location of the valley (the aircraft location at 10 UTC) where a large CO_2 concentration was observed (see Fig. 5.5).*

an atmospheric column from surface to ~190 m (pressure-weighted column average of lowest six model levels). The WRF simulated plume reached the aircraft location at 10 UTC with its northern edge, while the STILT simulated plume just misses it.The models show considerable differences in shape and advection of the plume under these nocturnal conditions. A relatively larger horizontal (east-west) spread of plume is simulated in WRF/STILT when compared to that in WRF. Also notably,

STILT transported the plume much faster from the source point, without leaving any presence of plume close to the source location.

The above result provides a clear indication that the interaction of wind shear and turbulent diffusion is simulated differently in WRF and WRF/STILT. Note that the turbulent transport is realized using K-diffusion in WRF, while a stochastic process (Markov chain) is used in WRF/STILT (see Sect(s). 5.2.1 and 5.2.2). In STILT, the spread of the plume is largely controlled by the rate at which the plume is turbulently mixed into the residual layer above the mixed layer, where wind speed and direction are different. In fact, limiting σ_w (i.e. vertical turbulent velocity variance) to 1 cm s^{-1} in STILT reduces the east-west-extent of the plume dramatically. A reason for the unusually large values of σ_w in the FT of up to 100 cm s^{-1} might be the high-resolution meteorological fields (6km horizontal, and 10 vertical levels below 2km) used in STILT to drive the particles, causing much stronger wind shear. This is due to the fact that the parameterization for σ_w in STILT was developed for coarser resolution fields. Similarly, the Lagrangian decorrelation time scale T_L has some control on the residence time at low levels, where winds are slower, after release of the plume. It thus controls how strongly the plume is flushed away by advection. Indeed, reducing T_L by a factor of ten causes the plume intensity close to the source location to increase significantly, and tends to result in a plume distribution that closer matches the one given by WRF. The intensity of FT turbulence determines the dissipation rate and the dilution of plume in the boundary layer. T_L determines the turbulent mixing between different vertical levels, i.e. larger T_L causes the plume to be transported faster from surface by the mean-wind.

The above results of sensitivity tests reveal that one can expect differences in WRF/STILT-VPRM and WRF-VPRM simulations of CO_2, corresponding to different tracer advection although the same meteorological fields, surface fluxes, and vertical mixing are used. The inter-model differences can be particularly high when signatures from strong sources such as fossil fuel emissions are transported from larger distances and dominate over those from local sources (e.g. biospheric fluxes). To achieve a better match between the Lagrangian and Eulerian transport models at high resolution, a refinement of the parameterizations determining the profiles of σ_w and T_L in STILT is required.

5.4   Summary and Conclusions

High-resolution simulations of CO_2 from online Eulerian (WRF-VPRM) and offline Lagrangian (WRF/STILT-VPRM) modeling systems for a domain over Ochsenkopf, Germany are presented and the consistency between Eulerian and Lagrangian transport models in parameterizing turbulent mixing and in transporting CO_2 as a tracer is examined. It should be noted that both models are driven with identical meteorological fields (from WRF) and surface fluxes (from VPRM). This consistency check is carried out as a first step towards applying STILT as an adjoint of WRF in an inverse modeling system. The study is motivated due to the fact that the flux estimates can be biased if different realisation of turbulence, vertical mixing and numerical diffusion exist in WRF and STILT.

Overall, the models show similar performance in predicting CO_2 concentrations at Ochsenkopf with high inter-model correlations. The factors to which remaining discrepancies between the models can be attributed have been investigated further. A set of explicit model parameters including mixing height parameterization and biospheric fluxes are examined to check the models' consistency. The inter-model difference in local z_i is found to have a negligible impact on simulated CO_2 concentrations between models due to the presence of a leaky boundary layer top, as parameterized by the models. The biospheric fluxes computed by the VPRM model are found to be consistent between both modeling systems.

The consistency of advection schemes in WRF and WRF/STILT is further examined by simulating CO_2 concentrations along an aircraft trajectory in the Ochsenkopf aircraft campaign. Both models provided similar results for most of the cases; however a short period is found when WRF and WRF/STILT showed a large deviation in their simulation of the contribution of fossil fuel fluxes at one of the Ochsenkopf valleys. The current sources of the discrepancies during this period are identified by conducting an emission pulse release experiment in WRF and WRF/STILT. A considerable difference was found in both models in simulating the emission plume distribution under normal conditions. Two sensitivity tests were carried out to assess the impacts of 1) reduced vertical velocity variance – σ_w – in the FT (Exp.1) and 2) reduced Lagrangian time-scale – T_L – in the entire column (Exp.2) on the spatial and temporal distribution of the plume. Exp.1 and Exp.2 give

rise to different horizontal and vertical extents of the plume, suggesting that the WRF/STILT predictions are highly sensitive to T_L and free-tropospheric σ_w . These results suggest that a further refinement of σ_w and T_L is required in STILT when driving with high-resolution meteorological fields. However no firm conclusions can be drawn about the relative merits of different advection schemes used in the models. In cases which are strongly influenced by advected fluxes, as in the extreme example discussed above, the footprints derived from WRF/STILT cannot be expected to exactly match the adjoint of WRF. However the similar results provided by WRF and WRF/STILT in most of the cases as well as the fact that, the inter-model differences are a factor of two smaller than the model-data differences and about a factor of three smaller than the mismatch between the current global model simulations and the data, justify using STILT as an adjoint model of WRF.

5.5   References

Ahmadov, R., Gerbig, C., Kretschmer, R., Koerner, S., Neininger, B., Dolman, A. J., and Sarrat, C.: Mesoscale covariance of transport and CO_2 fluxes: Evidence from observations and simulations using the WRF-VPRM coupled atmosphere-biosphere model, J. Geophys. Res.-Atmos., 112, D22107, doi:22110.21029/22007JD008552, 2007.

Ahmadov, R., Gerbig, C., Kretschmer, R., Körner, S., Rödenbeck, C., Bousquet, P., and Ramonet, M.: Comparing high resolution WRF-VPRM simulations and two global CO_2 transport models with coastal tower measurements of CO_2, Biogeosciences, 6, 807-817, 2009.

Errico, R. M.: What is an adjoint model?, Bull.Am.Meteorol. Soc, 78(11), 2577-2591, 1997.

Geels, C., Gloor, M., Ciais, P., Bousquet, P., Peylin, P., Vermeulen, A. T., Dargaville, R., Aalto, T., Brandt, J., Christensen, J. H., Frohn, L. M., Haszpra, L., Karstens, U., Rödenbeck, C., Ramonet, M., Carboni, G., and Santaguida, R.: Comparing atmospheric transport models for future regional inversions over Europe. Part 1: Mapping the atmospheric CO_2 signals, Atmos. Chem. Phys, 7, 3461-3479, 2007.

Gerbig, C., Lin, J. C., Wofsy, S. C., Daube, B. C., Andrews, A. E., Stephens, B. B., Bakwin, P. S., and Grainger, C. A.: Toward constraining regional-scale fluxes of CO_2 with atmospheric observations over a continent: 2. Analysis of COBRA data using a receptor-oriented framework, J. Geophys. Res.-Atmos., 108, 4757, doi:4710.1029/2003JD003770, 2003a.

Gerbig, C., Lin, J. C., Wofsy, S. C., Daube, B. C., Andrews, A. E., Stephens, B. B., Bakwin, P. S., and Grainger, C. A.: Toward constraining regional-scale fluxes of CO_2 with atmospheric observations over a continent: 1. Observed spatial variability from airborne platforms, J. Geophys. Res.-Atmos., 108, 4756, doi:4710.1029/2002JD003018, 2003b.

Gerbig, C., Körner, S., and Lin, J. C.: Vertical mixing in atmospheric tracer transport models: error characterization and propagation, Atmos. Chem. Phys, 8, 591-602, 2008.

Göckede, M., Michalak, A. M., Vickers, D., Turner, D. P., and Law, B. E.: Atmospheric inverse modeling to constrain regional-scale CO_2 budgets at high spatial and temporal resolution, J. Geophys. Res., 115, D15113, doi:10.1029/2009JD012257, 2010.

Gourdji, S. M., Hirsch, A. I., Mueller, K. L., Andrews, A. E., and Michalak, A. M.: Regional-scale geostatistical inverse modeling of North American CO_2 fluxes: a synthetic data study, Atmos. Chem. Phys., 10, 6151-6167, doi:10.5194/acp-10-6151-2010, 2010.

Grell, G. A., S. E. Peckham., R. Schmitz., S. A. McKeen., G. Frost., W. C. Skamarock., and Eder, B.: Fully coupled online chemistry within the WRF model, Atmos. Environ., 39, 6957-6975, 2005.

Heimann, M., and Koerner, S.: The global atmospheric tracer model TM3, Technical Reports, Max-Planck-Institute for Biogeochemie, 5, 131 p., 2003.

Hong, S.-Y., and Dudhia, J.: Testing of a new non-local boundary layer vertical diffusion scheme in numerical weather prediction applications., 20th Conference on Weather Analysis and Forecasting/16th Conference on Numerical Weather Prediction, Seattle, WA., 2003.

Hong, S.-Y., Noh, Y., and Dudhia, J.: A new vertical diffusion package with an explicit treatment of entrainment processes, Monthly Weather Review, 134, 2318-2341, 2006.

Jung, M., Henkel, K., Herold, M., and Churkina, G.: Exploiting synergies of global land cover products for carbon cycle modeling, Remote Sens. Environ., 101, 534-553, 2006.

Lauvaux, T., Uliasz,M., Sarrat,C., Chevallier, F.,Bousquet,P., Lac,C., Davis,K.J., Ciais,P., Denning, A.S.,and Rayner,P.J.: Daily CO_2 flux estimates over Europe from continuous atmospheric measurements: 1, inverse methodology, Atmos. Chem. Phys, 8, 3459-3471, 2008.

Lin, J. C., Gerbig, C., Wofsy, S. C., Andrews, A. E., Daube, B. C., Davis, K. J., and Grainger, C. A.: A near-field tool for simulating the upstream influence of atmospheric observations: The Stochastic Time-Inverted Lagrangian Transport (STILT) model, J. Geophys. Res.-Atmos., 108, 4493, doi:4410.1029/2002JD003161, 2003.

Lin, J. C., Gerbig, C., Wofsy, S. C., Andrews, A. E., Daube, B. C., Grainger, C. A., Stephens, B. B., Bakwin, P. S., and Hollinger, D. Y.: Measuring fluxes of trace gases at regional scales by Lagrangian observations: Application to the CO_2 Budget and Rectification Airborne (COBRA) study, J. Geophys. Res.-Atmos., 109, D15304, doi:15310.11029/12004JD004754, 2004.

Lin, J. C., and Gerbig, C.: Accounting for the effect of transport errors on tracer inversions, Geophys. Res. Lett., 32, L01802, doi:01810.01029/02004GL021127, 2005.

Mahadevan, P., Wofsy, S. C., Matross, D. M., Xiao, X., Dunn, A. L., Lin, J. C., Gerbig, C., Munger, J. W., Chow, V. Y., and Gottlieb, E. W.: A satellite-based biosphere parameterization for net ecosystem CO_2 exchange: Vegetation Photosynthesis and Respiration Model (VPRM), Global Biogeochemical Cycles, 22, GB2005, doi:2010.1029/2006GB002735, 2008.

Miller, S. M., Matross, D. M., Andrews, A. E., Millet, D. B., Longo, M., Gottlieb, E. W., Hirsch, A. I., Gerbig, C., Lin, J. C., Daube, B. C., Hudman, R. C., Dias, P. L. S., Chow, V. Y., and Wofsy, S. C.: Sources of carbon monoxide and formaldehyde in North America determined from high-resolution atmospheric data, Atmos. Chem. Phys, 8, 7673-7696, 2008.

Nehrkorn, T., Eluszkiewicz, J., Wofsy, S. C., Lin, J. C., Gerbig, C., Longo, M., and Freitas, S.: Coupled weather research and forecasting–stochastic time-inverted lagrangian transport (WRF–STILT) model, Meteorol Atmos Phys, 107, 51-64, 2010.

Pérez-Landa, G., Ciais, P., Gangoiti, G., Palau, J. L., Carrara, A., Gioli, B., Miglietta, F., Schumacher, M., Millán, M. M., and Sanz, M. J.: Mesoscale circulations over complex terrain in the Valencia coastal region, Spain - Part 2: Modeling CO_2 transport using idealized surface fluxes, Atmos. Chem. Phys, 7, 1851-1868, 2007.

Pillai, D., Gerbig, C., Ahmadov, R., Rödenbeck, C., Kretschmer, R., Koch, T., Thompson, R., Neininger, B., and Lavrič, J. V.: High-resolution simulations of atmospheric CO_2 over complex terrain- representing the Ochsenkopf mountain tall tower, Atmos. Chem. Phys.(submitted), 2010a.

Pillai, D., Gerbig, C., Marshall, J., Ahmadov, R., Kretschmer, R., Koch, T., and Karstens, U.: High resolution modeling of CO_2 over Europe: implications for representation errors of satellite retrievals, Atmos.Chem.Phys, 10, 83-94, 2010b.

Rödenbeck, C., Houweling, S., Gloor, M., and Heimann, M.: CO_2 flux history 1982-2001 inferred from atmospheric data using a global inversion of atmospheric transport, Atmos. Chem. Phys, 3, 1919-1964, 2003.

Rödenbeck, C.: Estimating CO_2 sources and sinks from atmospheric mixing ratio measurements using a global inversion of atmospheric transport. Technical Report 6, Max-Planck Institut für Biogeochemie, Jena, Germany, 53 pp., 2005.

Sarrat, C., Noilhan, J., Lacarrère, P., Donier, S., Lac, C., Calvet, J. C., Dolman, A. J., Gerbig, C., Neininger, B., Ciais, P., Paris, J. D., Boumard, F., Ramonet, M., and Butet, A.: Atmospheric CO_2 modeling at the regional scale: Application to the

CarboEurope regional experiment, J. Geophys. Res.-Atmos., 112, D12105, doi:12110.11029/12006JD008107, 2007.

Stephens, B. B., Gurney, K. R., Tans, P. P., Sweeney, C., Peters, W., Bruhwiler, L., Ciais, P., Ramonet, M., Bousquet, P., Nakazawa, T., Aoki, S., Machida, T., Inoue, G., Vinnichenko, N., Lloyd, J., Jordan, A., Heimann, M., Shibistova, O., Langenfelds, R. L., Steele, L. P., Francey, R. J., and Denning, A. S.: Weak northern and strong tropical land carbon uptake from vertical profiles of atmospheric CO_2, Science, 316, 1732-1735, 2007.

van der Molen, M. K., and Dolman, A. J.: Regional carbon fluxes and the effect of topography on the variability of atmospheric CO_2, J. Geophys. Res.-Atmos., 112, D01104, doi:01110.01029/02006JD007649, 2007.

6 Scaling Carbon fluxes from point to region using observational constraints from flux and mixing ratio measurements

Abstract

A mesoscale inverse technique, using a coupled biosphere-atmosphere modeling framework, is presented in order to derive the biosphere-atmosphere exchange fluxes with reduced uncertainties. The modeling framework – WRF/STILT-VPRM – consists of a weather forecasting model, a receptor-oriented transport model and a diagnostic biosphere model, which utilizes the high-frequency observational constraints from Ochsenkopf tall tower in Germany together with information provided by eddy covariance flux towers and remote sensing data streams. The fluxes are retrieved over Europe using inverse method and the reduction in uncertainties of these fluxes is assessed. Moreover, these retrieved fluxes (posterior fluxes) are compared with direct observations from independent eddy flux measurements. The inverse analysis shows large uncertainty reduction in posterior fluxes over Europe. The higher dependence of the adjustable scalars of biosphere model on seasonal variability suggests the importance of using long-term measurements in the inversion framework covering all seasons. In addition, the results show the potential of splitting the large domain into parent and nested domains when constraining the regional fluxes. Hence it is emphasized that the current estimates of regional CO_2 budget can be improved with the availability of observational constraints together with reasonable prior information and adequate transport, via mesoscale inverse modeling.

6.1 Introduction

Accurate accounting of source-sink distribution of carbon fluxes is essential in order to predict atmospheric CO_2 within reduced uncertainty limits and to monitor or manage changes in carbon cycle in response to climate anomalies as well as human intervention. Atmospheric inversions utilizing atmospheric signatures of trace gases have demonstrated its ability to determine CO_2 source and sinks at large scale (Gurney et al., 2002; Rödenbeck, 2005; Tans et al., 1990). Furthermore, these top-down (inversion) estimates can be used to validate bottom-up estimates, but also to bridge the spatial gap between these two approaches.

Long-term measurements in the planetary boundary layer over continents, such as those made from tall tower observatories, can provide information on fluxes at regional scales. Utilizing high-frequency measurements can improve the reliability of inversion estimates (Law et al., 2002). However, the above mentioned measurements are often influenced by strong variability of surface fluxes and mesoscale transport phenomena (Gerbig et al., 2003a, 2003b), which can complicate the interpretation of these measurements in inverse framework. In addition, highly variable surface fluxes from areas close to the observatories (near-field fluxes) causes strong variability in observed mixing ratio (Gerbig et al., 2009; Lin et al., 2004a), which calls for improved a-priori fluxes in the near-field together with their uncertainty estimates as well as spatial and temporal error correlations.

The strong variability exhibited in concentration measurements can be better reproduced when increasing the spatial resolution of the atmospheric transport models and using high-resolution fluxes (Ahmadov et al., 2007; Sarrat et al., 2007; van der Molen and Dolman, 2007). Lauvaux et al.(2009) showed significant reduction (30%) in mismatch between the modeled and the observed fluxes when using inversion at high spatial scale. This suggests the potential of atmospheric inversions to improve the flux estimates when transport and prior fluxes are adequately represented.

This study uses an inversion technique by deploying a high-resolution modeling framework to take into account spatial variability of CO_2 at regional scale. The modeling framework consists of high-resolution models: the Weather Research Forecasting (WRF), the Stochastic Time-Inverted Lagrangian Transport model (STILT) and the Vegetation Photosynthesis and Respiration Model (VPRM) to derive biosphere-atmosphere exchange on regional scales from measured CO_2 mixing ratios. Continuous mixing ratio measurements from a tall tower over a mountain region are used to constrain the modeling systems. VPRM uses a set of parameters, for which initial values are pre-optimized using eddy covariance measurements of CO_2 fluxes. The further optimization of these parameters is carried out via the inversion technique to match the atmospheric constraint imposed by concentration measurements from tall tower observatories. The approach is similar to that of the carbon cycle data assimilation system (CCDAS) (Kaminski et al., 2002; Rayner et al., 2005), but with a difference that our system operates at a high spatial resolution (e.g. 2 km × 2 km)

which is of several orders of magnitude higher than that of CCDAS ($8^\circ \times 10^\circ$). This has the potential to provide flux estimates that are consistent with both mixing ratio and eddy flux measurements, taking into account site specific complexities in flux distribution as well as transport.

The outline of the chapter is as follows: Section 6.2 describes the inverse approach and different components of the inverse framework. In Sect(s). 6.3 and 6.4, the main results are presented and discussed. Section 6.5 provides conclusions of this study.

6.2   Inverse Approach

6.2.1   Theory and Techniques

A receptor-oriented inverse modeling framework, as described in Gerbig et al.(2003a) and Lin et al. (2004b), which consists of a Lagrangian Particle Dispersion model – STILT – together with a biospheric flux model is used to infer the source-sink distribution of trace gases from the atmospheric measurements at high spatial and temporal resolution. The tracer concentration $C(x_r, t_r)$ at the receptor location x_r measured at time t_r is computed as the sum of changes in the tracer concentration at the receptor due to surface fluxes F in the domain V between initialization time t_0 and t_r, and the contribution from the advected tracers from the initial tracer field $C(x, t_0)$. That is, $C(x_r, t_r)$ is expressed as:

$$C(x_r, t_r) = \mathbf{f} \cdot F + \mathbf{I} \cdot C(x, t_0) \tag{1}$$

Here $\mathbf{f}$ denotes footprint elements which links the receptor concentrations to the surface fluxes F, and $\mathbf{I}$ represents the influence function that relates the initial concentration field $C(x, t_0)$ to the receptor concentrations. See Sect. 6.2.2.2 for details about the model domain. The flux estimates (F) are modeled by the surface flux model $F_m(p)$ in which p represents the model parameters. The linearized subset of these parameters, termed as scaling factors (λ), are optimized (using least-square fits) against eddy covariance measurements.

The inversion uses the observation constraint to adjust the n elements of the λ in order to obtain the modeled tracer concentrations to be consistent with the observed values. The state vector λ corresponds to the scaling factors of photosynthesis and

respiration fluxes from five different vegetation types and two different regions. In two regions, one corresponds to the near-field of the observatory and the other corresponds to the rest of the model domain (see Sect. 6.2.3.1).

Eq.1 can be re-arranged as:

$$C(x_r, t_r) - \underbrace{C_{bg}}_{(\mathbf{I} \cdot C(x,t0))} = \mathbf{f} \cdot F_m(\lambda) + \varepsilon_{error} \tag{2}$$

$F_m(\lambda)$ is assumed to be linear dependent on λ and can thus be expressed as:

$$F_m(\lambda) = \mathbf{\Phi}\lambda \tag{3}$$

Combining Eq. 2 and 3 gives rise to a linear model of the form:

$$y = \mathbf{K}\lambda + \varepsilon_{error} \tag{3a}$$

where $y(= C(x_r, t_r) - C_{bg})$ denotes the measurement vector and $\mathbf{K}(= \mathbf{f}\mathbf{\Phi})$ is the Jacobian matrix which gives the sensitivity of the observations to the scalable parameters.

The Bayesian inversion incorporates the measured data and a priori information – λ_{prior} – together with their uncertainties. The noise $- \varepsilon_{error} -$ is assumed to follow the Gaussian distribution described by the error covariance matrices of the measurement and prior estimates- $\mathbf{S}_e$ and $\mathbf{S}_{prior}$. The posterior estimates of λ are obtained by minimizing cost function J:

$$J(\lambda) = (y - \mathbf{K}\lambda)^T \mathbf{S}_e^{-1} (y - \mathbf{K}\lambda) + (\lambda - \lambda_{prior})^T \mathbf{S}_{prior}^{-1} (\lambda - \lambda_{prior}) \tag{4}$$

The state vector of the scaling parameters, at which the cost function is minimized, is given by Rodger (2000):

$$\hat{\lambda} = (\mathbf{K}^T \mathbf{S}_e \mathbf{K} + \mathbf{S}_{prior}^{-1})^{-1} (\mathbf{K}^T \mathbf{S}_e y + \mathbf{S}_{prior}^{-1} \lambda_{prior}) \tag{5}$$

and the error covariance matrix of $\hat{\lambda}$, i.e. the posterior uncertainty, is given by:

$$\hat{\mathbf{S}}_\lambda = (\mathbf{K}^T \mathbf{S}_e^{-1} \mathbf{K} + \mathbf{S}_{prior}^{-1})^{-1} \tag{6}$$

6.2.2   Inverse System

6.2.2.1 Observations

The inverse system uses continuous measurements of atmospheric CO_2 concentration obtained from one of the observatories in the CHIOTTO (Continuous High-precision Tall Tower Observations of greenhouse gases) network – the Ochsenkopf tall tower (OXK) in Germany. The tower is instrumented and operated by the Max Planck Institute of Biogeochemistry in Germany, and provides continuous measurement of CO_2 and other trace gases since 2006 (Thompson et al., 2009). The 163 m high Ochsenkopf tall tower is located on the mountain top, i.e. at the second highest peak (1022 m above sea level) of the Fichtelgebirge mountain range in Germany. The major vegetation cover surrounded by the site is coniferous forest. The site was selected because of its large-scale representativeness owing to its relatively high altitude and the less influence by the urban areas.

The air is sampled at three levels (23, 90 and 163m) on the tower in a 3-hour cycle (i.e. measurement at one level for 1 hour duration) and is analyzed for CO_2 by LiCor gas analyzer – LI-6262 – with a precision of ± 0.02 ppm. For this study, CO_2 measurements from all levels on the tower during different seasons: May (spring), August (summer), October (autumn) for the year 2006 and March (winter) 2008 are used. The measurements are aggregated to 3-hourly averages after applying data quality filters as given by Thompson et al.(2009). The CO_2 concentration measurement at OXK shows diurnal and seasonal variations, corresponding to the changes in surface fluxes and mesoscale transports (Pillai et al., 2010; Thompson et al., 2009), and hence has the potential to provide information on surface fluxes.

6.2.2.2 Atmospheric Transport

The Lagrangian transport model STILT is used to derive the sensitivity of the mixing ratio measurements to the changes in the surface fluxes (footprints) and thus to provide the information on **f** and **I** in the Eq. 1. The STILT, an offline transport model which requires wind fields from other sources, is driven here by three dimensional transport fields provided by either WRF or ECMWF (European Centre for Medium-Range Weather Forecasts).

The WRF domain is set up for a region centered over OXK with an area of approximately 500 km × 500 km. Two-way interactive nesting is used in WRF with a horizontal resolution of 6 km (parent) and 2 km (nest) as well as 41 vertical levels (lowest layer at about 18 m). The initial and lateral boundary conditions for the meteorology were prescribed from the ECMWF analyzed fields available at temporal and horizontal resolution of 6 hours and 25 km respectively. WRF produces hourly output for each day (hour 0 to 23) with a simulation starting at 18 UTC of the previous day, of which the first 6 hours are used for spin up. The WRF meteorology fields are evaluated with different measurement levels of OXK, aircraft measurements, surface stations and wind profilers (Pillai et al., 2010). The physics and the dynamics schemes used in the WRF set-up are given in Table 6.1.

Table 6.1 *Physics and dynamics schemes used in WRF set-up.*

Vertical coordinates	Terrain-following hydrostatic pressure vertical coordinate	
Time step	36 sec	
Physics schemes	*Physics Schemes*	*Option*
	Radiation	RRTM (Rapid Radiative Transfer Model) scheme (longwave radiation) (Mlawer, 1997) Dudhia scheme (shortwave radiation) (Dudia, 1989)
	Microphysics	WRF Single Moment (WSM) 3-class simple ice scheme (Hong, 2004)
	Cumulus	Kain-Fritsch (new Eta) scheme (Kain, 1993)
	Boundary layer	Yonsei University (YSU) scheme (Hong, 2003; Hong, 2006)
	Surface layer	Monin-Obukhov scheme (Monin and Obukhov, 1954)
	Land-surface	Noah land surface model (Chen and Dudhia, 2001)

The STILT is set up with a domain covering most of Europe and is nested with the WRF domains (outer and inner domains). A number of particles (e.g. 100) were released from the receptor point (i.e. OXK) and were transported backward in time for maximum of 15 days or until particles leave the entire domain. The particles were driven with WRF meteorological fields at respective horizontal resolutions (2 and 6 km) until particles leave the WRF domains and later on with ECMWF meteorological fields for the rest of the domain. The STILT backward simulations directly provide surface influence functions (or footprints, $\mathbf{f}$) at high temporal and spatial resolutions by interpolating the assimilated wind fields down to the measurement location. These functions represent the sensitivity of the mixing ratio measurements to the surface fluxes or to the initial and lateral boundary fields, and thus ideally equivalent to the adjoint of the transport equation. Note that the results from chapter 5 (Pillai et al., 2010) indicates that the STILT footprints are similar, but not identical, to the adjoint of the driven transport fields.

The STILT footprints are computed at high resolution at the close proximity of the tower location (near-field). The horizontal resolution of the grid cells in the footprint area was dynamically adjusted with the increasing distance from the tower in order to refrain from under-sampling of the surface fluxes when the statistical probability of finding a particle in particular grid box becomes smaller, and, as a side effect, to save the computation time (Gerbig et al., 2003a). The footprints are mapped to the surface fluxes which comprise of biospheric and anthropogenic (emission) fluxes (see Sect(s). 6.2.2.3 and 6.2.2.4) to derive the time series of biospheric (CO_{2veg}) and fossil (CO_{2foss}) signals at the measurement location. The advected background signals (CO_{2bg}) are obtained by mapping the influence elements derived from STILT to the initial CO_2 values at the boundary provided by the global model (see Sect. 6.2.2.5). The sum of all these CO_2 signals gives rise to the total distribution of CO_2 at the receptor location as given in Eq.1. A measurement-based ("measured") CO_2 biospheric signal ($CO_{2veg \cdot obs}$) that is isolated from the total CO_2 mixing ratio measurements (CO_{2obs}) can be defined as follows (see also Gerbig et al., 2003a):

$$CO_{2veg \cdot obs} = CO_{2obs} - (CO_{2foss} + CO_{2bg}) \qquad (7)$$

For this study, pressure-weighted column averages of CO_2 up to 163 m above ground are used (see Sect. 6.2.2.1). Using column averages reduces the problems in terms of resolving vertical structure of CO_2 in the model.

6.2.2.3 Fossil fuel emission fluxes

High-resolution fossil fuel emission data provided by Institut für Energiewirtschaft und Rationelle Energieanwendung (IER), University of Stuttgart (http://carboeurope.ier.uni-stuttgart.de/) is used to account for anthropogenic CO_2 emission. The emission inventory contains hourly emissions of greenhouse gases for the year 2000 at a spatial resolution of 10 km. In order to adapt these data for the simulation year, a day-of-week shift is introduced to preserve the temporal emission patterns (week vs. weekends), assuming no changes in the emission fluxes between years 2000 and 2006. The fluxes are interpolated to 2 km spatial resolution for the nested domains in STILT (i.e. WRF domains) and 10 km fluxes are used for the rest of the domain.

6.2.2.4 Biospheric (a priori) fluxes

The prior biospheric fluxes are provided by a diagnostic biosphere model, the VPRM (Mahadevan et al., 2008), which uses remote sensing, eddy covariance tower and meteorological data at high temporal and spatial resolutions. The model utilizes the remotely sensed data from MODIS satellite (http://modis.gsfc.nasa.gov/) and simulated or site meteorology to represent vegetation properties and ecosystem functional responses. The 8-day averaged satellite indices – the Enhanced Vegetation Index (EVI) and the Land Surface Water Index ($LSWI$) after applying loess (locally weighted polynomial regression) filtering – are used to provide the information on water stress and leaf phenology. VPRM simulates hourly Net Ecosystem Exchange (NEE) between the biosphere and the atmosphere as the sum of Gross Ecosystem Exchange (GEE) and ecosystem Respiration (R_{eco}):

$$NEE = \underbrace{-\gamma \times T_{scale} \times P_{scale} \times W_{scale} \times (1/[1+(PAR/PAR_0)]) \times EVI \times PAR}_{GEE} + \underbrace{(\alpha \times T) + \beta}_{R_{eco}} \quad (8)$$

where γ, PAR_0, α and β are the VPRM parameters, PAR is the photosynthetically active radiation and T denotes the surface temperature. T_{scale}, P_{scale} and W_{scale} are

scalars for temperature, phenology and water stress (see Mahadevan et al., (2008) for more details).

The VPRM parameters for different vegetation types are initially determined by fitting Eq. 8 to the eddy covariance data. The simulated shortwave radiation (SWDOWN) and the surface temperature (T_2) provided by either WRF or ECMWF are used to represent *PAR* and *T* respectively in Eq. 8. The 1-km global land cover product SYNMAP (Jung et al., 2006) provides the information on vegetation cover in the domain. To obtain a priori estimates of biospheric fluxes, the VPRM parameters are optimized against eddy flux observations, measured during the CarboEurope IP experiment, from various sites under different vegetation types within Europe. For the optimization, it is restricted to using the data from the flux sites outside the nested domain ("calibration sites"). The flux sites within the nested domain ("validation sites") are further used to evaluate the VPRM predictions before and after inversions (i.e prior vs. posterior). See **Fig. 6.1** for nested part and rest of the domain.

6.2.2.5 Initial and lateral boundary conditions

The contribution to the observed CO_2 mixing ratios by the initial concentrations at the boundary can be realized by prescribing CO_2 fields from a global model. The analyzed CO_2 concentration fields given by the Tracer transport model, TM3 (Heimann and Koerner, 2003) are used as the initial and lateral CO_2 tracer boundary conditions. The global tracer concentrations used for this study are at $4° \times 5°$ horizontal resolution, 19 vertical levels and 3-hourly temporal resolution (http://www.bgc-jena.mpg.de/~christian.roedenbeck/download-CO2-3D) and are generated by a forward transport simulation of fluxes that have been optimized using a global network of CO_2 observing stations (Rödenbeck, 2005).

6.2.3   Set-up of inversion

6.2.3.1 Definition of the State Vector and Jacobian matrix

The state vector and the Jacobian matrix are defined as followed by Gerbig et al.(2006) but with a difference that these are retrieved for the VPRM instead of a simple Light Use Efficiency (LUE) model as used in Gerbig et al.(2006). The state vector λ (quantities to be retrieved) is represented by a set of scaling factors which are used to scale up and adjust biospheric fluxes. These scaling factors are defined for

two processes: *GEE* (or Photosynthesis- light dependent term) and R_{eco} (light independent term) and are specific for each vegetation classes. A total of five vegetation classes are used for this study: evergreen forest, deciduous forest, mixed forest, crop and grass. The scaling factors are also specific for the nested region and the rest of the domain (see Fig. 6.1); hence the total length of the state vector is 20 ($2\times5\times2$). The prior values for all scaling factors (λ_{prior}), corresponding to the VPRM fluxes optimized with eddy flux stations, are set to one.

The Jacobian matrix **K** relates the measurement vector y to the state vector λ and has elements that represents the response in mixing ratios to the fluxes (*GEE* and R_{eco}) for different vegetation classes- specific for the nest and the rest of the domain. The total size of **K** is thus $n\times20$ in which n is the length of the measurement vector. The posterior estimates of the scaling factors (λ_{post}) are derived by minimizing the cost function, *J,* as given in Eq.4.
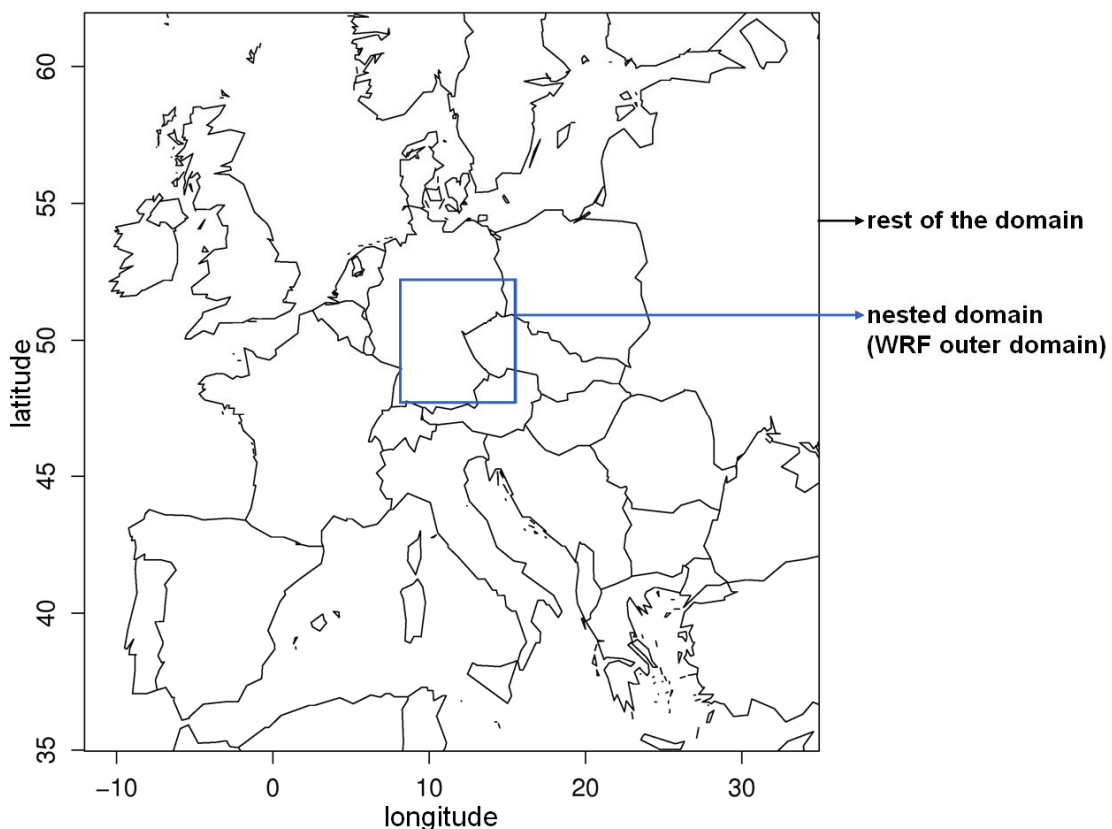

Figure 6.1 *Model domain showing nested and rest of the domain. The WRF outer domain is used as the nested domain in the STILT.*

6.2.3.2 Error Covariance Matrices

The diagonal elements of the prior error covariance matrix $\mathbf{S}_{prior}$ are estimated to 50% for *GEE* and 100% for R_{eco}, roughly corresponding to the day-time and the night-time residuals between the eddy flux observations from the CarboEurope flux sites and the modeled prior fluxes.

The error covariance matrix $\mathbf{S}_e$, accounting for the model-data mismatch, combines the error covariance in the "measured" vegetation signal ($CO_{2veg\text{-}obs}$, using Eq.6.) – $\mathbf{S}_{veg}$ and in the modeled transport – $\mathbf{S}_{trans}$. A measurement uncertainty of 2 ppm is assumed which also includes "representation error" that can be introduced due to insufficient grid resolution to resolve the changes in surface fluxes. Any cross-correlations in the measurement uncertainties are neglected and hence a diagonal matrix with diagonal elements of 2 ppm is used to represent $\mathbf{S}_{veg}$. The $\mathbf{S}_{trans}$ describing uncertainties in mixing heights as well as transport fields, is set to 30 % of the vegetation signal with a minimum value of 0.3 ppm during day-time and to 100 % of the nocturnal enhancement of the signal, with a minimum value of 1 ppm during night-time. A temporal correlation for this transport error is set to 12 hours, in accordance with the typical model-data mismatches for vertical mixing of tracers (Gerbig et al., 2008). The uncertainty introduced when excluding ocean fluxes is assumed to be negligible due to relatively small coverage of the ocean in the domain. Note that CO_2 fields from the TM3 are used at the boundary which includes oceanic exchange fluxes from Takahashi et al.(2002).

6.3   Results

6.3.1   Optimization of VPRM parameters against eddy flux measurements

The VPRM parameters (γ, α and β) are initially optimized for each vegetation classes using half hourly averaged eddy flux measurements ("prior optimization") from 13 calibration sites in Europe for the whole year 2006. These sites represent different vegetation classes in VPRM. The parameters are optimized using a non-linear least square method as followed by Mahadevan et al.(2008). The fluxes are estimated using air temperature and *PAR* measured at respective tower sites. **Figure 6.2** shows daily averages of flux observations (*NEE*) from certain calibration sites

together with flux estimates using the VPRM parameters before and after prior optimization. On adjusting the parameters, VPRM could reproduce the spatial and temporal patterns of the observed *NEE* with remarkable fidelity. These optimized

Table 6.2 *Overview of the VPRM parameters used for estimating prior fluxes.*

| VPRM class	γ	α	β	PAR_0
Evergreen	0.282	0.112	1.841	0.13
Deciduous	0.152	0.137	0.418	0.09
Mixed forest	0.361	0.240	-0.084	0.13
Cropland	0.085	0.159	-0.420	0.081
Grassland	0.175	0.133	0.294	0.070
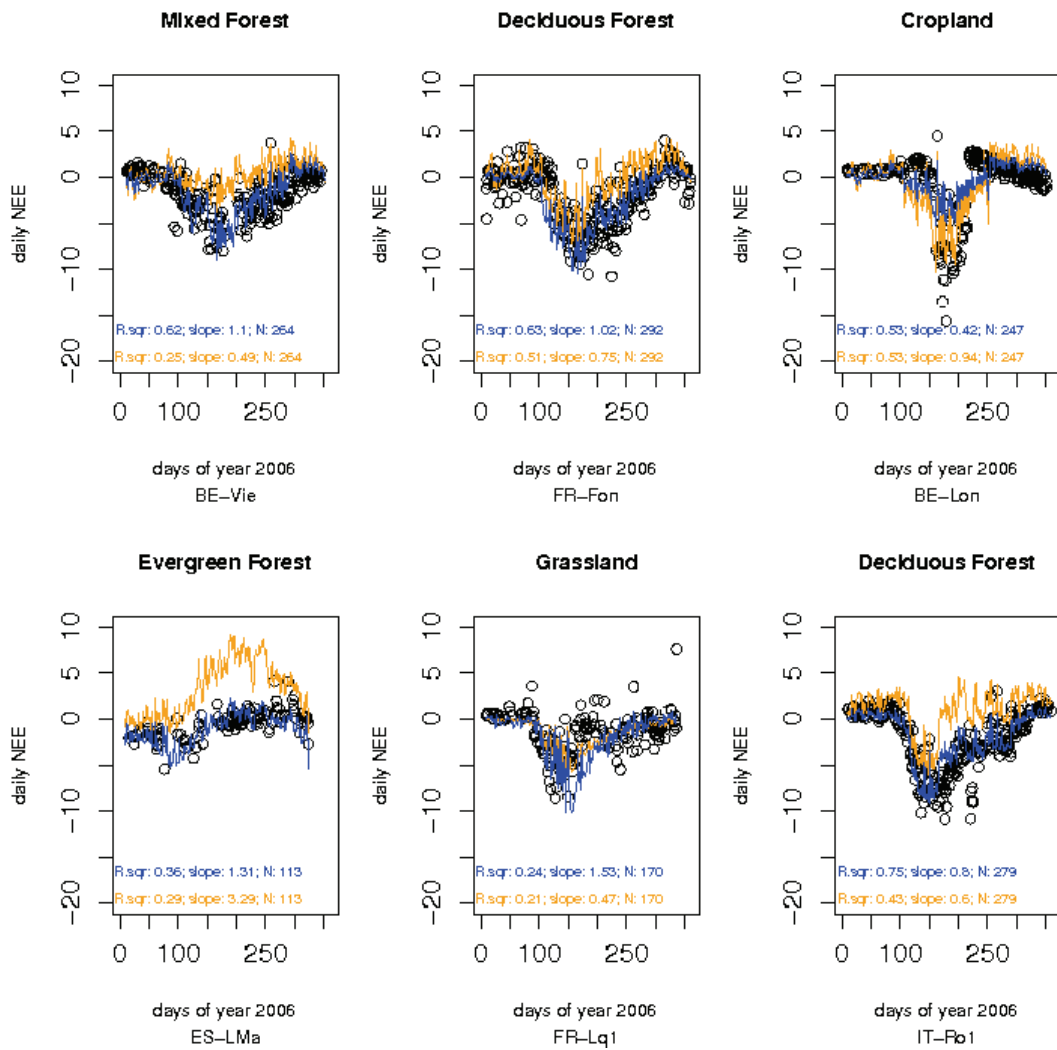
Figure 6.2 *Comparison between daily averaged flux observations (NEE) for typical stations over Europe and those generated by the VPRM model (before and after prior optimization). The black circles represent observation; orange and blue lines denote VPRM simulated fluxes before and after optimization with flux data respectively.*

140

Table 6.3 *Overview of the flux stations that are used as calibration and validation sites. The sites given in the italics are located inside the nested domain and are not used for the prior optimization of the VPRM scalars.*

Sites	*Abbrevation*	*Lat/Lon*	*VPRM class*
Lonzee	BE-Lon	50.55 N/4.75 E	Crop
Vielsalm	BE-Vie	50.30 N/6.00 E	Mixed forest
Gebesee	*DE-Geb*	*51.10 N/10.91 E*	*Crop*
Grillenburg	*DE-Gri*	*50.95 N/13.51 E*	*Grassland*
Hainich	*DE-Hai*	*51.08 N/10.45 E*	*Deciduous*
Klingenberg	*DE-Kli*	*50.89 N/13.52 E*	*Crop*
Tharandt	*DE-Tha*	*50.96 N/13.56 E*	*Evergreen*
Wetzstein	*DE-Wet*	*50.45 N/11.46 E*	*Evergreen*
Rimi	DK-Lva	55.69 N/12.12 E	Grassland
Las Majadas del Tietar	ES-LMa	39.94 N/5.77 W	Evergreen
Kaamanen	FI-Kaa	69.14 N/27.29 E	Others
Fontainbleu	FR-Fon	48.48 N/2.78 E	Deciduous
Le Bray	FR-LBr	44.72 N/0.77 W	Evergreen
Laqueuille intensive	FR-Lq1	45.64 N/2.74 E	Grassland
Laqueuille extensive	FR-Lq2	45.64 N/2.74 E	Grassland
Puechabon	FR-Pue	43.74 N/3.58 E	Evergreen
Carlow crop	IE-Ca1	52.86 N/6.92 E	Crop
Collelongo	IT-Col	41.85 N/13.59 E	Deciduous
Roccarespampani1	IT-Ro1	42.41 N/11.93 E	Deciduous
Loobos	NL-Loo	52.17 N/5.74 E	Evergreen
Griffin	UK-Gri	56.62 N/3.8 W	Evergreen

parameters (see Table 6.2) can be hence used to compute the prior fluxes for the model domain which will be discussed in the following section. A list of calibration and validation sites is given in Table 6.3.

6.3.2   STILT footprints

The footprints are derived from particle trajectories for 15 days backward in time in which particles were released from OXK tower location. The footprint analysis shows the areas that have major influence on the tower measurements. **Figure 6.3** shows

time-integrated footprints for tower observations at 23 m level, averaged during the period from 6 to 30 August 2006. Noticeably, the footprints extend to a large area, covering most of Europe, with spatial patterns corresponding to the different synoptic situations. The surface fluxes at the regions with higher values of footprints (given in units of $\mathrm{ppm}/(\mu\mathrm{mole/m^2s^{-1}})$) have greater influence on measured concentration at the tower. The analysis shows higher influence of near-field surface fluxes on tower measurements compared to far-field surface influence, which is as expected. As the footprints drop off sharply with distance (as seen in Fig. 6.3), the CO_2 fluxes at the near-field will be weighted strongly in resulting changes in total CO_2 signal. The footprints weighted by the VPRM fluxes (given in ppm, shown at inset in Fig. 6.3) displays sensitivities of biospheric fluxes ranging from -10 to +1 ppm at OXK near-field.
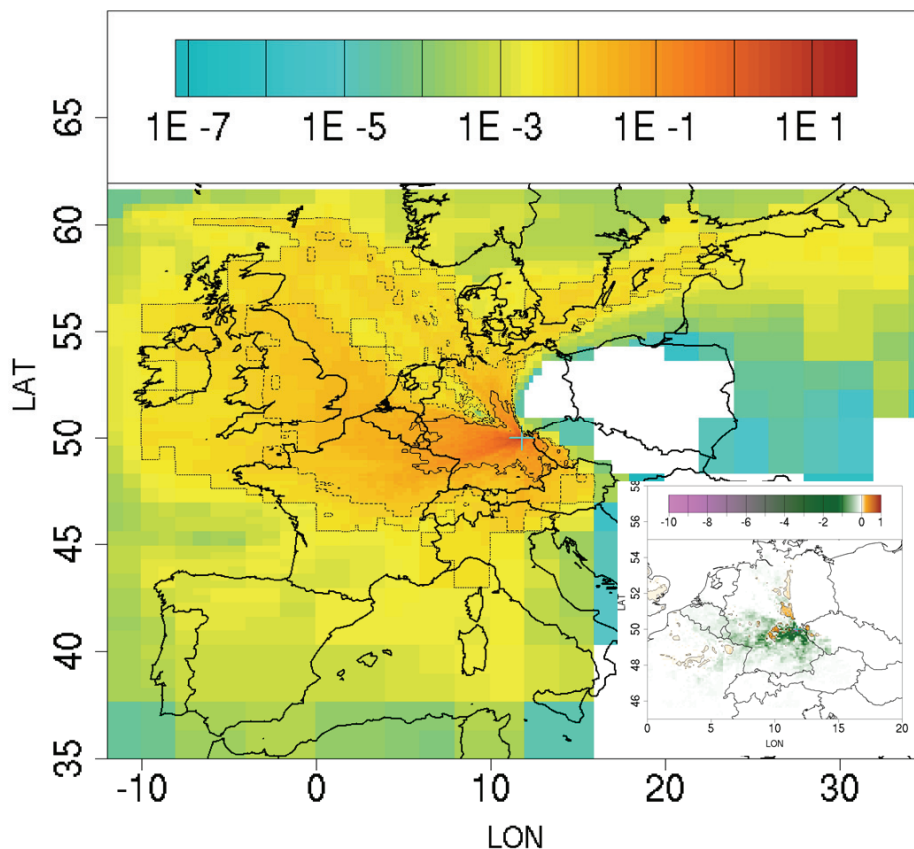

Figure 6.3 *Time-integrated footprints for tracer observations at the tower at an altitude of 23m above ground that are averaged during the period from 6 to 30 August 2006. Color scale is in units of* $\mathrm{ppm}/(\mu\mathrm{mole/m^2s^{-1}})$, *and contour lines indicate areas contributing to 50, 90 and 99 % of the influence to measurements made at the Ochsenkopf. The inset shows those footprints weighted by VPRM prior fluxes.*

142

6.3.3   Prior and Posterior Biospheric signal

The (observation based) biospheric CO_2 signal ($CO_{2veg \cdot obs}$) is derived using Eq. 7 in which the contributions from fossil and background signals are simulated using STILT-VPRM.   The model simulates biospheric signals using the prior optimized VPRM model parameters. The posterior biospheric signals are derived using adjusted scaling parameters (λ_{post}, see Sect. 6.3.4) that minimize the model-data mismatch. The pressure weighted column averages of CO_{2veg} comprising measurements from all levels are used for analysis (see Sect. 6.2.2.2).   A comparison of column averages of the observed and the modeled biospheric signals at OXK for a period from 6 to 30 August 2006 is shown, as an example, in **Fig. 6.4**. The given time period is chosen due to its enhanced biospheric activity and the existence of strong diurnal patterns in transport and fluxes. $CO_{2veg \cdot obs}$ at OXK shows strong diurnal, seasonal and synoptic variations, reflecting the strong variability of surface fluxes and mesoscale transport. The model simulates diurnal variations reasonably well (see inset in Fig. 6.4), by adequately representing the changes in environment drivers (such as temperature and solar radiation), changes in influence locations and changes in biospheric fluxes (sign shifts during day and night times). The model also reproduces synoptic variabilities with remarkable fidelity. For example a large positive (respiration) signal during a cold front passage over OXK on 18th August 2006 was captured in STILT-VPRM, although with a considerable bias of ~7 ppm. The comparison of the observed and the modeled CO_{2veg} for different seasons indicates its ability to predict seasonal variabilities observed at the tower (not shown).

The prior and posterior signals are of comparable quality as seen in Fig. 6.4 and also as indicated in summary statistics with similar correlations and standard deviations between observations and simulations. It should be noted that these differences, although in small magnitudes, are caused by changes in surface flux fields (prior vs. posterior) that are associated with significant differences in the regional flux budgets.

6.3.4   Scaling Parameters and Uncertainty Reduction

To provide some flexibility to adjust the parameters spatially, the inverse optimization of VPRM scalars is carried out by using fluxes at spatial resolution of 2 and 10 km for the nested part and the rest of the domain, respectively. Hence λ_{post} for different vegetation types are specific for these two domains as mentioned in Sect.

6.2.3.1. Note that λ_{prior} for all vegetation types is set to 1 with 50% uncertainty for *GEE* and 100% for R $_{eco}$. The scalars are adjusted differently for two domains (e.g. see Fig. 6.7; more discussion in section 6.4.1). The λ_{post} which are greater (less) than unity indicates the underestimation (overestimation) of the prior fluxes compared to the posterior estimations. When λ_{post} is close to unity, it indicates that the prior flux estimates agree well with the posterior fluxes.

**Biospheric Signals at Ochsenkopf, before and after inversion**
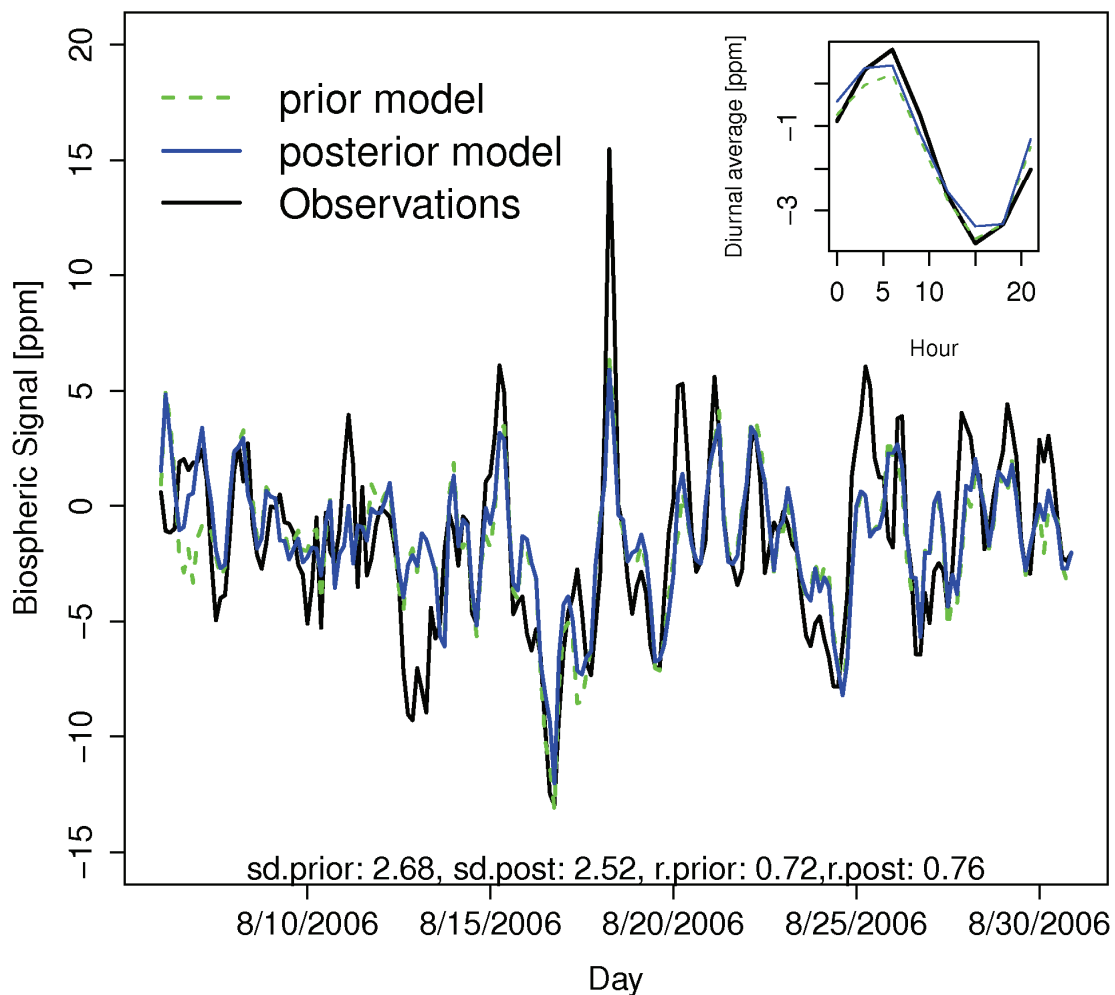
Figure 6.4 *Comparison of 3- hourly time series (column averaged) of observed (see Eq.7) and modeled (both prior and posterior) biospheric signals at OXK for a period from 6 to 30 August 2006. The inset shows the diurnally averages of these signals. The standard deviations of data-model mismatch (indicated by "sd") as well as correlations (indicated by "r") for prior (denoted as ".prior") and posterior fluxes (denoted as ".post") are shown inside the figure.*

The reduction in uncertainty, labeled ρ, for the individual elements of λ can be expressed as:

$$\rho = 1 - \frac{\sigma_{post}}{\sigma_{prior}} \qquad\qquad (10)$$

where the σ's are the square root of the diagonal elements of the corresponding covariance matrix. During August 2006, the posterior uncertainties are reduced considerably for crop with ~60 % uncertainty reduction for GEE and ~80 % for R_{eco} (e.g. see Fig. 6.8; more discussion in Sect. 6.4.1). The uncertainties are reduced to ~35% for mixed forest for both GEE and R_{eco}. For evergreen forest, the uncertainty reduction for the nested (rest) domain is ~40% (~35 %) for R_{eco}, whereas for GEE, it is ~18 % (~41%) for the nest (rest). For other vegetation types (deciduous forest and grass), the uncertainty reductions are small (below 10%). The details for other seasons are described in Sect. 6.4.1.
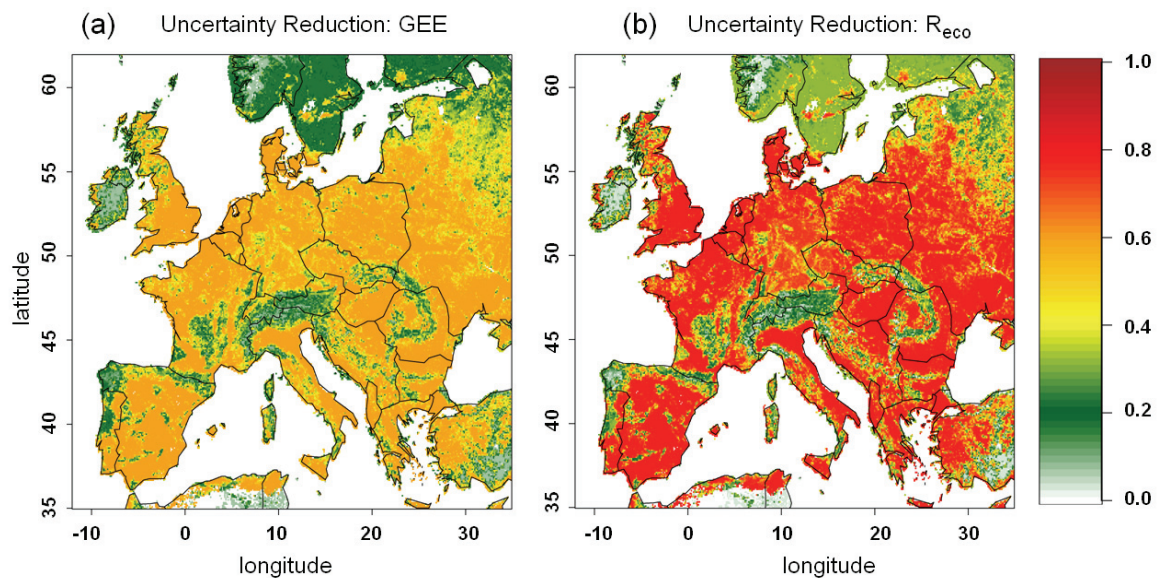

Figure 6.5 *The spatial distribution of uncertainty reduction for posterior fluxes- a) GEE and b) R_{eco} over Europe for August 2006.*

The uncertainty reductions of posterior fluxes are estimated by weighting ρ with vegetation fraction. **Figure 6.5** shows the spatial distribution of uncertainty reduction for posterior fluxes (separated for nest and rest of the domain) over Europe for August 2006. Notably, the posterior uncertainties are reduced considerably over Europe for both GEE and R_{eco}. It should be mentioned that the crop covers a large part of vegetation over Europe (see Table 6.4). However, the coastal and mountain regions are marked with less uncertainty reductions. The dominant vegetation types for these regions are either deciduous forest or grass for which values of the ρ are low.

145

Table 6.4 *Fraction of relative coverage of vegetation type for nested and parent domains.*

VPRM class	Nested Domain	Parent domain
Evergreen	0.09	0.11
Deciduous	0.08	0.06
Mixed forest	0.14	0.09
Cropland	0.68	0.68
Grassland	0.01	0.06

6.3.5   Prior and Posterior flux

The posterior fluxes are computed using λ_{post} derived from inverse optimization. **Figure 6.6** shows, as an example, the monthly averaged spatial distribution of prior and posterior fluxes at a spatial resolution of 10 km over Europe for August 2006 at 14 UTC.
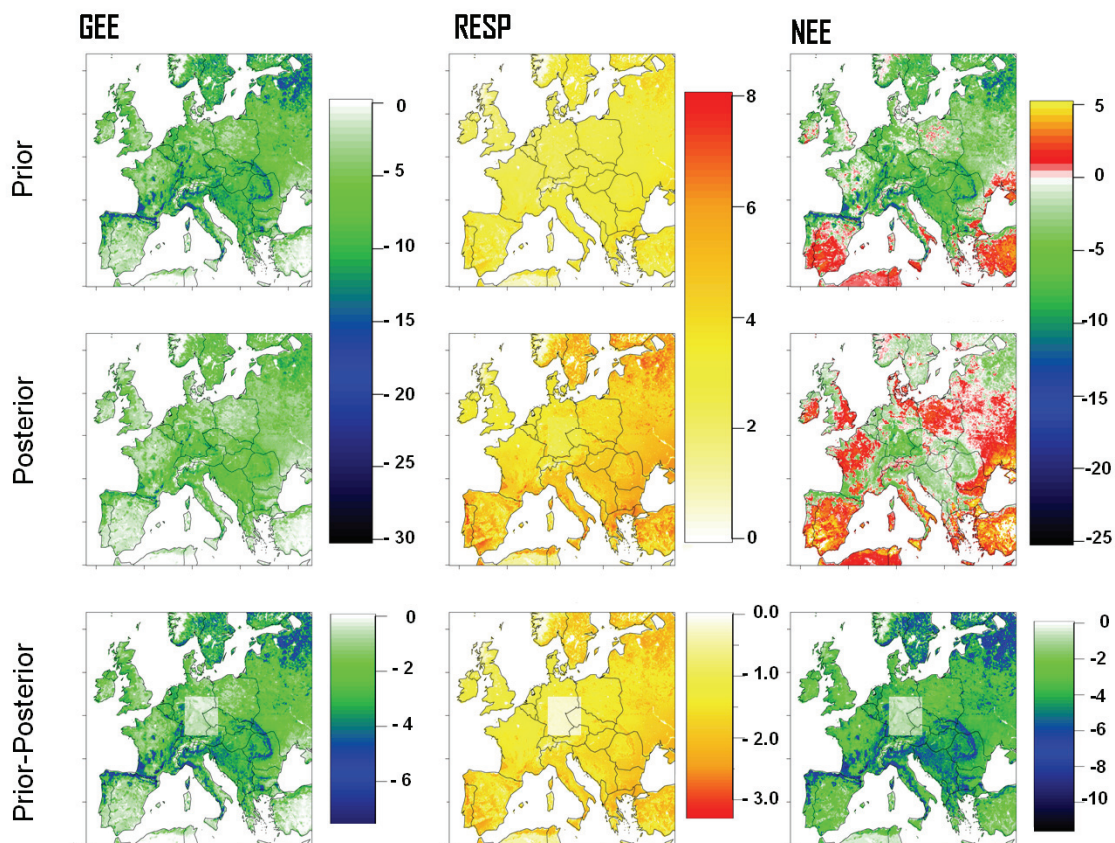

Figure 6.6 *Spatial distribution of monthly averaged prior and posterior fluxes at a spatial resolution of 10 km over Europe for August 2006 at 14 UTC. The panels from left to right denote GEE, R_{eco} and NEE respectively. The top panels show prior fluxes, middle panel gives posterior estimates and the bottom panels represent difference between prior and posterior fluxes.*

The posterior fluxes are estimated using λ_{post} separately for the nest and the rest of the domain. For these flux estimations, the temperature and radiation fields generated from the ECMWF model are used. Note that the WRF simulated fields are only available here for a smaller domain as mentioned previously. A relatively large CO_2 uptake can be seen during growing seasons over Europe, as indicated by large negative values for prior and posterior *GEE* and *NEE*. Positive values of *NEE* (CO_2 release) are found at the southern part of Europe (part of Spain and Turkey) where higher atmospheric temperature was simulated. Note that R_{eco} is linearly dependent on temperature. In general, the prior fluxes are slightly larger when compared to posterior estimations. This can also be seen as reduced λ_{post} for most of the vegetation types for both processes.

6.4   Discussion

6.4.1   Seasonal dependence of scaling factors

As seen in previous sections, the atmospheric measurements from the tower can provide important constraints for the VPRM scalars, allowing for flux retrieval at reduced uncertainty limits. The previous sections show the results from the mesoscale inversions using tower measurements from summer period where strong variability of surface fluxes and mesoscale transports are expected. Since diurnal patterns of biospheric fluxes and mesoscale transports vary seasonally, producing changes in the observed atmospheric CO_2 concentration, it is appropriate to examine the seasonal dependence of λ_{post}. For this, mesoscale inversions are conducted using tower measurements from different seasons separately (see Sect. 6.2.2.1), using the same prior VPRM scaling factors (see Sect. 6.2.2.4). **Figure 6.7** shows the seasonal variability of λ_{post} together with their uncertainty estimates for different vegetation types. Notably, the λ_{post} is found to be considerably different among the seasons for both *GEE* and R_{eco}. This result indicates the importance of using long-term measurements in the inverse framework which can constraint seasonal variability of surface fluxes.

The ρ of these scalars (see Sect. 6.3.4) for different seasons is shown in **Fig. 6.8**. The estimate of ρ depends on observational constraint as well as prior uncertainties. Consistent with the results for the summer period, ρ is found to be the largest for

cropland during other seasons also, however ρ for *GEE* is insignificant during the winter period. The other vegetation types – the deciduous and grassland – have low ρ for all seasons which indicates that the OXK measurements have only minor influence from these vegetation classes and thus cannot be expected to provide strong constraints on optimizing λ_{post} for these classes. Additional tower and
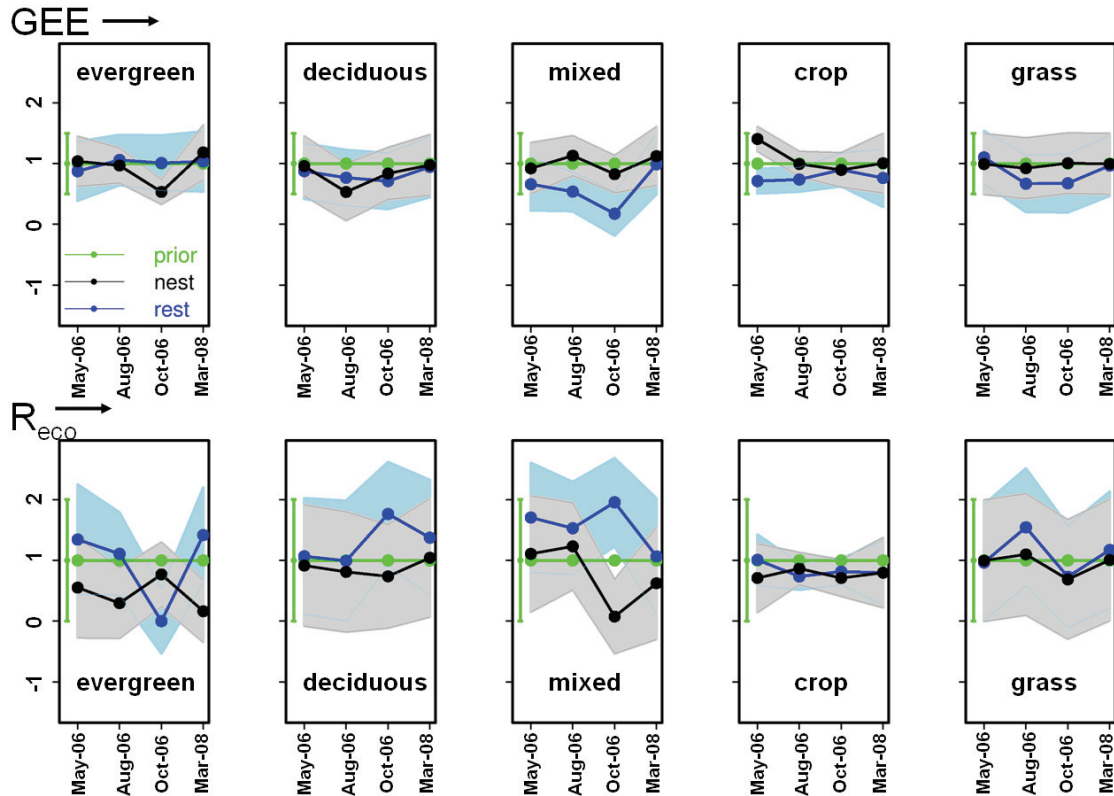

Figure 6.7 *The seasonal variability of VPRM scalars together with their uncertainty estimates for different vegetation types. The grey and light blue bands indicate the uncertainty of scalars from the nest and the rest of the domain respectively. The prior scaling factor is 1, indicated as green line and the uncertainty of prior scaling factors are shown as error bars at the extreme left side of each panel.*

airborne measurements at other locations, which exist but have not been used in this framework, can provide more constraints on carbon fluxes at large spatial scales, giving more reliable predictions of regional carbon budgets. Here the focus is on assessing the information that can be retrieved with this mesoscale inverse modeling framework for a single location with complex terrain.

The analysis show that ρ is larger for *GEE* (in particular for evergreen forest) in the nested domain compared to that in the rest of the domain, which indicates the importance of splitting the domain during inversion. A simple biospheric model like the VPRM – constrained with remote sensing and eddy covariance data streams – can

be a powerful tool to generate fluxes at high temporal and spatial scales which can greatly enhance the reliability of carbon budgets.
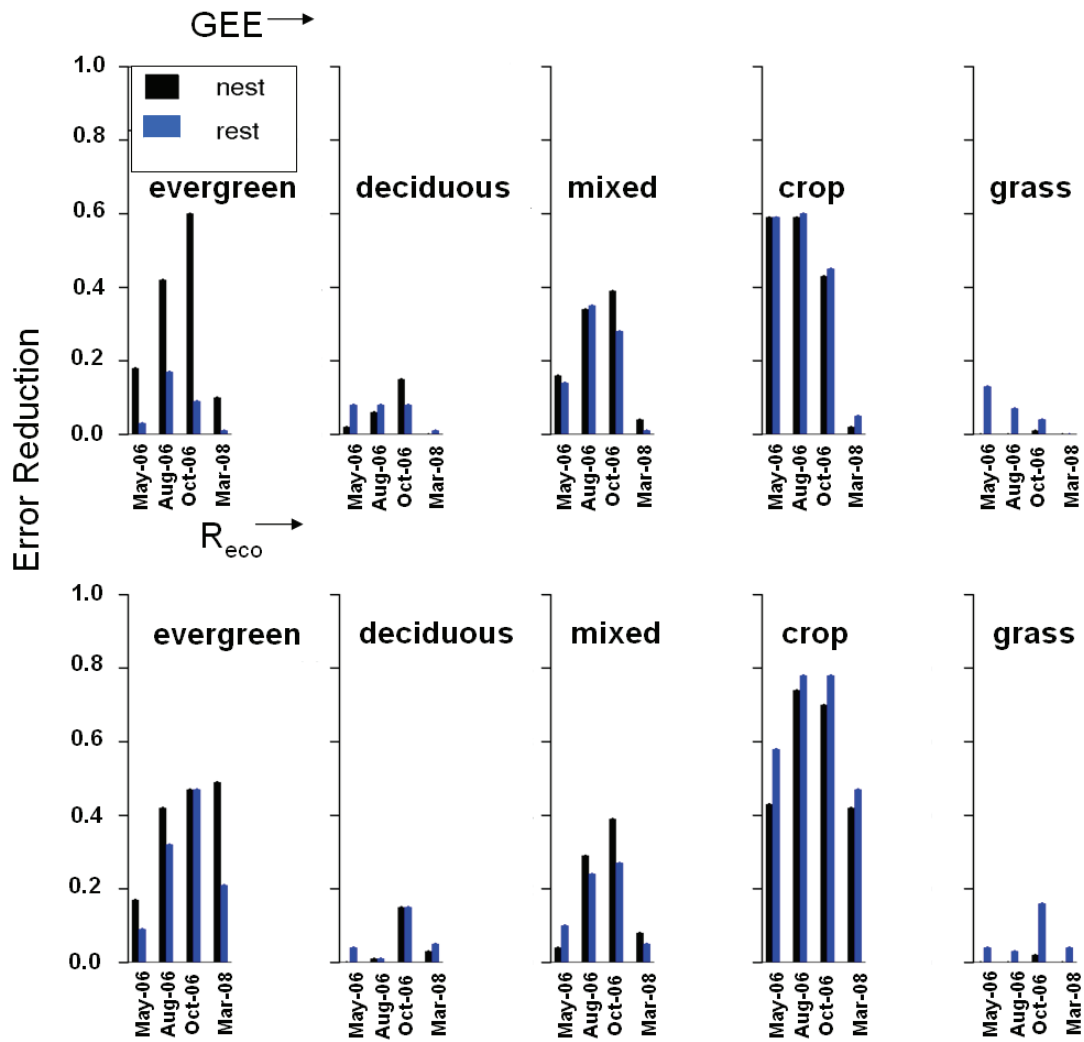

Figure 6.8 *The uncertainty reduction of posterior fluxes – GEE (top panel) and R_{eco} (bottom panel) – of different vegetation classes during different seasons. The panel from left to right shows different vegetation classes as indicated inside each graph.*

6.4.2   Flux comparison: Observed vs. modeled

The mesoscale inverse analysis illustrated the potential of using high-resolution transport and prior fluxes together with high-frequency (3- hourly) observational constraints to retrieve the information at reduced uncertainty limits. The mismatch between the modeled and the observed atmospheric CO_2 concentrations can be caused by uncertainties in prior fluxes (such as improper prior optimization (calibration) of the VPRM parameters and inadequate representation of processes) as well as transport error. Adjusting the scalars for each vegetation classes to best fit the observations increases the correlations of time series and diurnal patterns slightly (see

Fig. 6.4). However, only small changes in the general pattern of monthly averaged fluxes were found (see Fig. 6.6).

As a further investigation to this, the posterior fluxes from the nested domain are compared against observations from eddy flux sites. Note that these measurements used for comparison are completely independent of inversion analysis, as they were kept as validation sites (see Sect. 6.2.2.4). Since λ_{post} shows strong dependence on seasonal variability and greater uncertainty reduction in posterior fluxes for cropland, followed by evergreen, the comparison of fluxes from these vegetation sites are shown for different seasons in **Fig. 6.9** (winter is not included due to the limited availability of flux data in the area). The prior and posterior fluxes are able to capture the diurnal patterns of the observed fluxes. The enhanced biospheric activity (larger negative values) can be seen at the spring and the summer seasons when compared to the autumn season, however the reduced biospheric activity was observed at Klingenberg station (cropland) for the summer season that can be associated with the crop harvesting period.

For all these stations, the prior and the posterior fluxes have similar performance with smaller changes between them. The cropland where inversion produced the largest uncertainty reductions for all seasons (i.e. more constrained with atmospheric information) showed no further improvement at direct flux comparison. This can be due to two reasons: the existence of 1) a good prior or 2) transport errors in the inverse framework. The latter can be the most likely reason; however a further study is required to investigate the issues in detail. An enhancement in the positive fluxes of *NEE* (i.e. respiration signal) was observed at Klingenberg station during 5 to 10 August 2006, which was not captured by VPRM (neither in simulating prior nor in posterior fluxes). The WRF simulations show rain event (with maximum of ~15 mm) during this period and thus an increment in soil moisture. A well correlation was found between the respired flux and the soil moisture (figure is not shown) which suggests the structural improvement of VPRM to take into account of the soil moisture to calculate $R_{eco.}$
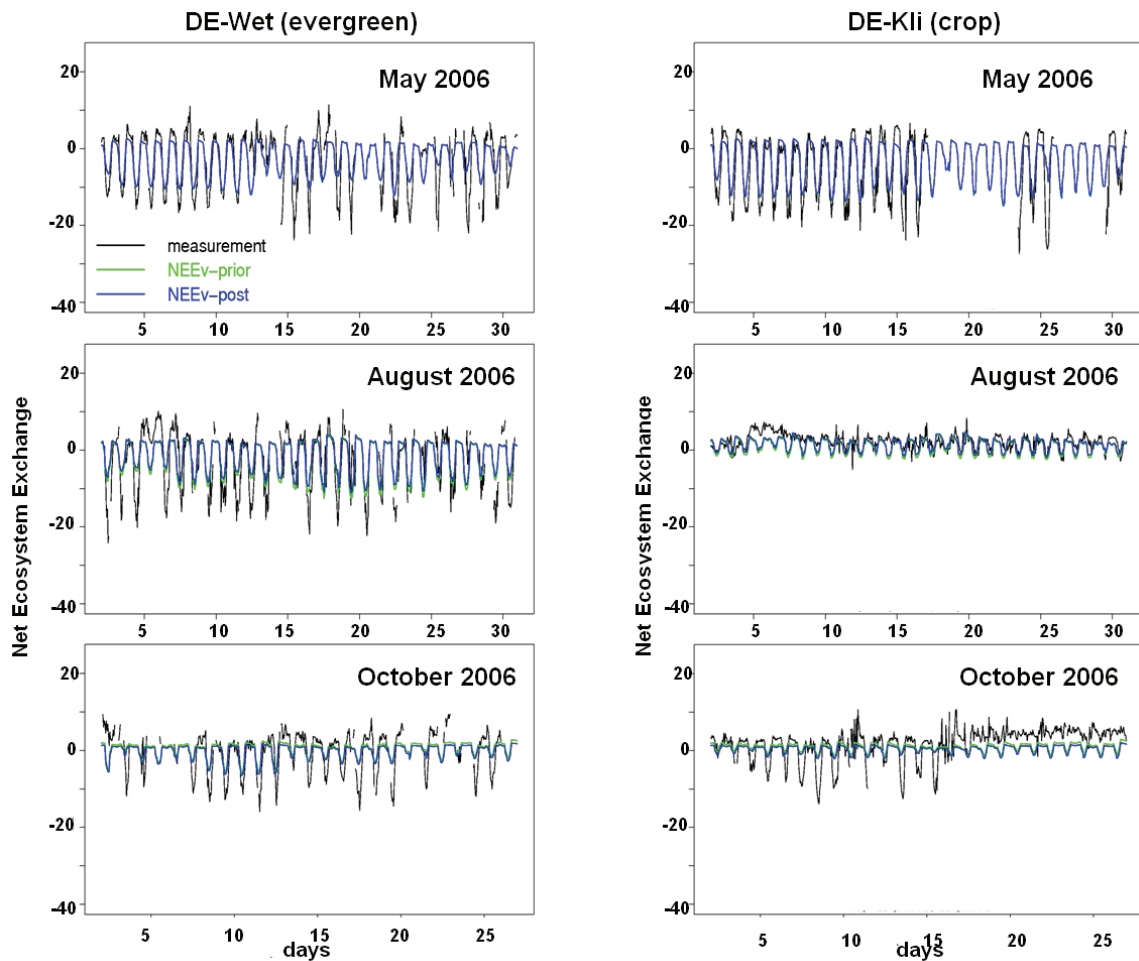
Figure 6.9 *Comparison of prior and posterior fluxes with observations from validation sites (DE-Wet and DE-Kli: Abbreviations of site names as in Table 2a) for different seasons. The panels from top to bottom indicate different seasons- May (spring), August (summer) and October (autumn) of the year 2006. The left panels indicate the site, DE-Wet and the right, DE-Kli. The vegetation type of the site is indicated in title within brackets.*

6.5   Conclusions

A mesoscale inversion framework using high-frequency observational constraints from Ochsenkopf tall tower as well as high-resolution transport and prior fluxes provided by WRF/STILT-VPRM modeling framework is presented in order to estimate the regional carbon fluxes with reduced uncertainties. The framework also utilizes the information provided by eddy covariance flux measurements and remote sensing data streams which are used to constrain prior fluxes in the inverse analysis. Hence this approach has the potential to provide the flux estimates that are consistent with both mixing ratio and eddy flux measurements.

A simple biospheric model – the VPRM – could capture reasonably well the spatial and temporal variability of CO_2 fluxes by using information from satellite and flux tower observations. Using the VPRM fluxes specified at high and temporal resolution can thus reduce the uncertainties associated with the representation of prior fluxes. In addition, the simple mathematical structure of the VPRM enhances the flexibility of optimizing respiration and photosynthesis fluxes separately in the inverse analysis. However, an enhancement in the positive fluxes of *NEE* observed in an eddy covariance flux station at Klingenberg could not be captured by the VPRM due to its structural deficiency in incorporating the effect of soil moisture to calculate the respiration fluxes. This suggests the importance of incorporating the soil moisture in parameterizing respiration fluxes in VPRM.

The inverse analysis shows large reduction in uncertainly of fluxes for cropland, followed by evergreen and mixed forests for both *GEE* and R $_{eco}$. As cropland covers most of the domain, the inversion generated large uncertainty reduction when deriving posterior fluxes over Europe. However, other vegetation types (the deciduous forest and the grassland) showed insignificant uncertainty reductions. This could be due to insufficient observational constraints to adjust the VPRM parameters for these vegetation types in the inverse analysis, i.e. the Ochsenkopf tower measurements alone might not be enough to constraint the VPRM scalars for all vegetation types. The higher dependence of the VPRM scalars on seasonal variability suggests the importance of using long-term measurements in the inversion framework covering all seasons. In addition, the results from nested domain show the potential of splitting the domains to constrain the regional fluxes.

The direct comparison between the observed and modeled fluxes at the validation sites produced similar performance between the prior and the posterior fluxes, although exists small differences between them. A further study is required to investigate whether these are caused by the transport errors in the inverse system. The validation of transport models with airborne measurements can greatly enhance the understanding of transport uncertainties in the model and can be used for further model development. It is thus emphasized that the current estimates of regional CO_2 budget can be improved via mesoscale inverse modeling, with the availability of more observational constraints together with reasonable prior information and adequate transport.

6.6   References

Ahmadov, R., Gerbig, C., Kretschmer, R., Koerner, S., Neininger, B., Dolman, A. J., and Sarrat, C.: Mesoscale covariance of transport and CO_2 fluxes: Evidence from observations and simulations using the WRF-VPRM coupled atmosphere-biosphere model, J. Geophys. Res.-Atmos., 112, D22107, doi:22110.21029/22007JD008552, 2007.

Chen, F., and Dudhia, J.: Coupling an advanced land-surface/hydrology model with the Penn State/NCAR MM5 modeling system. Part I: Model implementation and sensitivity, Monthly Weather Review, 129, 569-585, 2001.

Dudia, J.: Numerical study of convection observed during the winter monsoon experiment using a mesoscale two-dimensional model, Journal of Atmospheric Science, 46, 3077-3107, 1989.

Gerbig, C., Lin, J. C., Wofsy, S. C., Daube, B. C., Andrews, A. E., Stephens, B. B., Bakwin, P. S., and Grainger, C. A.: Toward constraining regional-scale fluxes of CO_2 with atmospheric observations over a continent: 2. Analysis of COBRA data using a receptor-oriented framework, J. Geophys. Res.-Atmos., 108, 4757, doi:4710.1029/2003JD003770, 2003a.

Gerbig, C., Lin, J. C., Wofsy, S. C., Daube, B. C., Andrews, A. E., Stephens, B. B., Bakwin, P. S., and Grainger, C. A.: Toward constraining regional-scale fluxes of CO_2 with atmospheric observations over a continent: 1. Observed spatial variability from airborne platforms, J. Geophys. Res.-Atmos., 108, 4756, doi:4710.1029/2002JD003018, 2003b.

Gerbig, C., Lin, J. C., Munger, J. W., and Wofsy, S. C.: What can tracer observations in the continental boundary layer tell us about surface-atmosphere fluxes?, Atmos. Chem. Phys., 6, 539-554, 2006.

Gerbig, C., Körner, S., and Lin, J. C.: Vertical mixing in atmospheric tracer transport models: error characterization and propagation, Atmos. Chem. Phys., 8, 591-602, 2008.

Gerbig, C., Dolman, A. J., and Heimann, M.: On observational and modelling strategies targeted at regional carbon exchange over continents, Biogeosciences, 6, 1949-1959, 2009.

Gurney, K. R., Law, R. M., Denning, A. S., Rayner, P. J., Baker, D., Bousquet, P., Bruhwiler, L., Chen, Y.-H., Ciais, P., Fan, S., Fung, I. Y., Gloor, M., Heimann, M., Higuchi, K., John, J., Maki, T., Maksyutov, S., Masarie, K., Peylin, P., Prather, M., Pak, B. C., Randerson, J., Sarmiento, J., Taguchi, S., Takahashi, T., and Yuen, C.-W.: Towards robust regional estimates of CO_2 sources and sinks using atmospheric transport models, Nature, 415, 626-630, 2002.

Heimann, M., and Koerner, S.: The global atmospheric tracer model TM3, Technical Reports, Max-Planck-Institute for Biogeochemie, 5, 131 p., 2003.

Hong, S.-Y., Dudhia, J.: Testing of a new non-local boundary layer vertical diffusion scheme in numerical weather prediction applications., 20th Conference on Weather Analysis and Forecasting/16th Conference on Numerical Weather Prediction, Seattle, WA., 2003.

Hong, S.-Y., J. Dudhia, S.-H. Chen: A revised approach to ice-microphysical processes for the bulk parameterization of cloud and precipitation, Monthly Weather Review, 132, 103-120, 2004.

Hong, S.-Y., Noh, Y and Dudhia, J: A new vertical diffusion package with an explicit treatment of entrainment processes, Monthly Weather Review, 134, 2318-2341, 2006.

Jung, M., Henkel, K., Herold, M., and Churkina, G.: Exploiting synergies of global land cover products for carbon cycle modeling, Remote Sens. Environ., 101, 534-553, 2006.

Kain, J. S., and J. M. Fritsch: Convective parameterization for mesoscale models: The Kain-Fritcsh scheme. The representation of cumulus convection in numerical models, K. A. Emanuel and D.J. Raymond, Eds., American Meteorological Society, 246, 1993.

Kaminski, T., Knorr, W., Rayner, P. J., and Heimann, M.: Assimilating atmospheric data into a terrestrial biosphere model: A case study of the seasonal cycle, Global Biogeochemical Cycles, 16, 1066, doi: 1010.1029/2001GB001463, 2002.

Lauvaux, T., Gioli, B., Sarrat, C., Rayner, P. J., Ciais, P., Chevallier, F., Noilhan, J., Miglietta, F., Brunet, Y., Ceschia, E., Dolman, H., Elbers, J. A., Gerbig, C., Hutjes, R., Jarosz, N., Legain, D., and Uliasz, M.: Bridging the gap between atmospheric concentrations and local ecosystem measurements, Geophys. Res. Lett., 36, L19809, doi:19810.11029/12009GL039574, 2009.

Law, R. M., Rayner, P. J., Steele, L. P., and Enting, I. G.: Using high temporal frequency data for CO_2 inversions, Global Biogeochemical Cycles, 16, 1053, doi:1010.1029/2001GB001593, 2002.

Lin, J. C., Gerbig, C., Daube, B. C., Wofsy, S. C., Andrews, A. E., Vay, S. A., and Anderson, B. E.: An empirical analysis of the spatial variability of atmospheric CO_2: Implications for inverse analyses and space-borne sensors, Geophys. Res. Lett., 31, L23104, doi:23110.21029/22004GL020957, 2004a.

Lin, J. C., Gerbig, C., Wofsy, S. C., Andrews, A. E., Daube, B. C., Grainger, C. A., Stephens, B. B., Bakwin, P. S., and Hollinger, D. Y.: Measuring fluxes of trace gases at regional scales by Lagrangian observations: Application to the CO_2 Budget and Rectification Airborne (COBRA) study, J. Geophys. Res.-Atmos., 109, D15304, doi:15310.11029/12004JD004754, 2004b.

Mahadevan, P., Wofsy, S. C., Matross, D. M., Xiao, X., Dunn, A. L., Lin, J. C., Gerbig, C., Munger, J. W., Chow, V. Y., and Gottlieb, E. W.: A satellite-based biosphere parameterization for net ecosystem CO_2 exchange: Vegetation Photosynthesis and Respiration Model (VPRM), Global Biogeochemical Cycles, 22, GB2005, doi:2010.1029/2006GB002735, 2008.

Mlawer, E. J., S. J. Taubman, P. D. Brown, M. J. Iacono, and S. A. Clough, 1997: Radiative trans-fer for inhomogeneous atmosphere: RRTM, a validated correlated-k model for the long-wave, Journal of Geophysical Research, 102, 16663-16682, 1997.

Monin, A. S., and Obukhov, A. M.: Basic laws of turbulent mixing in the ground layer of the atmosphere, Trans. Geophys. Inst. Akad. Nauk USSR, 151, 1954.

Pillai, D., Gerbig, C., Ahmadov, R., Rödenbeck, C., Kretschmer, R., Koch, T., Thompson, R., Neininger, B., and Lavrič, J. V.: High-resolution simulations of atmospheric CO_2 over complex terrain- representing the Ochsenkopf mountain tall tower, Atmos. Chem. Phys.(submitted), 2010.

Rayner, P. J., Scholze, M., Knorr, W., Kaminski, T., Giering, R., and Widmann, H.: Two decades of terrestrial carbon fluxes from a carbon cycle data assimilation system (CCDAS), Global Biogeochemical Cycles, 19, GB2026, doi:2010.1029/2004GB002254, 2005.

Rödenbeck, C.: Estimating CO_2 sources and sinks from atmospheric mixing ratio measurements using a global inversion of atmospheric transport. Technical Report 6, Max-Planck Institut für Biogeochemie, Jena, Germany, 53 pp., 2005.

Rodger, C. D.: Inverse Methods for atmospheric sounding: Theory and Practice, Atmospheric, Oceaninc and Planetary Physics, edited by: Taylor, F. W., World Scientific Publishing Co. Pte. Ltd Singapore, 240 pp., 2000.

Sarrat, C., Noilhan, J., Lacarrère, P., Donier, S., Lac, C., Calvet, J. C., Dolman, A. J., Gerbig, C., Neininger, B., Ciais, P., Paris, J. D., Boumard, F., Ramonet, M., and Butet, A.: Atmospheric CO_2 modeling at the regional scale: Application to the CarboEurope regional experiment, J. Geophys. Res.-Atmos., 112, D12105, doi:12110.11029/12006JD008107, 2007.

Takahashi, T., Sutherland, S. C., Sweeney, C., Poisson, A., Metzl, N., Tilbrook, B., Bates, N., Wanninkhof, R., Feely, R. A., Sabine, C., Olafsson, J., and Nojiri, Y.: Global sea-air CO_2 flux based on climatological surface ocean pCO_2, and seasonal biological and temperature effects, Deep-Sea Res. Part II-Top. Stud. Oceanogr., 49, 1601-1622, 2002.

Tans, P. P., Fung, I. Y., and Takahashi, T.: Observational constraints on the global atmospheric CO_2 budget, Science, 247, 1431-1438, 1990.

Thompson, R. L., Manning, A. C., Gloor, E., Schultz, U., Seifert, T., Hänsel, F., Jordan, A., and Heimann, M.: In-situ measurements of oxygen, carbon monoxide and greenhouse gases from Ochsenkopf tall tower in Germany, Atmospheric Measurement Techniques, 2, 573-591, 2009.

van der Molen, M. K., and Dolman, A. J.: Regional carbon fluxes and the effect of topography on the variability of atmospheric CO_2, J. Geophys. Res.-Atmos., 112, D01104, doi:01110.01029/02006JD007649, 2007.

7   Conclusions and Outlook

The main conclusions of the thesis are given here as brief answers to the scientific questions which were raised in **Sect. 1.6** (Thesis Objectives), together with possible future developments of the results (under the heading *Outlook*, specific for each chapter).

1. **How much of the spatial variability of atmospheric CO_2 concentration cannot be resolved by current global models?**

Chapter 3 addresses this question. Based on high-resolution model simulations, a quantitative assessment of spatial variability of CO_2 over Europe is carried out in the context of utilizing satellite retrievals of column-integrated atmospheric CO_2 concentrations in global inverse models with a horizontal resolution of about 1 degree or more. The spatial scale mismatch between remotely-sensed CO_2 and global models can induce so-called representation errors of up to 1.2 ppm, which is above the targeted precision of most satellite measurements. This may lead to a systematic bias in flux estimates when using inverse modeling approaches. The analysis with a hypothetical satellite (A-SCOPE) track together with MODIS cloud pixel information shows a larger representation error of 0.39 ppm over land compared to other regions. The results clearly indicate the necessity of using high-resolution simulations to assess variability on scales not resolved by global models.

2. **Can we parameterize this variability in coarser models without using high-resolution simulations?**

Knowledge about the size and the spatial and temporal patterns of the representation error is expected to improve inverse modeling of satellite data. Avoiding the representation error would involve using a high-resolution model to estimate the representation error, but is computationally very expensive and hence not feasible in global inverse modeling systems.   Chapter 3 demonstrates a potential way of describing representation error in coarser models without increasing the spatial resolution of the models. A linear model is constructed, separately for day- and nighttime, to parameterize the sub-grid scale variability (or representation error) as a function of local, grid-resolved variables, such as terrain heterogeneity, surface flux variability and mean CO_2 mixing-ratio at the surface. The proposed linear model

(using all three variables mentioned above) could explain about 50 % of the spatial patterns in the bias component of the subgrid variability during day- and nighttime. These findings suggest a parameterization which would enable a substantial fraction of the representation error to be taken into account more quantitatively, without using high-resolution transport models.

Outlook (1 & 2):

Future steps involve implementation of this parameterization in an inverse modeling system. An assessment using pseudo-data experiments has to be carried out to determine the degree to which biases in retrieved fluxes due to representation error can be avoided. A further refinement of the method would treat the subgrid variance as a tracer itself, allowing for advection of subgrid variance within the coarse transport models similar to the study by Galmarini et al. (2008), but with a focus on mesoscale variability. This would also allow for the better description of the representation error over the ocean near the coasts, which with the current linear (local) model cannot be described. It is anticipated that the retrieved information, such as regional carbon budgets and uncertainties, will improve significantly when including such a realistic description of the representation error into a data assimilation system that uses remotely-sensed column CO_2.

3. **What is the effect of complex mesoscale flows on the observed atmospheric CO_2 fields? Can we represent this effect in the model?**

Chapter 4 addresses this question by utilizing the measurements from the Ochsenkopf tall tower observatory (OXK), located in complex terrain on the second highest peak of the Fichtelgebirge mountain range in Germany, as well as using profiles from an airborne campaign at Ochsenkopf. The detailed analysis of two case studies concluded that the mesoscale transport features, such as mountain waves and mountain-valley circulation, can have a strong influence on the observed atmospheric CO_2 at OXK by changing the vertical mixing of the tracer concentrations. The meteorological simulations indicate that the buoyancy-driven drainage flows are more common at OXK during nighttime (especially in summer) and that mountain gravity waves are likely to occur in winter periods. The study shows that these effects can be reproduced reasonably well with high-resolution models at a spatial resolution of

2 km by appropriately representing mesoscale transport processes, such as advection, convection and vertical mixing as well as surface flux influences in the near-field.

4. How well are measurements from complex sites such as mountain observatories reproduced by the high-resolution modeling framework compared to current global models?

Chapter 4 further explores the advantages of using a high-resolution modeling framework to address the representativeness of greenhouse gas measurements when compared to coarse resolution models over a complex terrain associated with surrounding mountain ranges. The study utilizes available measurements obtained from OXK for different seasons and from an aircraft campaign together with a high-resolution modeling framework consisting of Eulerian- and Lagrangian-based tracer transport models. The spatial and temporal patterns of CO_2, caused by mesoscale flows and strong variability of surface fluxes (fossil fuel emissions and biosphere-atmosphere exchange) that are common for complex sites such as mountain stations, are reproduced remarkably well by the high-resolution models for different seasons when compared to the coarse model. This emphasizes the importance of using high-resolution modeling tools in inverse frameworks, since a small deviation in CO_2 concentrations can lead to potentially large biases in flux estimates. It is found that discrepancies in the representation of vertical mixing, which are typical for regions with complex terrain, can lead to strong biases in simulated CO_2 concentrations. The study points out the importance of vertical profiling of CO_2 (such as provided by aircraft campaigns) or meteorological fields (like wind profiler measurements) for assessing the impact of vertical mixing on tracer concentrations.

5. Can we use these measurements in future inversion studies?

Measurements from mountain sites provide larger scale representativeness compared to those made from towers located on flat terrain. Moreover, the longest greenhouse gas records are often from mountain sites, making them a valuable ingredient for assessing longer-term variations in carbon budgets. However, inversion studies often exclude the data from mountain or complex terrain sites, or give them less statistical weighting (larger uncertainty), or implement temporal data filtering of the measurements (e.g. selection of nighttime-only data at mountain sites) due to the models' (both global and regional scale models) inability to represent complex terrain and to capture mesoscale flow patterns at mountain sites. Chapter 4 addresses this

issue by using models with high spatial resolution. The study successfully demonstrates that the high-resolution modeling framework can capture the synoptic, seasonal and diurnal variability of observed CO_2 concentrations over a complex site such as OXK, which is a prerequisite for the inverse modeling systems to utilize measurements from these sites. This indicates that measurements from these sites can be included in future inversion studies by properly implementing high-resolution tools into the current global inverse models.

Outlook (3, 4 & 5):

The actual reduction in uncertainties of flux estimates when using high-resolution models (compared to lower-resolution models) needs to be further investigated. Future work will focus on inversions using high-resolution models nested in global models so that measurements from mountain stations can be utilized in inverse modeling frameworks to derive regional CO_2 budgets at reduced uncertainty limits. The feasibility of using these high-resolution nests in global models has already been demonstrated by Rödenbeck et al. (2009).

6. **How consistent are different model components of the model-data fusion system?**

The consistency of different components of the model-data fusion system is important since the flux estimates can be biased if different realizations of turbulence, vertical mixing and numerical diffusion exist between models. Hence a consistency check has to be carried out as a first step towards applying STILT as an adjoint of WRF in the inverse modeling system. This is addressed in Chapter 5. The modeling system involving two tracer transport models based on different governing equations of motion − STILT (Lagrangian based) and WRF (Eulerian based) − are examined for their consistency in parameterizing transport and vertical mixing of atmospheric CO_2 concentrations. The inter-model comparisons show similar performance in predicting CO_2 concentration at and around OXK with high correlations. The factors contributing to the remaining discrepancies between the models are identified. The inter-model differences, albeit small in most of the cases, are caused mainly by the discrepancy in the representation of the interaction between turbulent mixing and advection through wind shear between STILT and WRF. Based on observations and inter-model comparisons, it is concluded that a refinement of the parameterization of

turbulent velocity variance and Lagrangian time-scale in STILT is required to achieve a better match between the Eulerian and the Lagrangian transport at high spatial resolution. This is especially true for extreme cases when signatures from strong sources such as fossil fuel emissions are transported over large distances and dominate over those from local sources (e.g. biospheric fluxes). Nevertheless, the inter-model differences in simulated CO_2 time series at OXK are about a factor of two smaller than the model-data mismatch and about a factor of three smaller than the mismatch between the current global model simulations and the data, which justifies using STILT as an adjoint model of WRF. It is also concluded that the existing inter-model difference in local mixing heights (z_i) has only a negligible impact on simulated CO_2 concentrations between models due to a spatially variable boundary layer top in the simulation, which does not act as a barrier to the vertical mixing.

Outlook (6):

Future steps involve further refinement of the turbulent velocity variance and Lagrangian time-scale parameterizations in STILT, which were originally developed for coarse resolution meteorological fields (at spatial resolutions of at most 20 km). This is required to exclude any possible discrepancies between these models at high-resolution (e.g. using meteorological fields at a spatial resolution of 2 km) which will cause uncertainties on derived regional flux estimates. The parameterization of z_i in the transport models needs to be further improved in order to avoid unrealistic spatial variations in the boundary layer top as seen in the simulations.

7. **Do we have an inversion technique which has the potential to provide regional flux estimates at reduced uncertainty limits?**

Chapter 6 presents a mesoscale inversion framework using high-frequency observational constraints from OXK as well as high-resolution transport and prior fluxes provided by the WRF/STILT-VPRM modeling framework, in order to estimate regional carbon fluxes with reduced uncertainties. The approach, utilizing the information provided by eddy covariance flux measurements and remote sensing data streams, has the potential to provide flux estimates that are consistent with both mixing ratio and eddy flux measurements. Using the VPRM biospheric model at high and temporal resolution reduces the uncertainties associated with representation of

prior fluxes in the inverse modeling system. A large reduction in uncertainly of fluxes is found for the cropland vegetation type, followed by evergreen and mixed forests. The seasonal dependence of optimized (via inversion) VPRM scalars suggests the importance of using long-term measurements in the inversion framework and covering all seasons. The direct comparison between observed (which are not used in the optimization) and modeled fluxes show that the simulated fluxes − both prior (before inversion) and posterior (after inversion) − are able to capture the diurnal patterns of observed fluxes. For all these flux measurement stations, the prior and posterior fluxes display similar agreement with only small changes. We emphasize that with the availability of more observational constraints together with reasonable prior information and adequate transport, the current regional CO_2 budget estimates can be improved via mesoscale inverse modeling.

Outlook (7):

The study will be extended by using additional observational constraints from existing tower and airborne measurements at other locations. The information gain when using high-resolution models (compared to lower-resolution models) in the inverse framework will be further assessed. This is in line with the future work proposed in Outlook (3, 4 & 5).

A APPENDIX

A1 List of acronyms

CCDAS	—	Carbon Cycle Data Assimilation System
CarbonSat	—	Carbon monitoring SATellite.
CASA	—	Carnegie-Ames-Stanford Approach
CHIOTTO	—	Continuous High-precisIOn Tall Tower Observations of greenhouse gases
COBRA	—	CO_2 Budget and Rectification Airborne study
DIC	—	Dissolved Inorganic Carbon
ENVISAT	—	ENVIronmental SATellite
ESA	—	European Space Agency
GCM	—	General Circulation Model
LPDM	—	Lagrangian Particle Dispersion Model
LUE	—	Light Use Efficiency
MRT	—	MODIS Reprojection Tool
PBL	—	Planetary Boundary Layer
REMO	—	REgional MOdel
SCIAMACHY	—	SCanning Imaging Absorption spectroMeter for Atmospheric CHartographY
CERES	—	CarboEurope Regional Experiment Strategy
ECMWF	—	European Centre for Medium-range Weather Forecast
FT	—	Free Troposphere
HDF	—	Hierarchical Data Format
HYSPLIT	—	HYbrid Single-Particle Lagrangian Integrated Trajectory
IER	—	Institut für Energiewirtschaft und Rationelle energieanwendung
JAXA	—	Japan Aerospace eXploration Agency
GOSAT	—	Greenhouse gases Observing SATellite
MODIS	—	MODerate resolution Imaging Spectroradiometer
NASA	—	National Aeronautics and Space Administration
OCO	—	Orbiting Carbon Observatory
STILT	—	Stochastic Time-Inverted Lagrangian Transport model

USGS	—	U.S. Geological Survey
VPRM	—	Vegetation Photosynthesis and Respiration Model
WRF	—	Weather Research and Forecasting model
WPS	—	WRF Preprocessing System
YSU	—	YonSei University
TM3	—	Transport Model-3
TransCom	—	atmospheric tracer Transport model interComparison project
WMO	—	World Meteorological Organization
WRF-Chem	—	WRF-Chemistry

A2 List of physical constants

π = 3.1415926 (pi)

k = 0.4 (von Kármán's constant)

r_e = 6.370×10^6 m (Radius of earth)

g = 9.81 m s^{-2} (Acceleration due to gravity)

Ω_e = 7.2921×10^{-5} s^{-1} (Angular rotation rate of the earth)

σ_B = 5.67051×10^{-8} W m^{-2} K^{-4} (Stefan-Boltzmann constant)

R_d = 287 J kg^{-1} K^{-1} (Gas constant for dry air)

R_v = 461.6 J kg^{-1} K^{-1} (Gas constant for water vapor)

c_p = $7 \times R_d/2$ J kg^{-1} K^{-1} (Specific heat of dry air at constant pressure)

c_v = $c_p - R_d$ J kg^{-1} K^{-1} (Specific heat of dry air at volume)

c_{pv} = $4 \times R_v$ J kg^{-1} K^{-1} (Specific heat of water vapor at constant pressure)

c_{vv} = $c_{pv} - R_v$ J kg^{-1} K^{-1} (Specific heat of water vapor at constant volume)

c_{liq} = 4190 J kg^{-1} K^{-1} (Specific heat capacity of water)

c_{ice} = 2106 J kg^{-1} K^{-1} (Specific heat capacity of ice)

L_v = 2.5×10^6 J kg^{-1} (Latent heat of vaporization)

L_s = 2.85×10^6 J kg^{-1} (Latent heat of sublimation)

L_f = 3.50×10^5 J kg^{-1} (Latent heat of fusion)

ρ_w = 1.0×10^3 kg m^{-3} (Density of liquid water)

Acknowledgement

I would like to express my sincere gratitude to many people who have tremendously supported and inspired me to shape this thesis as it is now. I say thank-you to all of them. Some of them are particularly acknowledged below.

My PhD supervisors, Dr. habil. Christoph Gerbig and Prof. Dr. Christiane Schmullius, deserve a special expression of my gratitude due to their unstinting commitment, valuable insight and steadfast encouragement which have greatly influenced the content of this thesis. Christoph, being my "immediate" supervisor, always encouraged me to develop self-sufficiency in research, but at the same time, never failed to provide me with timely guidance, sound advice, constructive criticism and many good ideas. I especially thank him for his friendliness as well as open-door policy to various discussions which made my graduation study more or less smooth. I am honored to have Christiane as my university supervisor who often amazed me with her enthusiasm, understanding and cooperation. I thank her for the continued support, immediate responses and fruitful discussions.

I am indebted to Prof. Dr. Martin Heimann for his valuable suggestions, outstanding support and most importantly, his constant encouragement which was paramount to enhance my motivation especially during the writing phase of the thesis. It is my pleasure to thank him particularly for his inspiring talks and his efforts to provide a broad scientific picture of the topic. I would also like to thank Dr. Ute Karstens and Dr. Ravan Ahmadov for their support and active involvement in my PhD Advisory Committee (PAC). It was Ravan who helped me to familiarize with atmospheric models in the initial stage of my graduation study.

I am thankful to Max Planck Society for the funding and facilities. I wish to thank the Faculty of Chemical and Earth Sciences in Friedrich Schiller University Jena for their cooperation. The work presented in Chapter 3 has been supported through European Space Agency funding. I thank François-Marie Bréon for providing the algorithm to calculate the A-SCOPE track and to select cloud free pixels. I would like to thank Prof. Dr. Thomas Foken for providing wind profiler data. I am grateful to all co-authors of my publications for the scientific discussions and cooperation.

165

The group-leaders and the post-doctoral fellows of the BGC-Systems department in the institute have given me all sorts of support throughout my graduation study. I owe my gratitude to Dr. Christian Rödenbeck for his support and sincere efforts in organizing department seminar series. I would also like to thank Dr. Dietrich Feist, Dr. Sönke Zaehle, Dr. Jošt Valentin Lavrič and Dr. Gregor Schürmann for the interesting scientific discussions. Special thanks must go to Dr. Julia Marshall for her ever-ready attitude, scientific cooperation and willingness to proofread the thesis within the limited time. I say my thank-you to Dr. Daniela Dalmonech for having funny moments together and accompanying for a cup of coffee whenever needed.

The doctoral and the master students in the institute especially those from the BGC-Systems department have been influential in many ways. First and foremost, my special thanks to Veronika Beck for her friendliness and perfect listening. I must also acknowledge her for translating effectively the thesis abstract to German. I wish to thank Anna Görner, Dr. Julia Steinbach, Annette Filges, Marc Geibel, Bakr Badawy, Dr. Huilin Chen, Gionata Biavati, Jan Winderlich, Stephan Baum and Roberto Kretschmer for being friendly and supportive. It would have been desperately monotonous without the entertainment and the comradeship they provided.

I would like to thank Dr. Thomas Koch and Stefan Körner for their assistance in programming and data retrievals. I am thankful to Silvana Schott, Karen Harm and Birgitta Wiehl for their technical and organizational supports. I am grateful to whole Ochsenkopf tall tower team including Thomas Seifert, Uwe Schultz for their assistance in data processing and importantly for their friendliness. It is my pleasure to thank Dr. Rona Thompson for providing me with details of the tower data and answering many of my queries about the data. I would like express my appreciation to Dr. Bruno Neininger and David Oldani for their sincere efforts in the Ochsenkopf aircraft campaign and also for giving me the opportunity to be onboard as well as to fly around Jena.

In relation to a huge computational work in my modelling studies, all members of the IT department deserve a special appreciation for their tremendous and efficient support. Thanks must go to Dr. Peer-Joachim Koch, Bertram Smolny and Jörg Hollandmoritz for responding effectively many of my queries related to computer software/hardware. Many other people in the institute offered me a friendly

Curriculum Vitae

Education	1998	School education (High-school and Higher-secondary) Varkala, Kerala, India
	1998-2001	Bachelor of Science in Physics M. G. University, Kottayam, India
	2001-2003	Master of Science in Physics M. S. University, Tirunelveli, India
	2003-2005	Master of Technology in Ocean Technology Cochin University of Science and Technology, Kochi, India
	2007-present	PhD Thesis Max Planck Institute of Biogeochemistry/ Friedrich Schiller University, Jena, Germany
Experience	2004-2006	Indian Space Research Organization, Bangalore, India National Atmospheric Research Laboratory, Tirupati, India Indira Gandhi Centre for Atomic Research, Kalpakkam, India

Publications

Pillai, D., Gerbig, C., Marshall, J., Ahmadov, R., Kretschmer, R., Koch, T., and Karstens, U.: High resolution modeling of CO_2 over Europe: implications for representation errors of satellite retrievals, Atmos.Chem.Phys, 10, 83-94, 2010.

Pillai, D., Gerbig, C., Ahmadov, R., Rödenbeck, C., Kretschmer, R., Koch, T., Thompson, R., Neininger, B., and Lavrič, J. V.: High-resolution simulations of atmospheric CO_2 over complex terrain- representing the Ochsenkopf mountain tall tower, Atmos. Chem. Phys.(submitted), 2010.

Jena,   Dhanyalekshmi K. Pillai

Selbstständigkeitserklärung

Ich erkläre, dass ich die vorliegende Arbeit selbstständig und nur unter Verwendung der angegebenen Hilfsmittel, persönlichen Mitteilungen und Quellen angefertigt habe.

Jena,   Dhanyalekshmi K. Pillai